Study of innovative solutions to improve the quality of metallic components manufactured by additive manufacturing technologies

Politecnico di Bari

Department of Mechanics, Mathematics and Management
MECHANICAL AND MANAGEMENT ENGINEERING

Ph.D. Program
SSD: ING-IND/16 – MANUFACTURING TECHNOLOGY AND SYSTEMS

Final Dissertation

Study of innovative solutions to improve the quality of metallic components manufactured by additive manufacturing technologies

by
VITO ERRICO

Supervisor:

Prof.ssa Sabina Luisa CAMPANELLI

Coordinator of Ph.D. Program:

Prof. Giuseppe Pompeo DEMELIO

Course n°35, 01/11/2019 - 31/12/2022

Department of Mechanics, Mathematics and Management
MECHANICAL AND MANAGEMENT ENGINEERING

Ph.D. Program
SSD: ING-IND/16 – MANUFACTURING TECHNOLOGY AND SYSTEMS

Final Dissertation

Study of innovative solutions to improve the quality of metallic components manufactured by additive manufacturing technologies

by
VITO ERRICO:

Supervisor:

Referees:

Prof. Claudio LEONE

Prof.ssa Sabina Luisa CAMPANELLI

Ing. Fania PALANO

Coordinator of Ph.D. Program:

Prof. Giuseppe Pompeo DEMELIO

Course n°35, 01/11/2019 - 31/12/2022

Preface

This Ph.D. thesis has been submitted to report and describe the research carried out during the period from November 2019 to December 2022 at the Department of Mechanics, Mathematics, and Management (DMMM) of the University Polytechnic of Bari (PoliBa). This doctoral work has been performed under the supervision of Professor Sabina Luisa Campanelli.

Acknowledgments

…

Contents

Table of Figures

Thesis outline

This thesis consists of an introductory part (chapter 1 – "Metal Additive Manufacturing processes"), which describes the main technological processes investigated in this thesis work; two chapters (chapter 2 – "Laser-Directed Energy Deposition process monitoring methods", and chapter 3 – "Laser-Powder Bed Fusion process monitoring methods") introducing the research background and the current challenges to address and overcome on the monitoring methods of these processes; a collection of four journal papers showing the applications (chapter 4 – "Applications of the developed monitoring systems") of the monitoring systems developed and presented in the previous two chapters, and two conclusive chapters with main findings (chapter 5 – "Conclusions") and future challenges (chapter 6 – "Future perspectives"). A brief description of the chapters is given below.

Chapter 0 – *Introduction* – It introduces the main motivations and challenges addressed in the thesis.

Chapter 1 – *Metal Additive Manufacturing processes* – It presents an overview of the technological processes addressed in the thesis, the physical principles behind them and major applications.

Chapter 2 & Chapter 3 – *Laser-Directed Energy Deposition process monitoring methods* – & – *Laser-Powder Bed Fusion process monitoring methods* – The research background required to insert this thesis into a more general framework together with the current challenges partly addressed in the herein papers is presented.

Chapter 4 – *Applications of the developed monitoring systems* – It contains a collection of four journal papers showing applications of the monitoring systems developed and presented in the previous two chapters.

Chapter 5 & Chapter 6 – *Conclusions* – & – *Future perspectives* – The main findings of the thesis together with conclusive remarks on the future challenges to address and potential new research avenues are here reported.

Introduction

Aware of the small contribution one can provide to human knowledge, in this dissertation, I ambitiously attempt to understand what the technological limitations of Metal Additive Manufacturing (MAM) processes may be, which slow down their deployment in industrial sectors.

Under the main supervision and mentorship of Prof. Sabina Luisa Campanelli and the entire research team, Prof. Andrea Angelastro, Eng. Paolo Posa, Eng. Andrea Fusco and Eng. Marco Mazzarisi, the aim of my thesis work was to develop new process monitoring systems, which can be implemented in-situ and in real-time, in order to improve the final product quality and increase process repeatability by overcoming the main issues, which make MAM processes inadequate for high-value applications requiring high-performance standards.

Motivations & Challenges

The socio-economic context of the last decade was characterized by aspects such as flexibility, optimization of production, reduction of time, waste, costs, and respect for the environment; this has driven the academic and industrial world towards new production methods. Additive Manufacturing (AM) was born to overcome the problems and limitations of traditional subtractive processing techniques. With AM technologies, it is possible to optimize and make the design of parts more flexible without needing special molds and tools, thus reducing production time and associated costs [1]. As a result of the increasing number of AM technologies being developed, with different materials and equipment used, in 2010 the American Society for Testing and Materials (ASTM) formed the "ASTM F42-Additive Manufacturing" committee, that published a set of standards classifying the range of additive manufacturing technologies into seven categories, each one with its advantages and disadvantages: VAT Photopolymerization, Photopolymerization of Materials, Binder Jetting, Extrusion of Materials, Powder Bed Fusion (PBF), Plate Rolling and Directed Energy Deposition (DED) [2,3]. Specifically, in this thesis work, the two additive technologies addressed are Laser-Directed Energy Deposition (L-DED) and Laser-Powder Bed Fusion (L-PBF). The L-DED is an additive manufacturing process based on laser cladding, which mainly focuses on 3D manufacturing and repair applications. L-DED has a high potential for component production through 3D deposition strategies for the creation of clads with quite good microstructures less prone to cracks and also to build non-homogenous structures [4]. The laser deposition of metal powders is also particularly suitable to produce metal components with complex geometry or employing innovative materials, extremely difficult to work with utilizing traditional techniques. This explains the growing interest of

the industry in the L-DED process, mainly in highly specialized manufacturing sectors [5]. As for the L-PBF process, it is gaining more interest both from an academic and an industrial point of view, especially for high-value applications requiring high precision [3]. In fact, this process has a high potential to produce parts with complex geometry, not achievable with traditional technologies, having internal cavities, thin walls, and lattice structures, similar to foam, directly from powder in a single process [6–8]; this allows reducing production costs for the creation of small batches, or at the extreme, of single parts [6]. However, from an economic point of view, the spreading of these processes in the industrial sector is slowed down by technical challenges still to be solved. The main issues are the sub-optimal quality (in terms of dimensional accuracy and surface regularity) of the final parts and the low repeatability, which make these processes inadequate for high-value applications requiring high-performance standards. In order to overcome these problems and improve product quality and process repeatability, several research groups investigated in-situ process monitoring, characterization, and real-time process control. Process monitoring involves observation, information gathering, understanding of physical phenomena occurring in laser-material interactions, and finally, the development of automated process control systems. This is also an essential method to reduce costs and the amount of material waste. Starting from the possible defects, one of the main purposes of the in-process monitoring tools is to identify specific process signatures, in order to relate them to specific defects or process inaccuracies. In this context, in-situ monitoring tools have the potential to detect the onset of defects during the process, reducing the waste of materials, energy, and process time, allowing adjusting the process without interruptions, as well as the rework of specific areas characterized by defects, i.e. surface breaking pores [9]. The same tools are the start for more advanced real-time monitoring capabilities to detect and automatically classify anomalies occurring during the process, fundamental for real-time regulation and process adjustment [10]. This can be achieved by using different kinds of sensors and technologies [11,12]. Several classifications of monitoring tools exist, according to the working principle and the technology applied, or according to the monitoring tasks. They can be mainly related to acoustic, thermal (using thermal imaging cameras, pyrometers, and bolometers), and optical methods (using a camera with active-pixel sensors, such as CMOS or CCD sensors, or photodiode sensors) [13]. Thermal monitoring is usually used for monitoring temperature-related signatures, such as melt pool dimensions, temperature profiles, cooling history, and hot and cold spots [14]. Optical methods in the form of high-resolution imaging sensors are mostly used for the evaluation of melt pool dimensions, geometric features and identification of defects layer by layer [15]. Monitoring methods can be also classified, regarding the

topological setup, as on-axis (coaxial) and off-axis with respect to the laser beam. In co-axial configurations, sensors follow the optical path of the power source, while in off-axial configurations, sensors are placed with a given angle-of-view concerning the region of interest and they are outside the optical path. Equipment with different technical characteristics can detect different aspects of the process, and by combining different systems, more sophisticated analyses can be carried out [16]. Despite the many monitoring approaches already reported in the literature, the complexity of the L-DED and L-PBF technologies makes the research in this field ever more demanding for industrial implementation.

Here, I provide several contributions that attempt to address these challenges. Specifically, in this thesis work, I developed an image processing methodology that was implemented in combination with a coaxial optical system in order to study the melt pool geometry created during the manufacture of components or coatings using the L-DED process. In addition, I developed a cost-effective, flexible and easy-to-use optical monitoring system called 'High resolution-optical tomography', which was implemented to detect geometric distortions occurring during the L-PBF process. As far as the thermal field is concerned, I implemented a preliminary thermal monitoring methodology on the L-PBF machine in order to investigate defects such as local overheating, thus geometrical distortions in the final part, and lack of melting by monitoring the temperature profile over the whole slice area. Finally, the monitoring systems and methodologies developed were applied to several case studies, presented in the final chapter of the thesis, in order to ensure the high quality of the produced component, without additional expensive and time-consuming inspections, and to verify the stability of the process in-situ and real-time.

1. Metal Additive Manufacturing processes

Rapid prototyping is an automated production process that allows solid 3D prototypes to be produced quickly from a 3D CAD file [17]. Rapid prototyping processes can be subtractive, additive, and forming. Additive Manufacturing (AM) involves the production of artefacts through the addition of material [17]. Additive processes were initially developed as processes for plastic materials in order to obtain a prototype as the product of the processing; later, as technological development progressed, their use was extended to include metallic materials for the direct production of the artefact. The value of prototypes can be seen in the evaluation of the intended use of the final product, the analysis of the design, and the characteristics that can be used to improve the final component [17].

According to ISO/ASTM52900-15, additive manufacturing technologies can be classified into seven main categories [17]:

- Binder Jetting: in this process, a binding liquid is deposited between the layers of powder, acting as an adhesive between them. The materials typically used are plaster, glass, and sand. A head moves along the axes of the machine and deposits alternating layers of construction material and binder.
- Directed Energy Deposition: in this process, the material is either a metal powder or a wire, which is hit by an energy source, which can be an electron beam or laser, positioned on a multi-axial robotic arm or a Cartesian system. The material is thus melted and subsequently deposited on the surface to be coated, where it solidifies and creates the layer.
- Material Extrusion: in this process, the material, usually a thermoplastic filament, is melted in a special melting chamber and extruded through a heated nozzle onto the printing platform. This technique is also used to process very viscous materials such as cement, clay, organic textiles, and food.
- Material Jetting: in this process, print heads, often piezoelectric, are used to spray and dispense a liquid material, represented by a photosensitive resin (photopolymers), onto the printing platform. Subsequently, the material is polymerized or hardened using an ultraviolet source.
- Vat Photopolymerisation: in this process, a photopolymer resin, contained in a special tank, is exposed to an energy source, usually ultraviolet light, and polymerized layer by layer. The materials used are usually thermosetting plastics.
- Powder Bed Fusion: in this process, a laser or electron beam is directed at a powder bed. The latter is heated until the individual powder particles melt. Every PBF

process includes spreading the powdered material over the previous layers. There are several mechanisms to do this, such as a roller or blade. A hopper or tank below or to the side of the bed supplies virgin material. The materials subjected to this process can include both plastic powders, such as nylon powder, and metallic powders such as titanium and other alloys.

- Sheet Lamination: in this process, sheets of material are overlaid, fused, and welded together, and on each layer/sheet the desired shape, cross-section of the object being manufactured, is engraved. The process uses paper, plastics, and metals as processing materials.

However, additive manufacturing for metallic materials involves some of these mentioned technologies, which may differ in the type of process, the energy source used, and the nature of the metallic material [18]. Among the different categories, it is possible to adopt the classification carried out by the ASTM, which identifies the main technologies, those based on Directed Energy Deposition (DED), those based on metal foil lamination, Sheet Lamination (SL), and those based on Powder Bed Fusion (PBF) [18].

The main technologies involving a DED process are:

- Laser-Directed Energy Deposition, L-DED
- Wire and Arc Additive Manufacturing, WAAM

For metal foil lamination technology, the main process is:

- Ultrasonic Additive Manufacturing, UAM

The main technologies involving a powder bed fusion process are:

- Selective Laser Sintering, SLS, and subsequent Laser Powder Bed Fusion, L-PBF
- Electron Beam Melting, EBM

This thesis examined two of these mentioned processes, which are the L-DED process and the L-PBF process.

1.1 Directed Energy Deposition processes

The L-DED process is part of the direct energy deposition process family. Additive manufacturing systems based on DED deposit the material to be processed on a platform or a previously manufactured component, thanks to a nozzle mounted on a multi-axial device, and at the same time the direct action of the energy source occurs, melts the material itself. As with other AM technologies, the part is built layer by layer. For two or three-axis systems, the printing platform is fixed while the deposition head is mobile, rising as it deposits the various layers of material. While for four or five-axis systems, both the platform and the deposition head are mobile and independent of each other, allowing the realization of very

complex geometries. It can be deduced from the above that a flat printing platform is not essential for this process, which is why it is a suitable technology for adding material to already manufactured parts (e.g. producing coatings) and for repairing damaged components. Usually, the parts obtained at the end of the process, however, require further machining to optimize the mechanical characteristics. In this technology, the material is melted with a laser or electron beam directed toward the deposition point of the material. The deposition point represents the melt pool of the process, where the metal is melted as it exits the nozzle. Systems involving a laser beam, on the other hand, can use either metal powder or a metal filament and the process must take place in an inert atmosphere if working with reactive metals, please see Figure 1 [19].

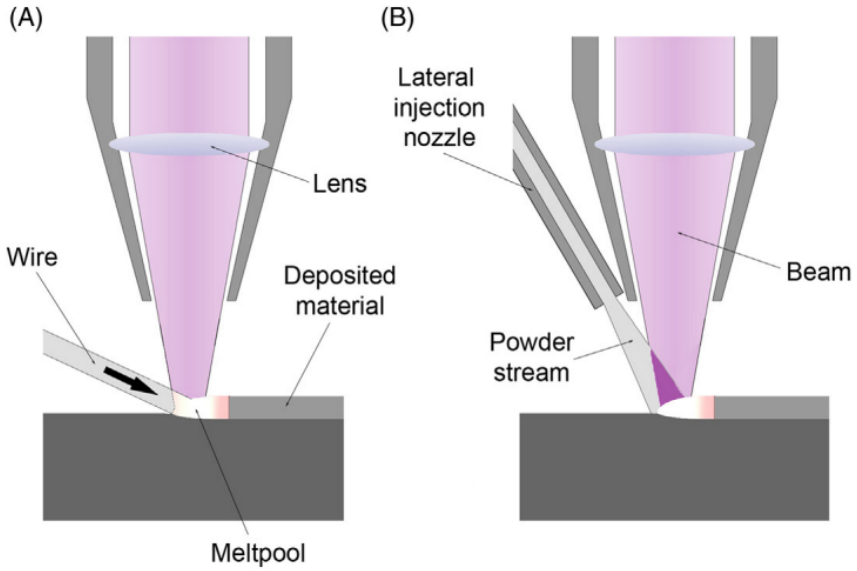

Figure 1. DED process with metal filament on the left (A), DED process with metal powder on the right (B) [19].

For DED processes employing metal powder as the material, a flow of inert gas, such as helium, is required to provide and control the flow of powder through the nozzle. Whereas, for DED processes using a metal filament, the processing machine must be equipped with a coil that supplies and forces the filament through the nozzle. This type of process usually uses one of the following lasers: CO2, Nd:YAG, and fiber lasers. The choice of laser is significant, as materials absorb energy at different wavelengths, so it is important to choose the appropriate laser with a specific wavelength according to the material to be treated. Given the high deposition speed of the material, DED processes are suitable for obtaining parts with bulky geometries that are not too complex compared to those obtainable with PBF processes. In fact, considering the deposition speed is about 9 kg/h for an electron beam DED process and about 3 kg/h for a laser beam DED process, against 0.2 kg/h usually obtained in PBF technologies. This difference in deposition speed is due to both thinner layers and smaller melt pool sizes, for PBF processes result in higher accuracy in the parts

produced [19].

1.1.1 Laser-Directed Energy Deposition (L-DED)

1.1.1.1 Process description

Laser-Directed Energy Deposition (L-DED) is an additive manufacturing process based on laser cladding, which mainly focuses on 3D manufacturing and repair applications [20,21]. This is usually used to repair and reconfigure worn or damaged components through the application of wear and corrosion-resistant coatings [22]. L-DED has a high potential for component production through 3D deposition strategies for the creation of clads with quite good microstructures less prone to cracks and also to build non-homogenous structures [4,21]. Machining always starts with the CAD model of the part to be manufactured, converted to STL format and subjected to the slicing operation to obtain the sections of the object in the XY plane. The data obtained are translated into toolpaths, then into the laser scanning path required to produce each layer. Each layer is thus produced by defining the contour of the section, which is then filled by following different scanning strategies. The process is repeated until the part is completed. The L-DED process is based on the SLS process with a few exceptions, i.e. instead of binding the material in a powder bed, the powder is delivered in a gas jet through a nozzle, which can be coaxial or multi-jet. The L-DED system consists of a laser system, a processing chamber in a controlled atmosphere, a three- or five-axis positioning system, and a metal powder feed system, please see Figure 2.

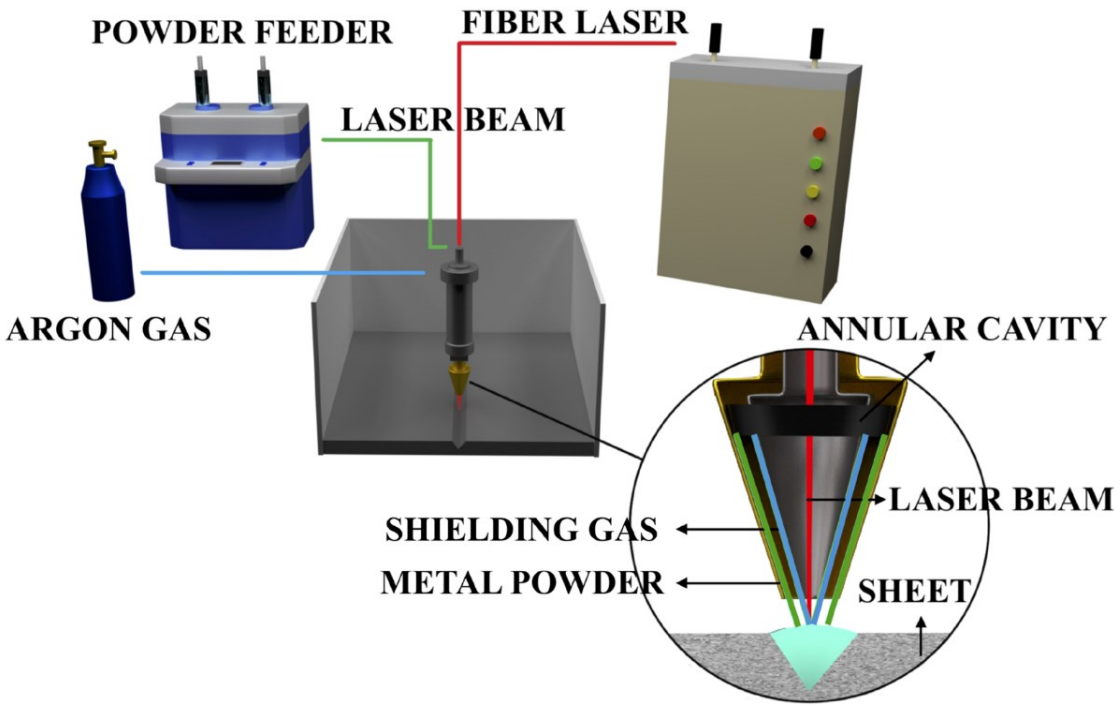

Figure 2. Schematic diagram of the L-DED device [23].

L-DED uses a laser beam to create a melt pool on a metal substrate in which a metal powder or a metal wire is added [21]. The generation of an appropriate melt pool during the process is essential to achieve a strong bond between the cladding material and the substrate [21]. The physical mechanisms behind the L-DED process are the creation of a high-temperature spot during the process inducing the melting of the substrate and the fed material, both contributing to the biphasic (liquid + solid regions) melt pool growth [4,21,23,24]; when the laser beam moves away, the heat dissipation into the substrate causes rapid cooling of the trailing molten material (leaving a semi-circular trace of solidified material) and the advancement of the leading solidification front [21,25]. The path of the laser beam into the processing chamber is allowed by the presence of a window in the working chamber. The laser head is usually equipped with a motorized optical collimator, which allows the size of the laser spot to be changed independently of the change in deposition height, and a focusing lens that focuses the laser beam at a specific distance from the nozzle exit. The latter can be above the workpiece when working in defocused mode (typical of the L-DED process) or coinciding with the powder focal spot and the top surface of the workpiece when working in focused mode. As aforementioned, deposits are typically performed in a controlled atmosphere of inert gas containing minus 10 ppm oxygen to avoid contamination or fire problems when processing reactive materials. Significant features of L-DED technology include the possibility of even five-axis control equipment; the ability to produce parts with considerable volumes compared to other AM techniques. This process, however, allows small melt pools to be realized during the process, enabling high melting and cooling/solidification speeds, and also enabling the production of composite components with different materials, using multiple powder feed lines [24].

1.1.1.2 Input process parameters

The L-DED process is very versatile and efficient in the combination of various metal alloys because it can use different materials. However, in order to exploit this feature of the process, it is necessary to carefully define the process parameters and their interaction in relation to the intrinsic characteristics of each material and their behaviour during processing in order to achieve the desired resolution. The main process parameters are listed below:

- Laser power (P)
- Translation speed (v)
- Powder feed rate (Q)
- Laser spot diameter (d)

- Standoff distance (H)
- Laser defocusing distance (F)
- Scanning strategy

As regards laser power, one of the main parameters of this process, is crucial for the final properties of the part. In fact, in order to obtain a part structure with a high density, greater than 99%, it is necessary to have a sufficient laser power in order to avoid partially melted areas and thus obtain porous structures. However, increasing the laser power up to a critical value can lead to an increase in grain size with a consequent reduction in hardness and other mechanical properties, or it can cause high penetration and thus achieve a keyhole regime unsuitable for this process [23]. Experimentally, for example, using various titanium samples as processing material, it was observed that increasing the laser power from 250 W to 300 W, all other processing parameters being equal, resulted in the workpiece being three times harder than before. An optimal result, like the previous one, was not achieved by further increasing the laser power [25]. However, the laser power has a significant impact on penetration depth, as shown in Figure 3. It can be seen in Figure 3, that the penetration depth increases with increasing laser power on the surface (assuming a constant laser spot diameter), which is due to the increase in heat input, as found also by Balasubramanian et al. in their study on modelling of laser beam welding of stainless steel sheet butt joint [26].

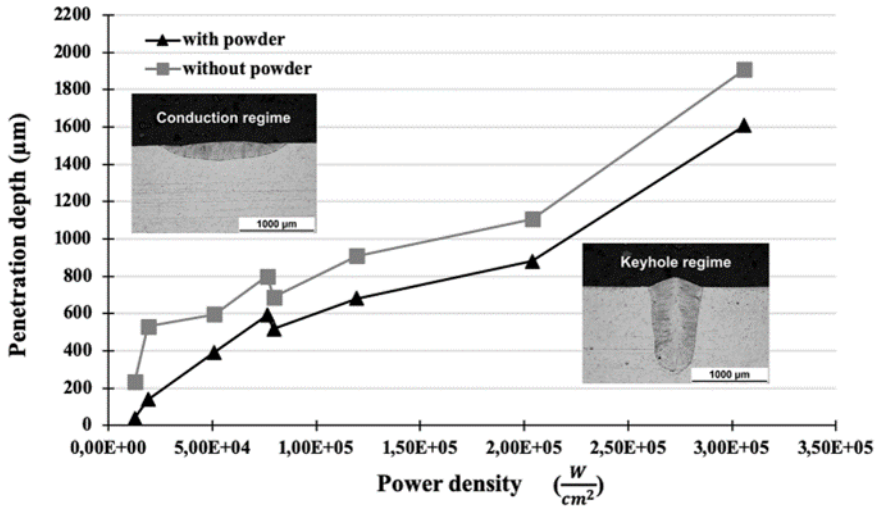

Figure 3. The relationship between penetration depth and welding procedures and power density [23].

In addition, laser power also has a significant impact on track width; as tested in the literature that the track width, similarly to penetration depth, increases with increasing laser power on the surface, which is due to the increase in heat input and resulting in more melting of the base material [26,27]. Increasing the laser power too much can sometimes cause residual stress between the layers of the workpiece and lead to an increase in surface roughness [28]. For example, with high laser power, during the deposition of brass powder on an AISI 410

steel substrate, lamination of the first layers built up occurred, while the phenomenon is less intense as the number of layers built up increases [29]. As far as surface roughness is concerned, during an experiment with metal Ti6Al4V, again keeping other parameters constant, reducing the power from 780 W to 330 W resulted in a reduction in roughness from 63.9 μm to 30.6 μm [24].

As for translation speed, it is also an important parameter because it is involved in combined parameters such as energy density (E = P/d * v). It consists of the translation speed of the deposition head. Keeping the laser power constant, an increase in translation speed causes a decrease in the energy density applied to the processing surface. Thus, the value of this parameter affects the size of the melt pool, the integrity of the workpiece and therefore its mechanical properties. In particular, an increase in translation speed leads to a reduction in the width and depth of the melt pool, as a consequence of the decrease in energy obtained by the laser [30]. This outcome is caused by a decreased heat transmission through conduction inside the base material, which results in a smaller molten pool, and a shorter contact period (t = d/v) between the laser beam and the substrate [23]. Additionally, the molten material fell out since the surface tension holding the molten pool's top flat failed to do so. Due to the rapid solidification of the molten metal at high speeds, undercuts were created on the sidewalls of the junction and a strong material flow was created towards the welding's centre [23]. However, the insufficient energy available on the processing surface could cause areas of material not to be melted, and therefore it is necessary to optimize this parameter, so as to find an optimal value based also on the material to be processed. There is a tendency to use a higher translation speed to reduce manufacturing time, but there may be cases where a low translation speed is required although this means an increase in machining time. Furthermore, the change in translation speed, precisely its increase, causes an increase in the cooling rate with consequences at the microstructural level of the processed material [31]. In fact, high cooling rates result in a very small grain size of the material [24,31]. Finally, Figure 4 shows some examples of track transverse cross-sections obtained using the process parameters written in Table 1 [23]. In fact, it is possible to switch from the conduction regime for high translation speed values, as shown in Figures 4c, 4d, Figure 4g, and Figure 4h, to the keyhole regime due to the excessive thermal input for low speeds, as shown in Figures 4a, Figure 4b, Figure 4e, and Figure 4f. As a result, as previously mentioned, changing only the translation speed and maintaining constant the other process parameters leads to very different results in terms of penetration depth [23]. The ratio of laser power to translation speed may be used to compute the thermal input [23].

Table 1. Process parameters of bead-on-plate tests (P = 600 W, d = 2.0 mm, G = 5 l/min) [23].

Sample	v (mm/min)	Q (g/min)
a	500	5
b	750	5
c	1000	5
d	1500	5
e	500	-
f	750	-
g	1000	-
h	1500	-

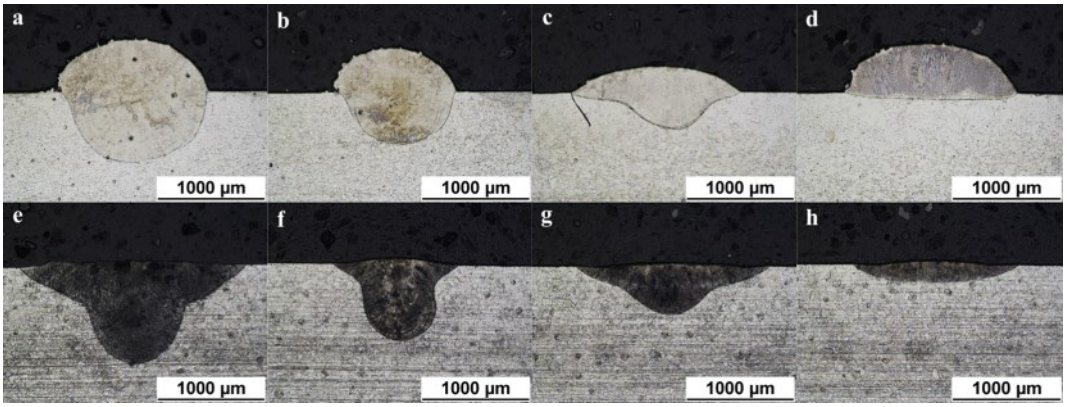

Figure 4. Process window representation depending on penetration depth and translation speed [23].

As regards the powder feed rate, i.e the rate at which the metal powder is fed into the melt pool, it determines various characteristics of the final part. In fact, if the powder feed rate were too slow, there could be a risk of not applying the proper amount of powder, such as between two parallel hatch lines and resulting in interlayer porosity, or of applying too much energy density to the part, resulting in excessive melting and keyhole type defects [23,24]. Viceversa, a high powder feed rate would result in a higher layer thickness and thus an uneven workpiece structure or uneven areas [24]. Typically, the powder feed rate is evaluated in g/s. Additionally, a crucial factor affecting penetration depth is the powder feed rate [23]. For instance, it was discovered that increasing the powder feed rate from 5 g/min to 10 g/min caused the penetration depth to decrease [23]. This finding is due to the fact that increasing the power density ($D = 4P/(\pi d^2)$) to achieve a similar penetration depth while maintaining the other process parameters at their current levels would be necessary to melt the additional powder feed. The track width was also significantly impacted by the powder feed rate [23]. The track width was found to decrease when the powder feed rate increased from 5 g/min to 10 g/min. [23]. This conclusion may be explained by the fact that as Q increases, more powder is used to block the laser beam, which reduces the base metal's ability to absorb the laser energy and narrows the melt pool [23]. Also important is powder flow distribution, which will be discussed in more detail later.

As for laser spot diameter, it is a parameter that cannot always be modified decoupled from the standoff distance. However, in new deposition systems equipped with optical collimators, changing it independently of the standoff distance is possible. Changing the laser spot diameter involves a change in the laser power density. From the work of Errico et al. [23] is resulted that also the laser spot diameter has a significant impact on the penetration depth. Figure 5 shows some examples of track transverse cross-sections obtained using the process parameters written in Table 2 [23]. It is evident that as the laser point width increases, the penetration depth decreases. Thus, significantly varied outcomes are produced by altering simply the laser spot diameter while maintaining the other process variables constant [23]. It is possible to range from low penetration depths for high values of the spot diameter, as shown in Figure 5c, Figure 5d, Figure 5g, and Figure 5h, to high penetration depths, due to the excessive power density, for a small spot diameter, as shown in Figure 5a and Figure 5e. Thus, with a spot diameter of 0.5 mm, a keyhole regime was always obtained, while it is never reached with a spot diameter of 1 and 2 mm; with the latter spot diameters, a conduction regime was always obtained. Also, for a spot diameter of 0.8 mm, both conduction and keyhole regimes could be obtained, depending on the values of the other parameters (Figure 5b and Figure 5f). However, the increment in the laser spot size, which is associated with lower power density, caused a wider track. This result is associated with an increase in interaction time. It can be asserted that the increase in spot size led to the growth of interaction time and therefore a growth of the heating time on the substrate [32,33].

Table 2. Process parameters of bead-on-plate tests (P = 400 W, v = 1000 mm/min, G = 5 l/min) [23].

Sample	d (mm)	Q (g/min)
a	0.5	5
b	0.8	5
c	1.0	5
d	2.0	5
e	0.5	-
f	0.8	-
g	1.0	-
h	2.0	-

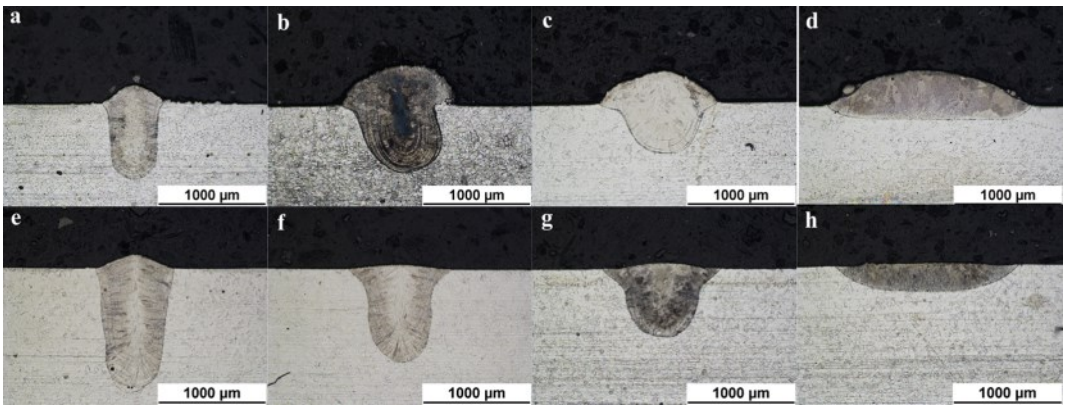

Figure 5. Using the spot diameter, penetration depth, and track width to represent the process window [23].

With regard to the parameters standoff distance and laser defocusing distance, extensive work was conducted by Mazzarisi et al. *(I'm co-author, please see section 7)* [22] on the influence of standoff distance and laser defocusing distance on the L-DED of a nickel-based superalloy. The standoff distance, between the nozzle and the substrate surface, is a critical process parameter [22]. In fact, by varying this distance it is possible to modify the laser spot size and the powder distribution on the deposition plane [22]. If the laser beam collimator is not adjustable, the variation of the standoff distance is the only way to modify the laser defocusing distance, which is the distance between the laser focus and the deposition surface [22]. The study of the effects of these issues on the deposition process and the investigation of the best strategies to mitigate them are crucial. A series of studies in the literature have investigated the effects of laser focal distance [34], standoff distance [34–36], and laser and powder defocusing distance [37] on the geometrical characteristics of the single clad or printed part produced by L-DED process. The results proposed by Ermurat et al. [34] show that a clad of minimum size (in terms of height and width) was obtained by using the highest values (among the levels used for this study) of the standoff distance combined with the value of the laser focal distance that generates the lowest laser spot size on the substrate distance combined with the value of the laser focal distance that generates the lowest laser spot size on the substrate. Moreover, the clad height is significantly influenced by the standoff distance. In fact, the clad height first rapidly increases and then decreases with the increase in the standoff distance [35,36,38]. In the study of Zhu et al. [35], it is shown that the maximum clad height was obtained when the standoff distance was equal to the powder focus distance. In addition, the clad height and its surface quality are significantly affected by the powder and laser-defocusing distance parameters. In particular, a high surface quality was obtained when the powder is focused below, and the laser is focused above the top surface of the substrate [37]. The same researchers developed different theoretical mathematical models that allowed the correlation between different process

parameters and investigate their effects on the final products [36,37]. Specifically, Zhu et al. [37] examined the influence of powder and laser-defocusing distance on clad height through a mathematical model. The results show that the clad height first increases and then decreases (after reaching the standard position) when the powder defocusing distance goes from a negative to a positive value with respect to the standard distance identified as zero position. On the other hand, the clad height first decreases and then increases when the laser defocusing distance goes from a negative to a positive value with respect to the setup in which the laser is focused on the substrate. Pinkerton and Li [36] developed a model to analyze the temperature distribution near the melt pool and estimate the powder mass deposition rate as a function of standoff distance. While Tan et al. in subsequent works [39,40] developed theoretical models to simulate the behavior of the powder flow of a multi-jet coaxial nozzle with four symmetrical tips [39]. They investigated the effects of the powder flow spatial distribution and other process conditions (such as the initial standoff distance and the orientation of the powder flow) on the deposited layer height [40]. The results showed the key influence of the standoff distance on the size of the deposited clad, due to the variation of powder mass concentration on the surface, and a good agreement between the experimental measurements and the model results. According to the literature, the combined effects of laser defocusing distance and standoff distance are ambiguous and reported results that are still not very robust in terms of the combined effects of laser defocusing distance and standoff distance. The in-depth work of Mazzarisi et al. *(I'm co-author, please see section 7)* [22] is aimed to investigate the effects of these significant process parameters on the geometrical characteristics of the single deposited clad. An experimental plan was carried out varying the standoff distance and the laser defocusing distance and an analysis of variance (ANOVA) on a general linear model was used to assess the statistical significance of the effects. The experimental investigation was performed using a fiber laser source and depositing a particular Nickel-based superalloy powder by means of a coaxial nozzle on an AISI 304 stainless-steel substrate. The deposition head equipped with an advanced and innovative motorized optics system allowed the variation of the laser spot size on the substrate surface, and consequently the size of the melt pool. This system modifies the characteristics of the laser decoupled to the standoff distance, without changing the laser head position and thus the powder distribution. In order to give an exhaustive explanation of the phenomena, an analytical model to determine the powder distribution and the laser-material interaction was proposed. An experimental setup for the analysis of the spatial powder distribution was realized to validate the results obtained from the analytical model. The results showed that the geometrical characteristics of the clad, such

as clad width, clad height, penetration depth, and dilution, are affected by standoff distance and laser defocusing distance. The variations of the standoff distance reproduce the roughness of the deposition surface that can be generated during a multilayer deposition or cladding of complex geometries, given by even modest process instabilities (especially of the powder flow) in the underlying layers. Therefore, this work is of paramount importance for an accurate design of these process parameters that can ensure a more stable deposition process with mutable conditions.

Experimental plan

A series of single-clad depositions of Nickel-based superalloy powder was performed on AISI 304 plates. The controlled process parameters were laser power (P), laser defocusing distance (F), translation speed (v), powder feed rate (Q), carrier gas flow rate (G), and standoff distance (H). Table 3 shows the full factorial experimental plan, with two independent variables: the standoff distance varies over five levels, and the laser defocusing distance on three levels. The other process parameters kept constant are listed in Table 4. A total of 15 combinations of process parameters were tested. Five replications were performed for each combination of process parameters. In order to better understand the procedure and the independence of the investigated process parameters, a schematic representation of the experimental setting is displayed in Figure 6. This experiment allowed an insight into the influence of the two investigated process parameters on the geometrical characteristics of the deposited clads. Each clad was cross-sectioned and analyzed through the optical microscope, as can be seen in Figure 7. Figure 8 shows the main geometrical characteristics considered in the analysis:

- Clad width (w);
- Clad height (hs);
- Penetration depth (hi).

Another key process parameter that must be controlled for an effective laser deposition process, aimed at both cladding and 3D printing, is dilution (Dil). It analyzes the ratio between the molten base material and the deposited material, and is usually calculated as:

$$\mathrm{Dil} = \frac{\mathrm{hi}}{(\mathrm{hs} + \mathrm{hi})} \tag{1}$$

Table 3. Experimental plan [22].

Parameter	Unit	Notation	Factor Levels				
			1	2	3	4	5
Laser defocusing distance	mm	F	17	25	31	-	-
Standoff distance	mm	H	5.0	6.5	8.0	9.5	11.0

Table 4. Process parameters kept constant in the experimental tests [22].

Parameters	Unit	N	Value
Laser power	W	P	600
Translation speed	mm/s	v	8.33
Powder feed rate	g/min	Q	5.0
Carrier gas flow rate	l/min	G	3.0

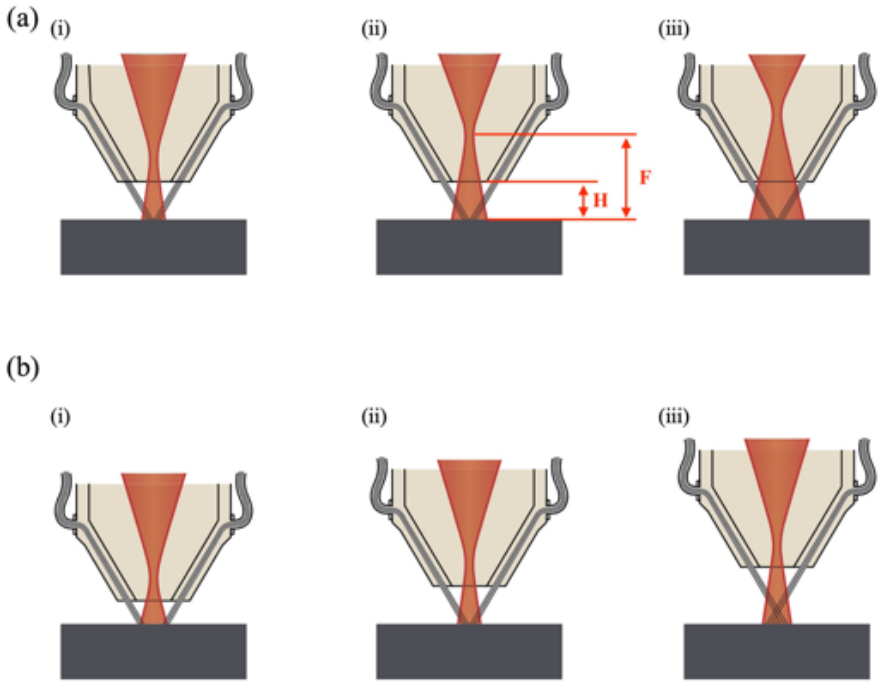

Figure 6. Schematic representation of the process in some employed configurations: a) varying the defocusing distance: (i) F = 17 mm, (ii) F = 25 mm, (iii) F = 31 mm; b) varying the standoff distance: (i) H = 5 mm, (ii) H = 8 mm, (iii) H = 11 mm [22].

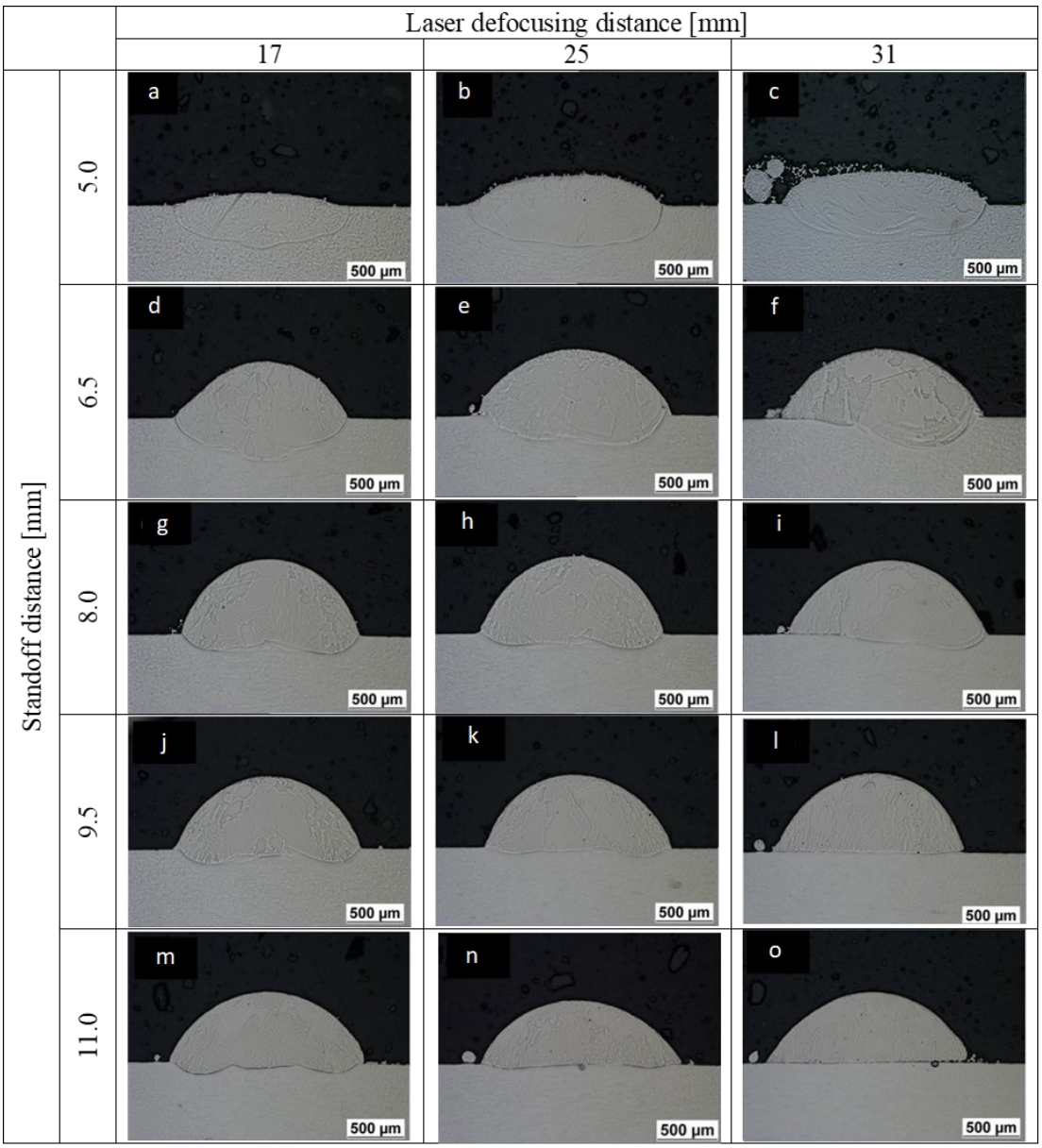

Figure 7. Cross-section macrographs of deposition tests using (a) H = 5.0 mm and F = 17 mm, (b) H = 5.0 mm and F = 25 mm, (c) H = 5.0 mm and F = 31 mm, (d) H = 6.5 mm and F = 17 mm, (e) H = 6.5 mm and F = 25 mm, (f) H = 6.5 mm and F = 31 mm, (g) H = 8.0 mm and F = 17 mm, (h) H = 8.0 mm and F = 25 mm, (i) H = 8.0 mm and F = 31 mm, (j) H = 9.5 mm and F = 17 mm, (k) H = 9.5 mm and F = 25 mm, (l) H = 9.5 mm and F = 31 mm, (m) H = 11.0 mm and F = 17 mm, (n) H = 11.0 mm and F = 25 mm, (o) H = 11 mm and F = 31 mm [22].

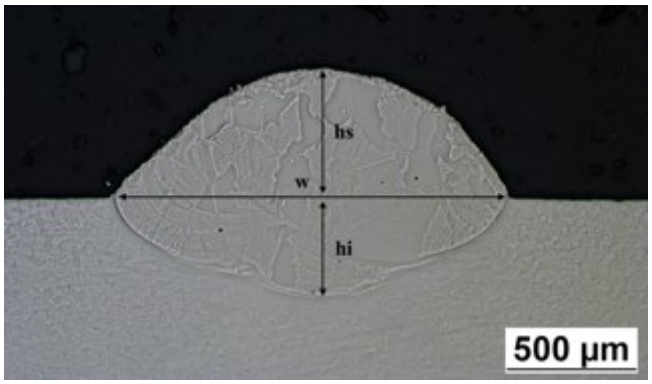

Figure 8. A typical track cross-section profile with its main geometrical characteristics: clad width (w), clad height (hs) and penetration depth (hi) [22].

The proposed experimental plan was also useful for precisely defining the mechanism

underlying the track formation in the L-DED process. This is a function of two laser-particle interaction modes. There is a mode called "direct" in which the laser beam acts on the powder particles, heating them until melting. On the other hand, there is a mode of track formation known as "indirect" in which the energy supplied by the laser is directed onto the substrate to create a melt pool in which the powder particles will be conveyed. It can be seen from the present work that these two modes are not totally separate and independent. Starting from the analysis of Figure 7 it can notice, in the depositions obtained with low standoff values, a preponderance of the resolidified area of the substrate caused by the establishment of a large melt pool. However, it can also be seen that this area is extremely limited in depositions obtained using high standoff values. It can be inferred that the first group originated by indirect mode, in which most of the laser energy reached the substrate, giving rise to a huge melt pool. This subsequently captured the metal particles carried by the gas generating to the track. The second group originated from a predominantly direct mode. The almost complete absence of a remelted area is a sign of an extremely limited, if not entirely absent, melt pool. However, this did not affect the generation of the clad, which originated from a direct fusion of the particles by the laser beam and subsequent adhesion to the substrate. Between these two extreme cases, there are depositions produced by a mechanism that is a middle ground between the two aforementioned modes. It can therefore be stated that these modes are not totally distinct, they are instead the extremes of a mechanism of track formation that focuses on the laser-particle interaction. The interaction time between the laser beam and metal particles and the spatial distribution of the particles in the region affected by the laser beam plays a major role in this mechanism. The present work is aimed to study how these features affect the geometrical characteristics of the track. The experimental plan was then developed keeping as constant the carrier gas flow rate for all the proposed cases. In this way, it is possible to assume that the particles exhibit the same velocity for all tests performed since it is mainly influenced by the carrier gas flow rate. Therefore, the path length of the particles in the volume affected by the laser is crucial for estimating the laser-particle interaction time. By assuming a constant powder flow geometry for all tests, the particle path is a function of the standoff distance, which characterizes the spatial evolution of the powder flow. For instance, using high values of standoff distance, the average path of the particles becomes very long, resulting in a longer laser-particle interaction time and consequently a higher absorption/reflection of the laser energy. As previously mentioned, the result of such phenomena is the establishment of a purely direct clad formation mechanism with a melt pool of negligible size.

Laser beam profile

The laser beam is strongly influenced by laser defocusing distance and standoff distance, which modify its power distribution in the deposition plane corresponding to the substrate surface. In order to evaluate and subsequently compare the effects of F and H parameters on the deposition process, the variation in shape and size of the laser spot was first assessed. In the setup of the L-DED equipment, the defocusing distance and the standoff distance are independent parameters and both contribute to the determination of the actual laser spot size. Specifically, the defocusing distance is characteristic of the innovative motorized optics system located in the deposition head. This optics system is used for the dynamic adaptation of the laser beam during the process. By changing the divergence, the position of the focus point of the laser beam shifts and consequently the way the beam impacts the deposition plane. In this work, the reference values for defocusing distance (Fstd = 17 mm, Fstd = 25 mm, Fstd = 31 mm) are evaluated with respect to the standard deposition plane defined by the manufacturer at a standoff distance of 8 mm from the nozzle. On the other hand, the standoff distance parameter characterizes the distance between the nozzle outlet and the component surface. The latter concerns the vertical movement of the deposition head and it can be modified in the equipment keeping the collimator settings unchanged (i.e. the defocusing distance). The interaction between the two process parameters was evaluated using the dedicated collimator software, capable of defining the shape and intensity distribution of the beam in the different planes considered. Figure 9 shows the circular shape of the laser beam used and the Gaussian-like intensity distribution profiles.

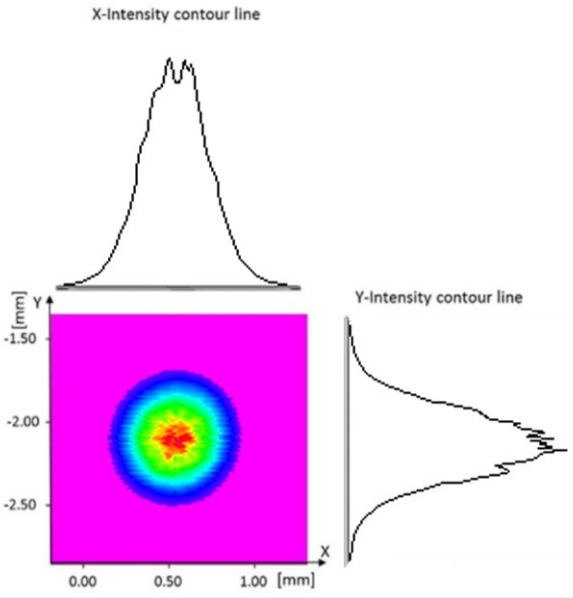

Figure 9. Intensity distribution profiles for the laser beam, as a function of radial coordinates and cross-sectional plot [22].

The laser beam, like any directional light beam, slightly diverges from the nominal

dimension as the distance between the deposition plane and the focus point increases. Figure 10 shows the variation of the laser spot size (defined using the diameter) on the deposition plane as a function of the defocusing distance and standoff distance. It is noticed that the variation of the defocusing distance, obtained through the motorized collimator, has a great influence on the final dimension of the laser spot, while the variation of the standoff distance reveals a limited effect, due to the low divergence of the beam.

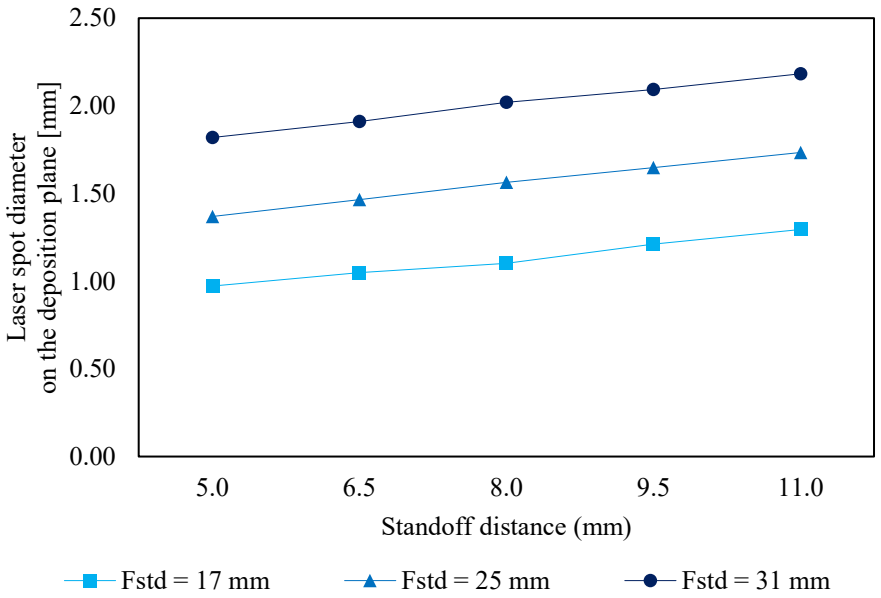

Figure 10. Laser spot diameter on the deposition plane with respect to standoff distance [22].

Powder flow distribution

In the L-DED process, the track is obtained by the interaction among the powder flow, the laser beam, and the substrate. Consequently, the spatial distribution of the metal powders assumes considerable importance, to define the size, shape, and geometrical characteristics of the clad. In this work, a deep analysis of the powder flow and distribution, produced by means of a coaxial nozzle, was carried out. The powder distribution is strongly influenced by the geometry of the nozzle, which requires a complex and accurate study to define its characteristics and shape [41]. In order to investigate the powder distribution, a specific experimental setup was developed of which a schematic representation is shown in Figure 11a. A light source was positioned inside the central cavity of the nozzle, which generates a blue light beam that develops coaxially with the laser beam and the powder flow. An IDS UI-5490SE camera, fitted with a 4.92 megapixel CMOS sensor, was placed transversely to the powder flow and was used to detect the light reflected by the metal particles. Figure 11b shows the blue detection light beam revealing the powder flow leaving the nozzle and defining its conical distribution. The blue light beam resulted imperceptible to the camera in the absence of the powder flow. The MATLAB® software was used to

perform image analysis on the powder flow detect using the detection light. The spatial powder distribution was determined by examining the light reflected by powder particles crossing the light beam. The use of the coaxial light beam, compared to the external orthogonal light beam used by Tan et al. [38–40], gives more emphasis on the examination of the deposition region. Furthermore, the reduced focus length and working distance that characterizes a coaxial nozzle make the study of a coaxial powder flow even more difficult, compared to the multijet nozzle that adopts longer working distances. The size of the area irradiated by the detection light beam is related to the diameter of the nozzle outlet hole (5 mm) and is considerably larger than that of the laser spot on the deposition surface (about 1-2 mm). Moreover, the convergent conformation of the powder flow concentrates most of the particles under the detection light beam, making this setup suitable for the powder flow analysis.

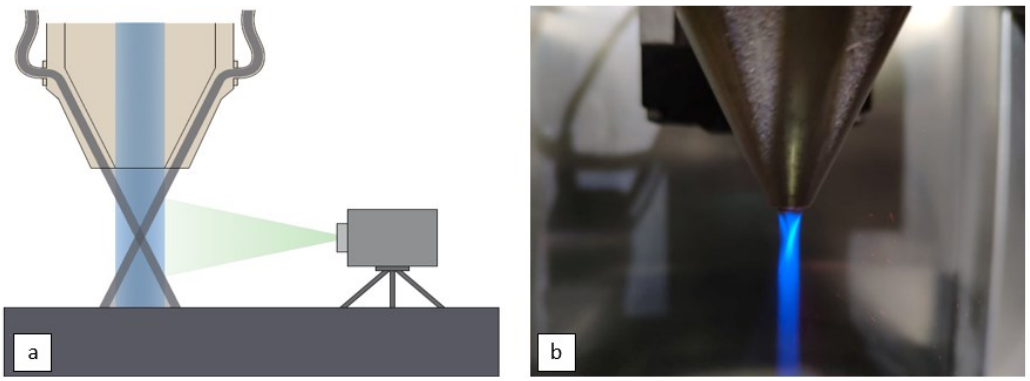

Figure 11. (a) Schematic representation of the experimental setup and (b) coaxial nozzle with blue detection light [22].

The first step of the analysis involved a preliminary calibration and an adjustment of the measurements obtained from the phenomena of optical distortion due to perspective. Figure 12 shows the image analysis performed on the median vertical plane (in section line A-A'). By establishing as a reference point the edge of the nozzle, the analysis identified the point of maximum brightness density of the image at a distance of about 8 mm. This is generated by the maximum powder concentration along the median vertical axis, which confirmed the manufacturer's requirements of the coaxial nozzle regarding the focus point of the powder flow. The transversal plane passing through this point was defined as the standard deposition plane.

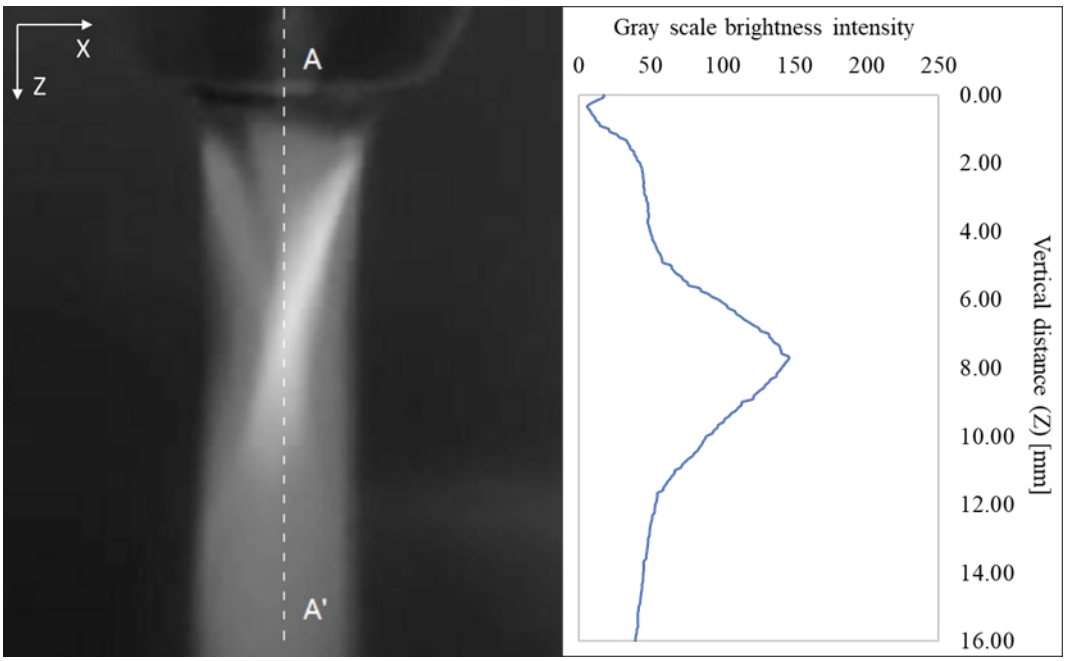

Figure 12. Grayscale brightness intensity distribution of the vertical median plane (A-A' section) [22].

The same study was carried out on several transversal planes, highlighted in Figure 13, identified according to the standoff distances chosen in the experimental plan (ref. Table 3). In addition, the diameter of the laser spot incident in the standard deposition plane, for the three considered values of F, are plotted using different dotted lines in Figure 13. These are useful as a reference for identifying the regions of interest of the powder flow for each setup. The results outlined in Figure 13 show how the powder distribution profile varies in the considered planes. In the standard deposition plane (8 mm) the powder flow assumes a Gaussian-like distribution, as reported by Tan et al. [38–40]. This deposition plane is fundamental for the process because the conjunction between powder flow and laser beam maximizes the powder catchment efficiency by the melt pool. In planes at 9.5 mm and 11 mm from the nozzle, the powder distribution has a transition from the Gaussian-like distribution to a smooth distribution. Especially for the farthest plane, the profile tends to flatten assuming a nearly constant intensity throughout the size of the light beam.

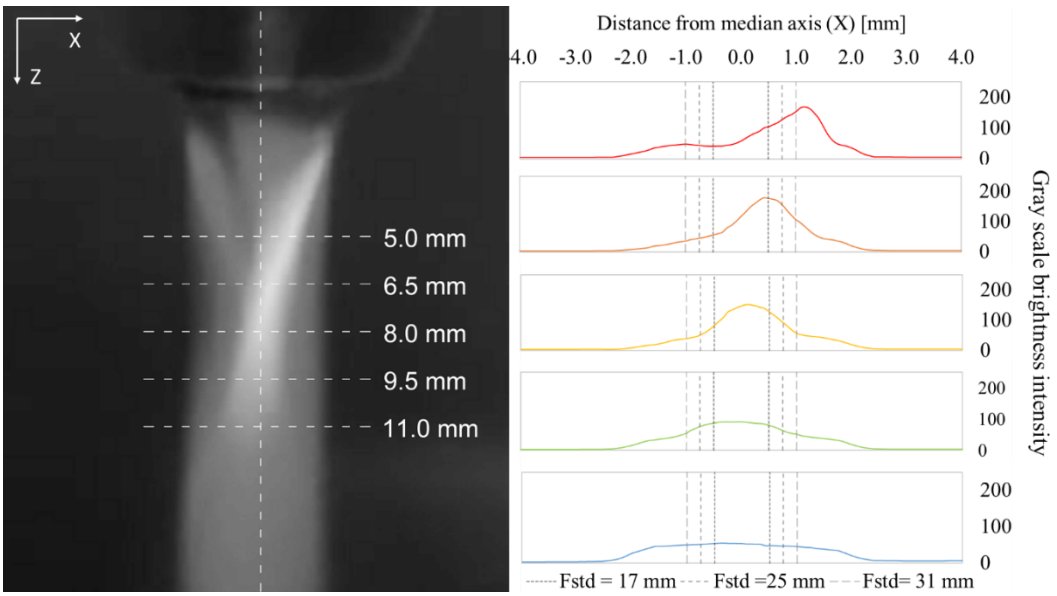

Figure 13. Brightness intensity distribution of transversal planes compared to the laser spot size in the standard deposition plane (in dotted lines) [22].

On the other hand, in the planes closest to the nozzle (6.5 and 5 mm), the powder flow tends to divert sideways. This effect owing to a slight misalignment of the parts that compose the nozzle and that constitute the wall of the cavity in which the coaxial flow is generated. As can be seen, a minimum misalignment has a strong effect on the powder flow close to the cavity. However, this problem is mitigated by approaching the powder focus point. The powder distribution in these planes reaches the maximum intensity laterally with respect to the central axis of the nozzle. This may be the source of the asymmetry of the fused region, which mainly characterizes the depositions realized at such standoff distances (see Figure 7). Finally, in the closest plane (5 mm), the powder distribution begins to split and shows two dissimilar peaks. This depicts the cross-section of the conical flow that characterizes the area closest to the nozzle. The analyses corroborate what was reported in the study of a coaxial powder flow by Eisenbarth et al. [42]. In this work, the axial-symmetrical flow converges from an annulus profile in the region closest to the nozzle to a Gaussian-like profile on the plane of powder focus.

As a first instance, the image analysis was useful to give a qualitative evaluation of the distribution of the powder flow in the different planes. Nevertheless, to determine an appropriate quantitative relationship between the powder mass flow and the brightness profile detected in the image analysis, the brightness spectrum of the entire powder flow was examined. For this purpose, the Cumulative Relative Brightness (CRB) intensity was introduced. The CRB is the integral of brightness values, expressed in grayscale, along a segment belonging to the image plane. In the work, the definition of "summation" was also used because this value was calculated on a variable evaluated in a discreet domain (pixel

by pixel), dependent on the resolution of the camera. In the analysis, planes transverse to the direction of propagation of the blue detection light and the powder flow (which are coaxial) were considered. For each transversal plane along the Z-axis, the CRB was calculated, and the results are plotted in Figure 14. As expected, planes with the highest brightness intensity were identified close to the nozzle. In fact, the CRB rapidly increases in the first 4 mm beneath the nozzle, due to the converging of powder flow coming from the outer annular cavity. Subsequently, the intensity gradually reduces and originates a descending section of the curve. This interval was evaluated using a linear regression function, reporting an R^2 of 0.9884, which certifies the consistency of the descendent part. In the section between the nozzle and the focus point, there is an amount of powder very close to the nominal powder flow. This is completely affected by the light beam, returning a total brightness that can be associated with the nominal amount of powder mass. Assuming a limited variation in powders particles size, and a light reflected by each particle substantially comparable, it is possible to relate the brightness profile with the amount of powder. The maximum brightness value calculated was equal to 3860 and was set as the reference value of the nominal powder flow rate (5.00 g/min). Similarly, the light reflected by the powder was calculated for all the planes and the setup proposed in the experimental plan. This obtained the percentage of powder that was processed. The image analysis of the powder flow is structured on the relationship between the powder mass and the light reflected by the particles. The reduction of the CRB along the Z-axis can be traced back to a reduction of powder mass and therefore to the ineffectiveness of the principle of conservation of mass in the analyzed system. The reasons behind this phenomenon were fundamentally attributed to two factors: the determination of the boundaries of the analyzed system and the powder dispersion. For the first point, it should be specified that the field examined in the image analysis must be considered as a portion of the entire closed system, which can ideally be identified with the volume confined by the chamber in which the L-DED operates. In fact, only the region irradiated by the blue detection light is taken into consideration. The boundaries of the system are therefore imposed by the light, but these are not binding for the particles moving inside that can pass through them and leave the field of observation. The dispersion of powder particles is the second source responsible for the non-conservation of the mass. It originates at the moment in which the flow comes out of the nozzle, passing from being confined by the tube (or from the walls of the nozzle) to being free from external constraints. Taking into account the section of the coaxial powder flow, this is characterized by a certain dispersion of particles that brings off the flow with respect to the direction imposed by the nozzle channel [43]. This dispersion pushes a portion of the particles out of the region

irradiated by the blue detection light. This originates a constant mass loss from the region of analysis, which amplifies with increasing the vertical distance in the Z-axis. For these reasons, the system taken into account in the present analysis must be considered open with constant leaks of particles, dropping the hypothesis of mass conservation. The decrease in the amount of light reflected by the particles is due indeed to the powder dispersion and it is characteristic of the analyzed powder flow and conditions. In the limited area of analysis, secondary factors such as the mutual shadowing of particles were considered negligible.

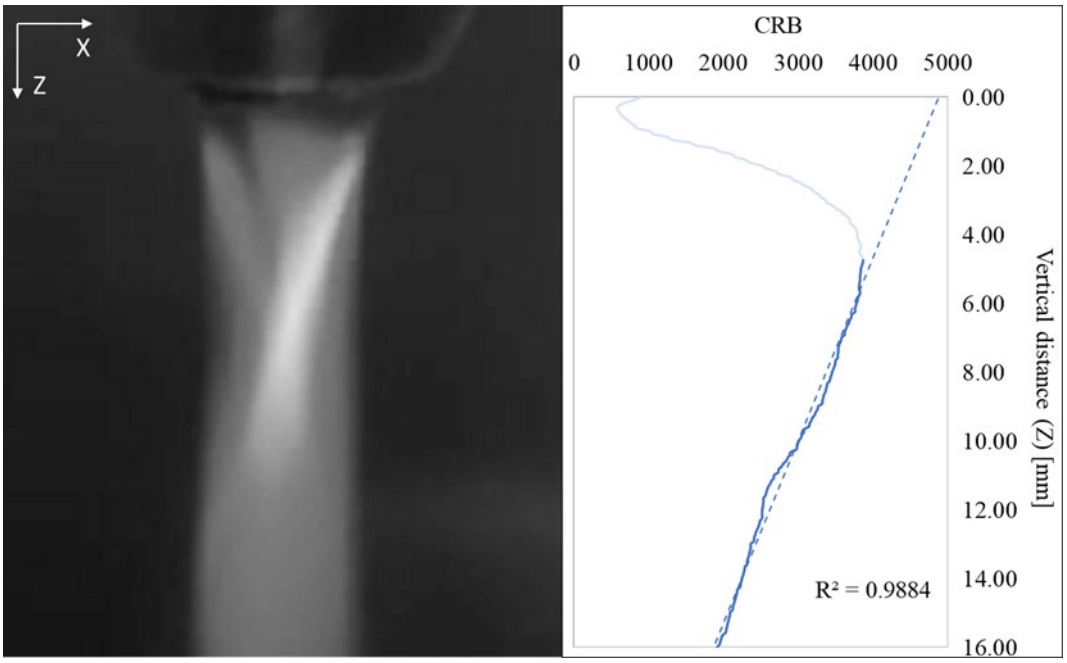

Figure 14. Cumulative relative brightness (CRB) of transversal planes along the vertical distance from the nozzle [22].

Figure 14 indicates the CRB generated by the amount of powder present in the entire area of interest identified by the detection light beam, although merely a fraction of this interacts with the laser beam during processing. In order to establish the amount of powder that is processed during the manufacturing process, the region of interest is compared to the size of the laser spot previously described. Figure 15a shows the CRB produced by the amount of powder in the area affected by the laser spot for each deposition plane related to the standoff distance and defocusing distance adopted in the experimental plan. As the defocusing distance and consequentially the laser spot size incident the deposition plane grows, the interaction area between laser and powder increases. As has already been pointed out in the definition of powder distribution profiles (see Figure 13), the standoff distance also plays an important role in determining the amount of powder processed by the laser beam. In fact, in the plane at 5.0 mm from the nozzle, the amount of powder incident in the laser beam is minimal because the flow focuses outside the region of interest. The powder concentration increases in the plane at 6.5 mm and reaches the highest intensity in the plane at 8.0 mm. In the subsequent planes, it gradually decreases, due to the dispersion of powder

flow after the powder focus point.

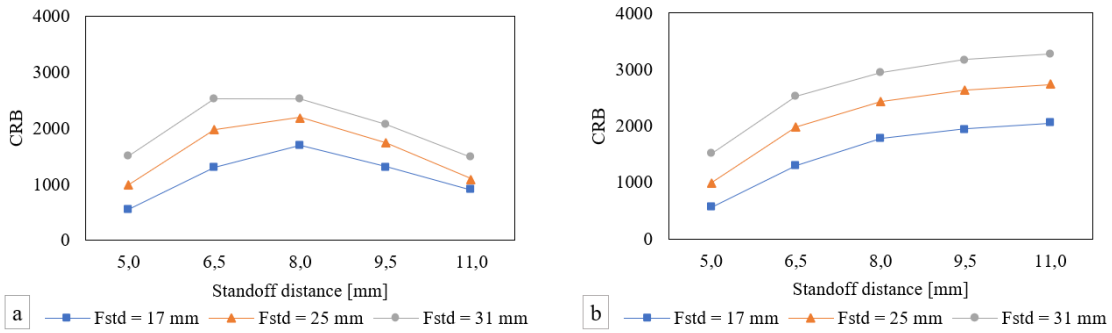

Figure 15. (a) CRB produced by the amount of powder in the area affected by the laser spot and (b) envelope function for each setup of the experimental plan (ref. Table 3) [22].

The definition of the mere amount of powder present in the deposition plane does not fully explain the complex laser-particle interactions that occur during the L-DED process. In fact, the powder particles along their path toward the deposition plane interact with the laser beam, absorbing and reflecting its energy. At a greater distance from the nozzle is the deposition plane, a higher number of particles interact with the laser beam for a higher average interaction time. For instance, considering the deposition plane at 11 mm of standoff distance, the powder particles before reaching the deposition point crossed the previous deposition planes (at 5.0 mm, 6.5 mm, 8.0 mm and 9.5 mm). In order to investigate in deep the mechanics of laser-powder interaction and clad generation, an envelope function of powder distribution profile was proposed. The envelope function is mainly used in construction theory to define the maximum stresses acting on a structure as the load combination varies [44,45]. This is also used in some of its variants in failure analysis in geotechnics [46]. In the present work, the principles underlying this function were applied to the case study in order to clarify the effect of laser-particle interaction on the geometrical characteristics of the clad. The analysis of the laser deposition process was approached as a superimposition of different loading profiles. This theory is applicable when the process assumes a stationary state, neglecting the sharp variations of boundary conditions that originate in the transients of the process. In the determination of the laser-matter relationship, the load profiles in the different deposition planes were determined by means of the powder distribution obtained by the proposed method. With respect to the laser path between the optics and the component surface, the laser encounters load profiles (defined by the powder distribution) in series, from closest to the nozzle outlet to deposition plane profile. The powder particles absorb/reflect the laser energy according to their physical characteristics and spatial distribution, gradually decreasing the useful energy for melting the substrate. The greater the standoff distance, the higher the number of planes are intercepted by the laser beam, each with a different particle distribution. The envelope function is used to obtain the

overall load profile that summarized the previously planes encountered by the laser. As shown in Figure 16, it is given by the maximum brightness value of the powder distribution for each point of the planes considered.

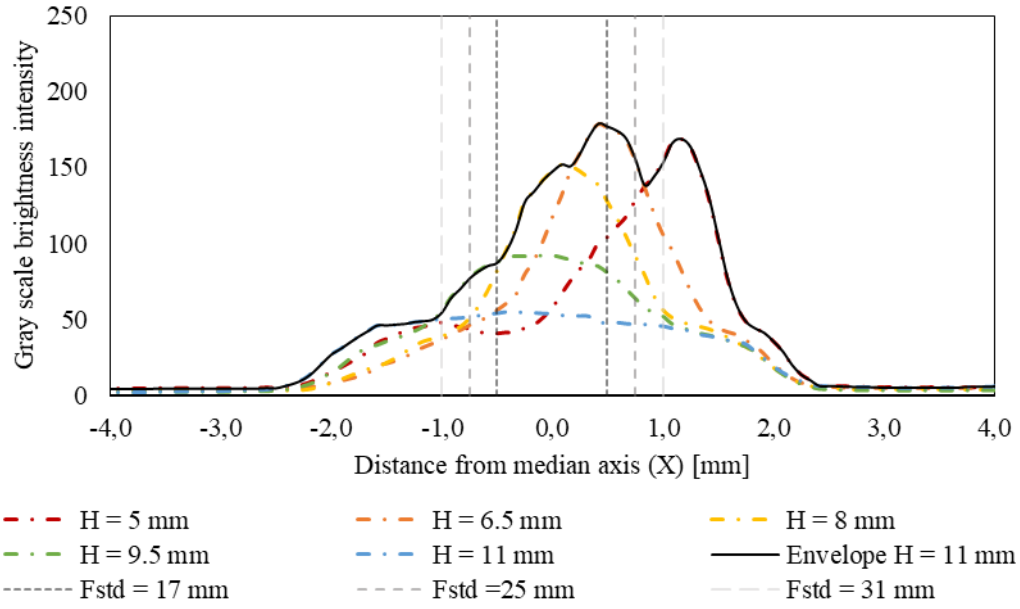

Figure 16. Brightness intensity distribution of transversal planes and envelope function of the deposition plane at a standoff distance of 11 mm [22].

Thus, the entire spatial development of the powder flow is taken into account, especially in the most remote deposition planes. The regions of interest considered in the upper planes were calculated considering the size of the laser spot on each specific deposition plane. The CRB values for each setup were calculated and plotted in Figure 15b. In this way, the laser-particle interaction was modelled along the entire particle path. Comparing the CRB of each deposition plane to the CRB of the envelope function, it is clear that the latter affects mostly the farther deposition planes that are strongly influenced by previous interactions.

Process model

Modelling of the powder distribution

The theoretical basis on which the whole proposed framework lies is obtained by starting from the hypothesis on the powder distribution stated by Liu and Li [47]. This is expressed according to a Gaussian distribution and the formulation is given below in Eq.(2):

$$n(x,y) = \frac{2\dot{m}_p}{\pi r_p^2} \exp\left[\frac{-2(x^2+y^2)}{r_p^2}\right] \quad (2)$$

where n(x,y) is the powder density over the cross-sectional area of the powder flow, $\dot{m}_p$ is the powder flow rate and r_p is the powder flow radius. Liu and Li considered the powder distribution derived from a coaxial nozzle in the plane of the powder focus (also defined as the standard deposition plane). This function, while valid for the standard deposition plane,

is unable to describe the powder distribution in different deposition planes. These planes are characterized by distributions with various peaks, which are difficult to model with the classical Gaussian function. Therefore, the function was modified with an annulus function with a Gaussian profile [48], as follows in Eq.(3):

$$n(x,y) = \frac{2k_p \dot{n_p}}{\pi[(R+r_{pa})^2-(R-r_{pa})^2]} \exp\left[\frac{-2(-R+\sqrt{(x^2+y^2)})^2}{r_{pa}^2}\right] \quad (3)$$

in which R(z) is the median radius of the annulus (where is positioned the maximum intensity), r_{pa}(z,div) is the half-width of the annular ring (or beam waist) and k_p is a calibration factor to ensure the mass conservation in the infinite x-y domain. The median radius is a function of the standoff distance and it represents the powder distribution of the conical flow of powder. This function is applicable for deposition planes different from the standard deposition plane. In the latter, the function degenerates into the circumference function as proposed by Liu and Li [47]. The half-section of the annulus is a function of the divergence of the powder flow and the standoff distance. The graphs in Figure 17 represent powder distributions in the deposition planes identified in the experimental plan.

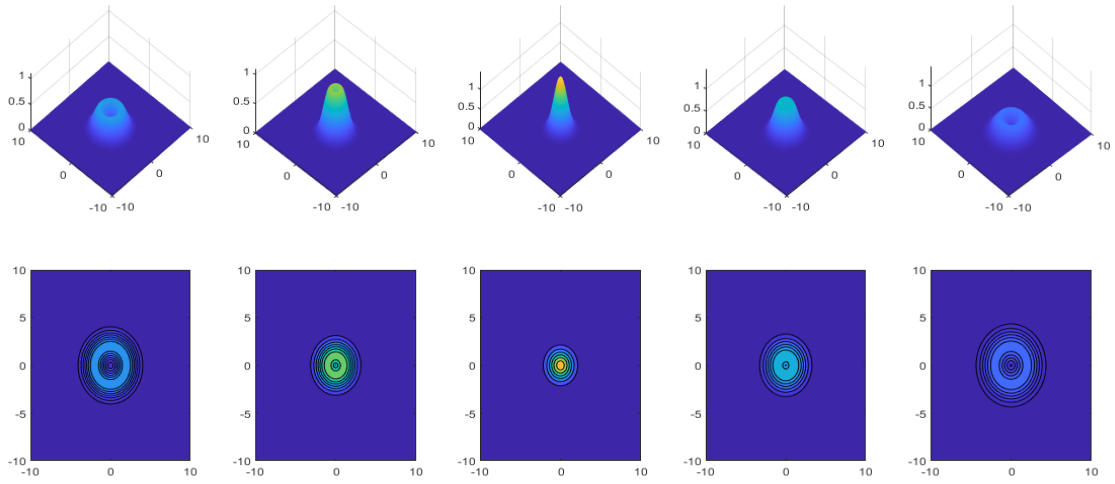

Figure 17. Powder distribution in deposition planes proposed in the experimental plan (ref. Table 3) [22].

Modelling of the laser-material interaction

Once the powder distribution was defined as the standoff distance varied, it was possible to model the laser-matter interaction and the amount of laser energy useful for the creation of the melt pool. By applying the annulus distribution of powder of Eq.(3) in the formulation proposed by Liu et Li [47], the thermal flux density at point (x, y) (I(x, y)) becomes the Eq.(4):

$$I(x,y) = I_0(x,y)[1 - \alpha n(x,y)] =$$

$$= \frac{2AP}{\pi r_b^2} \exp\left[\frac{-2(x^2+y^2)}{r_b^2}\right] * \left\{1 - \alpha \frac{2k_p \dot{n}_p}{\pi\left[(R-r_{pa})^2-(R+r_{pa})^2\right]} \exp\left[\frac{-2(R-\sqrt{(x^2+y^2)})^2}{r_{pa}^2}\right]\right\} \quad (4)$$

Consequently, the laser energy absorbed by the workpiece per unit of time (P_L) turns into the Eq.(5):

$$P_L = \int_\Omega \int I(x,y)\, dxdy = \int_\Omega \int I_0(x,y)[1 - \alpha n(x,y)]\, dxdy = AP - W'AP \quad (5)$$

where the W' is:

$$W' = \alpha \frac{4k_p \dot{n}_p}{\pi^2 r_b^2[(R-r_{pa})^2-(R+r_{pa})^2]} \int_\Omega \int \exp\left(\frac{-2(R-\sqrt{(x^2+y^2)})^2}{r_{pa}^2} - \frac{2(x^2+y^2)}{r_b^2}\right) dxdy \quad (6)$$

Eq.(6) represents the fraction of laser energy absorbed/reflected by the powder flow with an annulus distribution. In order to verify the aforementioned equation, a specific region of interaction (Ω) was identified. The region of the laser-material interaction was defined based on the size of the laser beam on the deposition plane. As suggested experimentally, this was coaxial with respect to the powder flow and has a radius smaller than that of the powder distribution (see Figure 13). The equation used for the region of interaction is expressed in Eq.(7):

$$\Omega = (x^2 + y^2) \leq r_b^2 \quad (7)$$

where $r_b(z,div)$ is the nominal radius of the laser beam that is a function of the standoff distance and the divergence of the laser beam. The three laser spot diameters were evaluated with the respective beam divergence, as previously indicated in the section before. The function plotted in Figure 18 was used as the region of interaction (Ω) in which the function was integrated.

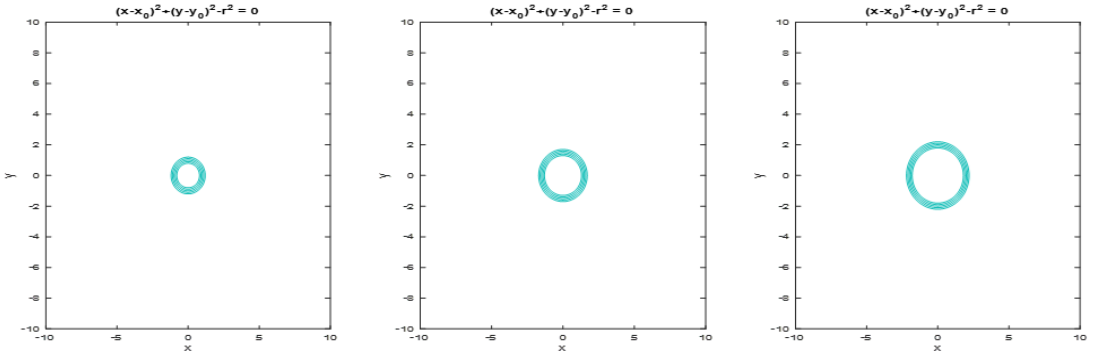

Figure 18. Region of interaction for each combination proposed in the experimental plan (ref. Table 3) [22].

Figure 19 shows the amount of powder mass interacting with the laser beam calculated by applying the proposed formulation for each combination proposed in the experimental plan (Table 3). It is clear how the trend identified using the proposed formulation agrees with the

experimental results previously shown in Figure 15a.

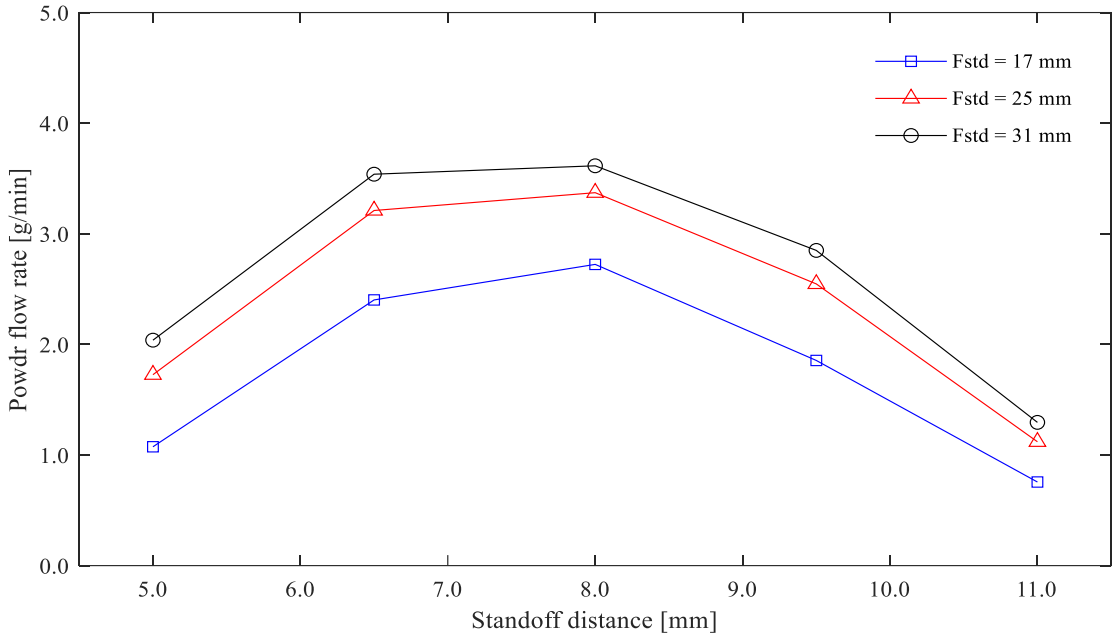

Figure 19. Amount of powder interacting with the laser beam for each combination of the experimental plan (ref. Table 3) [22].

Statistical analysis

The ANOVA with a general linear model was employed to statistically investigate the effects of the two analyzed process parameters on the geometrical characteristics of the single deposited clad. The standoff distance was evaluated at five levels, while the laser defocusing distance was evaluated at three levels. Five replications were performed for each combination of factorial levels. The main effects and the interactions of the investigated factors were analyzed: this represents the average effect of an independent variable and the interaction of two independent variables (as in this case F, H and F*H) on the dependent variable (w, hs, hi and Dil). The technique used for the test involved the use of p-value and the significance level α, considered equal to 0.05: when the p-value was less than or equal to α the effect of the considered factor on the output was statistically significant [49].

Table 5, Table 6, Table 7, and Table 8 contain the results of the ANOVA analysis. It was found that laser defocusing distance (F), standoff distance (H), and their interaction (F*H) had a statistically significant influence on the clad width, clad height, penetration depth, and dilution. In fact, p-values were very small for all the main effects and their interaction, lower than the limit of significance considered. Thus, it was demonstrated that the considered factors and their interaction influenced the main geometrical characteristics of a deposited clad, justifying further investigations. The importance of a combined analysis of the two factors, which is the main aim of the work, is underlined: this analysis was possible thanks to the advanced motorized optics system adopted, which allowed the variation of the size of

the laser spot on the deposition surface decoupled to the standoff distance.

Table 5. Analysis of variance for clad width (w) [22].

Factors	DoF	Adj SS	Adj MS	F-value	p-value
F	2	277488	138744	980,20	0,000
H	4	157689	39422	278,51	0,000
F*H	8	83921	10490	74,11	0,000
Error	60	8493	142		
Total	74	527592			

Table 6. Analysis of variance for clad height (hs) [22].

Factors	DoF	Adj SS	Adj MS	F-value	p-value
F	2	51358	25679	257,03	0,000
H	4	1984407	496102	4965,65	0,000
F*H	8	103218	12902	129,14	0,000
Error	60	5994	100		
Total	74	2144978			

Table 7. Analysis of variance for penetration depth (hi) [22].

Factors	DoF	Adj SS	Adj MS	F-value	p-value
F	2	78134	39067	670,95	0,000
H	4	1090669	272667	4682,86	0,000
F*H	8	20524	2566	44,06	0,000
Error	60	3494	58		
Total	74	1192821			

Table 8. Analysis of variance for dilution (Dil) [22].

Factors	DoF	Adj SS	Adj MS	F-value	p-value
F	2	2216,1	1108,03	1331,17	0,000
H	4	29355,3	7338,83	8816,78	0,000
F*H	8	722,3	90,29	108,48	0,000
Error	60	49,9	0,83		
Total	74	32343,7			

Experimental results and discussion

Effects on the clad width

In laser cladding and 3D manufacturing applications of L-DED technology, an important process variable is the clad width, which is mainly dependent on the melt pool size [50,51]. In Figure 20 are shown the effects of the laser defocusing distance (F) and standoff distance (H) variations on clad width (w). The averages of measurements, taken on five replications performed using the same set of process parameters, were used to plot the trends for each combination.

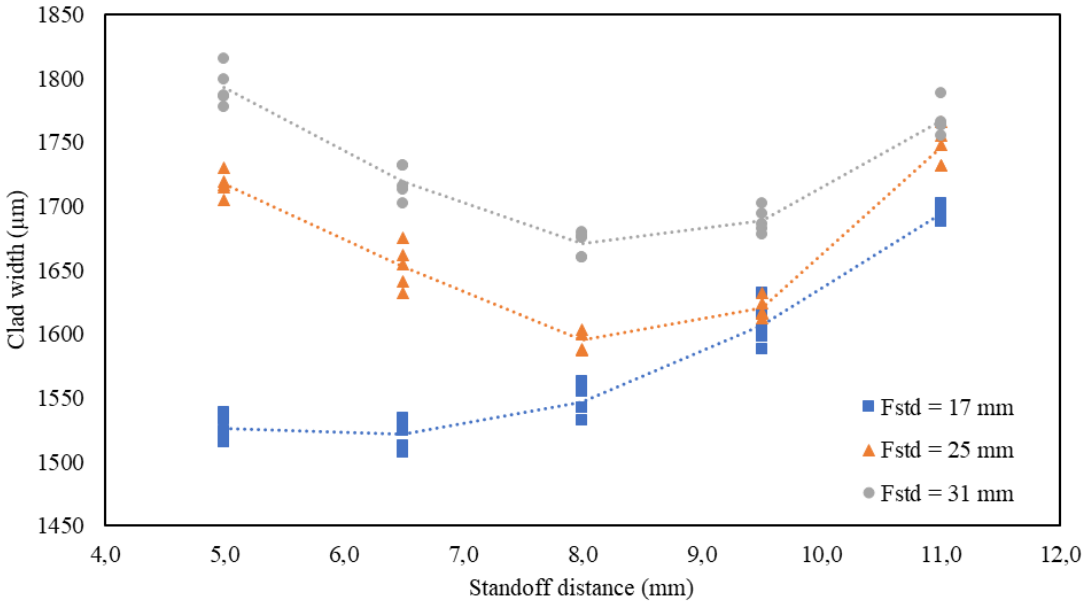

Figure 20. Influence of standoff distance and laser defocusing distance on the clad width [22].

Figure 7 shows cross-section macrographs, in which the width of the single deposited clad is modified with the F. This effect is derived from the shift of the laser focus point, and so from the spot size variation on the substrate surface. Consequently, with increasing F, the laser irradiation area changed and the interaction time between the laser beam and substrate increased, creating a larger molten pool and a larger clad width. Similar effects were also deduced by Tan et al. and Zhang et al. [40,50]. It can also be observed that the standoff distance variance had an impact on the clad width challenging to interpret. Similar considerations have also been indicated in the forecast model of the clad width proposed by Liu and Li [47] and modified by Zhu et al. [37]. The model is the following:

$$w = 2\left(\frac{P\,A\,(1-r_p)\,d^{1/2}}{2\,(T_m - T_0)\,\sqrt{\pi\,\lambda\,v\,\rho\,c_p}}\right)^{1/2} \quad (8)$$

where P (W) is the laser power, A is the laser absorptivity, r_p is the reflectivity factor of powder (from Pinkerton and Li) [52], d (mm) is the laser spot diameter, T_m (K) is the melting temperature, T_0 (K) is the initial temperature, λ (W/(m·K)) is the coefficient of thermal conductivity, v (m/s) is the laser translation speed, ρ (kg/m) is the density and cp (J/(kg·K)) is the specific heat. However, results found in this experimental work differed from the outcomes obtained through the model shown in Eq. (8) for a calibration coefficient k, which mean value is equal to 0.65. This coefficient originated from the usage of different materials of powder and substrate. Furthermore, it must be said that accurate values of the physical properties of the employed Nickel-based superalloy powder were not known because covered by copyright. Hence, values of physical properties of the AISI 304 stainless steel at

1000 °C, as listed in Table 9, were used in the model. Of fundamental importance are the temperature values of the process, which were compared with the results obtained from previous experimental tests carried out with the same metal alloy using an IR thermal camera [53].

Table 9. Physical properties of AISI 304 stainless steel [22].

Parameters	Unit	N	Value
Absorptivity	-	A	0.35
Reflectivity factor of powder	-	r_p	0.09
Melting temperature	K	T_m	1650
Ambient temperature	K	T_0	290
Thermal conductivity	W/mK	λ	28.12
Density	Kg/m^3	ρ	8000
Specific heat	J/kgK	c_p	500

Following what was stated by Zhu et al. [37], the reflectivity factor of powder related to the Gaussian powder distribution expressed in Eq. (2), here renamed r_{fp} (to avoid mistakes with the powder flow radius r_p), reports a value of 0.09. This reflectivity factor of the laser power caused by the metallic powder was experimentally determined [36] by means of an investigation concerning laser cladding. This factor was defined by varying powder feed rate and laser power in a standard configuration of the equipment used. This value of the rf_p factor is thus referred to standard deposition conditions. However, as previously stated, this factor is a function of the powder flow rate and its spatial distribution. Since no experimental values of rf_p are available for the W' of the annulus powder distribution (Eq. (6)) in the literature, in the present work it was proposed to relate this factor with the Gaussian powder distribution. It was, therefore, asserted that:

$$rf_{\mathrm{pi}} = rf_{\mathrm{p}}\left(\frac{Q_i}{Q_{st}}\right) \tag{9}$$

in which Qi is the powder flow (expressed as CRB) related to the area affected by the laser spot of the considered deposition plane, while Qst is the powder flow related to the area affected by the laser spot in the standard deposition plane (8.0 mm). Both factors are previously reported in Figure 15a. Therefore, the rf_{pi} proposed in Eq. (9) is the reflectivity factor of the powder referred to the specific deposition condition and is calculated as a proportion between the Qi and Qst. As noted by comparing Figure 15a and Figure 19, this factor can also be found as the ratio between the W' factor of the annulus powder distribution and the W factor of the Gaussian powder distribution.

The Eq. (8) for defining the deposited track width w is modified as follows:

$$w = 2k\left(\frac{A\,P\,(1 - rf_{\mathrm{pi}})\,d^{1/2}}{2\,(T_{\mathrm{m}} - T_0)\,\sqrt{\pi\,\lambda\,v\,\rho\,c_{\mathrm{p}}}}\right)^{1/2} \tag{10}$$

As can be seen from the model shown in Eq. (10), the clad width is intrinsically affected by the standoff distance and defocusing distance. Some parameters of the equation, proposed by Liu e Li, for the estimation of the clad width, are influenced by the standoff distance and the defocusing distance: these are the laser spot diameter (d) and reflectivity factor of powder (rf_p). As described in previous sections, the size of the laser spot on the deposition plane varies as a function of the standoff distance and defocusing distance. From Figure 10, it can be observed that the laser spot diameter took values from 0.972 mm to 2.183 mm, which strongly influenced the final clad width. On the other hand, the laser power reduction factor due to powder reflection should be proportional to the amount and spatial distribution of particles interacting with the energy beam. This distribution strongly varies with varying the position of the deposition plane. In the closer planes (5.0 mm) the powder flow concentrates on the outer edge of the laser beam, interacting minimally and allowing deeper fusion of the substrate. Inside the melt pool, given the very high thermal gradients, convective motions have been generated that lead to the enlargement of the pool. In the intermediate deposition planes (6.5 mm and 8.0 mm), the powder flow is higher and focused more centrally on the region of the laser beam. This leads first to an increased reflection of the laser power by the metal particles and consequently a reduction of the track width. Finally, in the more distant deposition planes (9.5 mm and 11 mm) the particle density drops radically assuming a substantially homogeneous distribution throughout the region of interest. In this way, the track width increases again, primarily because it follows the increase in the size of the laser beam and then because the retaining action given by the fusion and mixing with the substrate is reduced. In fact, depositions made with the highest standoff distance result in an extremely low dilution with the substrate, leading to a very low adhesion force between clad and the substrate.

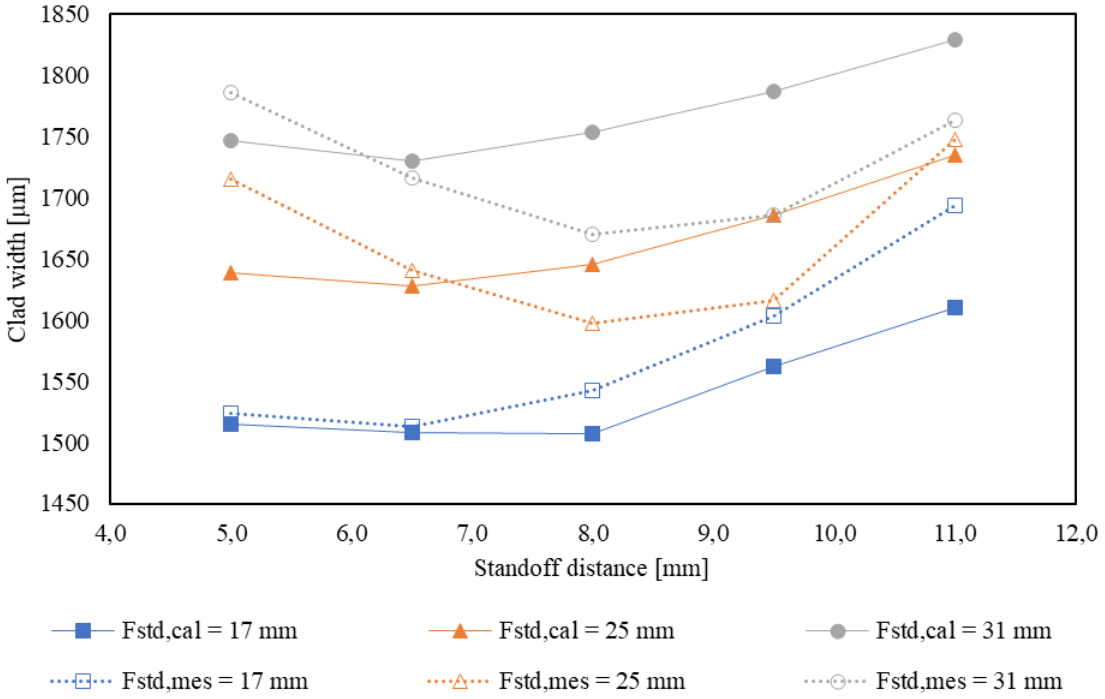

Figure 21. Comparison between calculated (solid line) and measured (dotted line)values of the clad width [22].

Figure 21 shows the calculated values of clad width compared to the measured values. Therefore, a good correlation between the trend of the experimental results and those obtained using the model can be observed. In fact, an average error of 35 µm, 44 µm, and 61 µm was detected for the values related to the defocusing distance of 17 mm, 25 mm, and 31 mm, respectively. This represents an average percentage error of 2.79% and a maximum value of 6.00%. It makes the model suitable for a careful forecast of the clad width.

Effects on the clad height

The clad height is another very important geometrical feature of laser deposition. This geometrical characteristic is important for the control of fabrication accuracy in the vertical direction [50]. In Figure 22 are shown the effects of the laser defocusing distance (F) and standoff distance (H) variations on the clad height (hs). Each plotted value is the average of the measures taken on the five replications performed with the same set of process parameters.

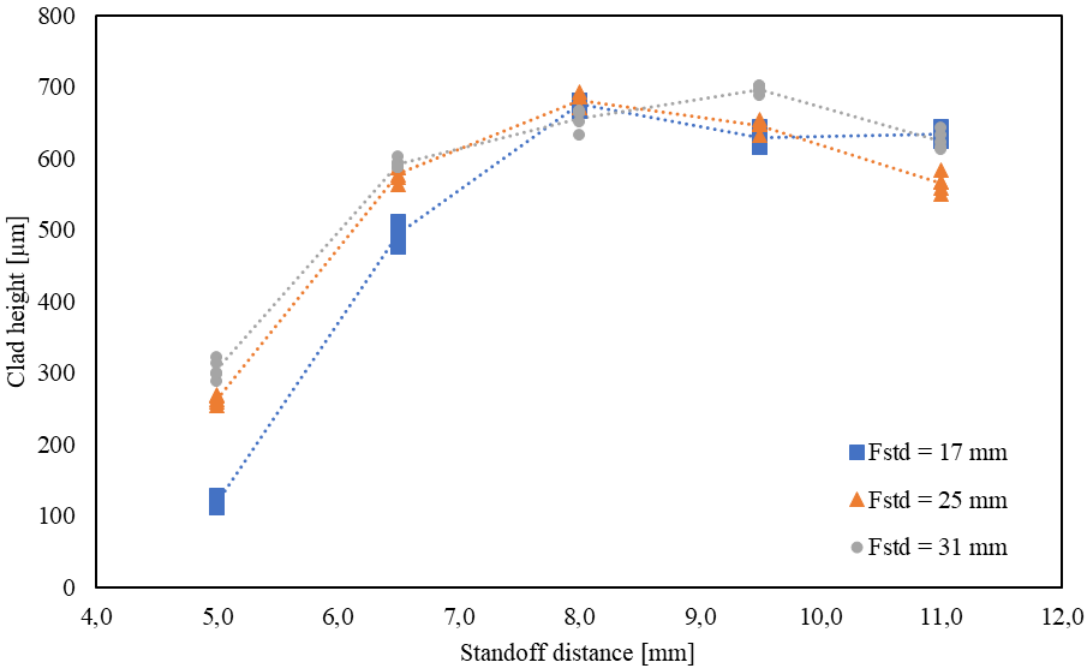

Figure 22. Influence of standoff distance and laser defocusing distance on the clad height [22].

The influence of laser-defocusing distance on clad height was not obvious [54]. In fact, in Figure 22 it is possible to notice that F had very little influence on the clad height. On the contrary, a strong relationship between clad height and standoff distance can be observed. The clad height is the geometrical characteristic most linked to the amount of powder injected into the melt pool [55]. The amount of powder and its spatial distribution in the region of interaction with the laser plays a fundamental role in determining the height of the clad. The macrograph analysis (see Figure 7) was corroborated by the image analysis of the powder flow. In Figure 22, it can be observed that the clad height increased very quickly in the transition from H = 5.0 mm to H = 6.5 mm. This phenomenon is caused by the powder flow cutting off: in fact, at such a low standoff distance, the powder cone was truncated by the substrate before focusing. As shown in Figure 13, the light reflected from the particles in the closer planes to the nozzle reveals a powder concentration in the side areas. Consequently, the laser beam invested less powder during its path and discharged almost all its energy on the substrate creating deposition with lower clad height and higher penetration depth. When the nozzle moves away from the substrate, the powder flow achieves to focus on the top surface of the substrate. In fact, the standard deposition plane (8.0 mm), shows a Gaussian-like distribution, centered in the center of the laser beam. Hence, a greater amount of powder was invested by the laser beam. The substrate returned to be shadowed from the powder flow, and the absorption of the laser energy was better distributed between powder and substrate, increasing the clad height. Hence, the interaction between the laser beam and

the powder flow is extremely important [34]. The further increase of H caused the conic powder flow to focus to a certain distance above the substrate. In the planes farther from the nozzle, the distribution flattens becoming nearly uniform for the entire surface reached by the energy beam (see Figure 13). Therefore, after the initial phase in which the clad height increased with the standoff distance, passing the plane in which powder flow focused on the top surface of the substrate, a slight decrease in the clad height was noticed.

The maximum track height was detected at the standoff distance equal to 8 mm (the standard deposition plane), therefore in the plane in which the powder flow focus maximized the catchment efficiency of the melt pool: the same result was found by Zhu et al. and Tan et al. in their studies [35,38–40]. The amount of powder captured during the processing was calculated by analyzing the envelope function, previously reported in Figure 15b at different deposition planes and defocusing distances. The relationship between the envelope function and the clad height is presented in Figure 23. The second-degree regression function exhibits a good correlation between the factors considered, highlighting how the powder flow plays a fundamental role in the clad generation.

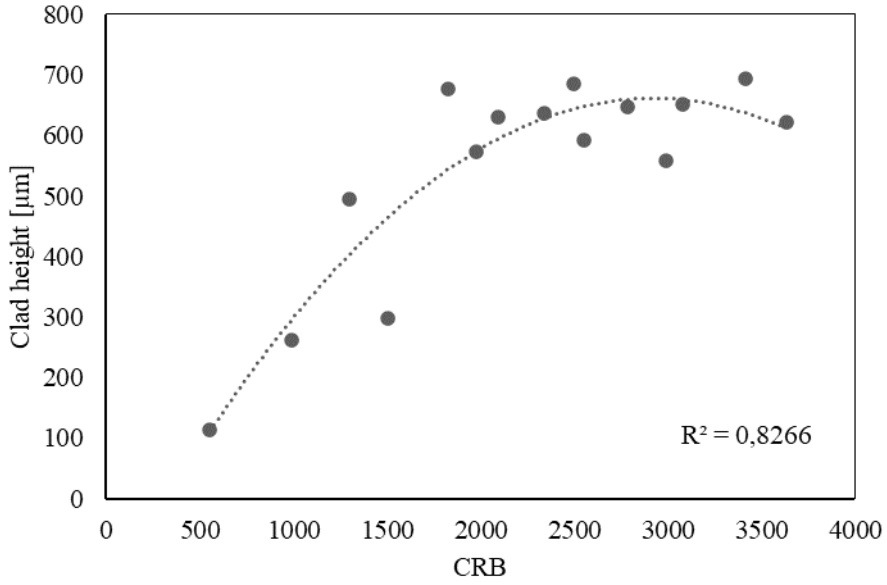

Figure 23. Clad height versus cumulative relative brightness (CRB) [22].

Effects on the penetration depth

As stated in the literature [51], the variation of laser defocusing distance and standoff distance affects the characteristics of the melt pool, consequently influencing the penetration depth of the single deposited clad. In Figure 24 are shown the effects of the laser defocusing distance and the standoff distance variations on the penetration depth.

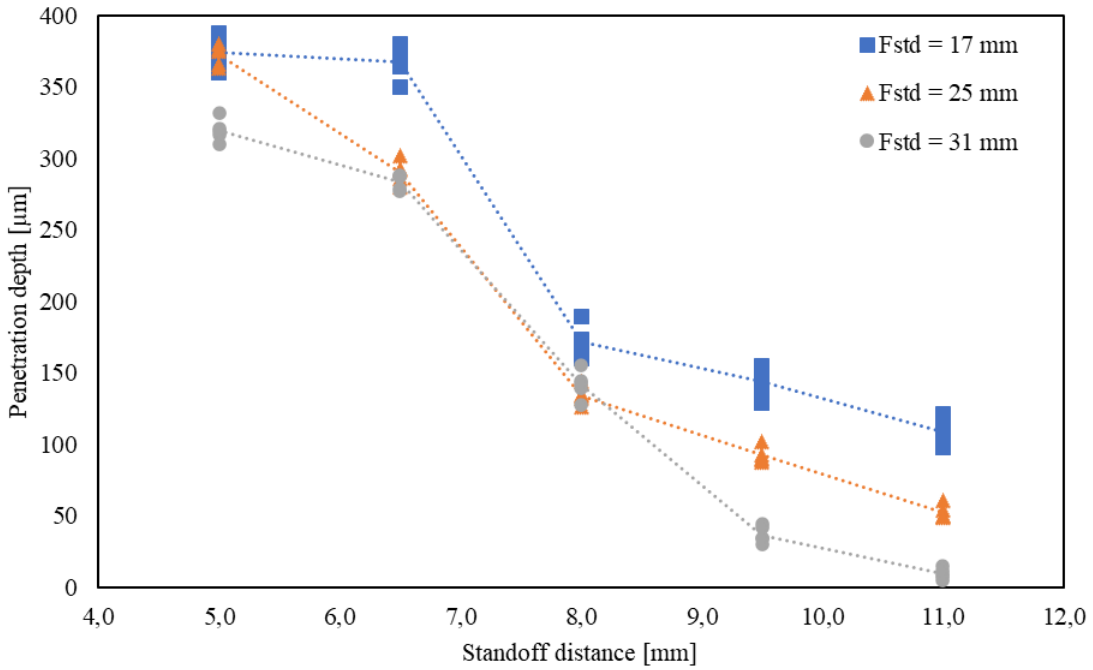

Figure 24. Influence of standoff distance and laser defocusing distance on the penetration depth [22].

It reveals that the penetration depth decreased while the laser defocusing distance increased. A significant parameter, the laser power density, was employed to explain this effect. Eq. (11) presents the formulation of laser power density (D).

$$D = \frac{4P}{\pi d^2} \tag{11}$$

D depends on the laser power (P) and the laser spot diameter (d) on the deposition plane. As already asserted in previous sections, the laser defocusing distance and the standoff distance influence laser spot size incident the deposition plane (see Figure 10). An increase in both parameters led to an increase of d, hence to a decrease in laser power density, which in turn led to a lower capacity for melting the substrate. This effect caused a decrease in the penetration depth of the melt pool. Quite the opposite, at lower laser spot diameter, the laser power density increased, and the laser power was concentrated on a smaller surface, causing a higher penetration depth. This trend is also discernible in Figure 7. It shows that low values of standoff distance led to excessive penetration into the substrate. Instead, an increase in standoff distance conducted to a rapid decrease in the penetration depth, which approximately became negligible at high values of standoff distance: the track appeared to be glued to the substrate.

In addition to the influence of energy density, there is another effect to be considered in the analysis of penetration depth: the shadowing effect of metal powders. The particles absorb or reflect part of the energy developed by the laser beam before it reaches the substrate. In

this way the fraction of thermal energy useful to produce the melt pool is reduced as the amount of powder grows, compromising the penetration depth into the base material. In this evaluation, it is essential to take into account both the amount of powder present in the deposition plane and the path taken by the metal particles in the region covered by the laser beam. The particles capture energy all along the path: so, the greater the distance from the deposition plane, the greater the length of the path, and the smaller the energy reaches the substrate.

For this analysis, it becomes critical to consider the envelope function developed in the previous section. This results in an inverse proportionality relationship between the amount of powder passing through the laser beam (considered in terms of CRB) and the penetration depth of the track, as shown in Figure 25.

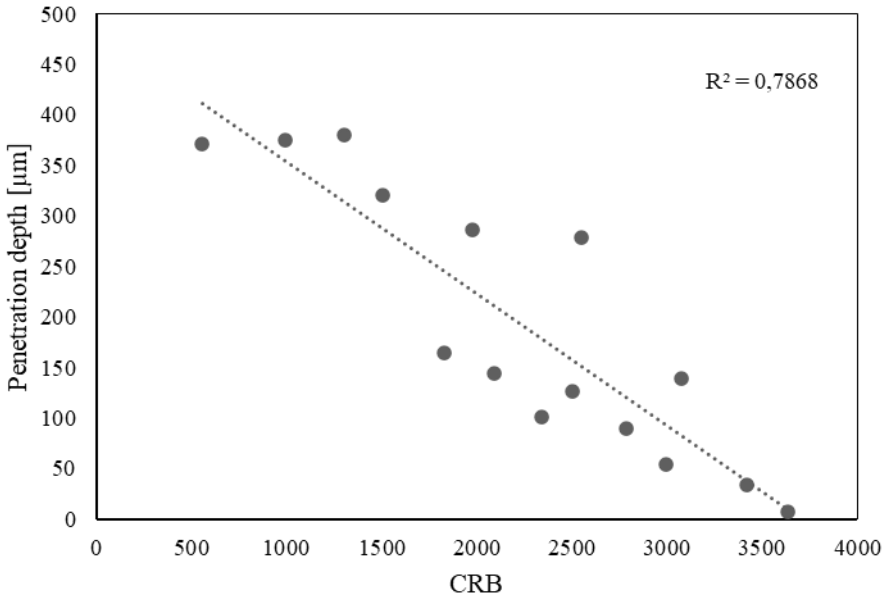

Figure 25. Penetration depth versus cumulative relative brightness (CRB) [22].

Effects on dilution

The dilution assumes a leading role in the quality assessment of the L-DED process, especially of dissimilar materials, and in determining the adhesion force between clad and substrate. Generally, the optimal value of the dilution parameter is between 10% and 30%. Since dilution is the ratio of geometrical characteristics discussed above (see Eq. (1)), all the considerations declared on the effects of standoff distance and defocusing distance must be considered. Clearly, the combination and superposition of these effects make the interpretation of their influences on dilution particularly complex. In Figure 26 it is noted that the dilution asymptotically decreases with the increase of the standoff distance. For low standoff distance values (5.0 and 6.5) the dilution is considerably high. This is due to the low powder mass captured by the melt pool, which does not allow adequate growth of the

deposited track but enables a large fraction of the laser energy to reach the substrate. On the other hand, the opposite effect is found when the deposition process is carried out with high values of H and the Dil parameter assumes remarkably low values. This makes the process unstable and increases the probability of track detachment due to poor adhesion to the substrate.

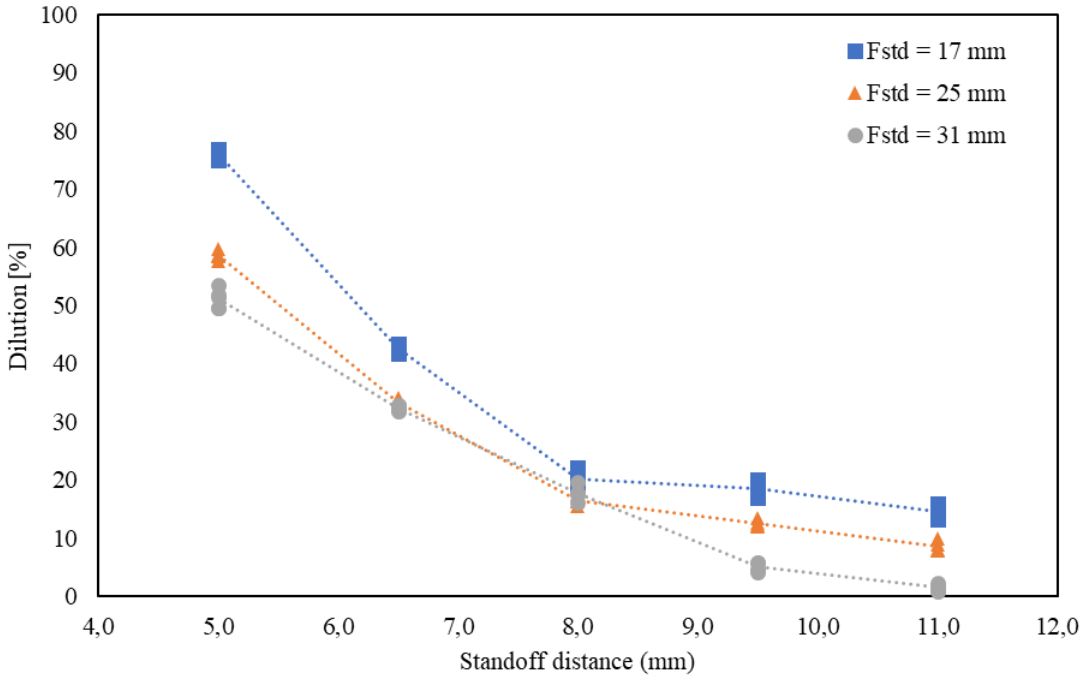

Figure 26. Influence of standoff distance and laser defocusing distance on the dilution [22].

As previously demonstrated by the statistical analysis, the defocusing distance also impacts the dilution value, albeit to a lesser extent. For each value of standoff distance, low values of F produce depositions with progressively higher dilution than the other setups. In fact, as F decreases, the size of the laser spot decreases, and the value of the power density increases (see Eq. 11). Hence, as the defocusing distance increases the dilution decreases, due to the superimposition of effects on clad and substrate. Combining the influences of standoff distance and defocusing distance on dilution is an excellent way to expand the operating windows of the laser deposition process. The defocusing distance could be increased when the deposition point approaches the nozzle and vice versa, to maintain the dilution values in the acceptability ranges. The effects on the dilution of the F and H parameters are explained through the analysis of the laser-powder interaction. As for the analysis of the penetration depth, it is essential to take into account the entire path taken by the powders to reach the deposition plane. For this reason, the envelope function presented in Figure 15b was employed. By relating this function with the dilution values, an excellent correlation between the two parameters with an R^2 value of 0.8344 was obtained, as shown in Figure 27. This is because the image analysis of the powder flow defined the amount of powder that goes to

create the deposited track, a fundamental part of the determination of dilution. Moreover, the powder particles passing through the laser beam capture the energy directed to the substrate. This changes the penetration of the laser beam into the base material and consequently the dilution value.

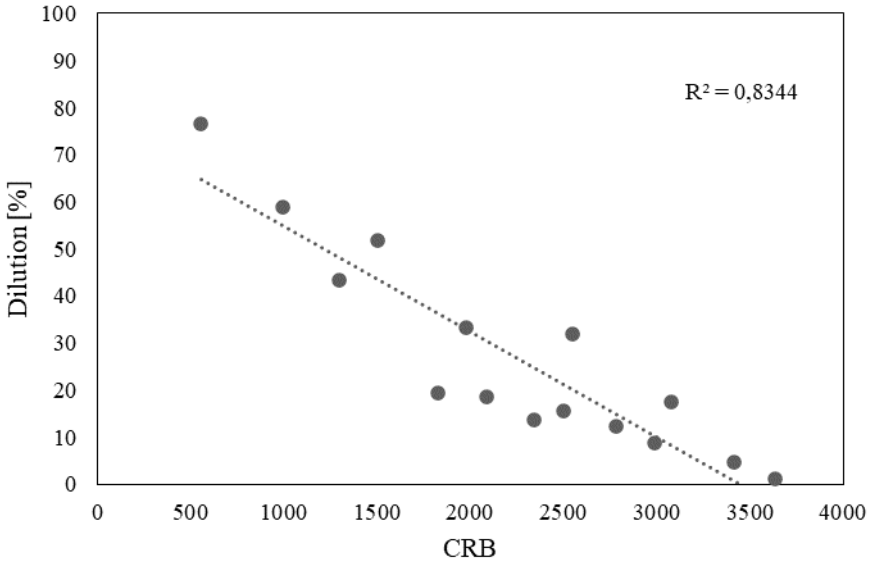

Figure 27. Dilution versus cumulative relative brightness (CRB) [22].

Conclusions

In summary, the results showed that the geometrical characteristics of the clad, such as clad width, clad height, penetration depth and dilution are affected by standoff distance and laser defocusing distance. The variations of the standoff distance reproduce the roughness of the deposition surface that can be generated during a multilayer deposition or cladding of complex geometries, given by even modest process instabilities (especially of the powder flow) in the underlying layers. Therefore this work is of paramount importance for an accurate design of these process parameters that can ensure a more stable deposition process with mutable conditions.

As far as scanning strategy (pattern or path) is concerned, it is another parameter that should not be underestimated and can strongly influence the final deposited structure or individual clad. The scanning strategy describes the path that the laser must take to perform the deposition; it indicates the priori-designed movements that the laser must perform. This 'path' that the laser must take is defined prior to deposition through the use of CAD/CAM programs; these programs allow the creation of a G-code file usually, which the machine will subsequently process. The strategy has various fields of influence on the finished product, so the best strategy is always tried to achieve the fewest defects on the clad or prototype produced. In addition to the path, when defining a strategy it is also important to

indicate the distance between two successive clads on the same plane (hatch distance) and the distance between two successive clads on two different layers (step height). In addition, the strategy between two layers is also defined, i.e. whether or not the n+1-th layer in relation to the n-th layer should have a different orientation, i.e. whether or not the next layer should be rotated by an angle in relation to the previous layer. Usually, strategies between layers if they have an orientation, this has multiple angles of 30° or 45° [56]. The most frequently used strategies for single-layer deposition are listed below and shown in Figure 28 and Figure 29, assuming, however, that a square section of a prototype has to be created [57,58]:

- Linear
- Zigzag
- Chessboard
- Contour
- Fractal

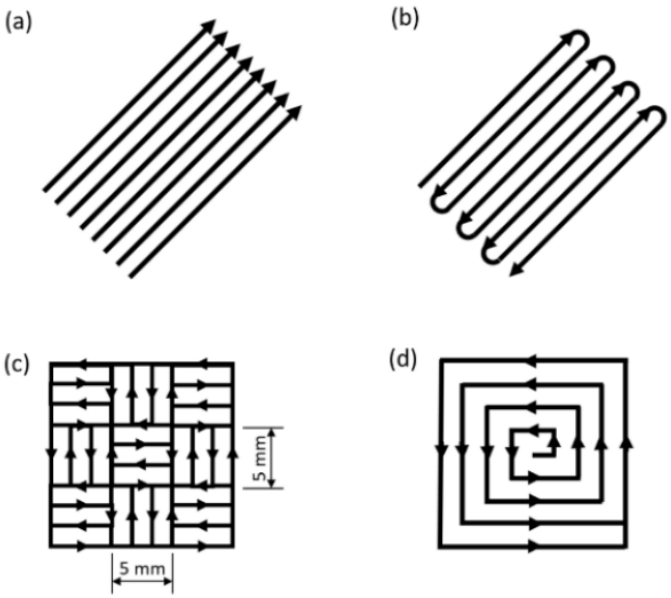

Figure 28. Deposition strategy: (a) linear, (b) zigzag, (c) chessboard and (d) contour [57].

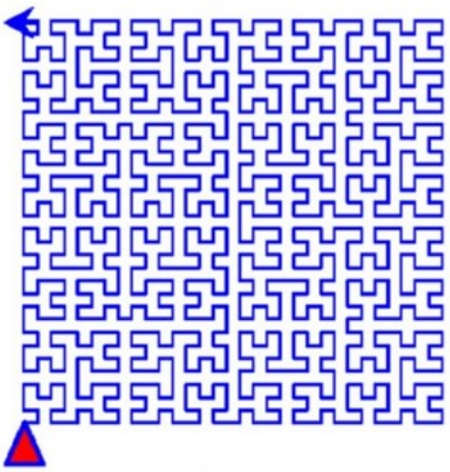

Figure 29. Deposition strategy: fractal [58].

In addition to the deposition strategies already mentioned, there are other important parameters, as mentioned above, to be considered for single-layer and multilayer strategies, which are the dwelling times, the orientation of the layers with respect to the previously deposited layers, the overlap, i.e. the overlap between two successive clads, as well as the distance between the midpoints of two successive clads, or in other words the distance between two vectors when designing the strategies and the step heigh [40,59–61].

It is also possible to adapt the above strategies to cylindrical prototypes, in some cases by adding a deposited outer circumference. A further strategy that can be used for cylindrical parts is that of concentric circumferences between them [62,63]. However, as has been written before, as strategies vary, clad and structure characteristics can be improved. The difficulty in choosing the best strategy for the best characteristics lies in comparing the strategies themselves, as one deposition strategy may or may not have characteristics compared to another strategy. Therefore, when making the choice of deposition strategy, one must always consider which final characteristics one wants to attribute to the finished product. Ribeiro et al. [57] performed studies on the first four strategies listed above: linear, zigzag, chessboard and contour. In their study, they designed two specimens for each strategy with different overlaps: one specimen with an overlap of 0.44 mm and the other with an overlap of 0.55 mm. Furthermore, the strategy was completed by imposing a rotation between successive layers of 67° in the case of the linear strategy and zigzag strategy, and a rotation between layers of 90° degrees in the remaining two strategies. The study involved specimens with a cubic geometry. The results showed that a well-defined cubic shape was obtained for all strategies with a lower overlap. Turning to the structural characteristics of the specimens produced, it was noted that, apart from the linear strategy, for an overlap of 0.55 mm a higher density was obtained in the specimen; in addition, the contour strategy presented the highest density among the specimens and was very close to that of the material

used (n.d.r. AISI 316L) equal to 8 kg/cm^2. As far as the microhardness is concerned, however, it is closer to that of AISI 316L if a linear, zigzag or chessboard strategy is used, although the microhardness analysed for the contour strategy is still high, but lower than that of the other test specimens, 209 HV compared to the range of 218-228 HV of the remaining three strategies. However, the study considers the contour strategy to be the best of the four strategies designed and used to produce the test specimens as it has better heat dissipation than the other strategies. Problems may arise when producing parts with more complex geometries [64]. However, it is possible to subdivide the section to be designed into several parts called islands. As depicted in Figure 30, it is possible to observe respectively the product to be obtained, a first island strategy and a second island strategy: for the strategy shown in Figure 30b, the product section was subdivided into three rectangles orthogonal to each other; in the second strategy (Figure 30c), the product was instead subdivided into squares of equal size with scan vectors orthogonal to the vectors of the previous scanning island. The island scan in Figure 30c has higher cooling rates than the island scan in Figure 30b, allowing for finer grain size. However, this resulted in a lower relative density, albeit very close (98.92% and 99.66%). This difference is the result of pores due to the lack of powder melting in the overlap zone between islands. On the other hand, however, the tensile strength and yield strength for specimens produced with the island scanning strategy are significantly higher than for specimens produced with the scanning shown in Figure 30b.

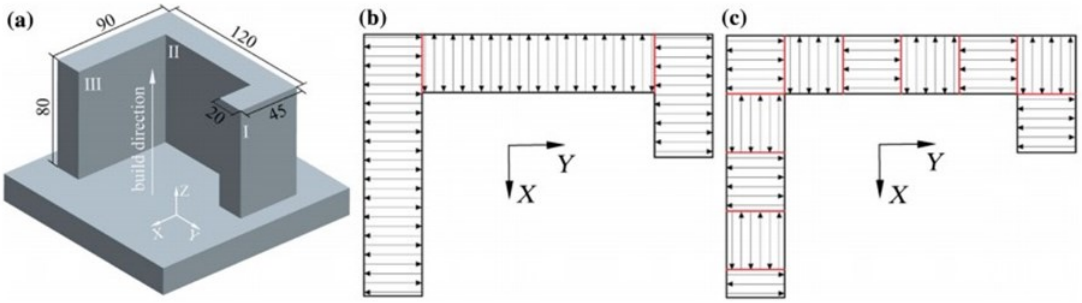

Figure 30. Direct laser-deposited Ti–6Al–4V structures (mm): a build dimension; b laser scanning path of orthogonal successive scanning on even layers; c laser scanning path of island scanning [64].

To explore this topic further, an in-depth study on the effects of scanning strategies on the final artefact produced by the L-DED process was conducted by Wang et. al. [65]

1.1.1.3 Applications

As already stated, the L-DED process finds wide application in various manufacturing sectors from the automotive to the aerospace, and biomedical sectors for the actual construction of parts but especially for their repair, considerably reducing costs and pollution [66,67]. It is also possible to selectively coat surfaces to improve their mechanical

performance [68,69]. For example, Oh et al. conducted a study on the repair of AISI 316L stainless steel specimens fabricated with PBF using the L-DED process, see Figure 31.

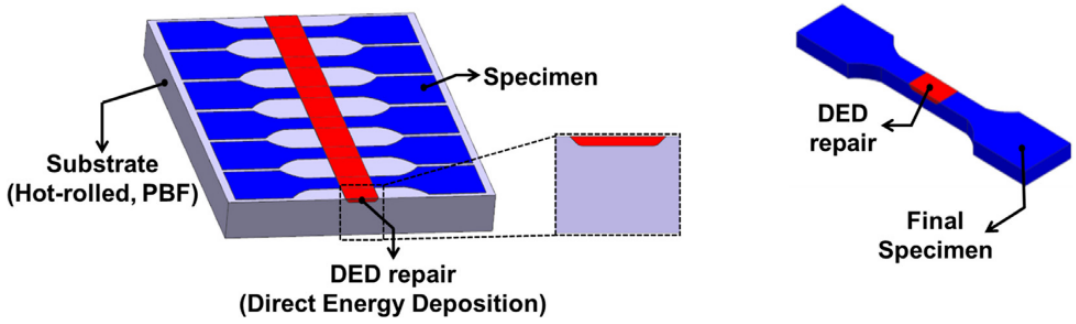

Figure 31. Example of a repair operation performed using the L-DED process [67].

Errico et al. conducted a study on the effects of L-DED coating and L-DED + Laser scanning on the surface performance of L-PBF stainless steel parts. The results of the work revealed many improvements in terms of surface roughness for the L-DED coating and even more for the LS treatment (please see Figure 32).

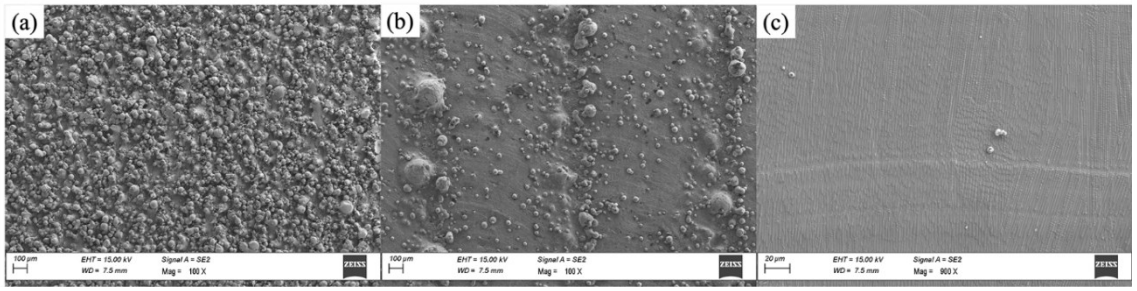

Figure 32. (a) L-PBF substrate; (b) DEDo coating; (c) DED-LS coating are shown in SEM images of the top surface [69].

However, new research trends are aimed at using this process for the multi-material fabrication of components in order to achieve tailored properties in the same part. Feenstra et al. [70] conducted a critical review of the state of the art in multi-material fabrication via directed energy deposition, which presents all the types of materials that have been selected for this type of AM so far and the different design approaches used to realize the multi-material component (including functionally graded techniques) (see Figure 33).

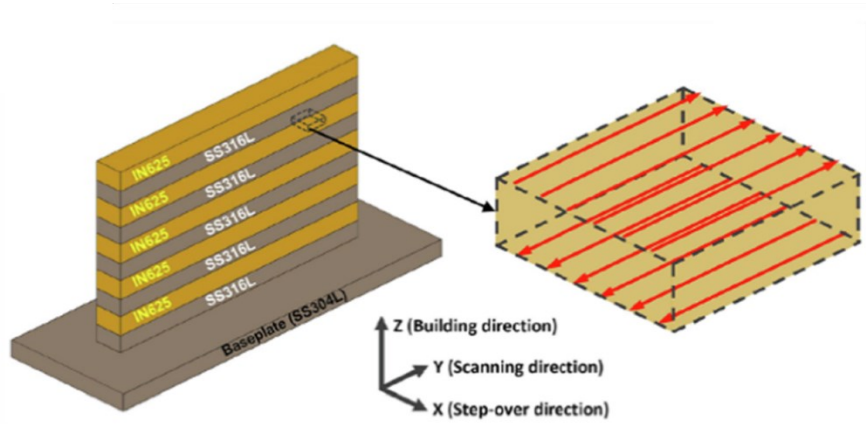

Figure 33. Example of multi-material manufacture between layers: AISI 316L - Inconel 625 [70].

1.2 Powder Bed Fusion processes (PBF)

As mentioned above, among the various AM processes are PBF technologies. The main among them are the Laser-Powder Bed Fusion (L-PBF) process and the Electron Beam Melting (EBM) process [19]. In both technologies, the material used is a metallic material in the form of a powder, typically produced by gas, water, or plasma atomization processes. Extremely important in the final process is the preparation of the powders, which must have a suitable sphericity in order to be evenly distributed on the printing platform before being hit and then fused by the laser or electron beam. Also in these technologies, the machining process starts with the design of the CAD model of the object to be printed. The latter is then converted into an STL (Solid To Layer) format and handed over to CAM software for the slicing phase. During this last phase, the 3D information of the model is transformed into 2D information, i.e. there is a transformation of the object into several layers, which represent the cross-section of the geometry to be produced. From the information for each layer, the tool paths (lasers) to be communicated to the printer are then obtained [17]. In terms of the fabrication mechanism, PBF technologies use an energy source to selectively melt thin layers of metal powder in order to build complex geometries. This type of AM process, specifically, begins with the spreading of a thin layer of metal powder on the printing platform, known as the substrate. Based on the information provided by the CAD file of the object to be built, different areas of the spread layer are fused, which will fuse together to create the indicated cross-section of the object, and to the printing platform, to prevent detachment from it. The energy source used during the process must be sufficiently powerful so that it does not act on a single layer but also on the previous layers, ensuring the optimum density of the finished part [19]. Next, the build platform is moved downwards, vertically, by an amount equal to the thickness of the layer, and the process is repeated until the part is completed. Figure 34 shows some parts made by the L-PBF and EBM process.

Figure 34. Some PBF metallic components: (a) cutting tool, (b) bike frame, (c) recuperator, (d) biomedical components [71].

However, there are some differences between the PBF technologies. One of them is the energy source used. The technology that uses a laser beam as the source is called Laser-Powder Bed Fusion; while the technology that uses an electron beam is called Electron Beam Melting [71]. As mentioned above, both laser-beam and electron-beam technologies use fine metallic powders with a highly spherical shape and an appropriate particle size as material. Typically, L-PBF processes use powders with a size in the range of 15-45 μm and therefore lower layer thicknesses, while the EBM process uses powders with a size in the range of 45-105 μm and therefore higher layer thicknesses. At the end of both processes, the part is welded to the substrate, for which an EDM wire is usually used to enable the part to be detached, and an appropriately designed support can also be included in the design of the part to facilitate detachment of the part from both the substrate and the printing platform [19].

The most commonly used materials are stainless steel, tool steels, titanium alloy Ti6Al-4V, aluminium alloys, nickel alloys, chromium, cobalt, and copper. For each type of material, it is necessary to determine the appropriate working parameters and the appropriate laser system, again due to the absorption mentioned above. The entire process usually takes place in an inert atmosphere of nitrogen or argon, free of humidity; both to prevent the risk of inflammability of the reactive metal powders and to prevent the powders from being contaminated and no longer suitable for the process. Systems using an electron beam as the energy source involve the use of a vacuum processing chamber to prevent the electrons of the beam from interacting or being deflected by air molecules. At the end of the process, the powder not involved in the melt can be reused following filtering, which is useful for removing powder agglomerates that have been sintered due to their proximity to the area involved in the melt.

1.2.1 Laser-Powder Bed Fusion (L-PBF)

1.2.1.1 Process description

The L-PBF process was developed by Dr. M. Fockele and Dr. D. Schwarze to produce metal components from metal powder. It is a process that melts localized areas, indicated by the CAD file, of the different powder layers with a laser beam, performing a complete melting of the material. However, before the CAD data are loaded onto the L-PBF machine, the STL files have to be processed through an interface software with the machine, to provide support structures in the case of overhanging or hollow surfaces, and to carry out the slicing phase, as mentioned earlier [71]. The build process starts by spreading a thin layer of powder on a platform by means of a levelling blade. Next, a high-energy-density laser beam hits and melts the powder in areas, appropriately indicated by the data transmitted to the machine. Usually, the machine is equipped with a special support PC with two software interfaced in serial mode (one for the machine and the other for the laser). During the process, the laser beam is moved, using appropriate scanning systems controlled by a PC (e.g. laser head connected to an X-Y table, optical scanner with oscillating mirrors), to the working point on the surface of the powder bed (identified within the X-Y plane) to melt the powder particles according to the data generated by the slicing of the model thus creating the desired section and, simultaneously, making it blend with the previous one [72]. Once this stage is complete, the platform is lowered by a height equal to the thickness of the layer, and a new layer of powder is deposited, which undergoes the same process as the previous layer. The process is repeated until the part is completed. During the process, due to the high temperatures, the part is built in a controlled atmosphere in the absence of oxygen and in the presence of inert gases such as argon and nitrogen, in order to prevent oxidation of the part or other problems that could damage its mechanical characteristics [71]. For the L-PBF process, the different layers must have an appropriate thickness to ensure both an optimal part finish and powder flow [73]; therefore, the thickness of each layer can vary between 20 and 100 μm [19].

It is also essential to consider the morphology and size of the powder as they influence powder flow, laser energy absorption, powder bed conductivity and powder bed density. A higher powder bed density, hence a higher powder packing density, is a positive factor as it allows for lower internal stresses, less distortion of the part, lower porosity and surface roughness. The powders most commonly used are gas atomized and have a spherical morphology, again to allow them to flow during the process. Particles with a non-spherical morphology tend to interlock, generating non-homogeneous powder layers, thus causing porosity and/or even incomplete melting [73]. L-PBF process mainly utilizes ytterbium fiber lasers or solid-state lasers, e.g. Nd: Yag, with power, generally ranging from 50 W to 1000 W; however, the most commonly used machines operate with powers between 200 W and

500 W [19]. The part obtained with L-PBF techniques is usually subjected to subsequent treatments; one of these is sandblasting in order to remove the not completely sintered powder present on the external surface of the part and decrease the roughness of the final part. During the process, the metal powder undergoes rapid heating to the point of melting and then rapid cooling; thus, the material undergoes a thermal shock that could cause internal stresses in the manufactured part. To remedy this problem, it may be necessary to carry out post-process heat treatment, or in some cases and for specific materials, it is also advisable to heat the printing platform [19]. The L-PBF system consists of a laser system, a processing chamber in a controlled atmosphere, a build platform and a powder platform, and a powder blade, please see Figure 35.

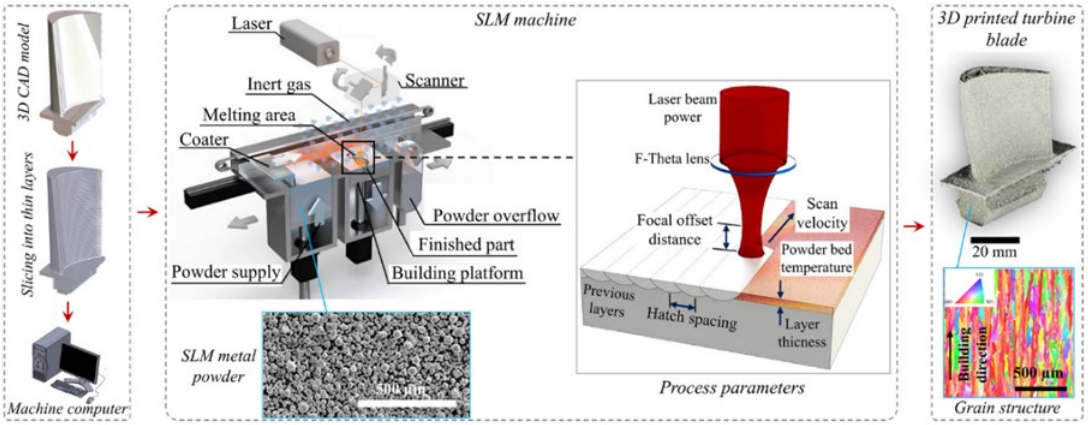

Figure 35. Schematic diagram of the L-PBF device and the main process parameter [71].

1.2.1.2 Input process parameters

From Figure 35 it is possible to identify the main process parameters to be considered in order to optimize machining. These play a fundamental role in both process control and the characteristics of the finished part. The main process parameters are listed below:

- Laser power, P: the power of the laser beam.
- Scanning speed, v: the speed at which the laser beam moves above the surface of the powdered material along the scanning paths.
- Laser spot diameter, d: laser beam size on the powder bed, usually in the range of 70-200 microns.
- Layer thickness, l_t: depth of a layer that is determined by advancing the construction platform by the same incremental amount.
- Hatch distance, h_d: distance between a couple of adjacent vectors, where a vector is defined as a narrow region of metal powder fused by laser scanning
- Scanning strategy: the path that the laser beam follows during fabrication.

The influence of the individual parameters on the individual fused track is very similar to that described above on the L-DED process. Described briefly, it can be seen that, at low laser power, high scanning speed and increased layer thickness, an undesirable effect known as the 'balling' phenomenon can occur, which results in the formation of discontinuous traces and the absence of bonding interline's, i.e. overlap [73]. As the L-PBF process is a manufacturing process by the addition of layers, balling is a severe impediment to subsequent powder deposition and causes defects such as porosity and even delamination. While high laser power and low scanning speed can generate evaporation of the material and create porosities referred to as the keyhole effect. Vapourization of the material during the process can result in the condensation of volatile materials on the laser lens, affecting the laser power itself [74].

1.2.1.3 Applications

As already mentioned, the fields of application for the L-PBF process are numerous. One of them is the manufacture of tools and molds (injection and die-casting molds), mold inserts, and functional components. The following are some examples that give a good idea of what is possible with this technology. Figure 36 shows some of the above examples.

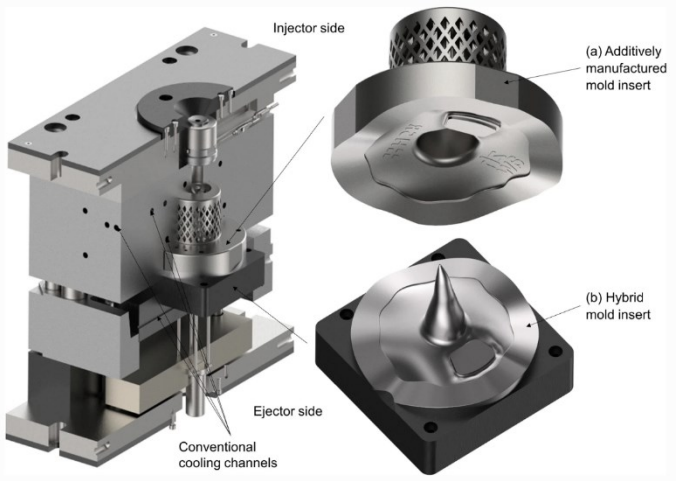

Figure 36. Examples of molds manufactured using the L-PBF process [75].

Functionalized components made with L-PBF have a number of advantages:

- complex geometries with the possibility of undercuts;
- production without tooling;
- no casting processes are required;
- manufactured components can be used for mechanical and dynamic tests;
- little post-processing is required.

Metallic materials currently available for the L-PBF process include stainless steel,

chromium-cobalt alloys, Ni-based alloys, aluminium alloys (such as Al-Si-Mg) and titanium (such as Ti6Al4V), and maraging steels. Mainly, these materials are used in aircraft and aerospace where mechanical properties (strength-to-weight ratio) and weldability are the most important characteristics [76]. 316L stainless steel is among the most studied for L-PBF due to its wide applications in marine and biomedical equipment. Cobalt-chromium-molybdenum-based superalloys are characterized by excellent mechanical properties, corrosion resistance, and high-temperature resistance. Over the years, cobalt-chromium-molybdenum (CoCrMo) has been used in biomedical applications, such as dental restorations and orthopedic implants (body joints and fracture fixation applications) because it is a biocompatible alloy with good corrosion resistance and good tensile and fatigue properties. Nickel-based super alloys are used to make aircraft turbine engine components, bolts and fasteners for high temperatures; and for nuclear engineering because of their excellent mechanical strength, tensile properties and resistance to corrosion and oxidation. Aluminium alloys, on the other hand, are of great interest, due to their low weight, in the aerospace and automotive sectors. In particular, the AlSi10Mg alloy has good mechanical properties. Moreover, due to its composition close to the eutectic Al-Si, the alloy possesses excellent fluidity in the liquid state and good weldability. For these reasons, AlSi10Mg is a good candidate for the L-PBF process and the process parameters, support structures, resulting microstructure, mechanical properties and surface roughness have already been meticulously studied for this alloy [76]. Figure 34 shows some of these components. However, also in the case of the L-PBF process, new research trends aim to use this process for the multi-material fabrication of components in order to achieve customized properties in the same part. Wei et al. [77] conducted a paper on the recent progress and scientific challenges in multi-material additive manufacturing via laser-based powder bed fusion, which presents all types of materials selected for this type of AM so far and the different design approaches used to realize the multi-material component (including functional grading techniques). Figure 37 shows some examples of the components manufactured so far and the equipment and methods used to make them.

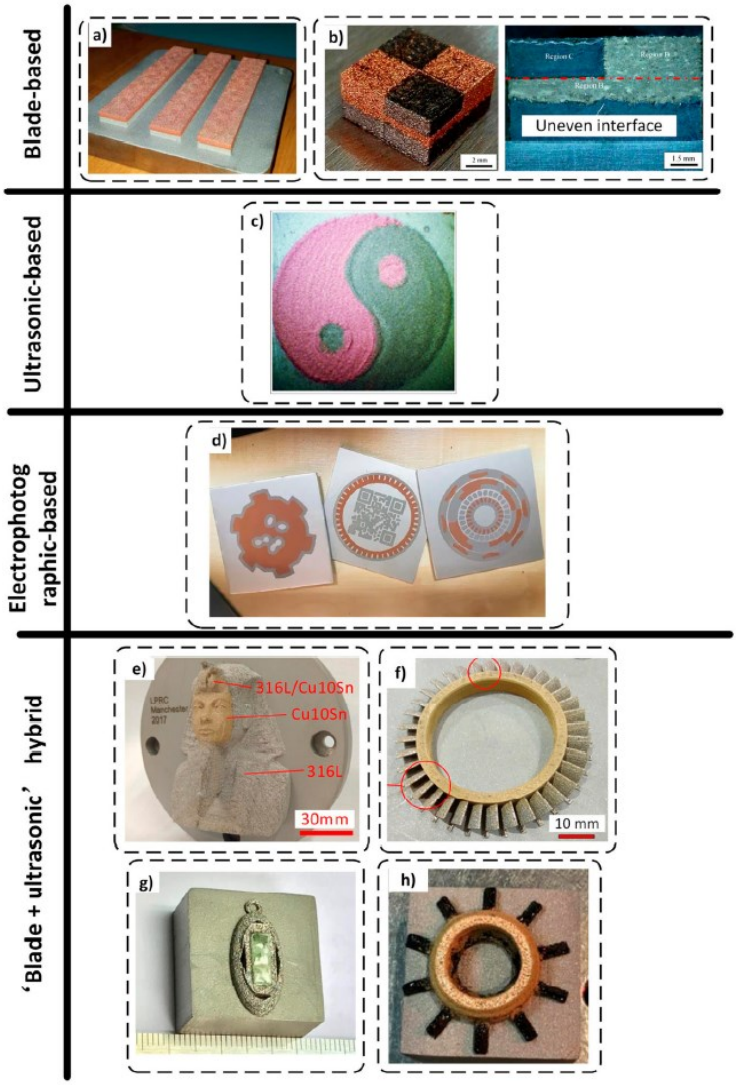

Figure 37. Examples of multi-material manufacturing using the L-PBF process [77].

2. Laser-Directed Energy Deposition process monitoring methods

2.1 State-of-the-art methods and systems for L-DED process monitoring

From an economic point of view, the deployment of the L-DED process in the industrial sector is slowed down by technical challenges yet to be solved. The main problems are the poor quality (in terms of dimensional accuracy and surface regularity) of the final parts and the low repeatability, which make this process unsuitable for high-value applications requiring high-performance standards [21]. In order to overcome these problems and improve product quality and process repeatability, several research groups investigated in-situ process monitoring, characterization, and real-time process control [21]. Process monitoring involves observation, information gathering, understanding of physical phenomena occurring in laser-material interactions, and finally the development of automated process control systems. This is also an essential method to reduce costs and the amount of material waste. A first classification distinguishes between near-IR thermal monitoring (using thermal imaging cameras, pyrometers, and bolometers) and optical monitoring by image analysis (using CMOS, CCD, or photodiode sensors) of the melt pool. Monitoring methods can be also classified, regarding the topological setup, as on-axis (coaxial) and off-axis with respect to the laser beam. CCD, CMOS, InGaAs, InSb and hyperspectral digital cameras are some of the tools used for monitoring. Depending on the wavelength of the light, digital cameras are divided into visible light or infrared (IR) cameras. In visible light cameras, charge-coupled devices (CCD) or complementary metal-oxide-semiconductor devices (CMOS) are used. In CCD cameras, a single circuit reconstructs all pixels signals, whereas, in CMOS cameras, each pixel has its own processing circuit. Therefore, the speed of CMOS cameras is higher than CCD cameras, which is why CMOS sensors are more complex and, as a result, the captured area is smaller than that of CCD cameras [12]. The use of CMOS and CCD cameras to monitor the L-DED process involves certain aspects that have to be handled carefully. Monitoring the melt pool requires continuous image acquisition to be able to extract useful information. Therefore, high-speed cameras with 1000 frames per second (fps) are generally used in the literature. Another problem to be taken into account is the need to process the images in order to be able to extract information [12]. IR cameras are an alternative for monitoring the temperature of the melt pool. Sensors of the InGaAs, InSb, PbSe types are used to detect the IR infrared signal. Although these types of cameras generally offer a much lower resolution than CMOS sensors, they allow more precise temperature measurements and a better dynamic range for

observing thermal emissions. Equipment with different technical characteristics can detect different aspects of the process, and by combining different systems, more sophisticated analyses can be carried out [16]. There are many areas of interest for process monitoring, some are listed below:

- Melt pool geometry.
- Melt pool temperature.
- Defects (porosity, geometric/surface, cracks, …).
- Deposition height.
- Deformations.
- Residual stresses.
- Powder flow.
- Microstructural inhomogeneity and impurity.

2.1.1 Optical monitoring field

As mentioned, some type of monitoring is carried out via optical techniques, which are mainly used to detect the geometry of the melt pool [21]. Analyzing the literature, it was found that optical systems and methods are more used than thermal methods for many advantages: the possibility of real-time and multi-functional acquisitions (i.e. temperature and images of the melt pool), intuitiveness, and flexibility [15]. The melt pool can be observed by digital cameras, especially CMOS, CCD, and IR, which allow a visual study of the target [21]. From the acquired images, the geometrical features of the melt pool can be measured after a post-processing phase. During the process, an attempt to keep primary dimensions as constant as possible is made in order to have a stable deposition. However, one of the main challenges for these cameras is the calibration of the sensors and threshold values in image processing [21]. With infrared cameras, images are captured in grayscale, based on brightness intensity. Each pixel has its grey value, and to calculate the width and length of the melt pool it is necessary to identify the value corresponding to the edge of the melt pool. Lei et al. [78] proposed the analysis and modelling of the melt pool for high-power diode laser cladding with a rectangular beam spot. The effects of the process parameters on the final geometrical characteristics were investigated. A camera with a frame rate of 31 frames/s was employed to monitor the melt pool during the process, see Figure 38a. The region-based active contours method, which was able to isolate regions characterized by nearly homogeneous intensities, was used to detect the melt pool boundaries, see Figure 38b. Results showed that the melt pool size (i.e. width and depth)

increases with increasing laser power while increasing translation speed leads to a decreasing in the melt pool size.

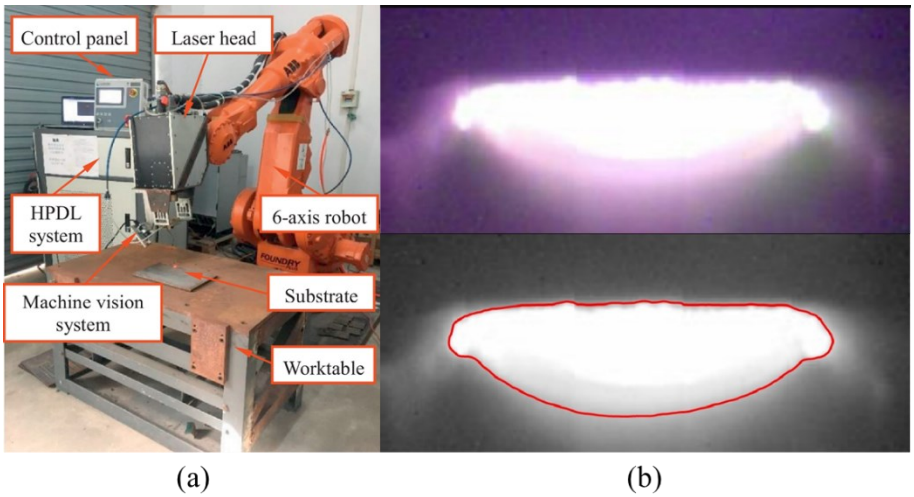

Figure 38. (a) 6-axis robotic system for the L-DED process equipped with an optical monitoring system, (b) image processing through active contour-based algorithms [78].

Other methods reported in the literature are related to "trial and error" image processing methods [21]. Akbari et al. [79] proposed work on coaxial optical monitoring of the L-DED process through the implementation of a closed-loop control of melt pool width, see Figure 39. The authors, in this work, set the grayscale threshold value by comparing the nominal width of deposited tracks with the width measured in the images, reporting a value of 80. The authors observed some glares upon the melt pool caused by hot incoming powder particles. Since these glares could generate measurement errors, a low-pass filter is applied to the images using the Fast Fourier Transform (FFT) technique. Regular intensity variations in the image corresponded to low frequencies, while abrupt and rapid intensity variations, such as those induced by glaring or noisy pixels at the edge of the melt pool, corresponded to high frequencies. A low-pass cut-off frequency of 5% was used to remove the noise. Finally, the edge of the melt pool was extracted, and all possible circumferences approximating the molten pool were detected in order to measure the largest section. The width of the melt pool was estimated as the largest of the calculated diameters. Figure 40 shows the whole flow of image processing conducted in this work.

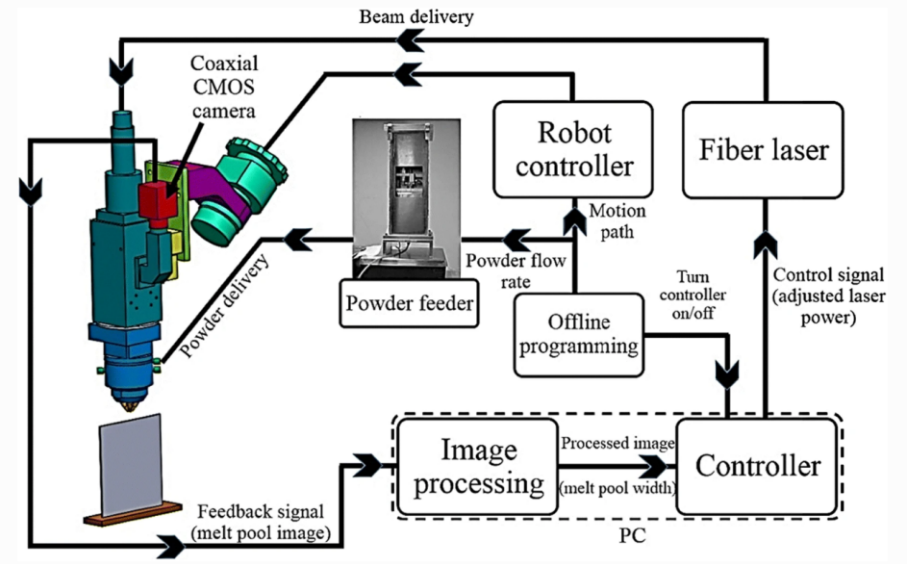

Figure 39. Schematic overview of robotized laser powder–directed energy deposition equipped with closed-loop control system [79].

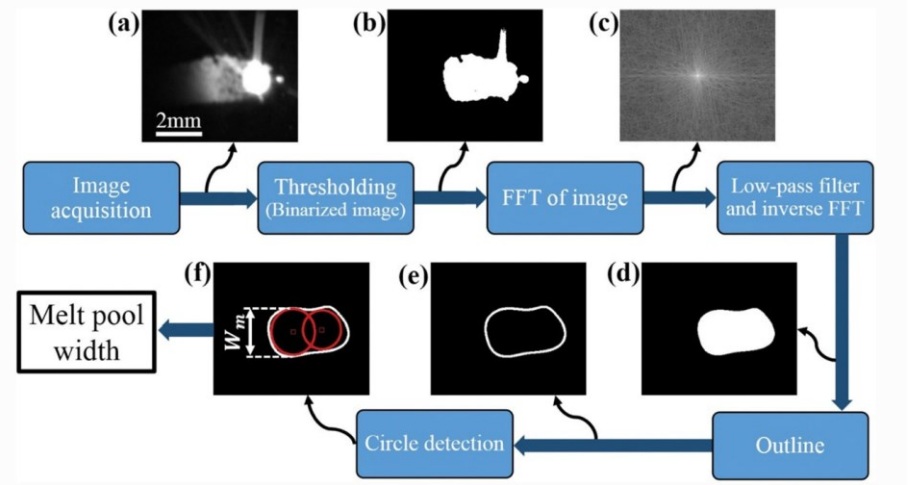

Figure 40. Image processing steps [79].

Ocylok et al. [80] also conducted a coaxial process monitoring and a study on the correlation between the geometry of the melt pool and the main process parameters of the L-DED process. A coaxial CMOS camera was used to record back reflections of the melt pool, useful for further analyses, see Figure 41. It was pointed out that thresholding has a great influence on the result of image binarization and when using a low threshold value an over-estimation of the melt pool size was obtained. The same threshold value was applied for all the analyzed images and results found a constant deviation of 150 µm between the width of the deposited track and the width measured in the images. Furthermore, the widening of the track is caused by heat accumulation and viscosity reduction of the melt pool, but also by the presence of sparks, see Figure 42. The effects of glares on the width and length measurement of the melt pool were reported to be less than 0.5%. In this work, the results also showed that the laser power has a positive correlation with the melt pool size, while the correlation between

translation speed and melt pool size was negative. Increasing the powder mass flow increases the thickness of the single track almost linearly and the penetration depth decreases, leading also to a small reduction in the melt pool size. The effect of preheating the substrate (up to 300°C) was also evaluated, proving that an increase of the melt pool size by more than 20% at all examined laser power values was observed.

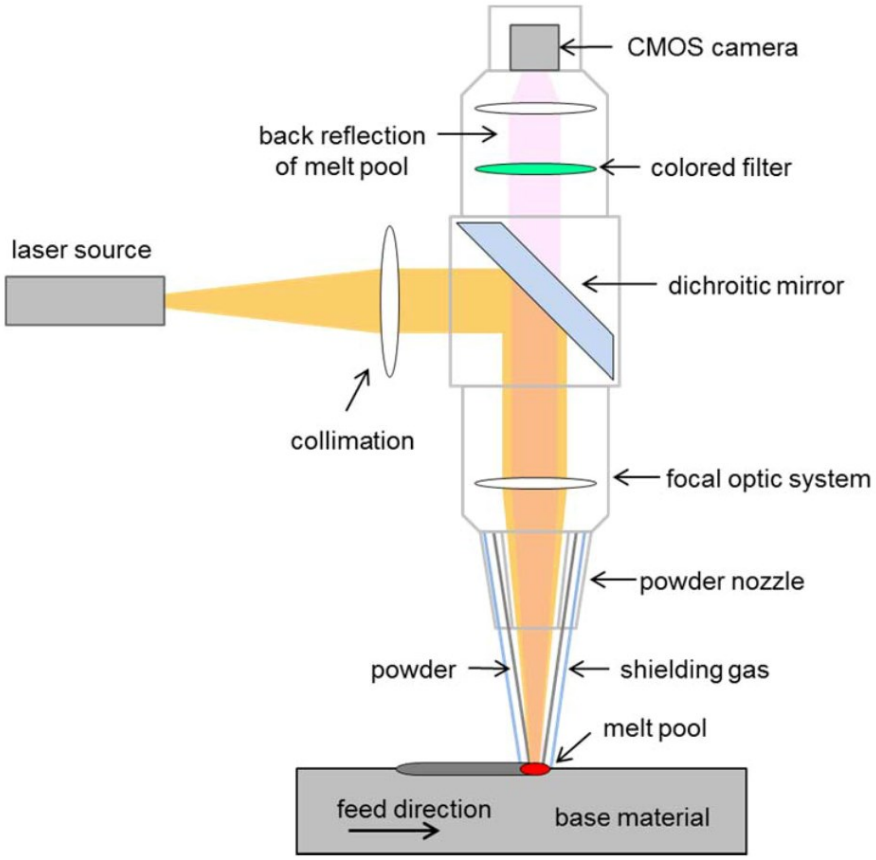

Figure 41. Schematic diagram of the L-DED process deposition head equipped with the coaxial optical monitoring system [80].

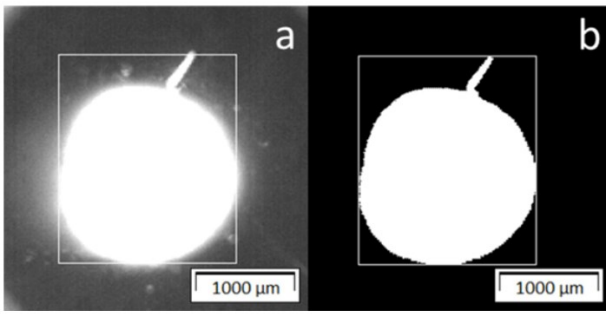

Figure 42. (a) Disturbances during melt pool measurement due to sparks, (b) wrong segmented melt pool [80].

Sampson et al. [81] implemented a new image processing algorithm for improving the accuracy and performance of melt pool measurements. It was not based on emissivity or material dependency, but it was based on a parametric study, comparing it to a study based on emissivity. The new algorithm uses the phenomenon of directional emittance to calculate the width of the melt pool, see Figure 43. For monitoring it, a NIR CMOS vision camera

with a 135 nm UV/VIS cut-off imaging filter was installed coaxially to the laser beam on the deposition head. The results highlighted that the melt pool edge often occurs at different thresholds. For this reason, this new technique detected the edge of the melt pool without problems, compared to conventional emissivity-based techniques.

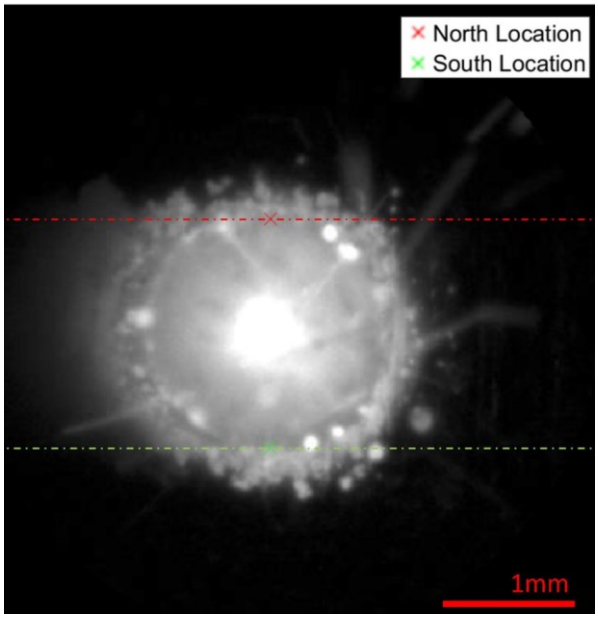

Figure 43. A frame of the segmented melt pool using the directional emittance technique [81].

Vandone et al. [82] split the process of image analysis into two parts. The images are first corrected because the brightness was elevated due to raising vapours. These vapours trapped the radiation from the substrate, generating a light halo that deceived the measurements. The pixel intensity distribution was analyzed, and the skewness index was evaluated. Negative indices indicated that the image was composed of bright pixels and revealed a deceptive intensity. In order to solve the problem at this early stage of the process, a corrective factor was applied to the images. In the second step, the images were analyzed to extract the geometry of the melt pool. For each image, the threshold value was calculated using the Otsu method. To extract spark data, the local thresholding approach was followed. Sparks were excluded based on the fact that they were composed of pixels with extremely variable intensity. The same authors in another work [82] carried out coaxial monitoring of the melt pool by using a FLIR Grasshopper 3 camera, see Figure 44. They performed V-track depositions tests to demonstrate that the image intensity signal was strongly linked to the local increase in power density, which occurred when the deposition head decelerated to change direction, see Figure 45. This phenomenon generated an over-deposition. Therefore, an image processing algorithm and different setup solutions to optimize image signals were studied to detect this phenomenon in real-time and generate a feedback signal to adjust the

process parameters. Results showed that a narrow band filter in addition to the image-processing algorithm and an optimal camera exposure time could improve the detection of errors during the process.

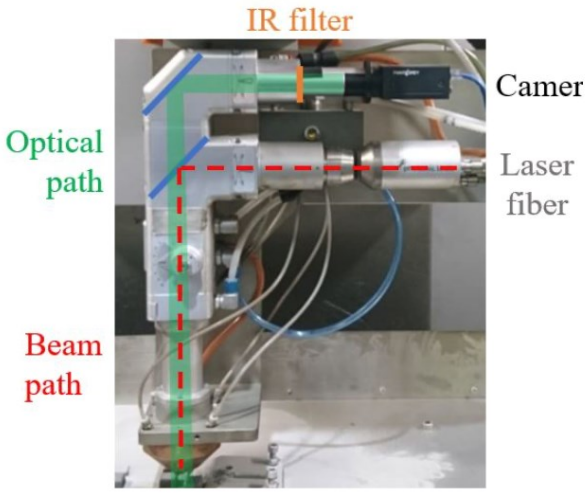

Figure 44. Deposition head for L-DED process and optical monitoring system paths [82].

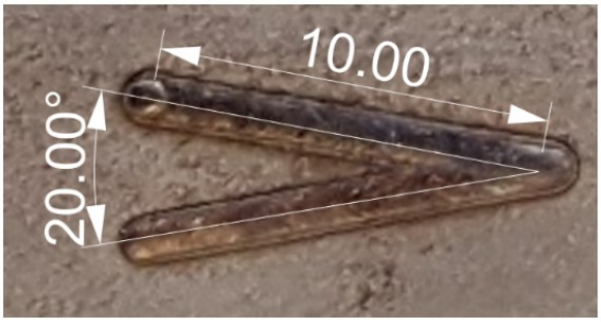

Figure 45. V-track depositions tests [82].

Ding et al. [83] conducted experiments using two different cameras, CCD and IR. An IR filter (>650 nm) was applied to the CCD camera to eliminate disturbances in the acquisitions due to the presence of powder above the melt pool. They calibrated the CCD camera by comparing the acquisitions of the IR camera. Both the CCD and infrared cameras were used to acquire a video from the molten pool in absence of powder and under the same process conditions. Since the edge of the melt pool was determined by the melting temperature of the material, the emissivity was constant along the whole contour and the edge temperature was described by an isotherm. In order to determine this isotherm, the images extracted from the videos of the two different cameras were overlapped. A video was acquired by replacing the IR filter with a 532 nm bandpass filter and illuminating the melt pool with a 5W green laser. By overlapping the greyscale images on the IR image, the greyscale threshold value for IR images was established at 97. This value was verified by experiments carried out at different scanning speeds without powder and the results corresponding to the size of the deposited tracks with a deviation of ±0.1 mm. The procedure is shown in Figure 46.

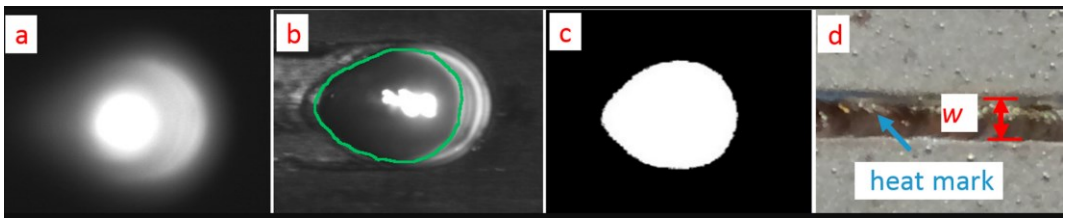

Figure 46. (a) image acquired with IR camera, (b) image acquired with CCD camera, (c) binarisation of IR image with the contour of melt pool as a threshold value, (d) welding on a substrate [83].

Also, in the research of Kledwig et al. [84], the intensity distribution of the signal coming from the melt pool surface was considered for the monitoring of the L-DED process. The intensity distribution was monitored using a coaxial CCD camera. The melt pool area was estimated taking into account the number of pixels (NOP) having intensities larger than a predefined threshold. This study showed how the minimum specific energy needed for a stable process can be determined. Outcomes indicated that a NOP having an intensity larger than a threshold intensity was a sign of an unstable cladding process. This result has been attributed to the variation in the working distance and this could be used as a warning signal for the automatic stop of processing. Concerning off-axis monitoring systems, recently Garmendia et al. [85] proposed a closed-loop control system that allowed the adjustment of the height of the deposited layer and recalculation of the deposition paths during repositioning. The monitoring was performed using a structured light scanner, please see Figure 47. The used device was an HP SLS3 (with an accuracy of 0.05 mm). The monitoring process implemented in this work was designed for the interruption of printing, after a predetermined number of layers, and on the consequent scanning of the previously made depositions. Once scanned, it compared the images to the related CAD profiles. Then, if necessary, a new toolpath was generated by updating the layer height to adapt the new deposition to the part growth. A new coordinate system was updated for each scan, please see Figure 48. The results showed that the usage of different coordinate systems for each scan improved the overall accuracy. This system has generated parts with better dimensional features.

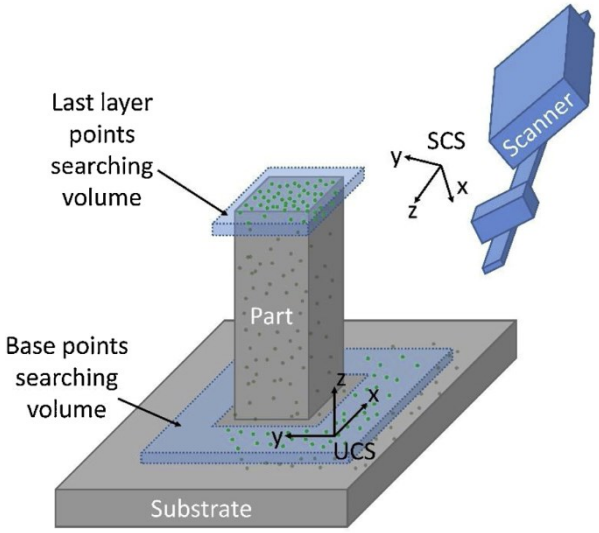

Figure 47. Schematic diagram of the structured light-based height control for L-DED [85].

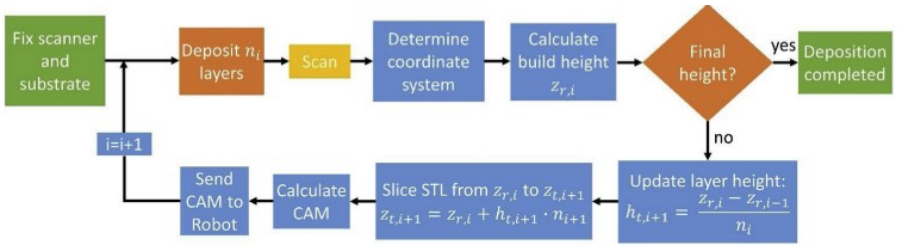

Figure 48. Control strategy flow chart [85].

Hsu et al. [86] proposed an inspection system to measure the height of the clad based on three digital cameras, please see Figure 49. These were placed at the same distance from each other and about 150 cm from the centre of the platform and inclined about 15 degrees from the vertical. In this system, a calibration bar was used to rectify the field of view and perspective effects of the trinocular system. An image processing technique was previously used to isolate the nozzle and the melt pool. Findings showed how the clad height was estimated based on the distance between two reference points located at the nozzle tip and on the centroid of the melt pool, please see Figure 50. The accuracy of the system was compared with 3D scan models (GOM ATOS-Compact scan), giving an error of 4.2%.

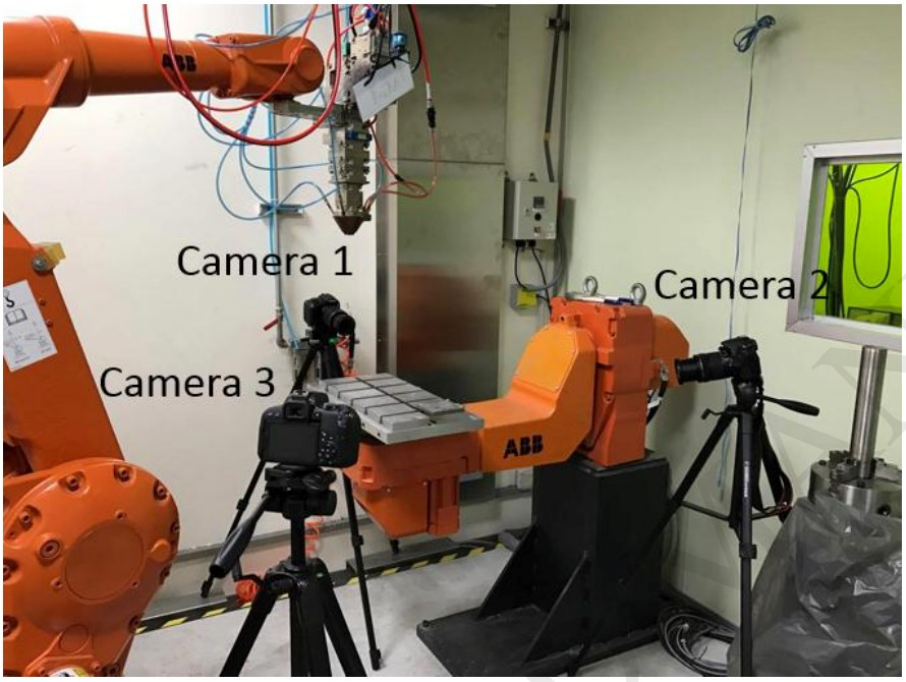

Figure 49. Experimental setup for L-DED process and off-axis optical monitoring on three digital cameras [86].

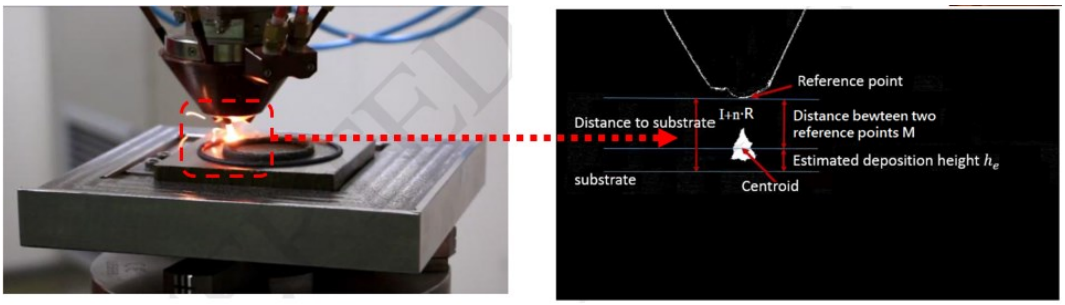

Figure 50. Schematic illustration of the algorithm proposed for clad height measurement method [86].

2.1.2 Thermal monitoring field

As regards the thermal monitoring field, through thermal analysis it is possible to identify defects such as porosity, lack of fusion, or surface irregularities, coming from non-optimal heat dissipation conditions [21]. In current practice concerning thermal monitoring, a series of studies have been carried out. R.D. Murphy and E.C. Forrest [87] have reviewed in-situ temperature measurement techniques for additive manufacturing technologies. In their work, the critical points of thermal monitoring are highlighted. Practically, the temperature field of a body is not easy to detect, due to the variable emissivity during laser interaction, with consequences on measurement accuracy. Owing to the complexity of the emissivity definition, monochromatic pyrometers are not recommended for applications where accurate measurements are required. However, some studies in the literature using monochromatic pyrometers are reported. Emamian et al. [88] performed thermal monitoring of the microstructure and carbide morphology of Fe-Ti-C metal matrix composites, establishing in their experiments a constant emissivity, not needing to know the correct temperature. The

authors employed the monochromatic pyrometer for a comparative study on cooling rates and temperatures of the melt pool under different conditions, setting the emissivity to a known value. An alternative way involves the pyrometer calibration through a black body, as in the case of Smurov et al. [89]. A high-temperature black body calibration source (MIKRON M390), with an emissivity of 1 in the band between 0.65 to 1.8 µm is used. Since the emissivity of the body was known, the measured temperature made it possible to calibrate with respect to the pyrometer. Usually, for L-DED processes, "ratio pyrometers" are used to measure the energy of the infrared radiation emitted by the body at different wavelengths. Measurements made by such types of pyrometers are sensitive to measurement noise [21]. For this reason, it is recommended to use dual-color pyrometers, which are the most widespread for industrial applications [90]. Song et al. [91] stated that by selecting wavelengths of 1.3 µm and 1.64 µm, an accuracy of ±10˚C is achieved at temperatures between 1000˚C and 3000˚C. Shuang Liu et al. [92] also conducted monitoring of high-power diode laser cladding using a pyrometer and an infrared camera in order to visualize the interaction of the laser beam with the powder flow and to record the temperature of the melt pool, please see Figure 51. In this study, the influences of the main process parameters on the thermal behaviour of the melt pool were investigated. It turned out that the trail of the melt pool temperature was increased by a rise in laser power or a decrease in carrier gas flow rate.

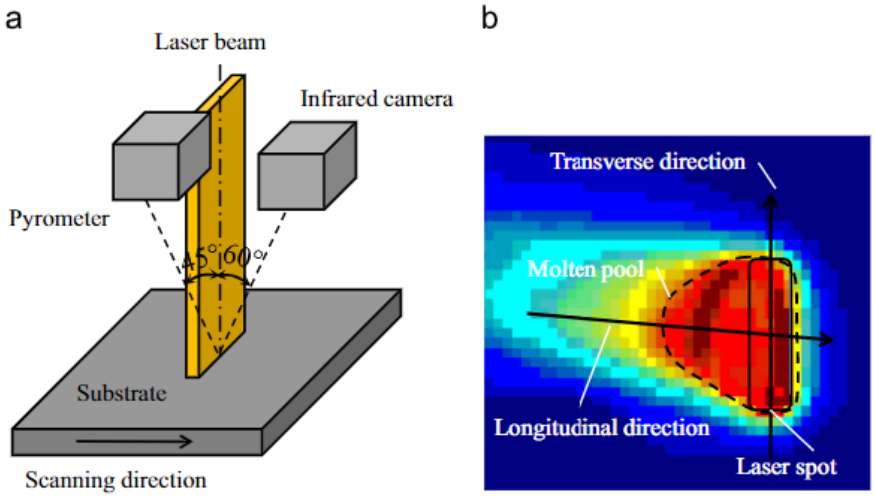

Figure 51. (a) Schematic diagram of the L-DED setup equipped with the off-axis pyrometer and infrared thermal camera, (b) frame of temperature measurement with the infrared camera [92].

2.2 Coaxial optical monitoring methodology developed

Although several papers in the literature focus on monitoring the melt pool, few of them adopt the algorithm proposed in the work conducted by Errico et al. [21] (named active contour) to retrieve the melt pool size in the L-DED process. This algorithm consists of

iterative modifications of an initial contour until reaching the minimization of an energy functional. The active contours logic was widely explored and applied in numerous applications such as image segmentation, visual tracking and similar tasks. It generally leads to better results than classical image segmentation methods [93]. Nevertheless, a challenge for this methodology regards the sensitivity of the geometrical results to the contour initialization [94]. A methodology evolution, employable to improve the algorithm performances, is the region-based active contours, which models different zones in terms of intensity and sets the region boundaries as the transition between different zones. The algorithm aims to identify each region of interest by applying a region descriptor leading the evolution of the active contour. The aim of this work was the optimization of deposition strategies for the fabrication of thin walls in AISI 316L stainless steel. For this purpose, a coaxial monitoring system and image processing algorithms were employed to study the melt pool geometry.

2.2.1 In-process coaxial monitoring equipment

A coaxial CCD camera (IDS UI-6230RE-M-GL PoE Rev.3) integrated into the deposition head, which allowed the laser beam path to be coaxially followed, was employed to monitor the melt pool during the fabrication of thin walls, please see Figure 52. The camera was characterized by a Mono CCD sensor, an acquisition frequency of 40 frames per second, and an optimal resolution to control the process of 1024 x 768 pixels. From the videos acquired by the camera, several series of frames were extracted and processed using algorithms implemented in the MATLAB software, for extracting the geometrical dimensions of the melt pool.

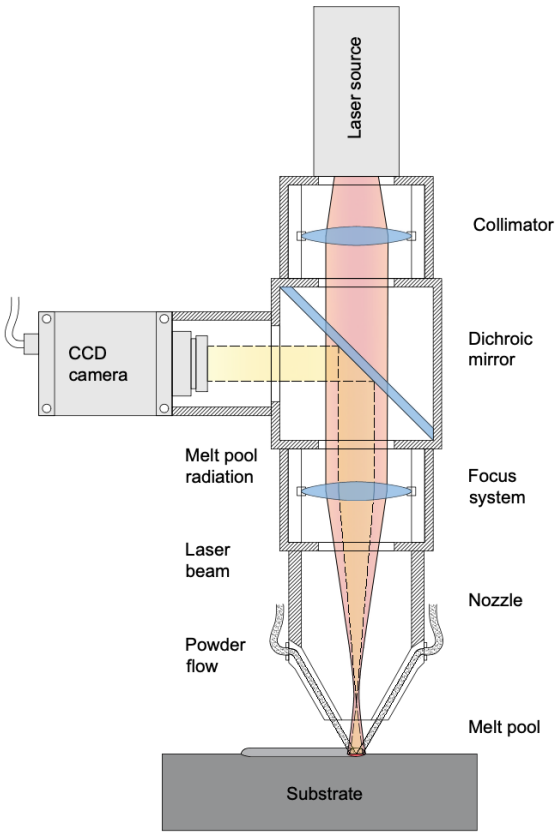

Figure 52. Schematic overview of the L-DED system used, equipped with the optical setup deployed for process monitoring.

2.2.2 Case study: Thin walls fabricated by Laser-Directed Energy Deposition

In this work, thin-wall depositions with different depositions strategies were built. The filler metal was an AISI 316L stainless steel powder. The granulometry of the gas-atomized powder is in the range of 15-45 µm. The experimental work was carried out by using an L-DED prototype machine, which includes a 4 kW fiber laser source (λ=1.070 µm, Ytterbium Laser System YLS by IPG Photonics), a 5-axis handling system, and a powder supply system by GTV. The deposition head was equipped with an advanced and innovative motorized optics system. The focal length of the collimation and focusing lenses were respectively 100 mm and 200 mm. The movement of the optics allowed the change of the circular laser spot size on the substrate surface from a diameter of 0.25 to 3.75 mm, without moving the laser deposition head.

The laser beam was measured using a rotating pin-hole beam profiler (Primes Focus Monitor). The laser beam was guided from the fiber source to the deposition head through an optical fiber with a diameter of 100 µm, please see Figure 52. Thin-wall depositions were performed with the same process parameters, that were obtained from prior studies and evaluated as appropriate for multilayer depositions. The process parameters that were kept

constant, based on previous tests, are listed in Table 10.

Table 10. Constant process parameters [21].

Parameters	Unit	Notation	Value
Laser power	W	P	400
Translation speed	mm min^{-1}	v	1000
Powder feed rate	g min^{-1}	Q	10
Carrier gas flow rate	l min^{-1}	G	10
Laser spot diameter	mm	d	1.5

The thin walls, consisting of 15 layers, were built with three different deposition strategies (see Figure 53):

S1: two-way without dwelling time.

S2: two-way with 10 seconds of dwelling time between two consequent paths.

S3: one-way with 12.5 seconds of dwelling time, including 2.5 seconds for the return to the beginning of each path.

The dwelling time is the waiting time between two consequent paths in which the laser is off. Two replications were performed for each deposition strategy.

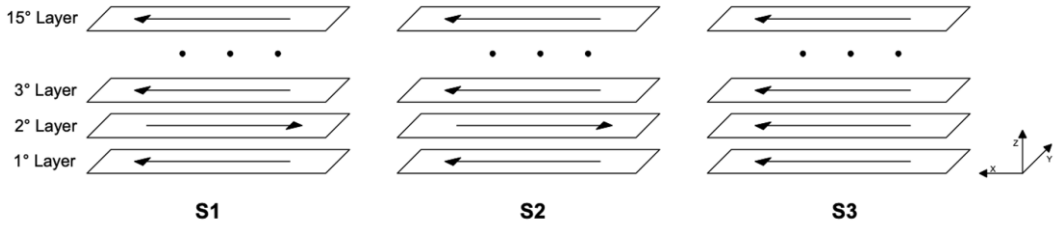

Figure 53. Schematic representation of three different deposition strategies [21].

2.2.3 Data analysis methodology

For each deposition test, a video of the molten pool evolution was acquired using the coaxial CCD camera with an acquisition rate of 40 frames per second. Image sequences were extracted from the acquired videos and subsequently processed and analyzed using dedicated algorithms developed in a MATLAB environment to identify and isolate the melt pool. For each deposited layer, frames were extracted and evaluated at three different key points: at the beginning, in the middle, and at the end of the deposition path, 25%, 50%, and 75% of the total length of the single track, respectively. The melt pool shape monitoring was performed by extracting its geometrical characteristics using advanced image processing techniques.

In particular, the study focused on the identification of the melt pool area through an algorithm based on the active contour method. This technique, previously used by Lei et al. [78], consists of an iterative method starting with the definition of the zero-level contour in

the form of a closed curve known as a mask. Subsequently, the zero-level contour iteratively evolves and adapts by applying shrinking/expanding operations called "contour evolution" driven by the minimization of an energy function [95]. In this work, a region-based algorithm was implemented, which aims to identify each region of interest using a region descriptor that guides the evolution of the active contour. The algorithm works by segmenting the image in order to connect regions with homogeneous properties. Among the various selectable shapes for the zero-level contour (elliptical, circular, rectangular, freehand), the circular shape was chosen, as it is similar to the incident laser spot. Figure 54 shows an example of an active contour where both the starting contour (blue) and the extracted melt pool contour (red) are represented. The brightness gradient at the top of the molten pool is steep due to intense heat dissipation through the substrate. The high brightness regions on both sides of the melt pool could be a consequence of the high emissivity, proper of the non-molten particles, and oxides [15,78]. Similar considerations were made by Doubenskaia et al. [96], who considered the high thermal emission in the peripheral area of the melt pool due to oxides and other non-metallic inclusions which are usually concentrated in that region. The weak brightness gradient detected in the trailing part of the melt pool is describing lower and quite uniform temperatures owing to the cooling and solidification of the material in that area.

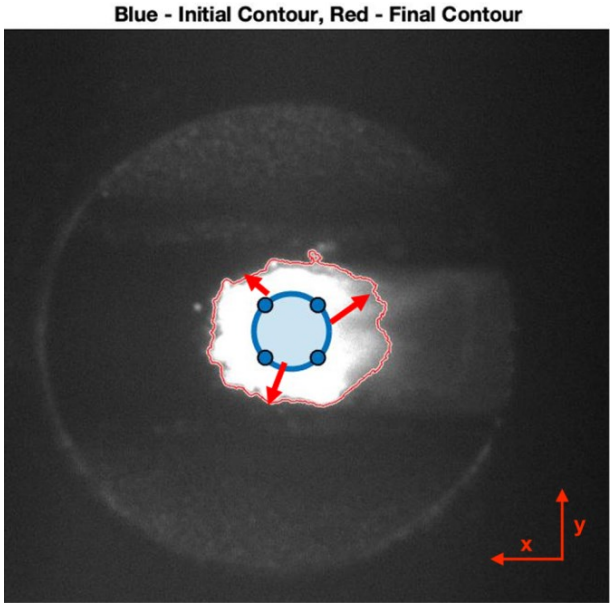

Figure 54. Automated detection of a melt pool edge from a video frame using the active contour algorithm [21].

2.2.4 Comparison of image segmentation techniques

In order to illustrate the advantages of the proposed image analysis algorithm, the region-based active contour was compared with three image segmentation techniques analyzed in

the literature: threshold segmentation, the Canny edge, and the edge-based active contour. Figure 55 shows the results of the algorithms comparison and the different melt pools identified. Four frames randomly extracted from the complete deposition were analyzed (see Figure 55(a)). As shown in Figure 55(b), Figure 55(c), and Figure 55(d), the region-based active contour algorithm, compared to threshold segmentation and Canny edge, demonstrated a superior accuracy in terms of edge detection and resolution. These results stem from some advantages proper of the region-based active contour over other algorithms [93]:

- achievement of sub-pixel accuracy for detected object boundaries;
- incorporation of prior image knowledge, such as intensity distribution (useful for robust image segmentation);
- realization of smooth and closed contours as segmentation results, which are crucial and easily manageable for further applications such as shape analysis and feature recognition.

The threshold value was chosen to be 80, as mentioned in the work by Akbari and Kovacevic [79]. However, the classical image segmentation methods (edge detection and thresholding) present problems due to the incapability to approximate edges with a single binary threshold, as mentioned in [80,93]. The latter operates by finding discontinuities in the brightness intensity of the image. These algorithms detect intensity discontinuities and identify the edge between two regions characterized by different properties (e.g. the intensity of pixels) as a limit. Therefore, since these techniques are based on a locally-derived analysis, they are not very effective in presence of weak object boundaries or noisy patterns, as the images examined in this work [93].

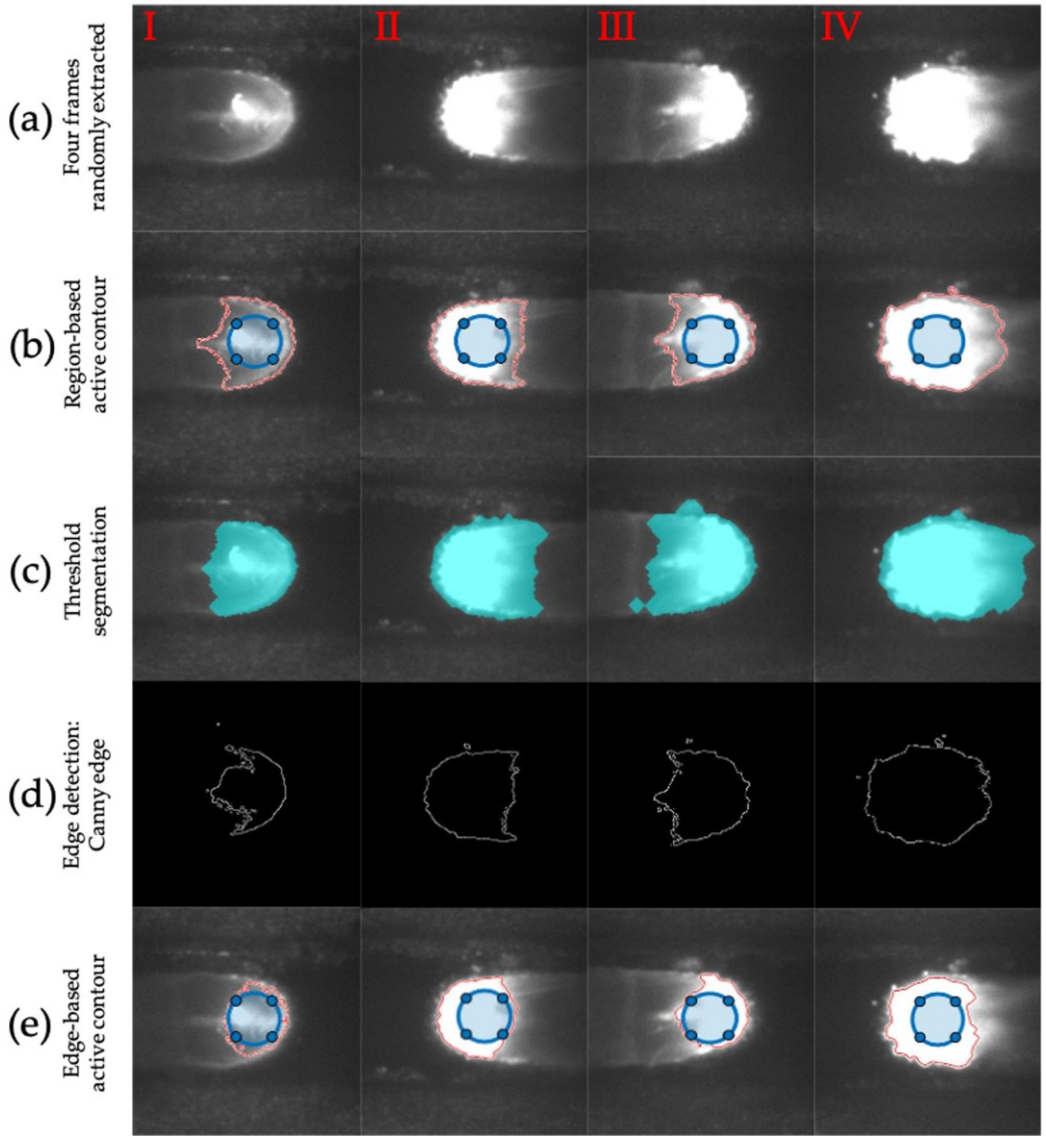

Figure 55. Comparison of the region-based active contour with other techniques: (a) four frames randomly extracted from the whole deposition; (b) region-based active contour; (c) threshold segmentation; (d) Canny edge; (e) edge-based active contour [21].

In fact, independently of the selected threshold value, a part of the surface of the substrate is erroneously identified as a melt pool part and vice versa, as shown in Figure 55(c) and Figure 55(d). The last drawback also appeared in the edge-based active contour algorithm (see Figure 55(e)), which uses the local edge information to attract the active contour to the edge to be detected; it is not very effective in the presence of objects with heterogeneous feature profiles or images with non-homogeneous intensity, as in the images obtained in our work [78,93]. Hence, among the four techniques, the region-based active contour method gave a higher performance in terms of resolution, edge detection accuracy, etc. Besides, a comparison of processing performances in terms of image segmentation computing time was performed. The processing times of different algorithms were evaluated (see Table 11). For each image, the processing time of the region-based active contour method was the shortest one, as shown in Table 11. The edge-based method is not supported for colour or multi-

channel images and therefore requires image pre-processing, thus increasing the processing time. Finally, in order to evaluate the outcome accuracy of proposed algorithms, four levels of image processing quality were defined in Table 11: very good, quite good, acceptable and bad.

In summary, the analysis indicates that the region-based active contour method outperforms the other three techniques in terms of processing speed, resolution, and edge detection accuracy.

Table 11. Comparison of the processing times and precision of the four selected image processing algorithms [21].

Parameters	Image	Region-based active contour	Threshold segmentation	Edge detection: Canny edge	Edge-based active contour
Processing time (s)	I	0,8344	0,8544	1,2114	3,9432
	II	0,7746	0,8876	1,1152	3,7735
	III	0,8355	1,0280	1,2799	4,2391
	IV	0,8167	0,8570	1,1992	3,8467
Average processing time (s)	I-IV	0,8153	0,9067	1,2014	3,9506
Accuracy		Very good	Bad	Quite good	Acceptable

2.2.5 Effects of deposition strategies on melt pool geometry

As has been said before, the melt pool size is an important feature for the characterization of L-DED depositions. Figure 56 shows the effect of the two-way deposition strategy without dwelling time (S1) on the final melt pool area. Each plotted value is the average of the measurements taken on the two replications performed with the same deposition strategy.

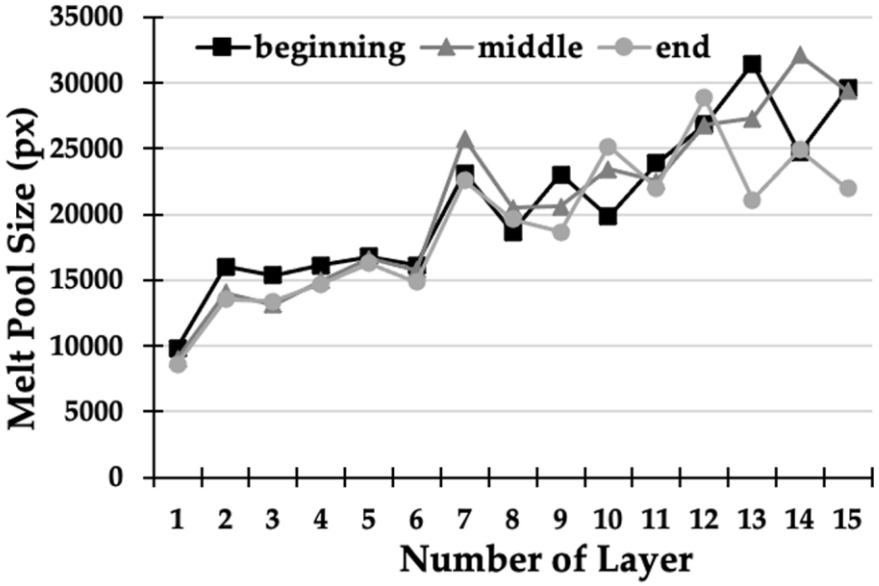

Figure 56. Melt pool size for each deposited layer with strategy S1 [21].

In order to investigate the effects of the above-mentioned deposition strategy on the melt pool size of the thin wall built, a geometrical analysis of the melt pool was carried out. In particular, three distinctive regions (beginning, middle and end) were observed along every single track, specifically at a distance of 25%, 50%, and 75% of the total length of the single track. Results show an increasing trend in the size of the melt pool with increasing deposited layers. As stated by Yang et al. [97], two-way laser scanning generates an excessive heat accumulation in a specific area of the workpiece in the proximity of the reversal point for scanning direction. This causes a rise in the substrate temperature and therefore the size of the melt pool is rapidly increased. Besides, there is no dwelling time in the deposition under examination, thus amplifying this effect. The analysis of the three key points considered for each deposited layer revealed the variation in the molten pool size along with the single deposition. In strategy S1 there is a substantial coherence of the dimension in the first layers. On the other hand, the variation in size becomes extremely marked, exceeding 10000 px in the last tracks. This effect is due to the uneven accumulation of heat inside the workpiece.

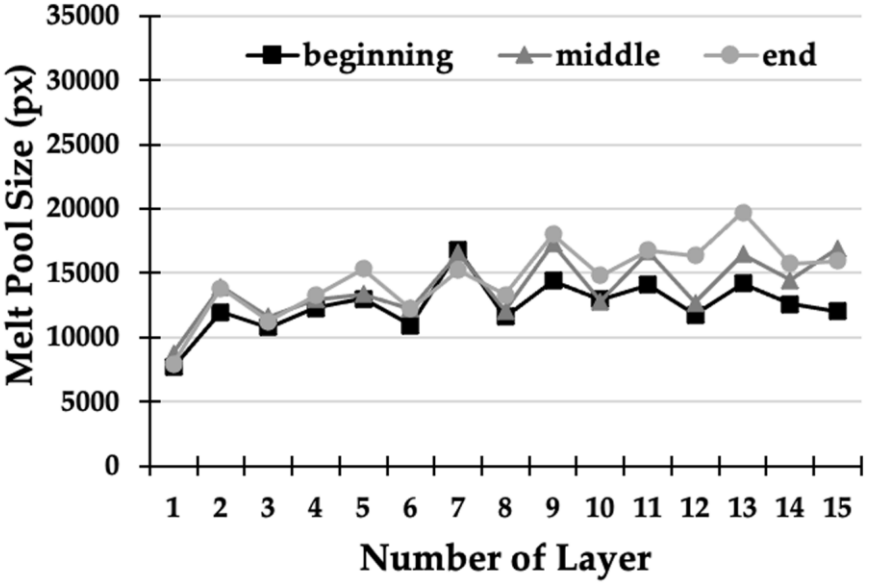

Figure 57. Melt pool size for each deposited layer with strategy S2 [21].

Figure 57 shows the trend of the extracted and measured melt pool areas in a two-way deposition strategy with 10 seconds of dwelling time (S2). Results show that even for two-way deposition with dwelling time there is an increasing trend in the melt pool area as the deposited layers increase. However, in this case, the increasing trend is less marked than the previous one because when the laser is switched off, there is enough waiting time between depositions for heat sinking. In this way, initial thermal conditions are nearly restored and kept as constant and repeatable as possible, throughout the process.

The robustness analysis of the L-DED process, performed by comparing the size of the three key points of each track, reveals significantly more consistent values for the S2 strategy. In

fact, there is a maximum deviation of the molten area of 5520 px in layer 13. Therefore, the strategy with waiting times is much more stable in the construction of components consisting of several layers, because it aims at diminishing the detrimental heat accumulation effects in thin walls.

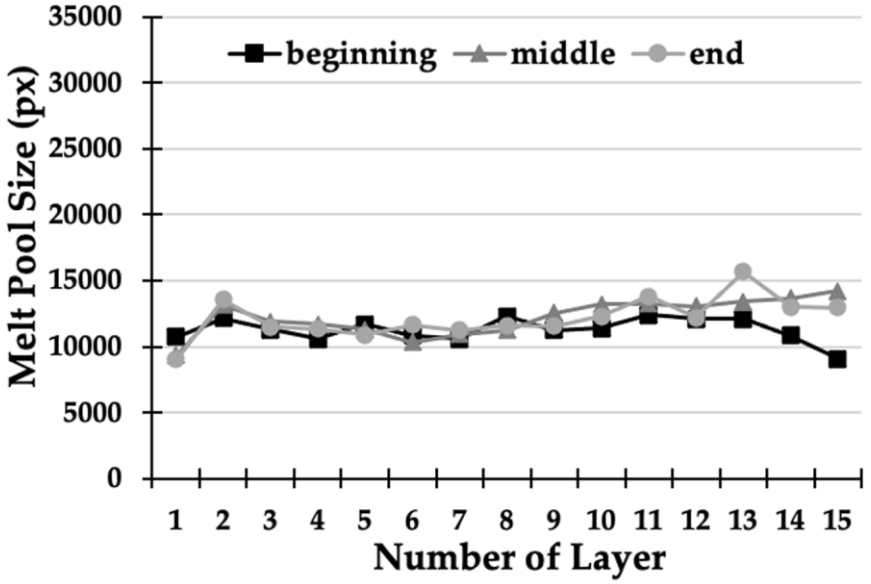

Figure 58. Melt pool size for each deposited layer with strategy S3 [21].

Finally, Figure 58 shows the trend of the extracted and measured melt pool area, in the one-way deposition strategy with 12.5 seconds of dwelling time (S3). In this case, the trend of the melt pool size is approximately constant with the deposited layers. This tendency is due to the combination of waiting times and constant deposition direction that are carried out with this specific deposition strategy. The unidirectional strategy avoids the formation of heat accumulation points at the extremes of the thin wall due to the reversal of direction, where the end of a track is the beginning of the subsequent. A consequent more uniform heating of the part is obtained, practically consisting of a superposition of the same thermal field over time. This, combined with the previously defined effects of the waiting time allows an effective diffusion of the accumulated heat. As can be seen in Figure 58, the S3 strategy turns out to be extremely robust and coherent than the previous ones. There is a maximum variation of the melt pool area within the single layer in the order of 5090 px, and an average variation of the area along with all 15 layers of only 1725 px. This value is definitely lower than the previous ones (3542 px for S1 and 2543 px for S2) which makes the unidirectional strategy with dwelling times the most suitable and stable for the long processing.

Moreover, overlapping the results obtained by the three analyzed strategies (see Figure 59) it is clear that the dwelling time between consecutive layers is a key variable in the deposition process. In the graph, the areas of the melt pool have been converted from pixels to square millimeters, with a surface conversion: 10 [px] x 10 [px] = 1 [mm^2]. This relationship was

found through a calibration process, using a millimeter-sized sample. The individual trends in Figure 59 were obtained with the average areas for each layer deposited. The average areas for the three deposition strategies were compared and it was found that the smallest melt pool area is always recorded at the first layer of each strategy, while the largest area was found in the last layers of each treatment. The melt pool size seems to stabilize as the number of layers increases and this fact is more evident if the adopted strategy does not favour heat accumulation. More in detail, strategy S1 increased the average melt pool area from 0.917 mm^2 to 2.698 mm^2, with a variation of 1.781 mm^2. For strategy S2, an increase in the average melt pool area was recorded, from 0.815 mm^2 to 1.497 mm^2, with a difference of 0.682 mm^2. Finally, for strategy S3, the melt pool area varied from 0.97 to 1.208 mm^2 from the first to the last layer, recording the smallest increase of 0.238 mm^2.

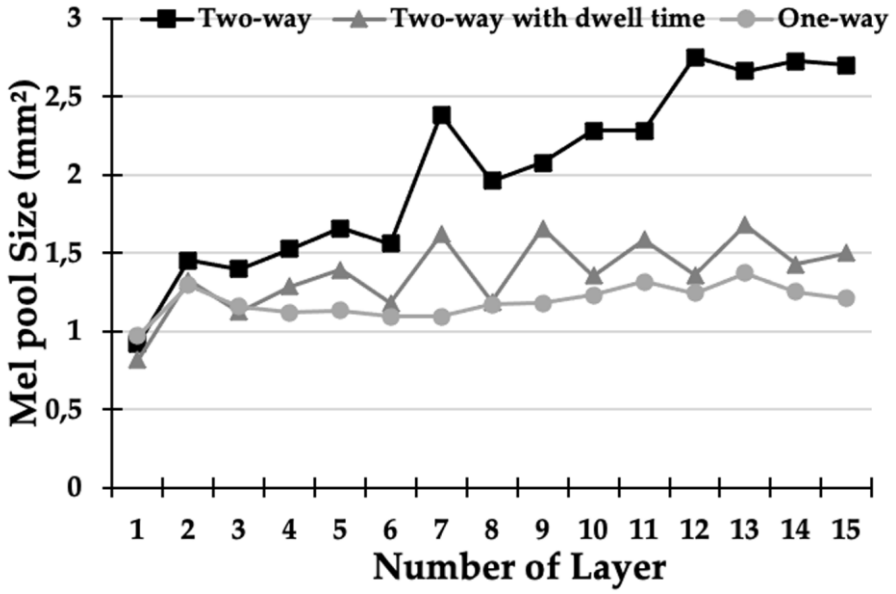

Figure 59. Comparison of melt pool sizes for each deposited layer for the three different strategies [21].

2.2.6 Analysis of macrography cross-sections

In order to validate the image segmentation outcomes, a comparison with the cross-section macrographs of thin walls, realized using the above-mentioned strategies, was carried out. Figure 60(a) shows the cross-section of the thin wall obtained using the deposition strategy S1. This macrography revealed that the width of the deposited thin wall increased as the deposited layers increased, confirming the trend determined in the melt pool assessment. On the other hand, Figure 60(b) shows the cross-section of the thin wall obtained using the deposition strategy S2. This macrography also revealed that the width of the deposited thin wall increased as the deposited layers increased. However, the increase in width is much less pronounced than the previous. Finally, Figure 60(c) shows the cross-section of the thin wall

obtained with strategy S3. This macrography once again confirms the outcomes of the melt pool monitoring, since the width of the deposited thin wall remains essentially constant along with the whole component.

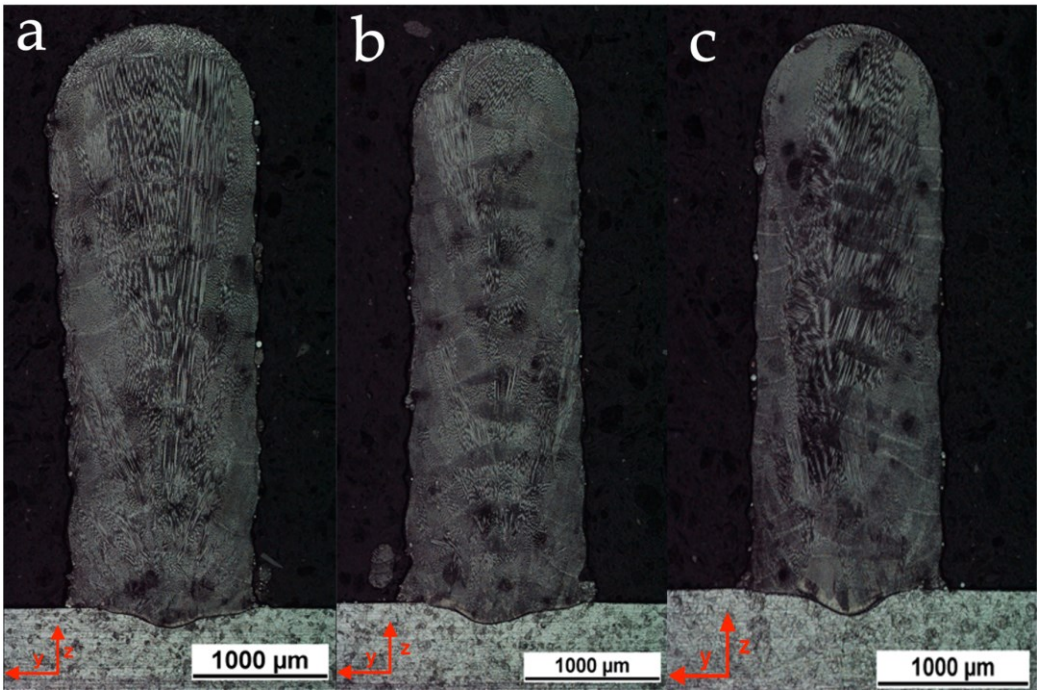

Figure 60. Macrographic cross-section of the thin wall obtained using a) strategy S1, b) strategy S2, and c) strategy S3 [21].

2.2.7 Conclusions

The following conclusions were drawn:

- The region-based active contour was compared with three image segmentation techniques analyzed in the literature: threshold segmentation, Canny edge, and edge-based active contour. Results show that the region-based active contour outperforms other algorithms in terms of processing speed, resolution, and edge detection accuracy.
- For the two-way deposition strategy without dwelling time (S1), as the deposited layers increased, a marked increase in the melt pool area was observed. The reason for achieving these results is the effect of bi-directional laser scanning, which generates excessive heat accumulation in the workpiece. In addition, there are no waiting times in the deposition under examination, so this effect was amplified.
- Concerning the two-way deposition strategy with 10 seconds of dwelling time between two consequent paths (S2), the same trend was achieved, but the increasing trend was less steep because the heat accumulation was attenuated by the waiting time between depositions.

- In the one-way deposition strategy with 12.5 seconds of dwelling time, including 2.5 seconds for the return to the beginning of the single path (S3), the trend of the areas is approximately constant throughout the process. This is due to the combination of waiting times and constant deposition direction, which allow an effective diffusion of the accumulated heat.
- By analyzing the key points of each track it can be noticed, regarding the melt pool size variation along with the single deposited layer, that the S3 strategy is the most stable, showing an average variation of 1725 px, while the S1 strategy proved to be the most uneven with a maximum variation of more than 10000 px.
- The average melt pool areas for the three deposition strategies were compared and the following outcomes were recorded: an increase of 1.781 mm^2 for strategy S1, 0.682 mm^2 for strategy S2 and 0.238 mm^2 for strategy S3. These results have corroborated the considerations given above.

This work is a study that might be useful for improving the accuracy and quality of depositions performed with complex deposition strategies and geometries. Results showed that the region-based active contour algorithm is a fast and stable image processing implementation and a successful methodology for closed-loop monitoring in real-time applications.

3. Laser-Powder Bed Fusion process monitoring methods

3.1 State-of-the-art methods and systems for L-PBF process monitoring

Also for the L-PBF process, an in-depth state-of-the-art study was conducted on the monitoring systems and methodologies implemented so far. As mentioned in the literature and described above, various operational factors, such as process parameters, powder properties, and other external factors, can affect the quality of the final part, which in some cases could lead to part rejection [98]. Although, in some cases, post-processing techniques can mitigate or remove defects from parts produced with L-PBF and improve build quality, preventing certain issues is critical to meeting stringent and demanding industrial requirements [99]. Due to the high number of factors affecting the L-PBF technique, in-situ and in-process monitoring has become necessary to comply with high-quality standards and high productivity rates, minimizing all kinds of waste [72]. Starting from the possible defects, one of the main purposes of the in-process monitoring tools is to identify specific process signatures, in order to relate them to specific defects or process inaccuracies [72]. In fact, according to the NIST (National Institute of Standards and Technology) report written by Mani et al. [100] process signatures are the 'dynamic' characteristics of the heating, melting, and solidification processes of powders, which occur during construction. Mani et al. [100] also suggested a classification of these characteristics into two classes:

- Observable characteristics.
- Derived characteristics.

Those belonging to the first group can be observed and measured, during the process, using in-situ sensing devices. The second can be determined through analytical models or simulations [99]. Process characteristics can be grouped into four main categories, depending on the level of detail required to observe the process [99]. These categories are:

- Melt pool.
- Track (scan path).
- Slice.
- Powder bed

The term slice refers to the cross-section of the workpiece, scanned by the laser beam, in each layer. The term powder bed, on the other hand, refers to the thin layer of powder deposited, by the levelling blade, before scanning the current layer [99]. Chapter 1 extensively described how the melt pool is generated and also mentioned its considerable importance on the final product; in fact, the size, stability and behaviour of the melt pool

largely determine the quality and stability of the overall process. Four main melt pool quantities are studied in the literature for monitoring objectives [99]:

- the size (area or diameter);
- the shape;
- the temperature intensity;
- the temperature profile.

As mentioned in Chapter 1, process parameters and scanning strategies have a strong influence on the size, shape and temperature of the melt pool. Therefore, carefully studying the melt pool and the quantities related to it by means of in-situ monitoring systems would make it possible to optimize process parameters and scanning strategies, for example, and reduce wastes and defects [99]. However, from the outputs that can be extracted by analyzing the melt pool, it is possible to determine the geometric accuracy of the track, and thus the geometric properties of the final part [99]. Therefore, the in-situ monitoring system of the melt pool represents the most important, but most challenging method from the measurement viewpoint [99]. The most challenging is because first of all the monitoring system must be able to measure an extremely small region and it must do so with a good resolution to extract quantitative and not just qualitative outputs. So, for example, for some more demanding analyses, it is necessary to use high-frequency cameras in order to follow the L-PBF process live, which is extremely fast compared to the L-DED process. Furthermore, as written above, another important factor that decides the final quality of the part is the individual track [99]. In particular, it is also possible to mention some quantitative characteristics related to the individual track that can be useful for monitoring it, and these are [99]:

- the geometry of the track (height, width, penetration depth, wetting angle, etc..);
- the temperature profile of the single track;
- the material ejected from the track and the surrounding area.

Extremely important are the quantitative analysis of the geometric characteristics of the track and the temperature profile, as they reveal important information on the generation of defects such as balling phenomenon, lack of melting or local overheating conditions, surface and geometric inaccuracies and porosity creation [99]. In addition, even studying single-track monitoring systems is a very difficult challenge in terms of the required spatial and temporal resolution of the monitoring systems, which could significantly increase their cost and not justify their purchase and implementation on L-PBF machines. Another process signature is the whole slice. For slice tracking, the main factors observed in the literature and related to it are [99]:

- the surface slice pattern;

- the slice geometry (and its variation from the nominal shape);
- the thickness of the corresponding profile;
- the temperature profile over the whole slice area (usually a 2D profile).

The phenomena of slice surface irregularities that can be detected by investigating the surface of the slice pattern could be related to defects such as interlayer porosity and balling [99]. The measurement of the slice geometry is also important, allowing a "metrology" system to be implemented that can reconstruct the actual shape of the slice itself, printed on the building platform, layer by layer and compare it with the nominal shape [99]. Another important defect that could be quantified by slice monitoring is super-elevated edges (thickness greater than expected that could cause a collision with the coating blade) [99]. While defects such as local overheating and thus deformations in the final part and lack of melting could be quantified by monitoring the temperature profile over the whole slice area [99]. The powder bed was mentioned as the last observable feature. Again, there are factors that can quantitatively characterize this process signature, and these are:

- the uniformity of the powder bed
- the temperature

The uniformity of the powder bed is important to avoid defects such as super-elevated edges due to remelting of improperly covered areas or overheating of areas where too much powder is present. However, many times the powder bed is contaminated by spattering that occurs during the process and which can affect the uniformity itself in some way [99].

Figure 61 shows an overview of in-situ monitoring solutions and systems present in the literature, the corresponding process signatures monitored and the related defects detected by these systems [101]. Due to the extreme importance of this topic, the literature is extensive and heterogeneous, especially in terms of terminology; therefore, the aim was to unify it in this Figure 61. The "X" in the figure shows relationships that have already been discussed and studied in depth in the literature; while "(X)" indicates relationships between process and defect signatures that have not yet been explored and are challenging and therefore extremely interesting for the academic world [101].

Laser-Powder Bed Fusion process monitoring methods

Level	Process signature	In-situ sensing method	Defects					
			Porosity	Residual stresses, cracks, delaminations	Microstructural inhomogeneity	Balling	Geometrical distortions	Surface defects
1 (powder bed)	Powder bed homogeneity	Off-axis imaging, visible range	(X)	X			X	
	Slice geometry	Off-axis imaging, visible range					X	
	Slice surface pattern	Off-axis imaging, visible range, fringe projection	(X)	X		X	(X)	X
2 (track)	Hot and cold spots	Off-axis video imaging, visible or infrared range	X	X		X	X	
	Temperature profile / cooling history	Off-axis thermal imaging		X	X			
	Process by-products	Off-axis video imaging, visible or infrared range	X		(X)			
3 (melt pool)	Size	Co-axial video imaging, visible or infrared range	X	X		X		X
	Shape	Co-axial video imaging, visible or infrared range	X	X		X		X
	Average intensity	Co-axial pyrometry	X	X	(X)	X		X
	Intensity profile	Co-axial video imaging, visible or infrared range	X	X	(X)	X		X

Figure 61. General mapping of relationships in the literature already explored or to be explored between process signatures, related defects and the in-situ monitoring systems implemented to detect them [101].

Furthermore, as described in Chapter 2, monitoring methods can be classified according to a macro subdivision into optical monitoring systems and thermal monitoring systems. Examples of systems present in the literature that work in these two fields will be explored in the following sections.

3.1.1 Optical monitoring field

Optical methods are in turn divided into subcategories represented by optical imaging, optical emission spectroscopy and tomographic methods. The substantial difference between optical or IR imaging and tomographic methods lies in the difference in the information provided. In fact, the former technique provides information on the part surface or powder bed, while the latter provides information regarding the internal structure of the part during manufacture [13]. Surveying the literature on melt pool monitoring work, Coeck et al. [102] developed work on predicting the presence and location of porosity within the final product. In the study, two fixed photodiodes were used with respect to the L-PBF machine that can capture the light emitted at a given time, without following the melt pool path (see Figure 62). The position of the laser is sampled by the machine and recorded together with the intensities of the photodiodes. The reconstruction was performed by observing the abrupt signal fluctuations within a scan vector. These fluctuations are correlated with anomalies and therefore the probability of finding a discontinuity in the material is high. By then comparing it with a CT scan analysis, the pore positions were found to be substantially overlapping (see Figure 63).

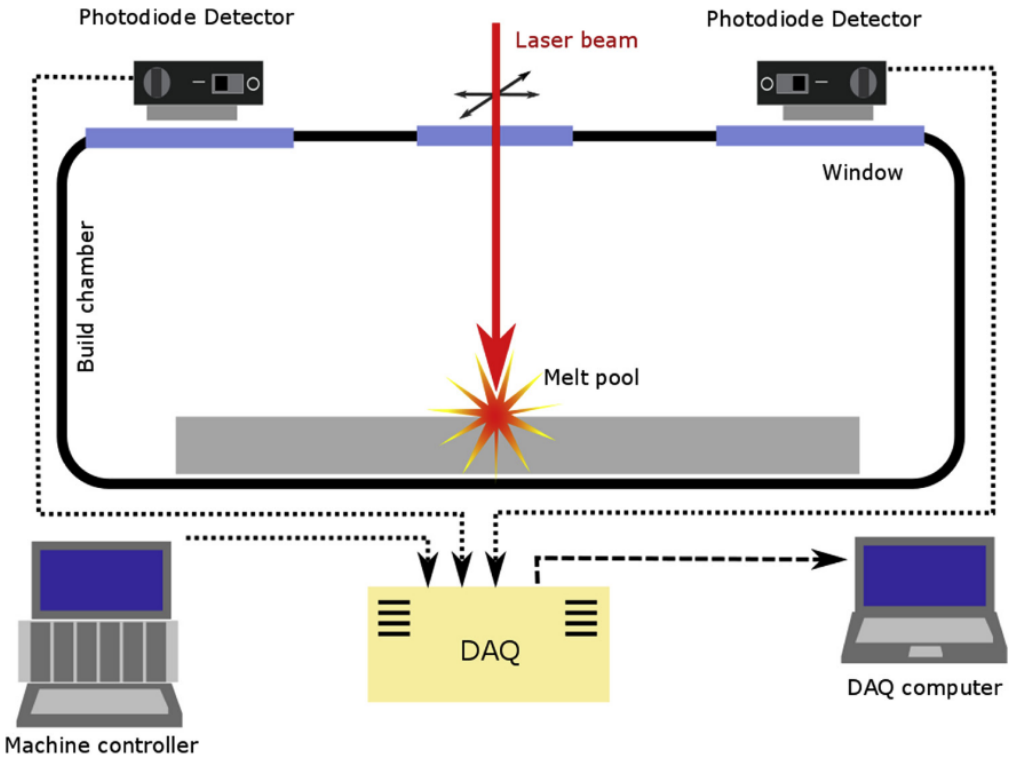

Figure 62. Schematic representation of the monitoring system applied in this work [102].

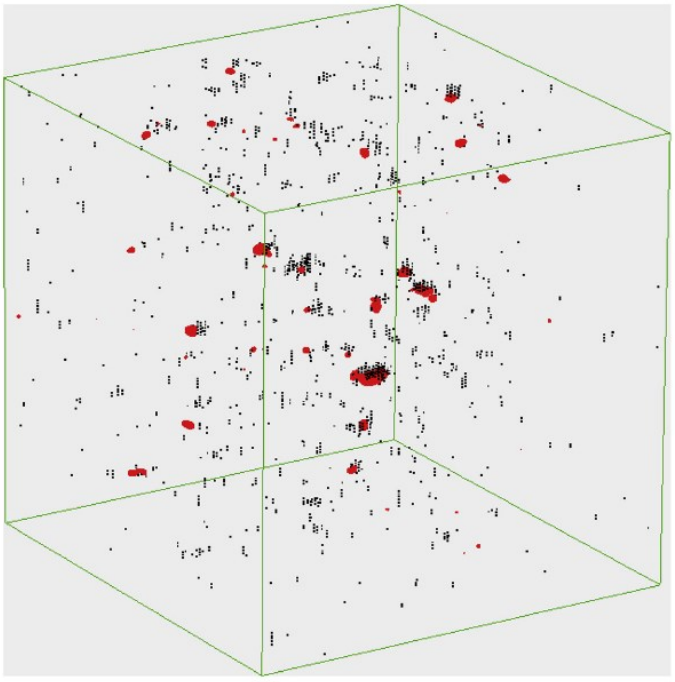

Figure 63. Overlap between predicted porosity (blue) and porosity detected by CT Scan (red) on a 10 x 10 x 10 mm³ cube [102].

Always considering monitoring systems for melt pool analysis, Berumen et al. [103] developed one of the first melt pool analysis systems in 2010, later patented by Concept Laser®. As described in Chapter 3, due to the high speed of the melt pool in this process (e.g. 2500mm/s in this work), high-frequency monitoring systems are necessary in order not to lose information and to have a complete overview of the print and subsequently be able to extract outputs to characterize the process. However, all this leads to increased costs for

the implemented systems and also to technical problems in data storage and processing. An innovation presented by the researchers in this work was to observe, through appropriate optical components (scanner mirror, f-theta lens, etc.), the laser-powder interaction directly without having to monitor the whole working platform (see Figure 64). In this study, a 10 kHz camera was used to measure the size of the melt pool. While a photodiode measures the radiation emitted by the melt pool at higher frequencies in the chamber. This setup developed and shown in Figure 64 avoids the need for the whole building platform to be observed because it follows the path of the laser and thus concentrates the field of view of the monitoring systems in the melt pool. The voltage emitted by the melt pool and measured by the photodiode was recorded and plotted against the number of samplings (see Figure 65). Thus, the camera and photodiode complement each other: using this configuration it is possible to reduce the resolution of the camera significantly, changing the image resolution from 4.62 MByte to 636 KByte for 16666 fps with all the advantages of analyzing these two different dimensions. In order to detect the simplest errors, the photodiode information is sufficient, while the camera is required for complete control. Using this camera and a photodiode, it is possible to monitor the area of the melt zone and its length-to-width ratio. The camera makes it possible to calculate the number of pixels in the fusion zone so that geometric information on the melt pool can be obtained; the photodiode emits a signal proportional to the fusion area. The preliminary step of the analysis is to correctly set up the system: identify a colour level associated with the melting zone isotherm and identify the correct level of light intensity related to the melt pool. Subsequently, a special algorithm deduces the area, length and amplitude of the melt pool by computing the pixels within the identified colour range: an incorrect length/amplitude ratio could be the cause of balling phenomena (especially in prominent areas). Algorithms are being developed to detect when the melt pool deviates from its optimum values and the corrective actions to be taken when this happens.

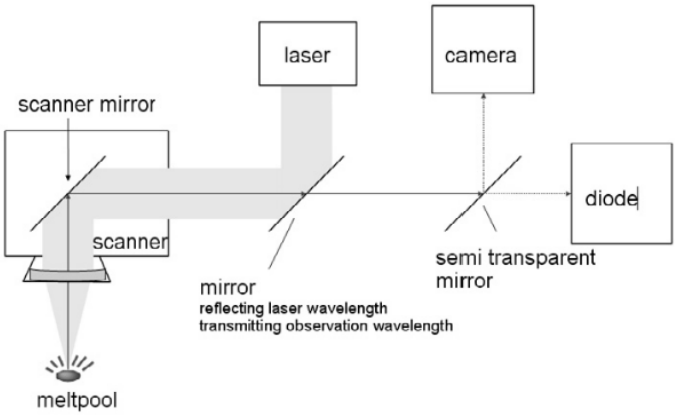

Figure 64. Schematic representation of the monitoring system applied in this work [103].

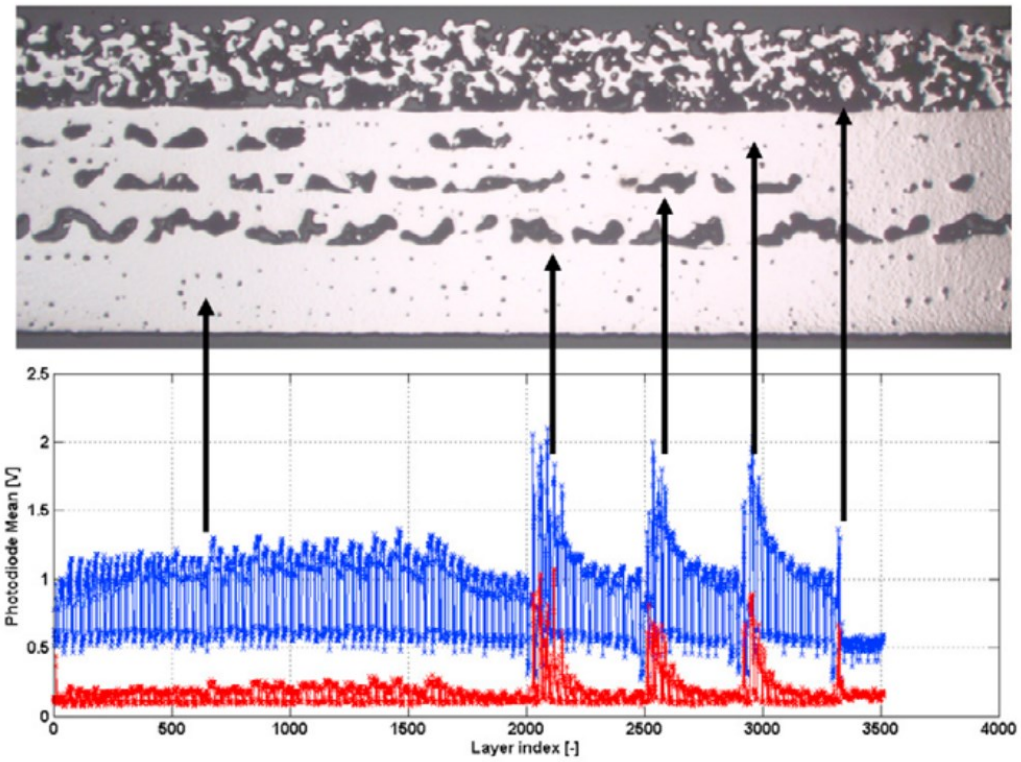

Figure 65. Above is a section of the sample. Bottom in blue average signal of the photodiode and in red the standard deviation of the part that was built with a platform adjustment error [103].

Another defect that compromises the final print is the spatter that leaks from the melt pool during laser-powder interaction. Spatter may adversely affect process stability if it falls on the powder bed and is influenced by laser power, hatch distance, scanning speed and layer thickness. It can be classified into droplets or powder, which are produced by different mechanisms. Yang et al. [104] presented an in-situ monitoring method for acquiring spatter images in L-PBF. A high-speed camera (3000 fps and 2000x2000 pixel resolution) was installed outside the production chamber at an angle of 65 degrees. With the set resolution, the camera can only capture droplets and not powder. The laser power was varied from 50 to 200 W and the probability of the occurrence of spatter was analyzed. A maximum entropy

double-threshold image processing algorithm based on a genetic algorithm (MEDTIA-GA) was developed to recognize spatter from pictures and its performance was compared with other conventional threshold segmentation algorithms: the Otsu method, K-means clustering algorithm and the Triangle threshold segmentation algorithm. Thanks to this image processing algorithm, three types of errors were eliminated: noise sensitivity, conglutination of spatter and failure to report spatter, while maintaining very fast processing times (37 ms) [104].

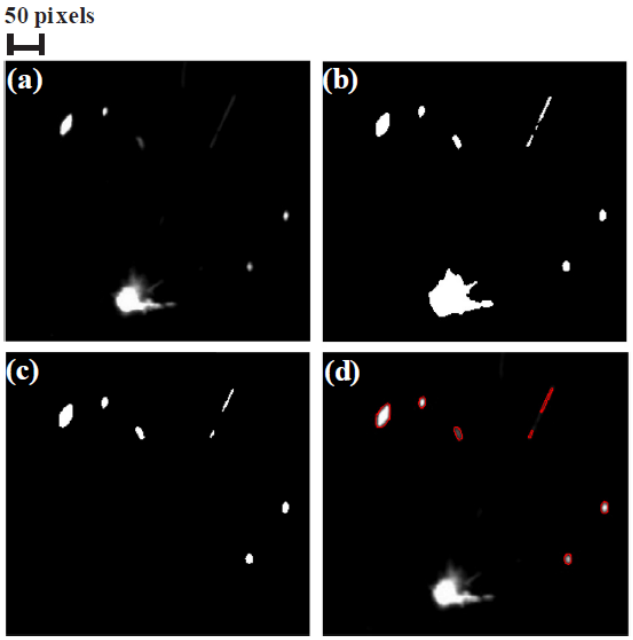

Figure 66. Image processing for spatter segmentation in the L-PBF process [104].

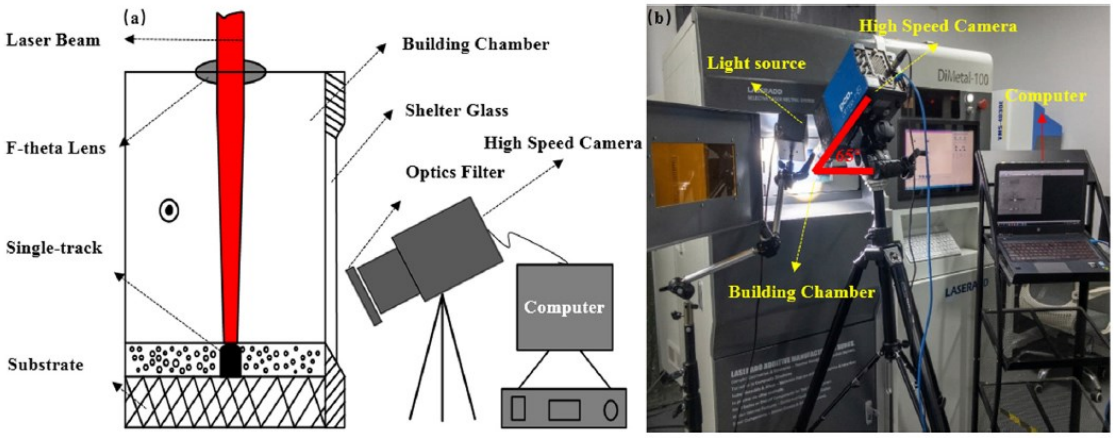

Figure 67. Monitoring system setup applied in this work [104].

As regards monitoring of slice and powder bed is usually conducted by using different imaging tools classified according to the monitored spectrum of light ranging from visible to Near Infrared (NIR) and from NIR to Long Wave-Length Infrared (LWIR) [72]. Images acquired by high-resolution visible light cameras and image-processing algorithms are widely used to acquire in-situ images of the scanned slice as well as of the powder bed for, at least, three main purposes: (i) defect detection, such as porosity, (ii) the evaluation of the

slice dimensions and geometry and (iii) the detection of superelevated edges or other defects related to the recoating system, by monitoring the powder bed [72]. Surface topography is also detectable as a layerwise quality monitoring, i.e. through the use of spectral domain optical coherence tomography (SD-OCT) [105] or fringe projection techniques [106]. As mentioned above, together with high-resolution systems and high-performing equipment, there is a need for image analysis tools and methods capable to capture relevant information and process signatures from the acquired images. In a work conducted by zur Jacobsmühlen et al. [107], an image analysis method able to segment part contours in high-resolution images was proposed. Moreover, in an in-depth study by Pagani et al. [108] a methodology suitable to deal with complex geometries that change layer by layer was developed by combining an active contours technique for image segmentation with a statistical process monitoring approach. As reported, slice and powder bed monitoring methods based on visible light are widely used in literature, since they are relatively inexpensive and easy to install. Moreover, using the same optical equipment it is possible to monitor the slice geometry and dimensions, and powder bed, as well as to detect small defects. However, issues related to perspective correction, the reliability in detecting edges and the resolutions achievable are still critical [93,107]. Optical Tomography (OT), is another recent approach that uses a CMOS camera with 5 Megapixels [109] for the monitoring of the complete platform with a lateral resolution of 0.1 x 0.1 mm^2. This technique allows to monitor of the laser-powder interaction and, according to [109], it is possible to detect lack-of-fusion and key-hole porosity. A more recent application of this technology is reported in a paper published by Mohr et al. [110], where for the OT a VIS-NIR CMOS camera, having 12.4 Megapixels and an optical resolution of 50 μm/pixel, was used for monitoring purposes. The maximum size of the Field of View (FOV) of the set-up in the configuration presented in this work was limited by approximately 64 mm × 51.2 mm.

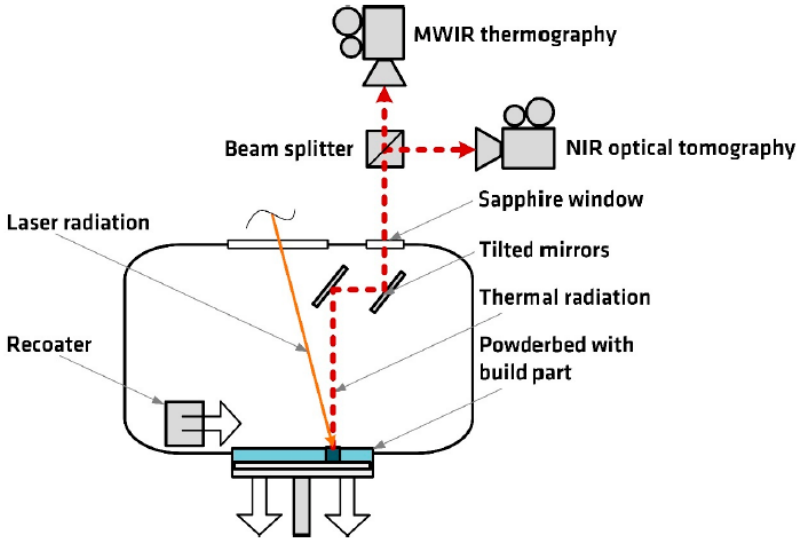

Figure 68. Schematic representation of the off-axis monitoring system applied in this work [110].

To relate the process inaccuracies identified during the in-process monitoring with real defects observed on the final part, it is also possible to integrate the in-process system with off-line measuring systems. In this context, X-ray-based methods and optical 3D scanning methods have become prevalent due to their many advantages concerning contact techniques [111,112]. Some examples are reported in [110,113]. In both cases, the off-line measuring method used is X-ray CT. More recently, some studies have implemented machine learning techniques to images acquired layer by layer in order to more easily correlate defects to certain process conditions [114]. In particular, a layer-by-layer monitoring system was developed from the acquisition of images through a DSLR camera in order to monitor and identify process conditions that cause porosity to occur [114]. The images, processed to extract the features of interest, were then linked to process parameters through machine learning techniques. It was found in this study that multi-fractal analysis leads to a 30 percent increase in accuracy in detecting discriminatory process conditions compared to using traditional statistical measurements. Further in-depth studies on optical monitoring systems developed for the L-PBF process can be found in the review presented by Everton et al. [11].

3.1.2 Thermal monitoring field

Analyzing the literature in the field of thermal monitoring, the aim of the study conducted by Lane et al. [115] was to provide calibrated and well-characterized temperature data to support research and acquire high-speed, high-fidelity observations and measurements for in-situ melt pool and track monitoring. The study was conducted using an EOS M2701. According to this work, defects, such as the occurrence of porosity, can be detected by observing changes in the temperature gradient and the cooling rates of the area near the

defect. Therefore, a system capable of high magnifications is required to monitor the melt pool. Knowing the isotherms near the melt pool helps determine the magnification required, while the cooling/heating rates determine the frame rate needed. Lane noted that a 500°C isotherm is 1 mm wide (about 37 pixels), while a 1000°C isotherm is 0.5 mm wide (about 14 pixels). Acquiring at a rate of 1800 fps resulted in a resolution of 360 x 128 pixels or an area of 12.96 mm x 6.82 mm. The monitoring was conducted through a thermal imaging camera (see Figure 69), tilted 43.7 degrees, which was calibrated with a blackbody capable of reaching temperatures of 1050°C. A 16 x 16 x 16mm cube was constructed from Inconel 625 material. All the collected videos were calibrated according to an equation for calculating the correct emissivity value and found values in the order of 0.5. The results showed that the isotherms varied depending on where in the deposition track they were measured: at the beginning of the trace the 1000°C isotherm was less than 0.5mm, in the middle it was 2.5mm and at the end 1.5mm (see Figure 70). The temperature gradient was approximately 500°C over a distance of 3.5mm (143°C/mm). When the laser is in the terminal parts of the deposition, the temperature drops below the measurable range, while in the central areas, it remains around 650°C until it moves onto the adjacent track. In addition, the study revealed spatter that disturbed the acquisitions and had a propagation direction opposite to the scanning direction, with a velocity of about 10 m/s.

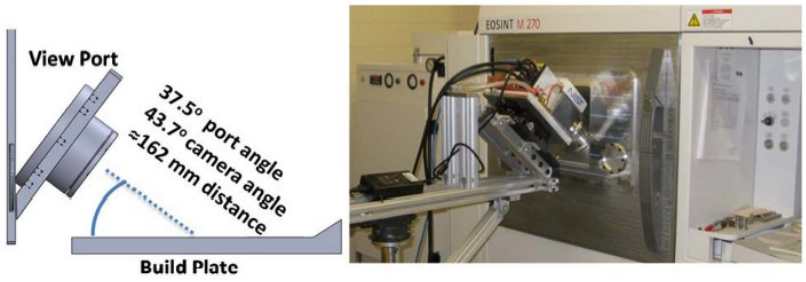

Figure 69. On the left schematic representation and on the right setup implemented in this work [115].

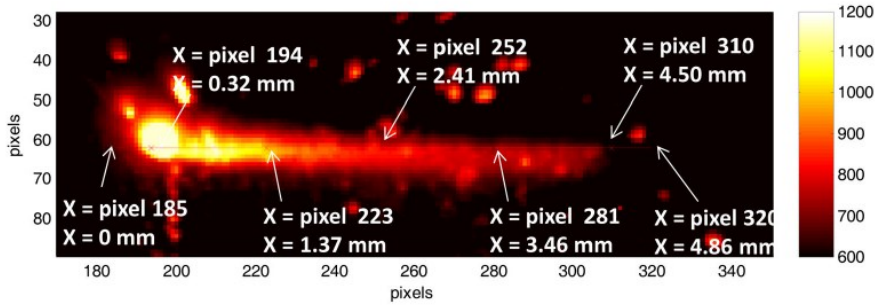

Figure 70. Examples of a track monitored through the thermal imaging camera, with the different temperature and size indications of the track at different positions [115].

There are other thermal monitoring systems in the literature that can extract other thermal parameters. For example, with the use of the bolometer, by the study of Krauss et al. [116], it was possible to monitor the thermal diffusivity, maximum temperature and cooling rate

for each layer and correlate this with various process parameters, so that possible defects in the parts or process instabilities could be defined. Again, Krauss [117], using an infrared camera with a high acquisition speed (50 Hz), focused on the detection of defects such as porosity and irregularities (on Inconel718) due to insufficient heat dissipation during laser processing. By detecting internal cavities, it is also possible to identify certain defects. When temperature deviations from the optimum occurred within a time frame of more than 20 ms, they were detectable as defects. This technique makes it possible to analyse both the melt pool and the powder bed, in particular the curling and stresses within the structures, which could have negative feedback on both the workpiece and the recoating blade, damaging it.

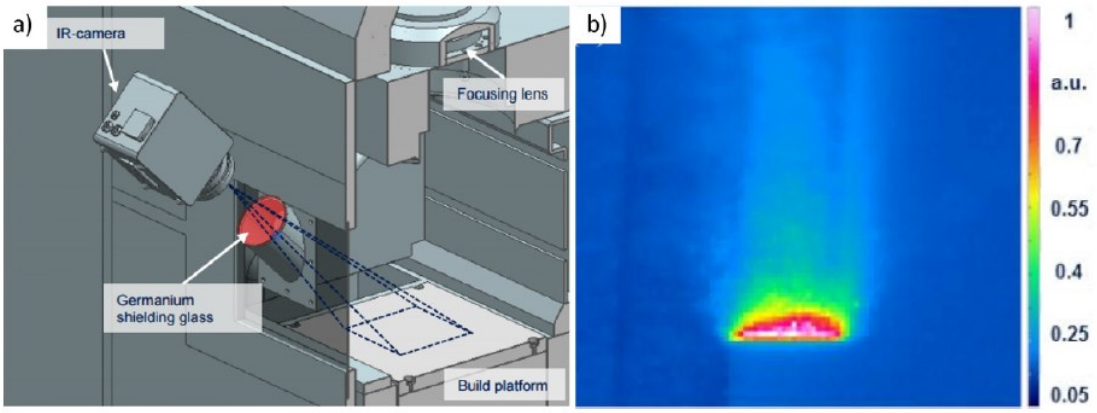

Figure 71. (a) Schematic representation of the setup of the monitoring system implemented in this work, (b) thermogram of the laser-affected zone in a sample with an artificial defect [117].

Whereas, in the study by J.C. Heigel and B.M. Lane [118], the aim was to measure the temperature and melt-pool length under different operating conditions. The study was conducted on an L-PBF machine equipped with a Yb laser source with a power of 200W and a laser spot of 100 µm. A high-speed infrared camera (1800 Hz), equipped with a filter that allows wavelengths between 1350 nm and 1600 nm to pass through, was positioned with an off-axis configuration (please see Figure 72) that creates a relative angle between it and the target surface of 44°. The effect of laser power and scanning speed on the length of the melt pool was assessed by making a single track on each specimen. These were positioned on a rotary table so that each specimen was within the FOV of the infrared camera. The measurement of the width of the melt pool cannot be conducted because in some cases there is the presence of vapour and reflections that would alter the result (Figure 73, Case 3). Scans longer than 4 mm were carried out to verify the achievement of steady-state conditions, a prerequisite for which the melt pool is fully developed. The measurement of the melt pool length is based on the detection of the liquid-solid transition point, which is evident in the cooling section of the temperature profile. Discontinuities detected in the cooling section are related to the phase transformation and are most relevant in cases with high laser beam

power. An algorithm was implemented that detects such discontinuities when the absolute minimum of the 2nd derivative of a 3rd-degree polynomial is reached, which is used to fit the temperatures detected along the scan track (Figure 74). Once the temperatures corresponding to all discontinuities in each replication of a case have been identified, the outliers are eliminated and the average is calculated. The latter was used to identify the leading and trailing edges of the melt pool for each replica of that case, allowing its length to be calculated. The results of this study indicate that the length of the melt pool of individual scan lines generally stabilizes within 1 mm to 2 mm from the start of the scan, reaching a steady-state value that correlates strongly with the nominal laser power. Contrary to this, the relationship with scanning speed appears less clear.

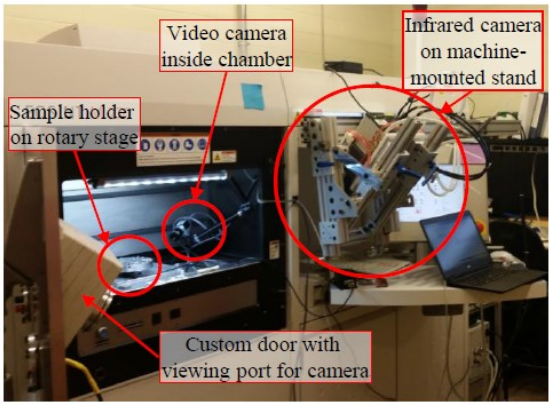

Figure 72. Off-axis thermographic setup implemented in this work [118].

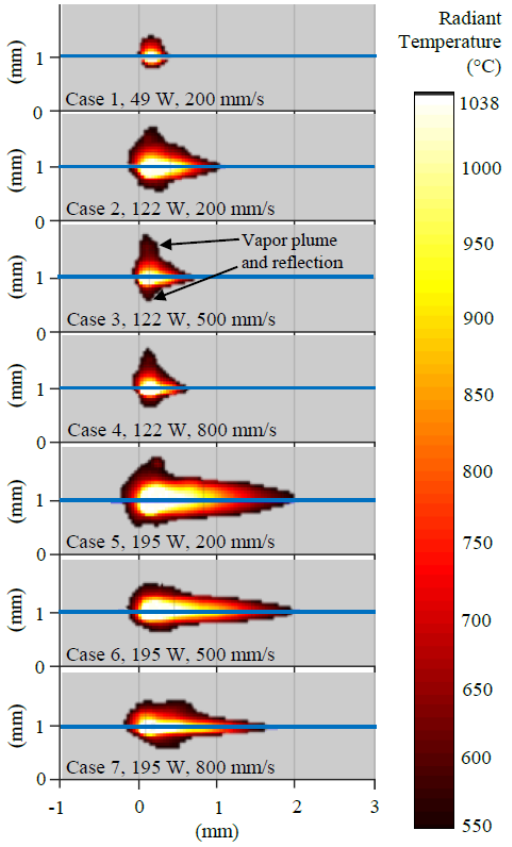

Figure 73. An example of frames acquired by the infrared camera for each chosen combination of process parameters [118].

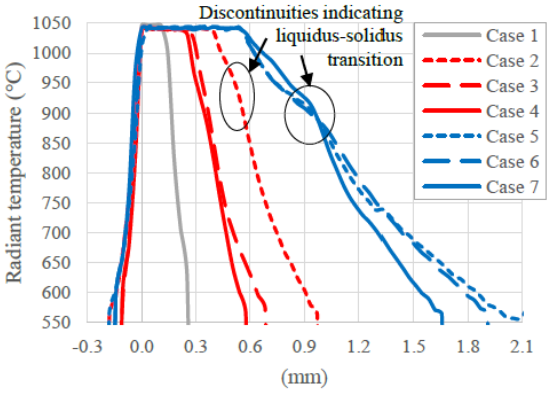

Figure 74. Radiant temperature profile extracted along the melt pool [118].

Reviewing the literature on work conducted on slice and powder bed monitoring through thermal systems, in their work, Lough et al. [119] used a short wave infrared (SWIR) camera to monitor the rapid dynamics of the L-PBF process and characterize the melt pool. Stainless steel 304L was used for the work. Thermal characteristics are extracted from the SWIR imaging data and allowed for the identification of defects in the three-dimensional reconstruction of the parts. These characteristics are the result of the correlation between the melt pool and the process parameters. The thermal characteristics are then correlated to the engineering properties of the part to understand how the thermal history can influence the mechanical properties. During this work, the laser power (100W, 125W, 150W, 175W, and

200W) and exposure time (50, 75, 100, and 125 µs) were varied. The chamber used communicates through a window above the machine. For each pixel, the time above the melting temperature was calculated. This total time in which the pixel is above a set threshold is then proportional to the size of the melt pool. An algorithm was developed to compress the data collected by SWIR during process monitoring into a voxel (three-dimensional pixel) allowing a 3D reconstruction of samples produced with L-PBF for tensile testing. The voxel was determined from the characteristics extracted from the thermal data: time above the melting temperature, maximum gradient, and maximum cooling rate. The three thermal characteristics were compared by evaluating their correlations with process parameters and specimen properties. Time above melting temperature and maximum cooling rate were shown to be linearly correlated with energy density (with variations in exposure time and laser power). The maximum gradient, on the other hand, is not correlated with energy density. Time above melting temperature correlated with strength, microhardness and porosity: a time value above 2ms resulted in better performance for mechanical properties and above 3ms porosity was minimal. Ensuring a uniform melt temperature time on a layer by means of controls could therefore lead to greater homogeneity of mechanical properties. The correlation between thermal characteristics and part properties can potentially be used to create voxels based on mechanical property data.

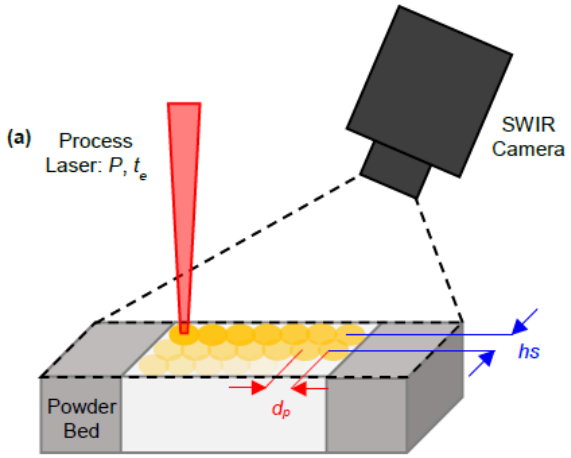

Figure 75. Schematic representation of the thermal monitoring system implemented in this work [119].

A further experimental study [120] on the thermal field of lattice structures involved the use of a thermal imaging camera to acquire in-process data. This study provided insight into how topology affects the thermal flow within the lattice structure.

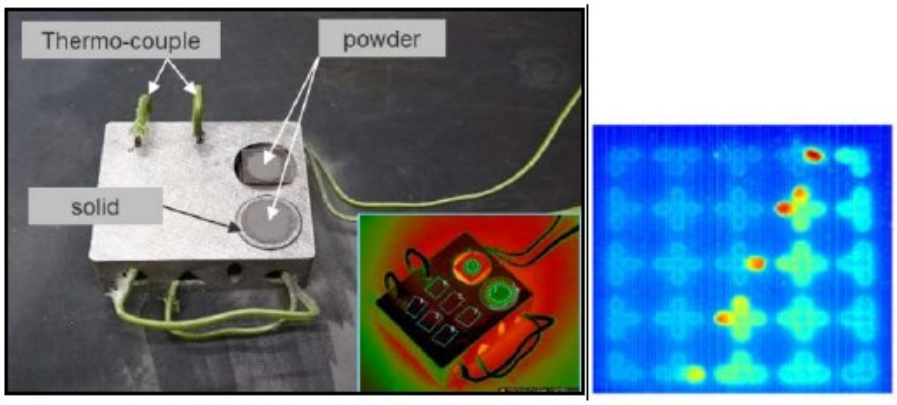

Figure 76. Left, experimental setup used to calibrate the monitoring system implemented in this work; right, single frame of the Face centre cubic sample with vertical z struts (FCZ) 2 mm [120].

Despite the opportunities that thermal monitoring offers, there are technical challenges associated with implementation: avoiding plasma monitoring, monitoring short periods of peak temperatures (needing recordings with frame rates above 10KHz) and assessing uncertainties in thermal measurements that are sometimes in the order of 100°C. This study implements wide-area monitoring to better understand the effect of topology on heat transfer. This allows new laser strategies to be implemented, process-appropriate designs to be developed (design for additive), a closed control and monitoring system to be created, and numerical simulations to be validated. The chamber used has an area of 100 x 100mm. In experimentation, it was necessary to calibrate the temperatures, correct the viewing angle and remove idle periods to reduce the recorded data. The 3D temperature field allows the association of temperatures to specific coordinates throughout production. Special attention was paid to the duration of the cooling cycle (from the peak to a temperature of 260°C). As the cooling time is related to the heat transfer, checking this helps to verify that the process parameters are correct. The results show that geometry and topology have a significant effect on heat transfer in laser processes such as L-PBF. For example, it was found that nodes have a lower cooling temperature than beams, which means that heat conduction is favoured in the connections. Another result was that in structures with 1-mm struts, the cooling temperature was the lowest due to the reduced heat input when printing a smaller geometry.

3.2 Layerwise off-axis optical monitoring developed

Although numerous works in the literature on developed optical and thermal monitoring systems were mentioned in Section 3.1, as shown in Figure 61, some relationships between process signatures and associated defects are still a challenge for the academic world. One of these challenging relationships is the characterization of geometric distortions through slice surface pattern monitoring. A significant scientific advancement was made in this

direction by the work of Guerra et al. *(I'm co-author, please see section 7)* [72], who implemented a High Resolution-Optical Tomography (HR-OT) system for the in-process detection of geometric distortion during the fabrication of inclined thin walls. This system operates in the visible light spectrum. This method makes use of a sensor with a very high resolution and a wide field of view that encompasses the whole printing platform. In particular, compared to the literature study, it is possible to achieve a resolution of 26 μm/pixel on a FOV of around 160 × 105 mm. This made it possible to keep an eye on every aspect of the working environment. Specific geometric indices were created based on the captured pictures, and real-time process monitoring was achieved using control charts that displayed the trend of those indices and promptly highlighted the start of process deviation. In addition, 3D digital photogrammetry was employed to confirm the outcomes of the in-process HR-OT and to produce an accurate off-line 3D reconstruction of the manufactured samples. This is an innovative use of off-line 3D reconstruction techniques and in-process monitoring to fabricate crucial geometries.

3.2.1 Layerwise in-situ optical monitoring system and methodology

In this study, HR-OT was applied as a real-time process characterization technique for in-process monitoring during the manufacture of inclined thin walls. The goal was to keep an eye on the whole slice and spot geometric deviations by using particular geometric indices [99,121,122]. With an optical resolution of 26 μm/pixel, the suggested system is capable of acquiring a fairly broad area of the field of view (around 160x105 mm). The system consists of a Canon Eos 760D off-axis camera with a Canon EF 50 mm f/1.8 II lens and a sensor size of APS-C (22.2 14.8 mm). The smallest camera aperture, f-stop 22, was chosen to get the greatest depth of focus, and the exposure period was adjusted to the amount of time required to complete the scan of each object. Additionally, the lens was equipped with three Neutral Density (ND) filters (ND2, ND4, and ND8) (please see Figure 77).

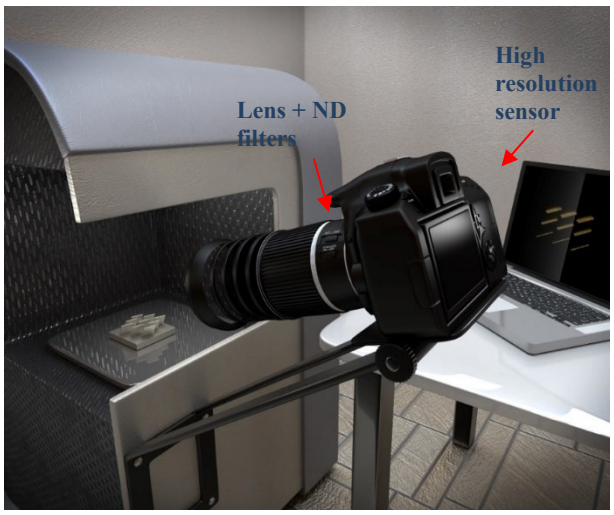

Figure 77. Schematic of the L-PBF device with the 2D optical monitoring apparatus: Optical tomography with high resolution and neutral density filters [72].

The optical density of ND filters is described as "-log10(T)" [123], where T is the filter's transmittance, or the material's capacity to pass incident light through it. As illustrated in Figure 78, images obtained through this method enable the identification of the sample boundaries as well as individual laser tracks and other light emissions produced by the laser-material interaction. Figure 78a depicts the actual image, whereas Figures 78b–c show the same pseudo-color image produced using two different Lookup colour tables (LUTs): "spectrum" and "3–3-2 RGB" [72]. Each picture array element's 8-bit intensity is an index that corresponds to a colour table entry. The pseudo-colored image's many hues serve to distinguish between variations in the obtained object's colour and intensity [72].

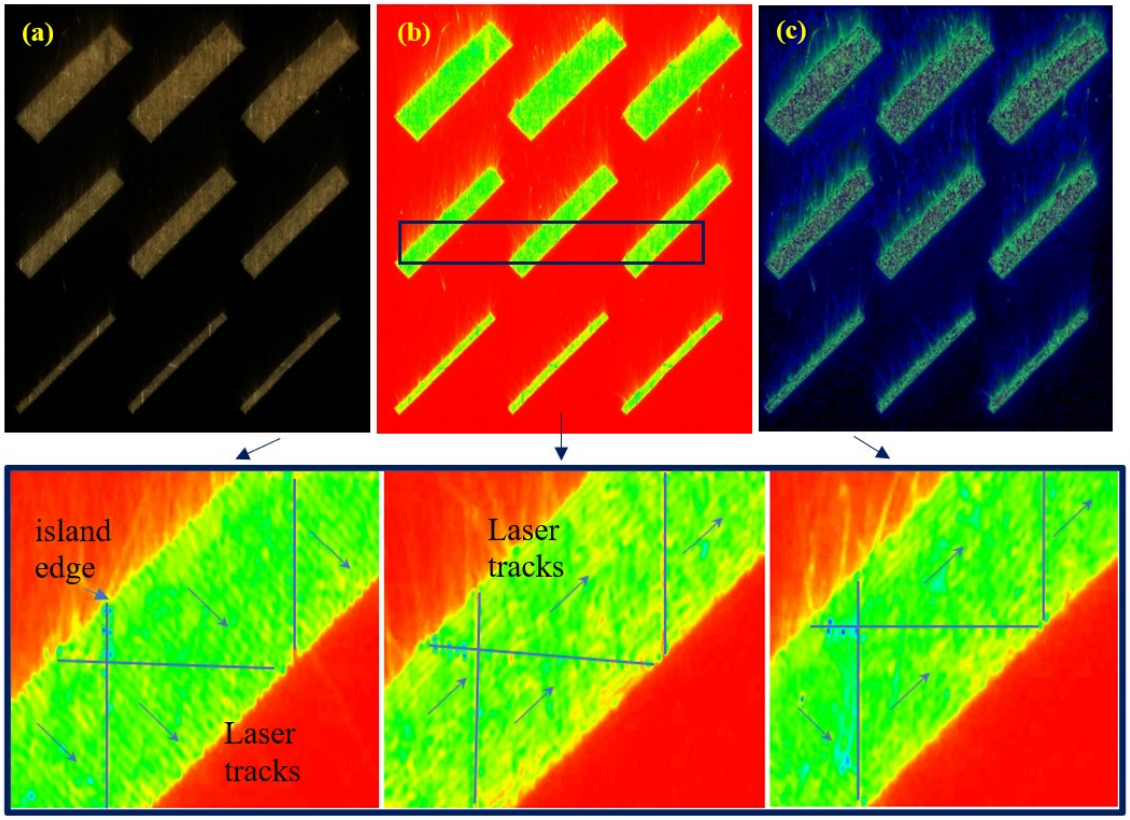

Figure 78. An illustration of the original image (a), a pseudo-color image with LUT "spectrum" (b), and LUT "3-3-2 RGB" (c) [72].

This approach was used in this work to monitor geometric distortions as they occurred using certain geometric indices. Using HR-OT photos to look for geometric distortions and dimensional imperfections has a number of benefits. First, non-uniform illumination may have a greater impact on pictures utilized commonly for layerwise monitoring. This effect is dependent on the sensor's location in relation to the region being gathered. Second, a more involved pre-processing of the photos is required due to the blurry contrast between the melted area and the powder bed. The latter might offer various outcomes depending on the chosen threshold values. As was already noted, OT pictures operate differently; they capture all of the light emissions produced by the laser's contact with the material in a single frame using a technique called bulb exposure, which entails an exposure period equal to the time required to complete a slice. This results in a picture that only shows the region where the laser-material interaction takes place. Thus, HR-OT pictures can avoid the onerous pre-processing of the obtained images as well as the aforementioned criticalities. In order to do this, Figure 79 reports the workflow of the picture acquisition and processing processes while emphasizing the key results of the carried-out study. The whole slice was obtained at the conclusion of each scanned layer (see Figure 79a). The Matlab program for projective transformation and four control points were used to do a perspective correction first (see Figure 79b). The latter was acquired using four 3 mm cylinders that were manufactured at

each vertex of the steel platform, and whose centres (intersection of cylinder axis and section planes) were then measured using a CMM Demeet 400 with a 2 mm diameter ruby touch probe (accuracy x, y, and z of 3.923μm). To find pertinent information, captured and corrected photos were analyzed. By examining the picture of each slice, the major objective was to develop certain geometric indices capable of highlighting the beginning of deformations. Matlab and ImageJ, two distinct software applications, were utilized (Image processing and Computer Vision Toolbox Release 2021). To make the picture afterward analyze-able, a macro was made in ImageJ to automate a number of fundamental procedures. The captured picture was converted into 8 bits as the initial step. After performing a thresholding operation and setting a fixed threshold value for each picture, the noise was reduced using a median filter (see Figure 79c). A Sobel edge detector, which recognizes a closed contour and can identify abrupt changes in picture intensity, was employed for contour identification. Additionally, the contour was reduced to a curve made by one pixel per point using the skeletonize tool (see Figure 79d). Finally, for each layer, the pixel coordinates of the points that make up the retrieved contours were acquired and used for the analysis that followed. The same cylinders that were used for perspective correction were also utilized to evaluate the precision of the monitoring mechanism that was put into place, which included picture capture and processing. They would in fact offer an excellent indicator of the fabrication accuracy as they would be made under identical circumstances as the slanted walls. Therefore, distances between cylinders were retrieved in this assessment and assessed at five parts along the cylinder height. The distances between two pairs of cylinders positioned at the opposite corner were taken into account, and the two diagonal measurements were obtained since they better depict the monitored area. Additionally, these distances are recognized as unidirectional lengths and are typically employed for evaluating the precision of measurement equipment [111]. Using the method outlined, the largest relative error estimated to have occurred was 0.2±0.1 %.

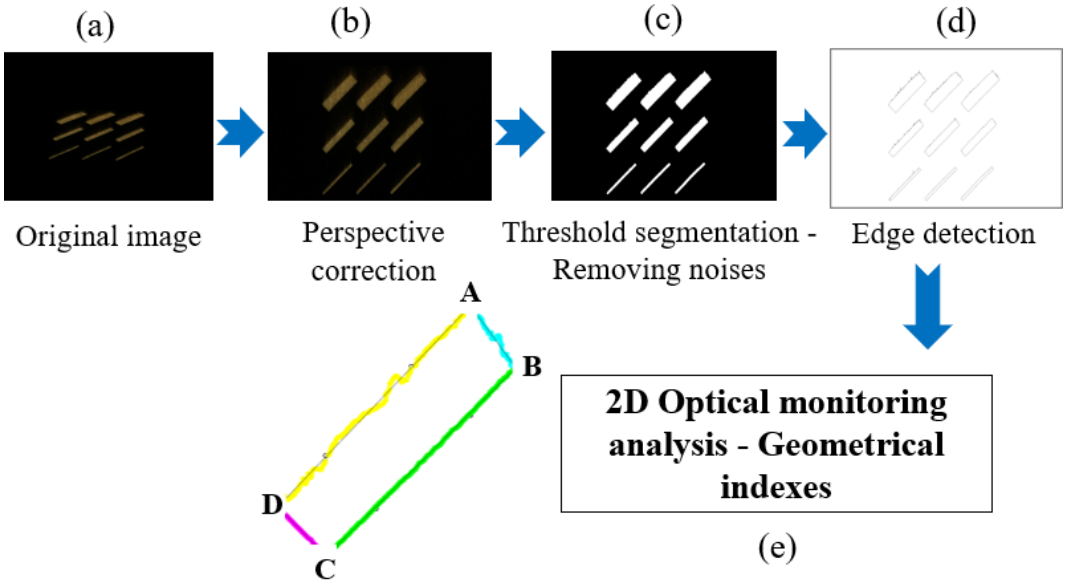

Figure 79. Image processing steps followed in this work [72].

3.2.2 Case study: Laser-powder bed fusion of inclined thin walls

The primary component examined in this study is an inclined thin wall with an overhanging surface that has three distinct wall thicknesses and dimensions of 30 mm in length and height (please see Figure 80). Since it turns out to be a significant inclination and is thus interesting to watch, the inclination with regard to the construction direction (z-axis) was set equal to 45° for all the thin walls constructed [124]. In particular, wall thickness and scanning angle were examined as major influences. Three levels were taken into account for each of the aforementioned criteria, resulting in nine experimental situations (they will be described in Table 12). The three distinct scanning angles that were looked at in relation to the overhanging surface edge are schematically represented in Figure 81. In order to raise the degrees of geometric distortions and process deviations, which are noteworthy from a monitoring perspective, these tactics were selected from prior research [124]. The samples were also created using a series of manufacturing procedures that were refined via earlier research and are listed in Table 13. This generated components with a relative density of more than 99% as determined by Archimedes' technique. In order to generate walls with lower residual stresses, the island scanning approach was also used, with islands that were 5x5 mm2 in size. In the next layers, the islands were relocated by 1 mm in the XY plane. The thin walls created in this manner are seen in Figure 82. In order to confirm the reproducibility of the procedure, samples were also reproduced three times. Si (S1, S2, and S3) will now be used to denote the scanning angle factor, while Ti will be used to represent the wall thickness (T1, T2 and T3). The Concept Laser M1 machine, which is available for purchase, was used for the tests in this work. It is outfitted with a Nd: YAG solid-state laser

source that has a wavelength of 1064 nm, a maximum laser power of 100 W, and a laser spot diameter of 200 µm. The device has a dedicated support PC with two software interfaces that operate in serial mode (one for the machine and the other for the laser). Using the right scanning systems controlled by a PC, the laser beam is moved to the working point on the powder bed's surface (located within the X-Y plane) to melt the powder particles in accordance with the data produced by the model's slicing (created using Materialize Company's Magics® 11 software), creating the desired section and, simultaneously, melting the powder particles. The working chamber was filled with N2 to lower the initial oxygen level to 0.8% in order to produce excellent results, reducing both oxidation and deterioration of the melt pool. Cogne Acciai Speciali S.p.a. (Italy) provided the AISI 316L stainless steel powder utilized in this project. Cogne Acciai Speciali S.p.a. produced the powder via gas atomization, and it had a spherical form and a particle size in the range of 15 to 53 µm.

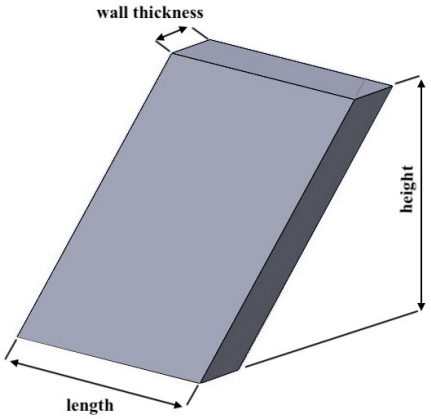

Figure 80. An illustration of an inclined thin wall with its basic measurements [72].

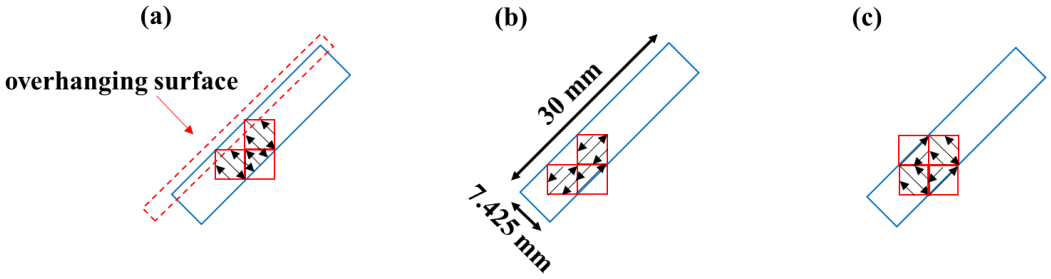

Figure 81. Diagrammatic representation of the three possible scanning angles with respect to the overhanging surface edge: (a) 90°; (b) 0°; and (c) 0°/90° [57].

Table 12. Plan of the experiment: variables and their corresponding levels utilized to create the specimens [72].

Factor	Unit	Factor Levels					
		T1	T2	T3	S1	S2	S3
Wall thickness	mm	1.768	4.596	7.425	-	-	-
Scanning angle	°	-	-	-	90	0	0/90

Table 13. A collection of process optimization parameters used in experiments [72].

Parameter	Notation	Unit	Value
Laser power	P	W	100
Scanning speed	v	mm/s	200
Laser spot diameter	d	µm	200
Layer thickness	l_t	µm	30
Hatch distance	h_d	µm	140

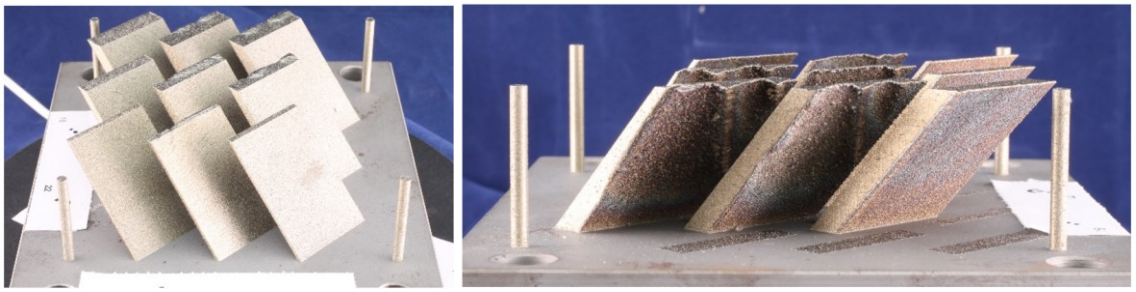

Figure 82. Photographs of the L-PBF-fabricated inclined thin walls [72].

3.2.3 Data analysis methodology

The size of each sample section and three geometric indices that may identify the beginning of a process deviation and, therefore, the deformation of the sample layer by layer, were retrieved as the macro's four primary numerical outputs (see Figure 79e). The absolute value of the percentage deviation (AD) was computed for the area of each individual wall since it was intended to find sudden departures from the nominal value (see Eq. (1)):

$$\mathrm{AD}_{i\%} = \left|\frac{A_i - \mathrm{A}_{\mathrm{nom.}}}{\mathrm{A}_{\mathrm{nom.}}}\right| \times 100 \quad (1)$$

Where i= 1, ….n is the layer number, and A_i is the area recognized by the developed macro for each layer and $A_{nom.}$ is the corresponding nominal area.

While the three suggested geometric indices are:

1. the Deviation Along the Overhanging Surface Edge (DAOSE). For each layer, it was specifically determined for each layer's average deviation of the point distance on the overhanging surface edge from the nominal distance (see Eq. (2)):

$$\mathrm{DAOSE}_{i\%} = \left|\frac{\frac{\sum_{p=1}^{m}|d_p|}{m} - d_{nom.}}{d_{nom.}}\right| \times 100 \quad (2)$$

where d_p is the distance from a point belonging to the overhanging edge with respect to the line interpolating the points belonging to the non-overhanging edge $\overline{BC}$ (please see Figure 79e), $d_{nom.}$ is the nominal distance corresponding to the wall thickness and m is the total number of points that make up the overhanging surface edge and i=1,

…n is the layer number.

2. The Orthogonal Deviation (OD), is defined as the deviation from the orthogonality between the overhanging edge and the short side of the wall section (i.e. the wall thickness) (see Eq. (3)):

$$OD_i(°) = \frac{\pi}{2} - \alpha \tag{3}$$

where α is the angle $D\hat{A}B$ (calculated in °) between the line interpolating the points belonging to the overhanging edge ($\overline{AD}$) and the line interpolating the points belonging to the wall thickness ($\overline{AB}$), see Figure 79e, and i=1, …n is the layer number.

3. The Punctual-DAOSE (P-DAOSE) is computed as the absolute percentage deviation of the distance of each point belonging to the overhanging surface edge with respect to the nominal point distance, according to Eq (4).

$$P - DAOSE_{\,p,i\%} = \left|\frac{d_p - d_n}{d_n}\right| \;\; x\,100 \tag{4}$$

Where p=1, ….m is the individual point belonging to the overhanging edge and i= 1, ….n is the layer number.

To perform statistical process monitoring, the parameters (ADi, DAOSEi, and OD (°)) were utilised to build the relevant control charts (explained in detail in Section 3.2.4). While the P-DAOSE was employed for more accurate localization of the distortion along the considered edge after an anomaly was discovered using the control chart that was put in place. Offline dimensional analysis was then employed to characterize the geometric aberrations seen on the manufactured samples in general, to enable the creation of ad hoc control charts, and to assess the efficacy of the chosen monitoring strategy.

3.2.4 Statistical process monitoring

The Shewhart Control Chart for Individual Measurements was developed in order to automatically detect significant anomalous deviations from the nominal form since, once the monitoring system has been installed, layer by layer, the sample now only consists of individual units [49]. For the purposes of this investigation, each individual unit generated was measured automatically. However, if a slight movement in the process average needs to be tracked, the cumulative sum and moving-average charts with exponential weighting, used in the works [108,125], are a reasonable substitute [49]. The moving range derived on two consecutive observations (n = 2) was employed in our statistical process monitoring to quantify the process' variability. The following is how this value is defined (see Eq. (5)):

$$MR_i = |x_i - x_{i-1}| \tag{5}$$

The following variables are displayed on the control chart for each measurements (see Eq. (6)):

$$\begin{aligned} \mathrm{UCL} &= \bar{\mathrm{x}} + 3\frac{\overline{\mathrm{MR}}}{\mathrm{d}_2} \\ \mathrm{CL} &= \bar{\mathrm{x}} \\ \mathrm{LCL} &= \bar{\mathrm{x}} - 3\frac{\overline{\mathrm{MR}}}{\mathrm{d}_2} \end{aligned} \tag{6}$$

where UCL, CL and LCL stand for Upper Control Limit, Center Line and Low Control Limit, respectively; $\bar{\mathrm{x}}$ is the sample mean of the identified numerical outputs, described in Section 3.2.3, and $\overline{\mathrm{MR}}$ is the average of the moving ranges over two successive observations. Since a moving range with n = 2 observations was employed in this study, then $d_2 = 1.128$ [49]. Whenever an out-of-control point is observed, i.e., the calculated index value exceeds the limits described in Eq. (6), an alarm is signaled. However, the values of $\bar{\mathrm{x}}$ and $\overline{\mathrm{MR}}$, were calculated for the first 100 layers, since no significant distortions were found in these layers compared to the nominal and were considered representative of the statistics monitored in the subsequent layers.

3.2.5 3D comparisons and 2D analyses for off-line 3D reconstruction.

The generated samples' off-line 3D reconstruction was carried out utilizing 3D digital close-range photogrammetry and a rotary table, the PSSRT [126]. The Canon EF 50 mm f/1.8 II lens was utilized with two Digital SLR cameras Canon Eos 760D (24.2 Megapixels, Sensor Size APS-C 22.2 × 14.8 mm), at their closest focusing distance (350 mm). The Ground Sampling Distance (GSD), determined by the chosen optical setup, was 24.2 μm/pixel. The distribution of the samples on the platform and their shape were taken into consideration when designing the acquisition approach. Thus, the two cameras were angled at 45° and 0°, respectively. 90 photos were collected by each camera, which translates to a 4° rotation step of the rotating table, while 180 images were processed in total. Previously, the NPL150 freeform artefact (realized in 6082-T6 — Aluminium Dural with a Rz of 0.6 mm) was used to calibrate the photogrammetric system [126]. After that, the collected photos were edited using the expensive program Agisoft Metashape v. 1.7.1. Using 12-bit coded targets (1 mm in central radius) that were mounted on the platform and whose centre coordinates had previously been determined by a video CMM Demeet 400 (accuracy in x = 5.33 μm, y = 5.33 μm, z = 4.33 μm), the scaling procedure was carried out. The GOM Inspect software application was then used to evaluate the 3D reconstruction of the materials (www.gom-inspect.com). In order to more accurately compare the data from the in-process monitoring and the off-line 3D reconstruction, first, a 3D comparison was done to identify the areas

most impacted by deformations. Next, a more in-depth 2D section analysis was done using the same indexes established in Section 3.2.3. The layer height utilized during the procedure equates to a section every 0.03 mm, therefore a total of 1000 sections were made for this purpose (equal to the total number of layers). The ADi, DAOSEi, and P-DAOSEp,i were calculated for each drawn 2D section to identify the beginning of any geometric distortions and statistically evaluate it to see how well the in-process monitoring worked.

3.2.6 Off-line 3D reconstruction analysis

The initial 3D comparison took into account the whole sample surface. In particular, it made it possible to assess the deformation on the inclined walls' overhanging surfaces, which, from a monitoring standpoint, were the most important and intriguing portion of the sample. Figure 83 shows how the scanning angle and the wall thickness influenced the overhanging surface's deformation in relation to the nominal. When taking into account the wall thickness T3, scan strategies 2 and 3 in particular created the biggest deformations that reached their maximum value and had the broadest diffusion. S1 produced the lowest deformations.

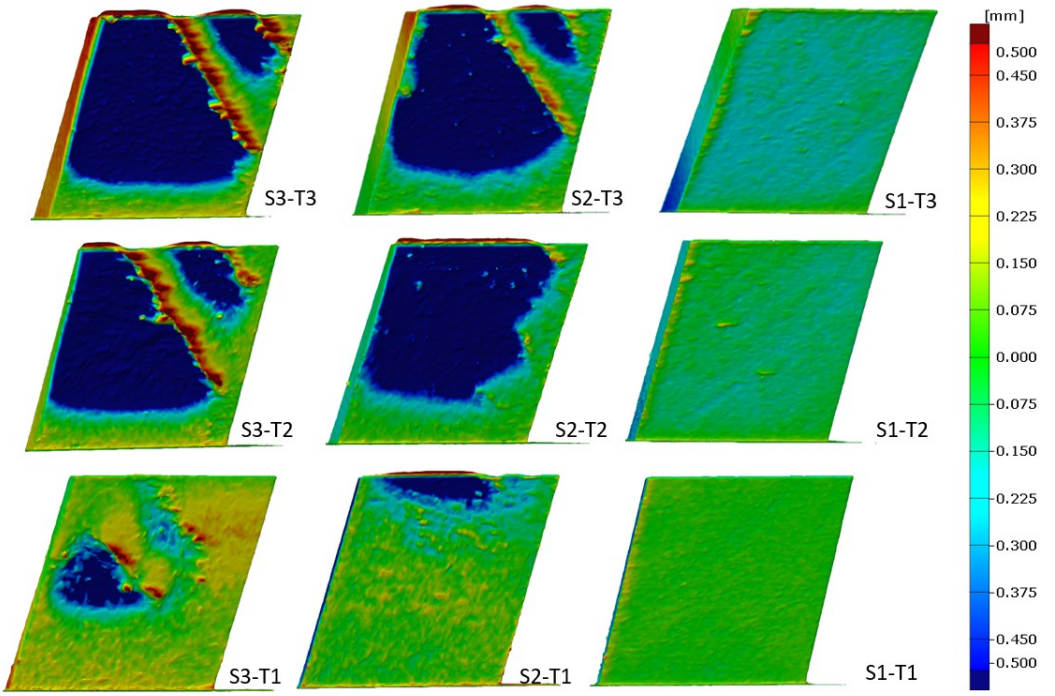

Figure 83. Comparisons in three dimensions of the distorted downskin (overhanging portion) of thin walls made of Si and Ti [72].

To better comprehend the section evolution along the wall height, certain 2D sections of the sample with the larger thickness, T3, were further taken into consideration in Figure 84. As can be seen, the first layers for all three techniques under consideration have relatively unexpanded geometry up to the first 3 mm (100 layers). The geometry for methods 2 and 3 was then altered, indicating the presence of significant deformations.

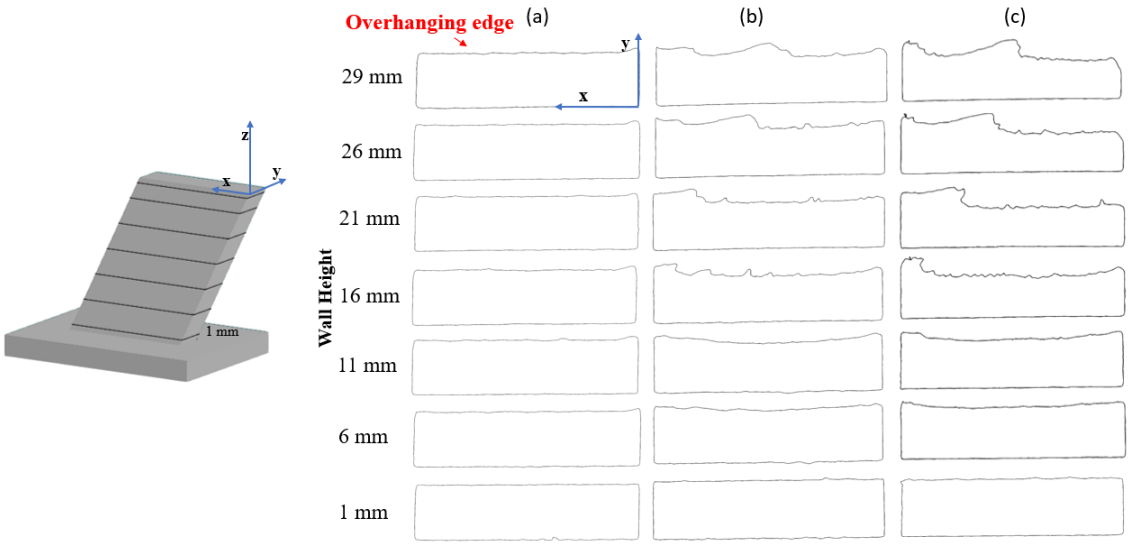

Figure 84. Section evolution of S1-T3 (a), S2-T3 (b) and S3-T3 (c) [72].

This sample segment has to be monitored since this section evolution often indicated a decrease in the wall section and an increase in the variability of the overhanging surface edge. The area of each section was accurately regarded as a monitoring parameter since it would be more likely to be changed by this effect, as the deformation detected on the overhanging surfaces was largely discernible by a variation of the section shape.

3.2.7 2D optical monitoring analysis

Specific indexes were computed in accordance with the image acquisition and analysis procedure outlined in sections 3.2.1, 3.2.3, and 3.2.4, and then ad-hoc control charts were created to automatically detect, in-process and in-situ, large deviations from the nominal shape and, consequently, geometric distortions or anomalies in the process itself. The Shewhart control charts for individual measurements applied to specimen S1-T3 and computed for the ADi index (see Eq. (1)) on the top 100 layers are shown in Figure 85. The study supports the findings of the post-process analysis discussed in Section 3.2.6 by demonstrating that no out-of-control circumstances occurred.

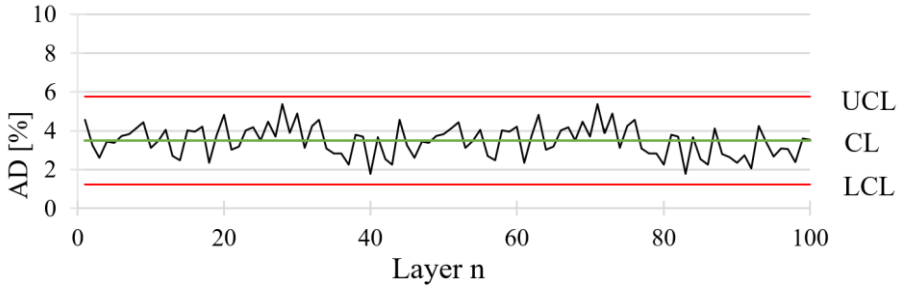

Figure 85. Proposed Shewhart control charts employed to sample S1-T3 on the first 100 layers [72].

The control chart used on the S3-T3 specimen for the entire sample is displayed in Figure 86. The picture depicts an increasing shift in the average ADi beginning at layer 150, or at

4.5 mm in height for the walls.

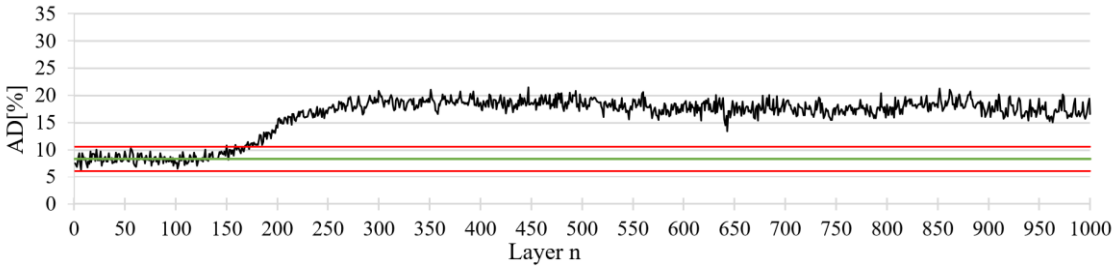

Figure 86. Proposed Shewhart control charts used for the whole sample S3-T3 [72].

Figure 87 illustrates the flaw created in the layer under investigation, which is the curling of the overhanging surface's edge (please see Figure 87a), as a result of an ineffective scanning strategy in the particular S3. This causes non-optimal heat dissipation, thermal stress in the overhang area, and the onset of geometric distortion. This out-of-plane distortion (see Figure 87b) results in a less-than-ideal recoating (see Figure 87c), which then causes the uncoated area to remelt, leaving the final printed specimen with insufficient material. The suggested technique has so successfully caught the printing flaw both in-process and in-situ.

Figure 87. Layer 800 of sample S3-T3 signalled as out of control. (a) OT of the whole layer, (b) scanned layer image, and (c) powder bed recoating [72].

The S3-T2 and S3-T1 test specimens, whose values are listed in Table 14, both exhibited comparable distortion. The control chart used with the S3-T2 test specimen is displayed in Figure 88. The same distortion is also present in this instance, beginning with layer 170. Figure 89, on the other hand, depicts the control chart used on the sample S1-T3 and makes clear that there are no outliers. Thus, as reported by the study of T. Yang et al. [124], no substantial deformations occurred in the specimen, verifying the optimum scanning method.

Table 14. Summary of the control chart parameters calculated for all samples and sample height at which the onset of geometric deformation occurs (AD_i) [72].

	Unit	**Sample**								
		T1-S1	T1-S2	T1-S3	T2-S1	T2-S2	T2-S3	T3-S1	T3-S2	T3-S3
Sample height of detected distortions	mm	-	24.1	11.1	-	6.0	5.1	-	5.7	4.5

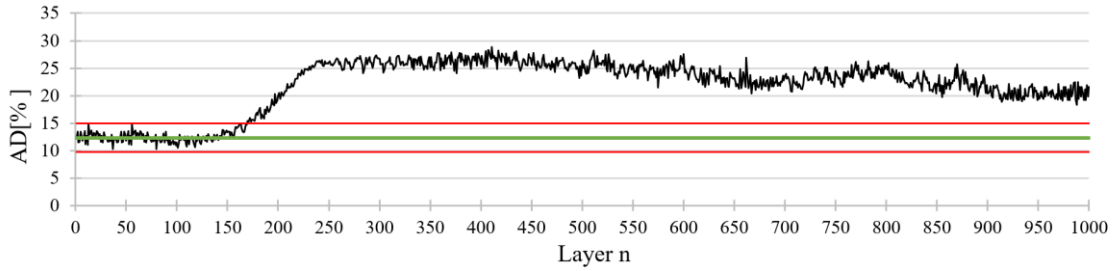

Figure 88. Proposed Shewhart control charts used for the whole sample S3-T2 [72].

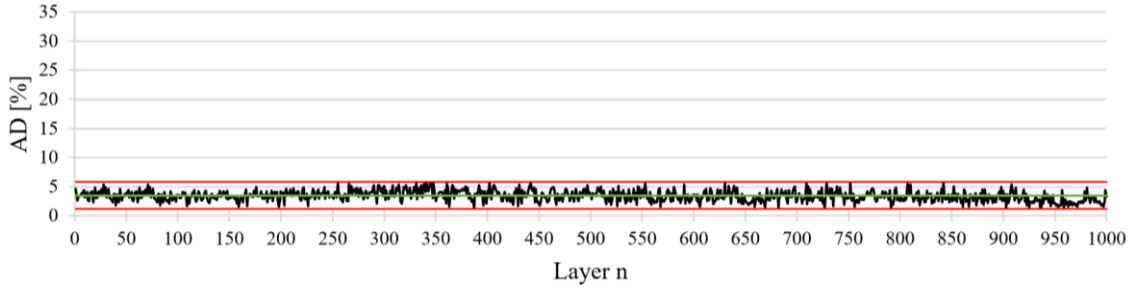

Figure 89. Proposed Shewhart control charts used for the whole sample S1-T3 [72].

The heights of the samples at which geometric distortion started to manifest are reported in Table 14's summary of the findings from the suggested control charts (ADi) for all samples. The DAOSEi and the ODi were then examined in further detail while taking into account the T3 and the best and worst tactics. The Shewhart control charts for the DAOSEi index (see Eq. (2)) for each layer are shown in Figure 90 for individual measurements taken on the specimens S3-T3 and S1-T3. The analysis supports the Adi's findings. In the first 100 layers for either sample, there are no out-of-control locations. Regarding sample S3-T3, layer 150 (see Figure 90a) shows an initial deformation along the overhanging surface edge that progresses to a shifting of the average DAOSEi. Figure 90b, on the other hand, depicts the control chart used with specimen S1-T3, where no outliers were found. The geometric distortion that starts to appear in the inclined thin wall S3-T3 at a height of 4.5 mm and the least deformation observed on the overhanging edge in the inclined thin wall S1-T3 are both confirmed by these results, which support earlier findings about the ADi. We were able to detect geometric distortion more precisely using this particular geometric index.

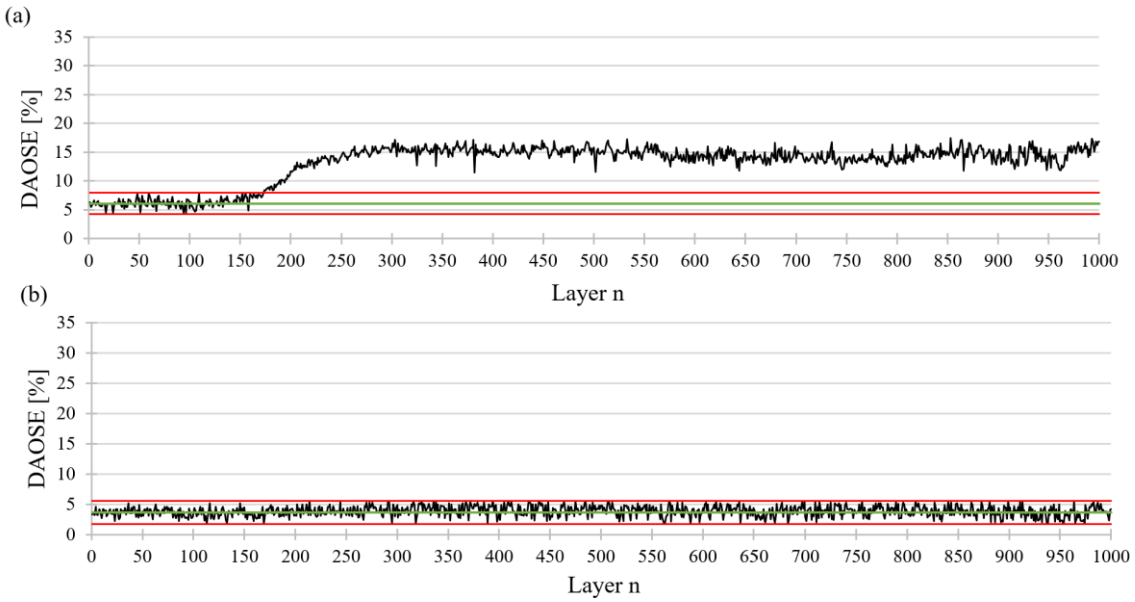

Figure 90. Proposed Shewhart control charts used for the whole sample [72].

Additionally, Figure 91 displays the chosen control charts used on the complete samples S3-T3 and S1-T3 for the ODi index (see Eq. (3)) computed in relation to the $D\widehat{A}B$ angle (please see Figure 79e).

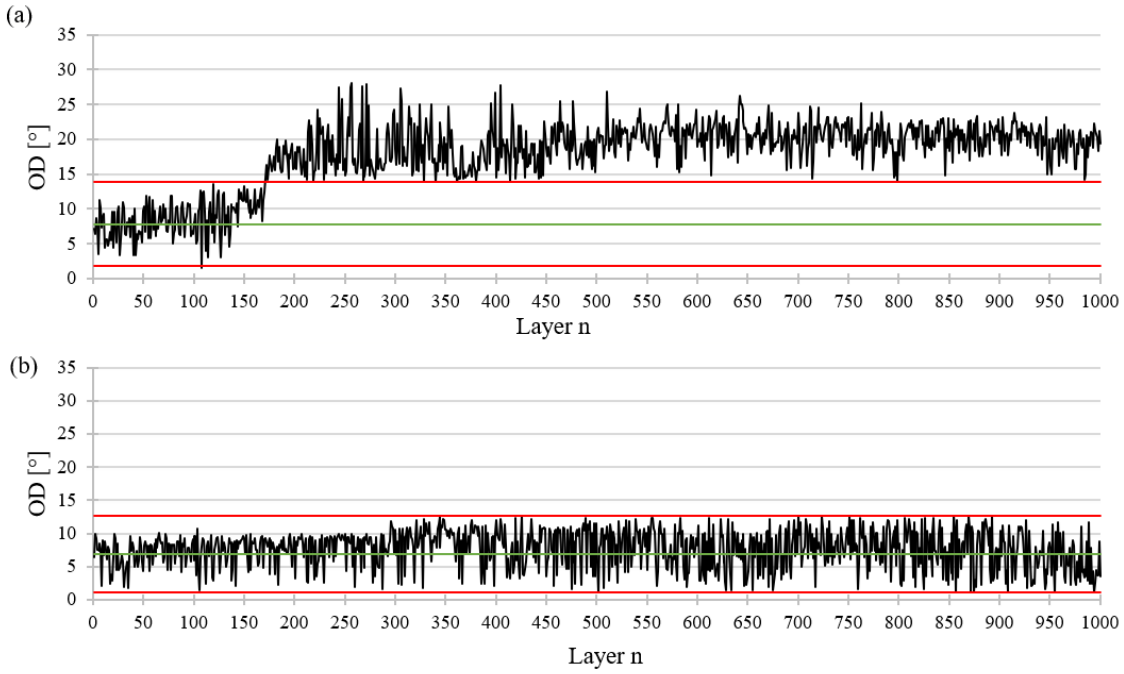

Figure 91. Proposed Shewhart control charts used for the whole sample S3-T3 (a) and S1-T3 (b) [72].

Also in this case, the ODi index trend showed that for sample S3-T3, layer 150 marked the beginning of geometric distortion (see Figure 91a). There aren't any out-of-control points for sample S1-T3 (see Figure 91b), demonstrating that S1 was the method with the least amount of geometric distortion, or nearly none at all, when compared to S2 and S3.

For both samples examined, the DAOSEi and ODi trends seem to be comparable. Both in fact displayed points outside of control for sample S3-T3 at layer 170 (sample height:

5.1mm). Thus, it follows that these two geometric indices, when examined and correlated with one another, would enable the identification of a localized deformation of the printed part, as the first one, DAOSEi, enables quantifying the distortion of the wall on the overhanging edge while the second one enables localizing the deformation.

In the end, it is feasible to draw the conclusion that combining the three indices for analysis and comparison paints a clearer image of the deformation's nature. In reality, if only the ADi index is examined, it may be feasible to determine that there were no process irregularities, but that there was a distortion flaw in the final print. For instance, ADi would be compensated if one edge shrank to the same size as the opposing edge widened. However, the position of the distortion relative to the overhanging edge cannot be determined using the DAOSEi index.

The distortion is recognized both quantitatively and qualitatively by the ODi index, which measures the divergence of the angle from the nominal value and, consequently, from the orthogonality of the edges. In reality, it has been determined that the zone of greatest geometric distortion corresponds to the angle $D\hat{A}B$ (please see Figure 92). In fact, the lack of distortion in that region of the sample is noted by the ODi index, which was computed in accordance with the $D\hat{C}B$ angle (please see Figure 93a-b and Figure 92). As can be seen, these three indices follow the same pattern layer by layer, making it feasible to pinpoint the defect's exact location, accurately categorize it, and take remedial action to ensure that it doesn't recur.

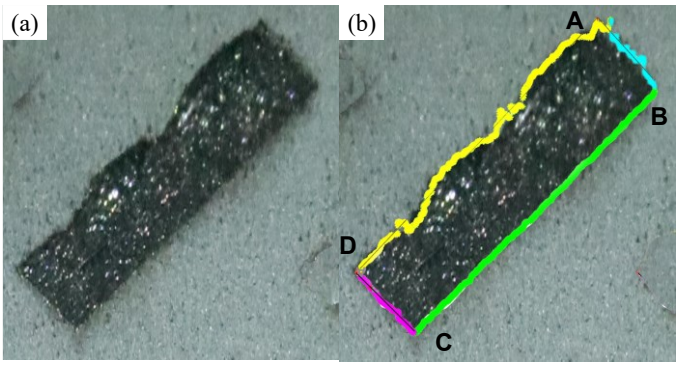

Figure 92. Layer 750 of the inclined thin wall S3-T3 [72].

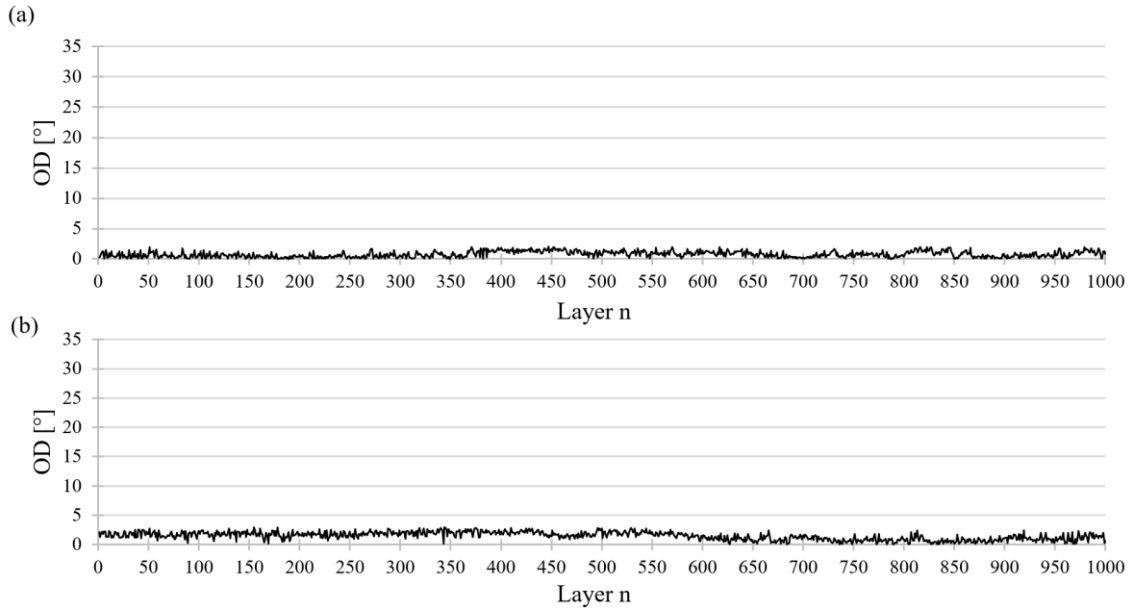

Figure 93. Geometric index OD calculated with respect to $D\hat{C}B$ angle and evaluated along with sample height. (a) refers to sample S3-T3, (b) refers to sample S1-T3 [72].

3.2.8 Comparison of monitoring output and 2D off-line photogrammetric analysis

Data from the off-line photogrammetric reconstruction were utilized to support the findings from the deployed monitoring approach.

Thus, the ADi, the DAOSEi, and the P-DAOSEp,i mentioned in the preceding sections were tested in order to make the findings from the off-line photogrammetric reconstruction comparable with those obtained from the 2D in-process monitoring. PH_ was placed before each index in order to differentiate the photogrammetric data from the HR-OT ones.

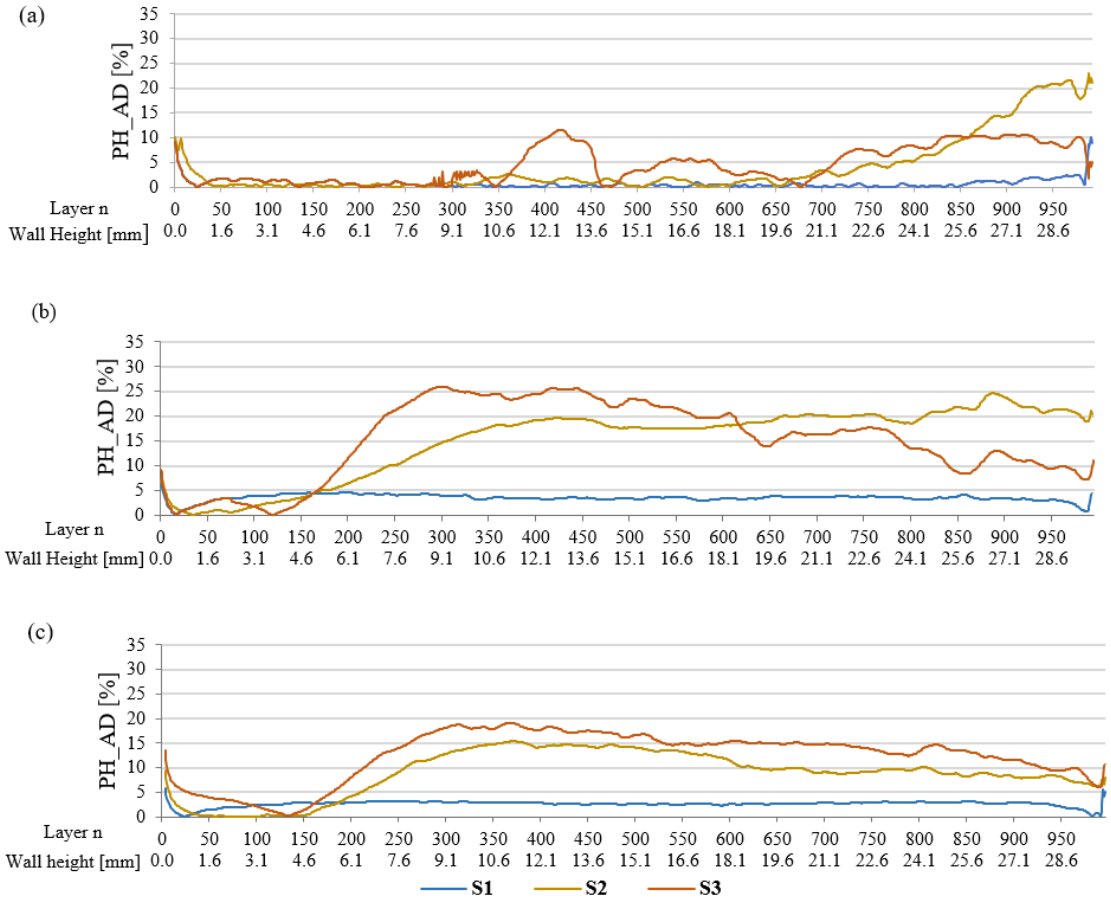

Figure 94. Trend of the PH_AD$_i$ computed for each section and each wall. In (a) are shown walls characterized by thickness T1, in (b) the T2 and in (c) the T3 [72].

The plots in Figure 94a, b, and c displayed the ADi's trend as it was calculated for each part and contrasted with the nominal value as determined by Eq (1). This study made it feasible to compare the findings with those from the in-process monitoring by allowing us to pinpoint the beginning of the process deviation and its progression along the wall height. Regarding the T1 in particular (Figure 94a), S1 demonstrated a fairly consistent trend with the lowest percentage error around zero, whereas S2 and S3 emphasized the presence of geometric distortions in relation to various wall heights. The in-process monitoring was successful in spotting this undesirable tendency, as shown in Table 14. The ADi increased with increasing wall thickness. For both scan strategies 2 and 3, the onset of deformation was typically seen at lower wall height values, whereas S1 displayed lower and stable percentage area deviations that were consistent with the coloured maps shown in Figure 83, the section evolution shown in Figure 84, and the data reported in Table 14, where no deformation exceeding the UCL and LCL was detected for this strategy and all the wall thicknesses analyzed.

The S3-T3 and the S1-T3 features, which are the most and least essential features, respectively, were examined for the DAOSEi index, reproducing the outcomes from the in-process monitoring, for their maximum thickness. The pattern shown in Figure 95 was

closely aligned with the trend seen during in-process monitoring, with S1 recording a nearly steady trend and S3 exhibiting the largest divergence. Additionally, the trend that was reported was virtually identical to the one that was observed when the ADi was taken into account, indicating that the overhanging surface edge was where most of the deformation on the wall section was registered.

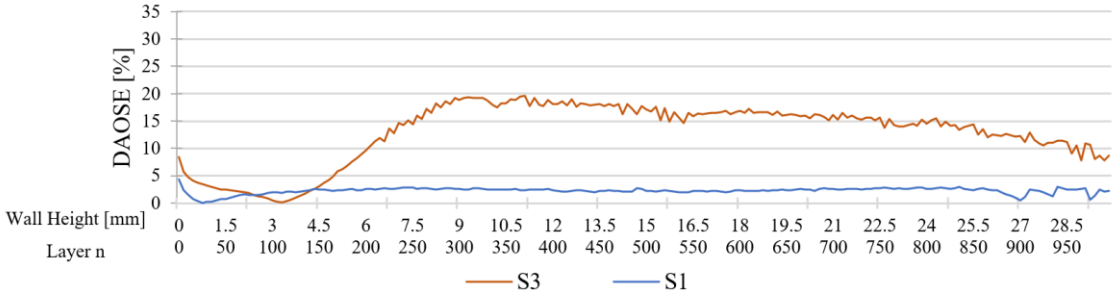

Figure 95. PH-DAOSE computed for S1-T3 and S3-T3 [72].

The DAOSEi takes into account the average deviation of points that correspond to the overhanging surface edge for its definition, see Eq. (2). It was able to measure and emphasize deformations along the overhanging edge, as seen by the results presented in sections 3.2.6 and 3.2.7. It does not, however, specify precisely where the distortion is along the edge under consideration. It could be helpful to think about the DAOSE index point by point for this purpose, using Eq. (4) and labelling this parameter Punctual-DAOSE (P-DAOSEp,i). As a result, when an abnormality is discovered using the ADi, DAOSEi index, and the ODi, P-DAOSEp,i index, it should be possible to pinpoint more precisely where the deformations are concentrated along the edge under consideration. Then, using the points retrieved from the HR-OT pictures and the corresponding points of the 2D sections produced from the photogrammetric reconstructions, this parameter was assessed for the T3-S3 for four distinct layers at various heights. The reported graphs, shown in Figure 96, show that there was generally good agreement between data from the HR-OT and data from the photogrammetric reconstruction, with a maximum difference estimated to be on the order of 10% in correspondence of some points where the deformation was most severe. However, the registered trend was fully converging in all cases.

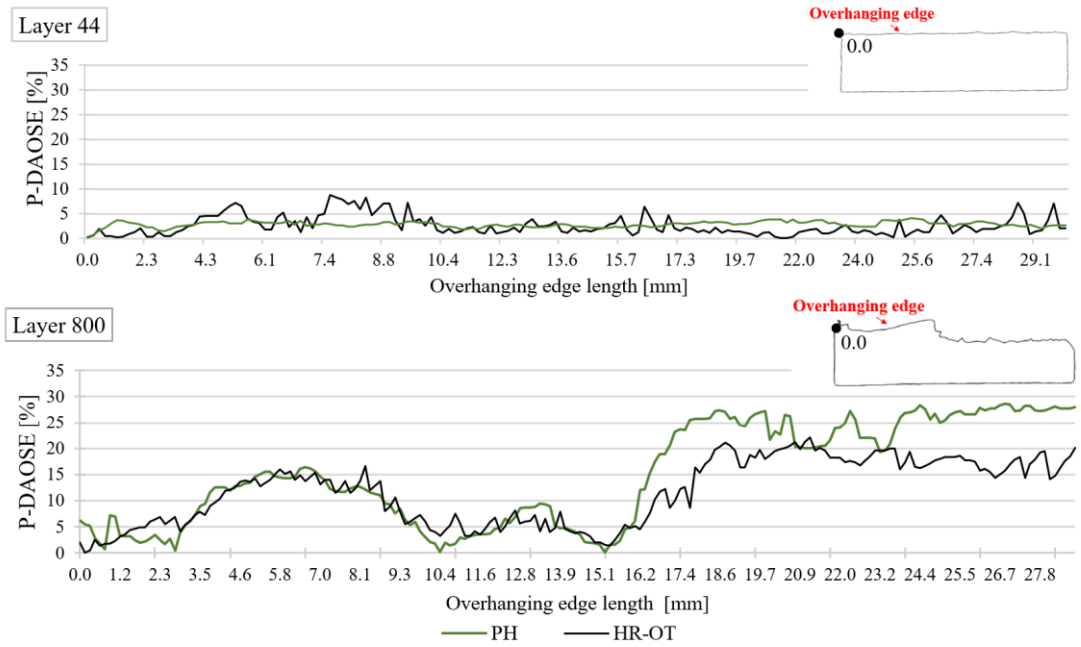

Figure 96. P-DAOSE computed for layers 44, and 800 [72].

The results shown above demonstrate that the implemented control chart, in conjunction with the implemented layerwise in-process monitoring, was useful for further and more in-depth localization of the most deformed part as well as for self-detecting potential print anomalies during the fabrication of inclined thin walls. The output information from this approach might serve two purposes:

1. evaluating in real-time whether an urgent process halt is required and assisting the machine operator in making that choice;
2. off-line post-processing functions as a diagnostic tool to facilitate further qualifying procedures.

As a result, the flaws produced during the process have been accurately located, in-situ, and in-process, by the suggested monitoring approach, as can be observed from the analysis just presented.

The efficiency of the suggested monitoring approach for the identification of geometric distortions occurring during the building of overhanging structures was supported by all of the data that were reported.

3.2.9 Conclusions

In order to provide a real-time process monitoring of geometric distortions, a technique known as High Resolution-Optical Tomography was used in this research to monitor the manufacture of inclined thin walls made using an L-PBF process. The constructed walls were made more interesting from a monitoring perspective by varying the scanning angle

and wall thickness to produce various degrees of deformations and dimensional accuracies. For the process's in-process real-time monitoring, certain geometric indices were used. For a better understanding of the reported anomaly, the percentage area deviation and three additional geometric indices linked to the overhanging surface edge—the DAOSEi, the ODi, and the P-DAOSEi—were taken into consideration. According to the data, the beginning of deformation was accurately recorded in all of the instances studied. Additionally, using a statistical technique and the Shewhart Control Chart for Individual Measurements, it was possible to determine precisely when a process deviates from its expected behaviour. The information from a 2D/3D study of the photogrammetric reconstruction of each sample was then used to confirm these findings. The geometric indices taken into account in the study were computed after this analysis was helpful for a 3D examination of the manufactured walls, allowing the discovery of the most crucial places. This comparison showed that there was a fair overlap for all the indices taken into account, for each scanning angle and wall thickness concerned. The applied monitoring approach, which was characterized by high resolution and a high field of view, was able to detect the occurrences of geometric distortions, which were mostly focused on the overhanging surface, according to all of the reported results. These findings show that it is possible to detect geometric distortions using this technology, which is typically used to identify volumetric defects (such as lack of fusion and key-hole porosity) during the manufacturing process, while still taking full advantage of all the benefits associated with less labor-intensive image processing steps. Additionally, compared to the literature review, the actual sensor/lens combo was able to achieve a resolution of 26 μm/pixel on a FOV of around 160 × 105 mm. This made it possible to maintain a very high resolution while monitoring the whole operating area. Further research will be done to expand the applicability of this method to other crucial aspects and fully use the large information content the HR-OT photos give.

3.3 Development of innovative solutions for the thermal monitoring

Moving on to the field of thermal monitoring, an in-depth study was carried out in collaboration with the ENEA (Italian National Agency for New Technologies, Energy and Sustainable Economic Development) Research Centre in Brindisi, aimed at implementing a thermal monitoring methodology on the L-PBF machine (used at the Politecnico di Bari) in order to investigate defects such as local overheating, thus geometrical distortions in the final part, and lack of melting by monitoring the temperature profile over the whole slice area. We are therefore once again in the field of exploring the process signature 'slice' and

identifying the above-mentioned defects. These relationships, as can be seen in Figure 61, are challenging in the scientific literature due to the limitations of the thermal monitoring systems already commercialized and the difficulties involved in extracting quantitative information related to the thermal history of a component manufactured using the L-PBF process.

The work was structured as follows. During the first step of the work, the main parameters of the L-PBF process and the geometry of the different parts to be manufactured were defined. In particular, the focus of this work was the fabrication of 'thin walls', the thermal behaviour of which was studied by varying two geometric parameters: thickness and inclination with respect to the building axis. The aim was to analyze the stability of the process during the manufacture of thin-walled products; a stability that becomes increasingly critical as the inclination and height of construction increase. Therefore, the thermograms corresponding to each slice and the average temperature of the individual walls as the construction height changes were analyzed.

Subsequently, an optimal set-up was prepared for the realization of the monitoring system. In particular, thermographic monitoring was realized using an IR thermocamera, supplied by ENEA, with an optimal configuration. Specifically, an off-axis configuration was adopted, with an appropriate angle of inclination of the IR camera with respect to the building platform, capable of monitoring the whole slice during the process itself.

In addition, immediately after the thermographic data were collected, they were analyzed in the MATLAB environment to study the different behaviour of the different walls constructed and to identify thermal parameters that could be indicative of the efficiency of the process and the quality of the print. Finally, micro-tomographic scans of the manufactured products were conducted at the ENEA centre in order to identify defects and possible correlations with the thermographic data obtained during monitoring.

3.3.1 Thermal monitoring and Optical tomography system and methodology

As detailed in section 3.1, one of the commercial thermal monitoring systems used to identify possible defects in the printing process is the IR camera. In this work, thermal monitoring of the L-PBF process was carried out using a cooled thermal imaging camera with a mid-infrared sensor (1.5-5.1 μm) placed outside the printer. A FLIR SC7200 thermal imaging camera was used for the thermographic measurements (please see more information in Figure 97), designed to take thermal and radiometric measurements with the highest sensitivity, precision and speed. It is a cooled detector with Focal Plane Array, high

acquisition speed and 20 mK NETD (temperature difference equivalent to background noise). The image acquisition frequency is programmable up to 190 Hz, the resolution is 320x256 pixels (14 bit) and it is possible to choose between different sub-windowing modes to reduce the size of the saved files. The integration time is adjustable in 1 μs increments. This parameter is directly related to the detector energy and thus the temperature. Depending on the filter chosen, different wavelengths and temperatures up to a maximum value of 2500 °C can be evaluated. The choice of lens to be used is closely linked to the wavelength to be evaluated and this also influences the temperature range to which the sensor is sensitive. The management of the camera settings is entrusted to the Altair proprietary software, through which the camera is remotely controlled. Thanks to its advanced technology, this software offers the possibility to observe recordings in real-time and archive them at a rate of 200 frames per second. In combination with other software components such as Cirrus, this software can be used to manage the shooting specifications and post-processing of images that can be exported in different formats (ascii, bmp, tiff, jpeg, avi). As the camera could not be placed inside the building chamber, it was placed externally in an off-axis configuration (please see Figure 98). Due to the small opening of the machine to observe the process, it was necessary to find the right tilt of the thermal imaging camera in order to capture the region of interest. The camera was installed at an angle of 26.7° to the building platform and at a distance of 0.4 m from it. In addition, the machine's protective window had to be replaced with one that was transparent to radiation in the 1-5 μm range. Therefore, a 7 mm thick sapphire slide was fitted; a solution that is particularly suitable for this type of application, as this material is transparent to infrared radiation over a wide wavelength range.

Detector Materials	InSb
Number or Pixels	320x256 pixels
Spectral Response	1.5-5.1µm
Sub Windowing	160x128 pixels 64x120 pixels 64x8 pixels
Frame Rate	up to 190 Hz Full Frame 11kHz@64x8
Image Capture	Snapshot Integrate then Read mode (ITR)
Pitch	30µm x 30µm
NETD	<25mk @ 25°C
Aperture	3

Figure 97. FLIR SC7200 technical specifications

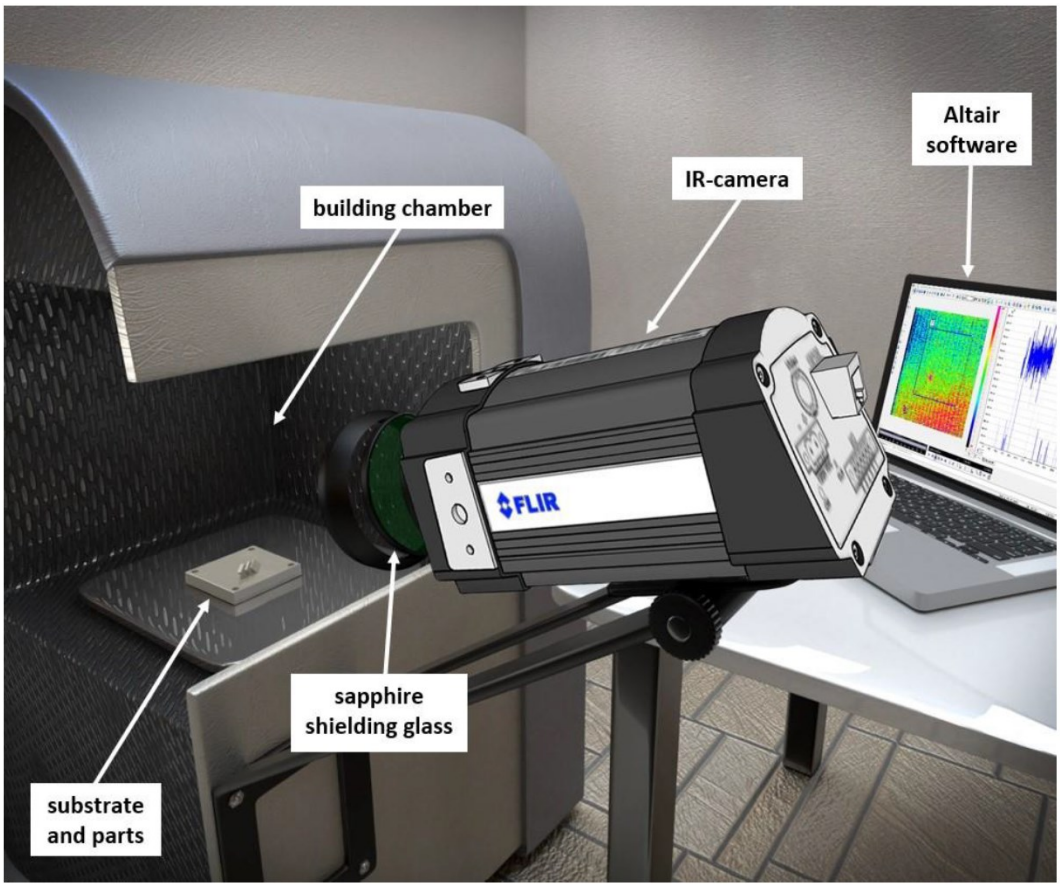

Figure 98. Overall configuration of the experimental setup used during the experiment: MWIR thermal imaging camera with 25mm lens, sapphire protective glass, desktop for image acquisition using Altair software, building chamber in N_2 atmosphere, building platform with manufactured samples.

In order to carry out the thermographic measurements at high temperatures, the FLIR manufacturer calibrated the camera to extend the temperature measuring range from the 5÷300 °C interval to the 300÷1500 °C and 1500÷2500 °C intervals. A lens with a focal length of 25 mm and an f/2 aperture was fitted, giving a field of view of 22° (HFOV) and 17° (VFOV). Known horizontal and vertical viewing angles; known as the distance of the lens from the target zone, an Instantaneous Field of View (IFOV) pixel size of approximately 0.5 mm/pixel was identified. In addition, the camera is equipped with two filters (F0122 and F0123) to enhance the wavelength ranges of interest for the investigation. The IFOV is the camera's ability to give resolution to details; it, therefore, defines the smallest object that can be reproduced on the thermal image, depending on the measurement distance. Finally, the temperature range was decided, which, as the melting temperature of steel is around 1450 °C, was chosen as 300÷1500 °C and filter F0123 was used.

The acquisition parameters that were adjusted are:

a) acquisition frequency (in Hz)
b) integration time (in μs)
c) acquisition interval (in s)

The image acquisition frequency must be chosen appropriately in order to find a compromise between the amount of information required and the file size to be managed. Given the extreme speed characterizing the L-PBF process, a frame rate of 100 Hz was chosen for the current monitoring.

The integration time (IT) is directly related to the energy incident on the sensor and, therefore, the temperature reached in the process. The integration time represents the exposure time of the sensor to radiation and must therefore be inversely proportional to the radiant energy. Even having selected a temperature range of 300÷1500 °C, the actual temperature range that can be evaluated depends on IT. In this case, an integration time of 50 μs was defined.

The chosen calibration curve allows the camera to correctly evaluate temperatures in the range of 260÷1100 °C. This choice was dictated by the impossibility of detecting the melt temperature of the powder due to the size of the melt pool (approx. 100 μm), which is smaller than the size of a single pixel. As there is no trigger compatible with the thermal camera, it was necessary to choose a suitable acquisition interval considering both the number of layers acquired and the saving time of each video. As a high sampling rate is required, the save time cannot be too high as it would increase the number of unrecorded layers. Therefore, an acquisition interval of 60 seconds (6000 frames) was defined followed by a pause of 120 seconds to allow the video to be saved before the next one begins.

The thermographic data were saved with the extension .ptw, and then converted into .asc format using Altair and subsequently into .m format with a special algorithm implemented in the Matlab environment.

During the post-processing of the images, the radiometric parameters were defined; in particular, the emissivity value to be associated with the material was defined. This material-dependent calibration of the thermal imaging camera can also be defined after acquisitions because the sensor operates with digital levels (DL, Digital Level) of the signal.

All bodies with a temperature above absolute zero (0 K) emit thermal radiation due to the thermal vibrations of atomic particles. The emissivity (ε) represents the ability of an object to emit thermal energy in the infrared range and varies depending on the surface properties, the material and, for some materials, also the temperature of the measurement object. It can take a value between 0 (when all energy is reflected) and 1 (black body, when all energy is absorbed). In reality, the two extremes are purely theoretical, as only grey bodies, i.e. materials with intermediate emissivity values, are found in nature. Determining the emissivity of a material is crucial for measuring the surface temperature of an object undergoing thermographic testing. If a higher emissivity value is set in the thermal imaging camera than the actual value, the detected temperature will be lower than the actual temperature, provided that the object temperature is higher than the ambient temperature. This error is all the more pronounced the lower the value of the emissivity. For the elaborations in this work, it was decided to further investigate the literature in order to take into account the variation of emissivity with temperature and to decide whether the emissivity of the substrate or the filler material (powder) should be taken into account. According to [127], it is practically impossible to obtain real temperature values even with accurate calibration. The aim of the present work is to carry out a qualitative comparison of the thermal behaviour of different manufactured samples. Since the emissivity of the AISI 316L material is not known for the entire temperature range considered, it was necessary to assume an approximate value for the temperature range, spectral range, viewing angle and surface condition (substrate or powder).

After a careful evaluation of the scientific literature, it was decided to use the emissivity of the material in the powder state obtained experimentally in [128] for the temperature calculation. In fact, the thermal imaging camera frames the powder bed that is selectively melted by the laser. The emissivity is highly variable with temperature and the latter varies greatly during the process. Furthermore, the pixel size is larger than the size of the melt pool, making it difficult to capture temperatures close to the melting temperature of the material. Therefore, the emissivity value referred to as room temperature ($\varepsilon = 0.35$) was chosen, and

the assumption was made to assume this value to be constant as the temperature varies; an assumption that was found in most of the works researched in the literature [103,127].
Finally, the radiation reflected by the surroundings on the surface is neglected, as well as all the spectral characteristics of all optical elements and the camera detector because they are difficult to determine. With these settings, a surface temperature distribution similar to that found in articles found in the literature was noted [116].
As mentioned above, in order to find a correlation between thermographic data and wall morphology, micro-tomographic scans were performed at the ENEA Research Centre.
Computational Micro-Tomography (micro-CT) is now considered a powerful inspection tool for non-destructive analysis that, by exploiting the penetrating properties of X-rays, is able to provide information not only on the surface of the sample but also on its internal structure. The CT system used in this work is a GE Phoenix 'nanotom s' at the ENEA Research Centre in Brindisi (please see Figure 52). This instrument is equipped with a high-performance nano-focus X-ray tube (180 kV / 15 W) with a tungsten (W) or molybdenum (Mo) transmission target. The nanotom is also equipped with a 5-megapixel CMOS detector (Hammamatsu Photonic) consisting of 2300x2300 pixels; each pixel has a size of 50 x 50 μm2 and a dynamic range of 12 bits. Before starting X-ray scanning, the acquisition parameters of the CT system were set appropriately, in order to obtain 2D X-ray images with a good signal-to-noise ratio (SNR), and consequently an adequate quality in tomographic reconstruction. As the sample has a high absorption level, the tungsten target was used with an acceleration voltage of 150KV and a tube current of 70 μA. The resolution of the tomography depends on the ratio of the detector pixel size (50μm) to the set magnification. The magnification is calculated as the ratio between the distance of the detector from the target focus (FDD) and the focus-object distance (FOD). Both the FDD and FOD distances can be set by moving the detector or sample holder along the direction of the optical axis of the X-ray tube. In this case, the selected magnification was 2.5 times, resulting in a resolution of 20 μm. In addition, to improve the SNR value associated with each projection, each recorded X-ray was the average of three acquisitions. For each scan, 1800 radiographs were recorded, with an angular step of 0.20°; the total acquisition time was approximately 2h.

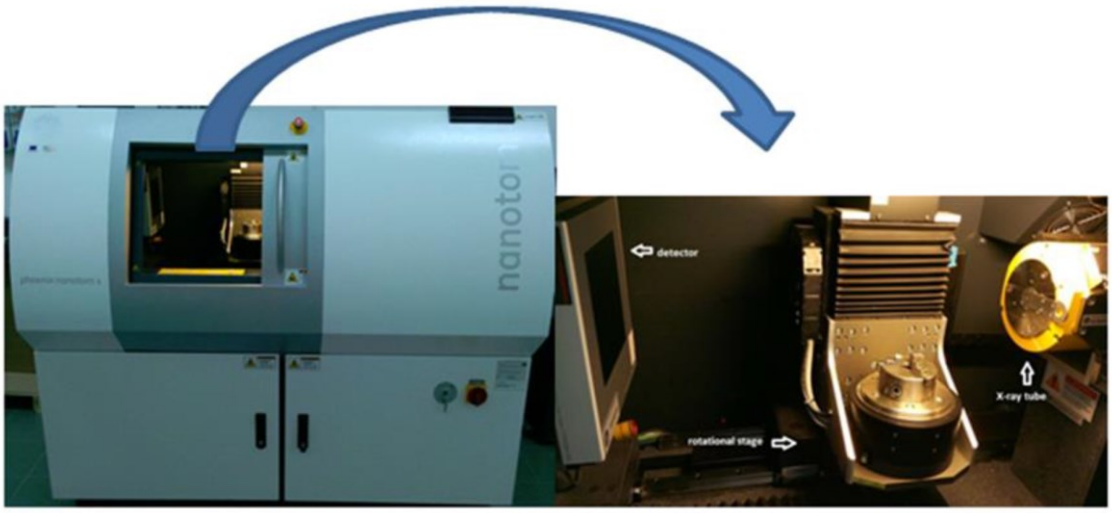

Figure 99. GE phoenix nanotom s

3.3.2 Case study: Laser-powder bed fusion of straight and inclined thin walls

A case study very similar to the one presented in section 3.2.2 was carried out in this work. Specifically, thin walls were manufactured by varying two geometric parameters: wall thickness and inclination with respect to the building direction (z-axis). The other two wall dimensions are height equal to 10 mm and length equal to 30 mm. They were manufactured using the same equipment and powders mentioned in section 3.2.2.

In particular, two different print batches were produced:

- straight walls;
- walls inclined at 45° to the axis of construction.

Table 15 shows the full experimental plan.

Table 15. Experimental plan: factors and relative levels used for the fabrication of the specimens.

Factor	**Unit**	**Factor Levels**				
		T1	T2	T3	S1	S2
Wall thickness	mm	1	3	5	-	-
Building angle	°	-	-	-	0	45

Both batches were manufactured with process parameters optimized in previous work and presented in Table 16. The scanning strategy was also the same for all fabricated thin walls. Specifically, a scanning strategy was adopted that included scanning of the 'contour' followed by scanning of the 'core'; in particular, the random island scanning strategy, a scanning strategy patented by Concept Laser, was chosen for scanning the core. As mentioned in section 3.2.2, this is a scanning strategy that allows thermal stresses to be reduced; in fact, it involves dividing the core into smaller islands to create a grid. These islands, measuring 5x5 mm (a size optimized in the literature), are scanned in a random order

with parallel vector tracks oriented at 45° to the main directions of the individual island. Finally, in the next layer, the islands are shifted by 1 mm in both x- and y-directions. Figure 100 shows the thin walls produced in this way.

Table 16. Set of optimized process parameters used for experimental tests.

Parameter	Notation	Unit	Value	
			Contour	Core
Laser power	P	W	100	100
Scanning speed	v	mm/s	180	200
Laser spot diameter	d	µm	200	200
Layer thickness	l_t	µm	30	30
Hatch distance	h_d	µm	-	140

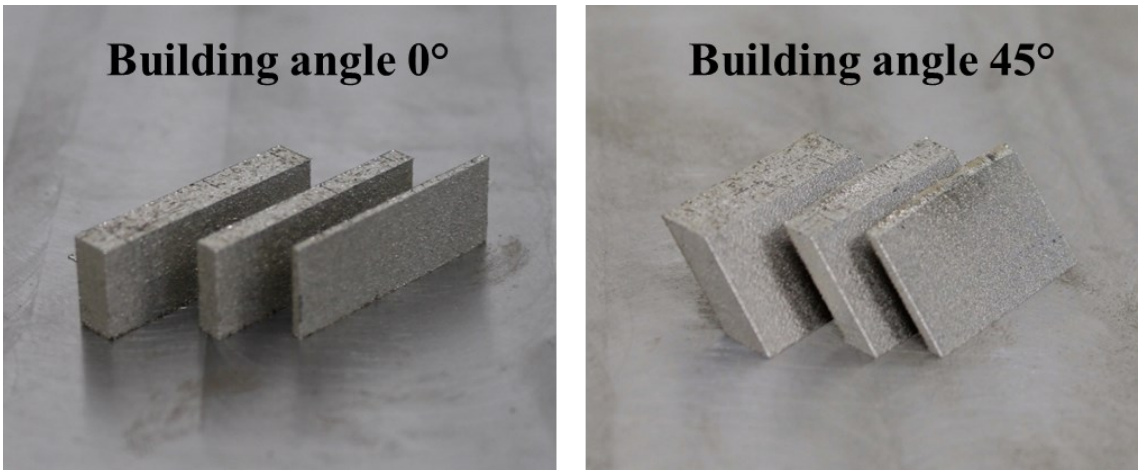

Figure 100. Images of the thin walls fabricated using the L-PBF process.

3.3.3 Data analysis methodology

In this section, an analysis of the data and methodologies developed to characterize the case study identified and any critical printing issues arising through an off-axis thermal monitoring system is discussed in more detail. In particular, two different thermographic monitoring was realized, as straight walls and 45° inclined walls were manufactured in two separate printing jobs. Each sample is realized as an overlay of 335 layers. Although the building height is identical, the duration of the printing process for the inclined walls (3h 31m) is longer than the time taken for the straight walls (2h 54m). This difference is due to the larger slice size of the inclined walls, a difference which will be explained below.

Therefore, several algorithms were implemented in MATLAB to process all the thermographic data collected during the L-PBF process. These routines on MATLAB, built ad hoc for this study, are standardized to be used also for other thermographic processing of the L-PBF process, with the aim of defining a unique way of processing in-situ and in-process thermographic data. In particular, it was possible to analyze:

- the temperature profile over the whole slice area;

- the maximum temperature reached;
- the geometric distortions.

All routines, which will be described below, allow:

- obtain results as a function of time (as well as with respect to the number of frames acquired) by entering the acquisition frequency;
- adapt the graphs to the actual deposition (instead of considering the entire acquisition);
- modify the graphs according to the temperature calibration interval.
- modify the graphs according to the geometries to be analyzed;

3.3.3.1 Temperature evolution over time

The trends and temperature distributions obtained during printing are the first steps in the study of thermographic data. Temperature readings are necessary to understand how melting and solidification phenomena occur during the process.

The first routine implemented allows the maximum temperature trend of the image to be evaluated over time. The temperature distribution obtained has only qualitative value but is of fundamental importance in understanding the thermal behaviour of the observed area. In fact, only by analyzing this graph is it possible to identify the two characteristic phases of the process: contour scanning and core scanning. In particular, the process begins with the scanning of the perimeter of the three walls and continues, after a pause of about 200 frames (2 seconds), with the scanning of the core of each wall according to the strategy indicated. In Figure 101, three zones can be identified:

A. contouring phase of the three walls;
B. idle phase (approx. 200 frames);
C. core-scanning phase of the three walls.

This graph, however, does not allow the thermal cycle of each wall to be evaluated separately due to the overlapping of the temperature fields between the three samples made during both the contour and core scanning phases. Indeed, in Figure 102a, one can see the presence of a portion of the contour of one wall being cooled (green circle) and simultaneously a portion of the contour of another wall being melted by the laser beam (blue circle). Similarly, Figure 102b shows the presence of an island of the core of one wall being cooled (green circle) and at the same time, an island of the core being fused by the laser beam (blue circle).

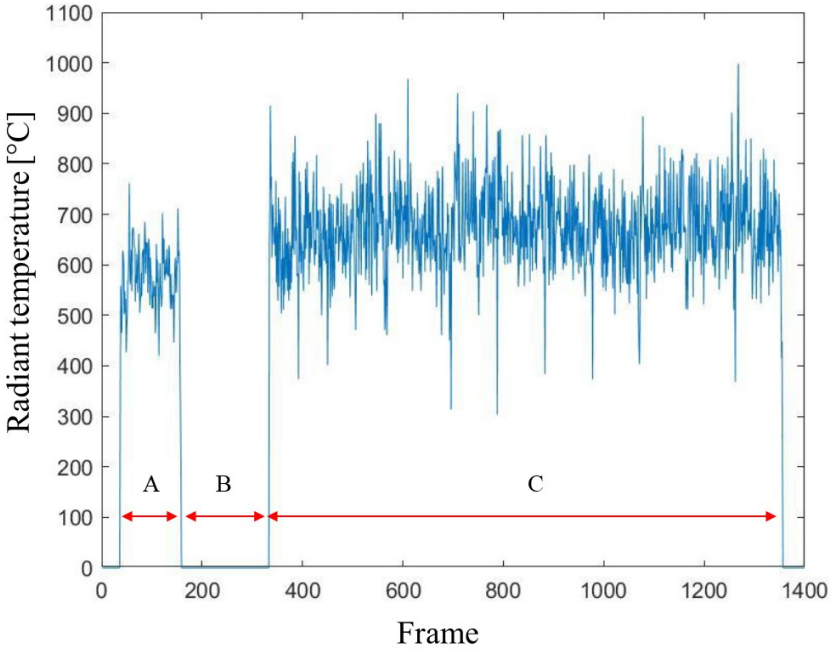

Figure 101. Example of maximum temperature distribution corresponding to a generic straight thin wall layer.

Figure 102. (a) Overlapping thermal cycles between two different thin walls during the contouring phase; (b) overlapping thermal cycles between two core islands belonging to the same thin wall. In both cases, the area being cooled is shown in green; the area affected by the laser beam is shown in blue.

In addition, an algorithm was implemented to calculate the duration of the individual phases (A, B and C) to also facilitate the implementation of other routines, which will be explained below. The algorithm takes advantage of the instants of laser inactivity, and thus the instants when the average temperature of the image is zero, to sequence the different phases of the process. The slice duration is understood as the duration of scanning the whole layer. Comparing the printing process of straight walls with that of inclined walls, a longer duration of the individual steps can be seen for the latter due to the increase in the size of the slice (since the parameter held constant is the wall thickness, which in the case of inclined walls is a dimension outside the 2D plane). Table 17 summarizes the average durations of the individual phases expressed in frames and seconds, considering the image acquisition frequency of 100 Hz.

Table 17. Duration of characteristic process steps.

Factor	Straight thin walls			Inclined thin walls		
	contour	core	slice	contour	core	slice
Frame	119	1033	1330	126	1569	1864
Seconds	1.19	10.33	13.30	1.26	15.69	18.64

Subsequently, another algorithm was implemented to identify which layers the processed images correspond to. As there was no trigger compatible with the thermal imaging camera, it was not possible to acquire all layers. Furthermore, since an acquisition time interval of 60 sec was set, the recorded videos did not always contain the same number of observed layers. Therefore, it was necessary to extrapolate the log file of the laser machine, which contains all the information regarding the process parameters and exposure times of each slice. An example of the exposure information of a generic slice is shown below (Figure 103).

```
Oxygen concentration 0.60[%] at : 18.11.2021 3:48:51 PM
part "Piastra media_3" building level : 0.03 - 0.06 [mm]
part "Piastra piccola_1" building level : 0.03 - 0.06 [mm]
part "Piastra Grande_5" building level : 0.03 - 0.06 [mm]
                exposed at : 18.11.2021 3:49:20 PM
              exposed file : D:\PROGRAM FILES\CONCEPTLASER\bia\job_0005_000_wfc.bia
slice 5 finished at : 18.11.2021 3:49:22 PM
```

Figure 103. Extract of a machine log file indicating the end time of a generic slice.

By extrapolating the scan end time of each slice contained in the log file and comparing it with the exposure end time of each slice derived from the algorithm calculating the slice duration, it was possible to identify which layer a generic camera video corresponds to.

3.3.3.2 Image processing

Another routine was implemented to analyze the thermogram corresponding to a generic frame. Through this visualization, it is possible to observe how the laser beam, and the resulting surface thermal signature, move as the frames change. The possibility of observing the temperature distribution in a generic frame was fundamental in order to understand what could be monitored according to the resolution of the thermal camera. In fact, as shown in Figure 104, the resolution of the camera does not allow the evaluation of parameters related to the melt pool because the latter is much smaller than the size of a single pixel. The diameter of the laser spot used is about 200 µm, but the size of a single pixel is about 500 µm/side of the pixel. This makes precise monitoring of the melt pool impossible and makes it impossible to read the melt temperature in each individual pixel. It is important to point out that not knowing the exact emissivity value does not allow the 'true' temperature to be read. Therefore, the following graphs represent the radiant temperature, which is not the true temperature. The "radiant" temperature range, for which the camera is calibrated, is 260÷1100 °C, as is the colour scale range of the following images.

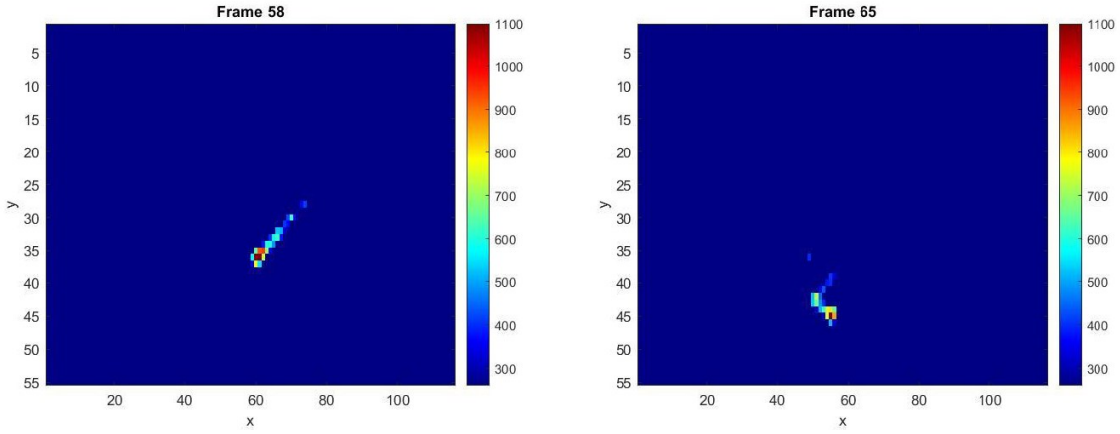

Figure 104. Thermograms of two frames of the same layer.

In addition, since the frame-by-frame visualization does not provide an overall view of the process, and in particular, of the maximum temperatures reached at each point of the scan, it was decided to implement another algorithm that would allow a "global" thermogram to be obtained, representing in a single image the maximum temperature reached in each pixel of the slice, as evident in Figure 105a. The image obtained, however, has a background noise due to the presence of 'spatters', a defect typical of an L-PBF process. The presence of such defects makes the interpretation of the following images more difficult and is useless for the analyses that have been carried out. Therefore, in order to make the image cleaner, masks were applied, with the rectangular geometry corresponding to each individual wall, which replace the pixels corresponding to the ' spatters' with zero-value pixels. Specifically, the poly2mask() function creates a binary matrix, consisting of 0 and 1, within which a closed 2D polygon can be drawn. All points that fall within the polygon take value 1; all those outside the polygon take value 0. Three rectangular masks were thus created, one for each wall, whose geometry was defined by entering the coordinates of the 4 vertices in the XY plane. In order to define the geometry of the masks more precisely and to obtain a better visual rendering, the resolution of the image was increased by dividing the area of one pixel into four smaller pixels. By doing so, the size of each pixel becomes 250 μm/side, as in Figure 105b. After increasing the image resolution, it is necessary to distribute the temperature among the newly created pixels. Using the interp2() function allows a linear interpolation between the pixels without altering the maximum and minimum values within each image. Finally, with the use of the bsxfun() function, the individual masks were multiplied with the matrix containing the maximum temperature at each point, resulting in Figure 105c. Thus, the thermographic maps of the maximum temperature reached at each pixel of the image, which can also be represented by the addition of the isotherms in Figure 105d, provide a complete and visual picture of the geometry and temperature distribution of

the realized slice, as is evident in the following images.

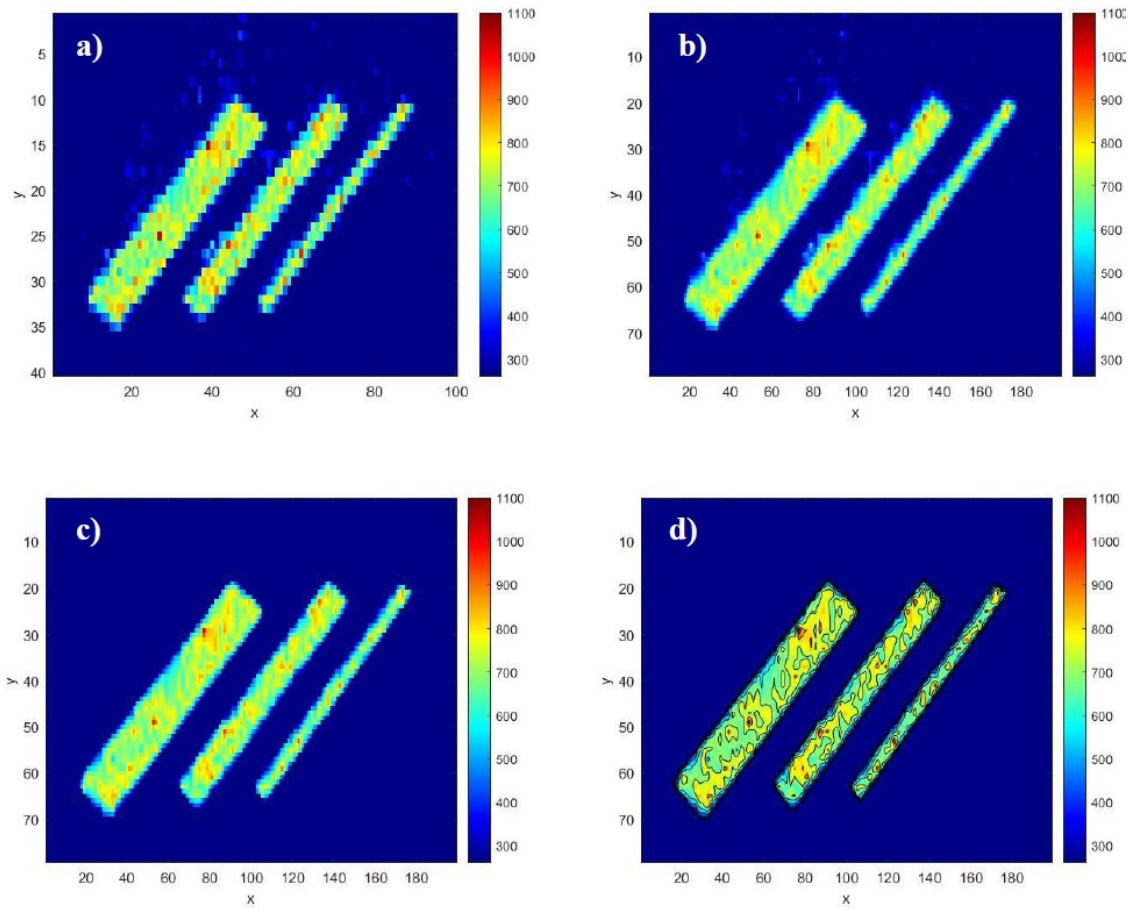

Figure 105. (a) thermogram with a resolution of 100x40 pixels; (b) thermogram with a resolution of 200x80 pixels; (c) removal of sputters by application of masks; (d) application of isotherms in a generic thermogram of a slice of straight thin walls.

However, while the slice of each straight wall assumes a fixed position in the XY plane, the slice of the inclined walls moves more and more towards quadrant II as the building height increases. Therefore, it was necessary to define a method to remove spatters in an automated manner on all analyzed layers. The basic idea is to express the coordinates of the vertices of the individual walls with respect to an easily identifiable characteristic point P in each layer, such as the rightmost vertex of the 1 mm thickness wall. However, while the slice of each straight wall assumes a fixed position in the XY plane, the slice of the inclined walls moves more and more towards quadrant II as the building height increases. Therefore, it was necessary to define a method to remove spatters in an automated manner on all analyzed layers. The basic idea is to express the coordinates of the vertices of the individual walls with respect to an easily identifiable characteristic point P in each layer, such as the rightmost vertex of the 1 mm thickness wall. This point, shown in Figures 65a and 65b, was chosen as a reference as it is less subject to the noise generated by splashes. Since splashes reach very low temperatures on average, the P point is identified by analyzing all those points that

exceed a threshold temperature set at 600 °C. Of these points, point P is identified as the one with the highest x-axis value and the highest temperature value. In this way, a fully automated algorithm was implemented to identify this point and move the masks following the vertical development of the walls. In fact, note how, in the transition from Figure 106a to Figure 106b, point P moved towards smaller values of the x-axis and larger values of the y-axis (the displacement vector $\overline{PP'}$ is shown in red).

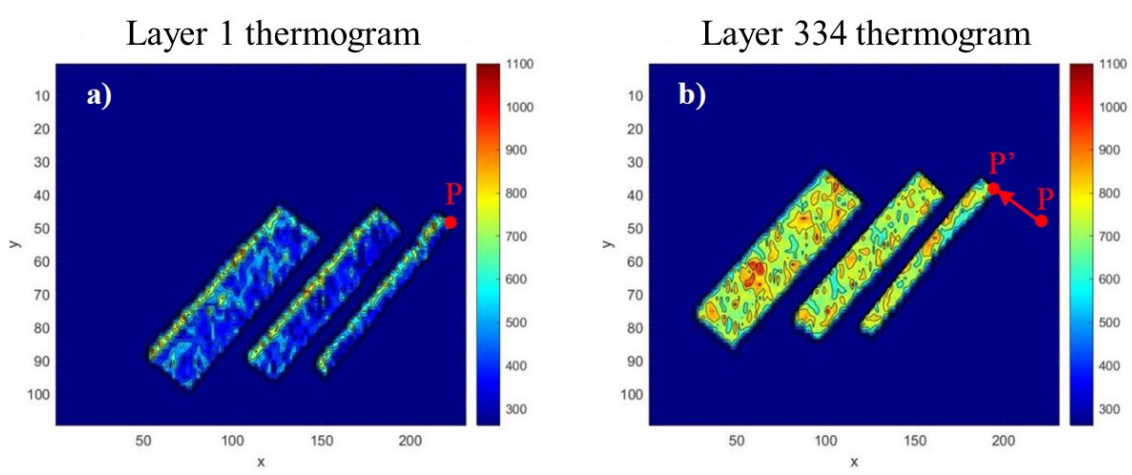

Figure 106. (a) First layer of inclined thin walls; (b) last layer of inclined thin walls.

The increase in image resolution has the only purpose of making the thermograms clearer and thus improving their visual rendering. It is important to point out that the graphs presented in the following paragraphs are constructed with reference to the original image resolution in order to preserve the temperatures extrapolated from the thermal camera.

3.3.4 Thermal analysis of straight thin walls

After processing the thermogram images representing the maximum temperature value reached in each pixel, the individual straight walls of 5-, 3- and 1-mm thickness were analyzed thermally. It was considered appropriate to study the contouring and scanning phases of the core separately. To do this, the algorithm discussed in Section 3.3.3.1 was used to process the thermograms for the two phases separately. This algorithm allows the contouring and core scanning phases to be sequenced.

3.3.4.1 Thermal analysis of the contour scanning phase of straight thin walls

Given the initial and final instants of the slice perimeter scan, it is possible to define the corresponding maximum temperature distribution in the XY plane as depicted in Figure 107.

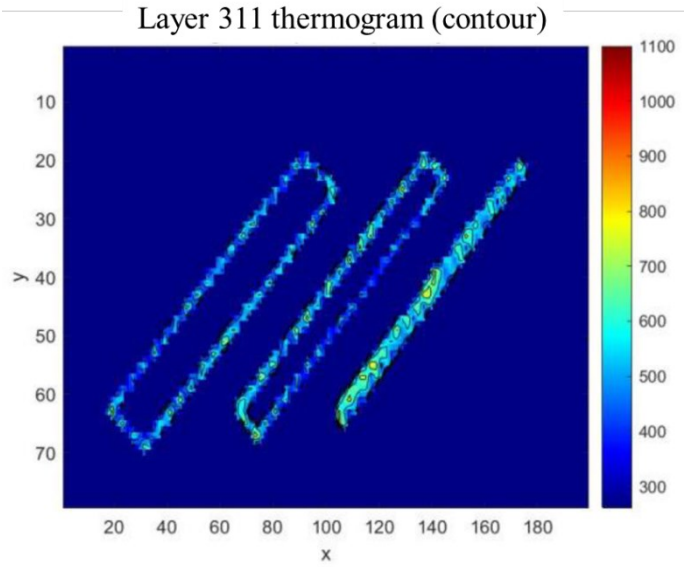

Figure 107. Thermogram of a generic straight thin wall layer.

Note how, for the 1 mm thick wall, the core area is particularly difficult to detect with this representation. Also, note how the IR camera is unable to detect temperatures higher than the melting temperature (~1450 °C) at any point in the scan. This limitation can be attributed to the low resolution of the sensor, i.e. the high pixel size in relation to the size of the melt pool, and to the calibration curve of the chamber, which correctly detects temperatures in the 260÷1100 °C range. In particular, it was interesting to note how the temperature distribution varies as the layers vary and whether there are differences between walls of different thicknesses. In this regard, the average maximum temperature as the layers vary was evaluated. This parameter calculates, for a given layer and a given wall, the average value of the maximum temperatures that are reached at all points of the wall under analysis. It is important to point out that only those pixels with a non-zero temperature are taken into account in the calculation of this parameter. Comparing the results of the three straight walls summarized in Figure 108, a substantial temperature increase can be seen for the wall with a thickness of 1 mm compared to those with a greater thickness. This behaviour can be explained by the extreme proximity between the two larger sides of the perimeter, which results in a greater accumulation of heat than the other two walls. In this sense, an analogy can be made with what has been reported in a work in the literature [129], which points out that an increase in the hatch distance leads to a reduction in the signal (temperature) picked up by the sensor. On the other hand, analyzing the contour of the 3- and 5-mm walls does not reveal any significant differences because the thickness is sufficiently large not to generate a heat build-up. In fact, analyzing Figure 107, it can be seen that the two largest sides of the contour are well-spaced in both cases.

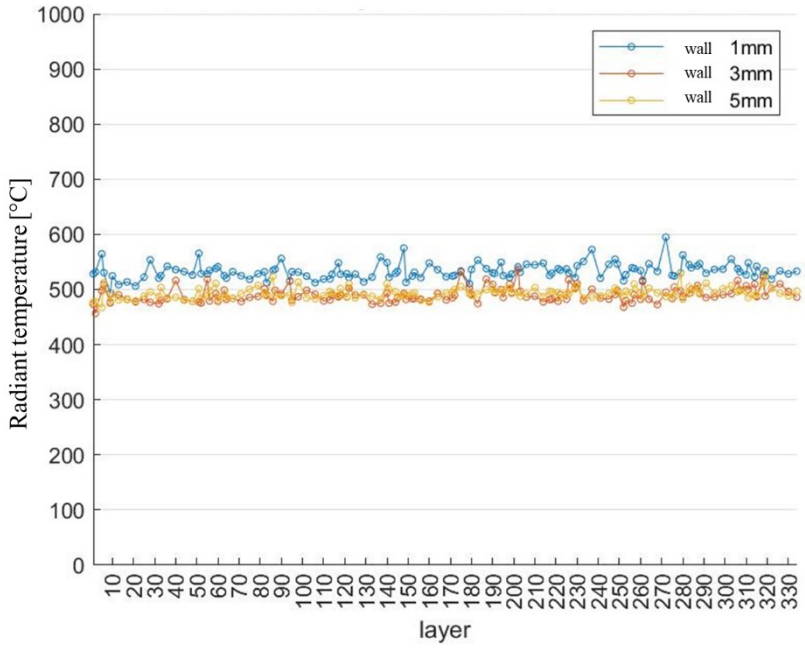

Figure 108. Average maximum temperature of the contouring phase for the three straight thin walls.

3.3.4.2 Thermal analysis of the core scanning phase of straight thin walls

Given the initial and final instants of the core scanning phase, it is possible to evaluate the temperature distribution between the different samples made and at varying build heights. An example of temperature distribution at a generic build height is shown in Figure 109.

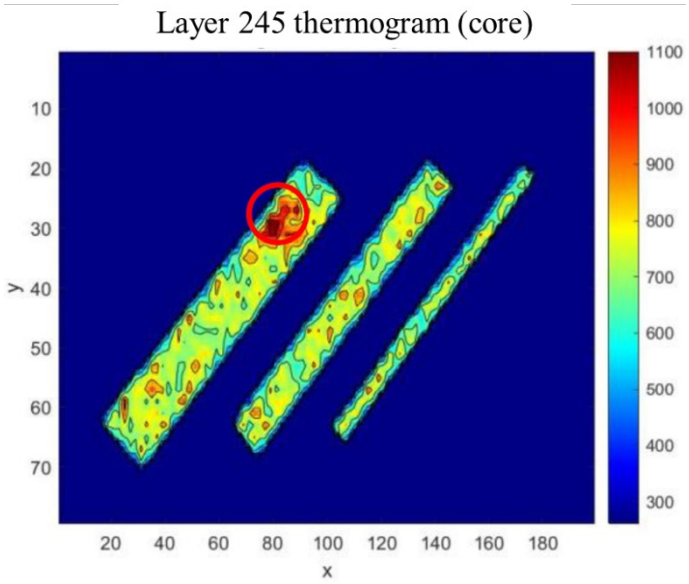

Figure 109. Thermogram of a generic straight thin wall layer. An area with heat accumulation is shown in red.

In particular, it can be seen that there are areas with higher temperatures than the rest of the surface. This behaviour may be due to the presence of defects, such as lack of fusion and porosity, in the underlying layers. Several studies associate the process with unidirectional heat dissipation towards the lower layers, such as the one reported in [116]. The presence of

a lack of fusion and voids, and thus of unmelted powder, hinders the dissipation of heat to the lower layers due to the reduced thermal conductivity compared to the melted and then solidified material. Also for the core analysis, it is possible, as already seen in the contour analysis, to analyze the average maximum temperature for all three specimens, as shown in Figure 110. Analyzing this parameter for all the samples realized, it can be seen that there is an initial peak followed by a stabilization of the signal. The first slice is made in the absence of powder by remelting the exposure slice layers to ensure adequate adhesion of the parts to be made on the build plate. Therefore, due to the high thermal conductivity of the substrate, the temperatures recorded for the first slice are low. With the exception of the first layer, the temperature increase recorded for the first 10 layers, which can also be seen by comparing Figure 111a and Figure 111b, is related to the 150% increase in the thickness of the powder bed.

This increase is realized in order to have a better distribution of the powder bed at the beginning of the process until a certain regime is reached for the recoating phase. The modified parameter is the 'dose step'. In fact, according to the study conducted by Pavlov et al. [129], the temperature increase with the thickness of the powder layer is the result of the energy balance between powder melting and heat loss in the substrate (or a previously fabricated layer). Bearing in mind that the thermal conductivity coefficient of a powder bed is 20 times lower than that of the melt, the average temperature increases with the thickness of the powder bed [129]. The reduced thermal conductivity of the powder is attributable to the gaps between the powder particles, which hinder heat transfer. Thus, increasing the thickness of the powder bed creates a heat build-up that is difficult to dissipate to the lower layers.

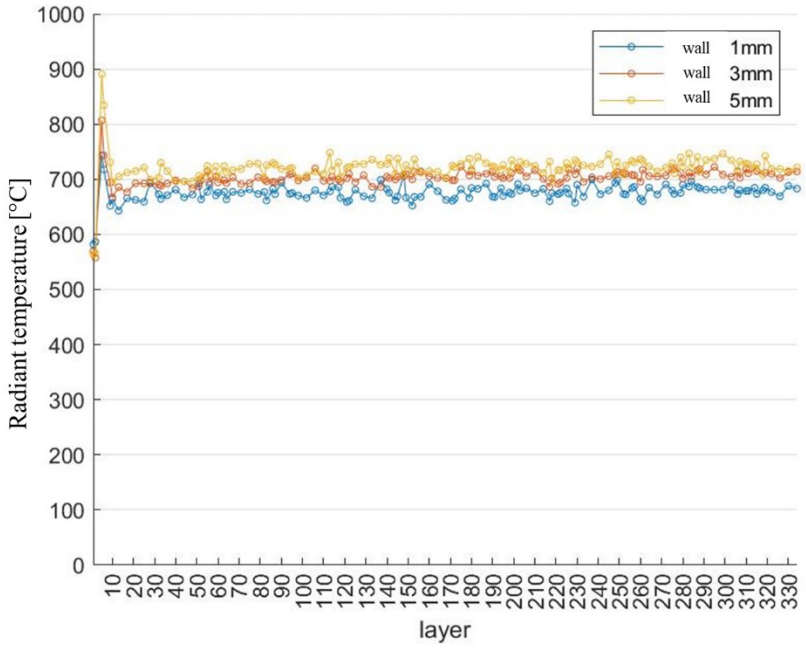

Figure 110. Average maximum temperature of the core phase for the three straight thin walls

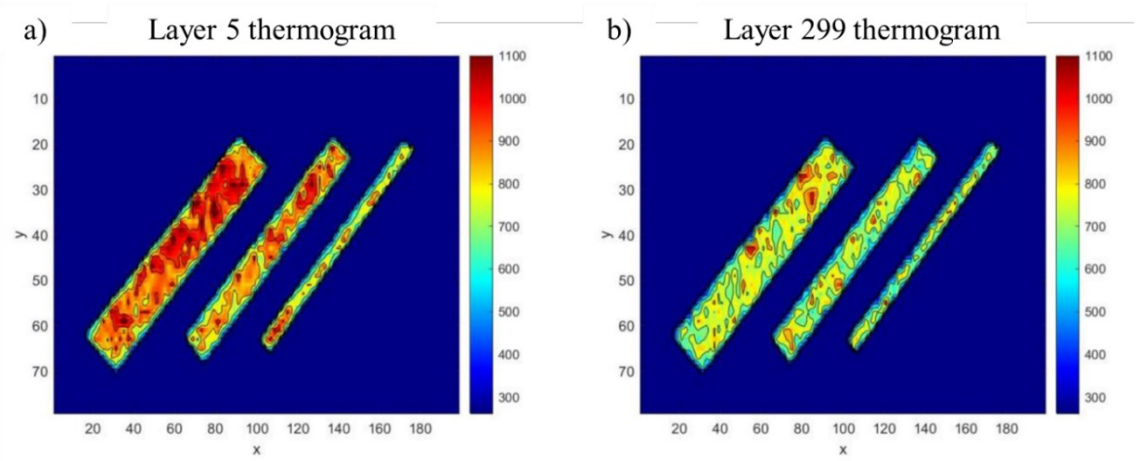

Figure 111. (a) Thermogram with dose step increase of 150 %; (b) thermogram without layer thickness increase.

Furthermore, it can be seen that as the thickness of the wall increases, there is an increase in the temperature perceived by the thermal imaging camera.

This behaviour is linked to the presence of larger and larger islands as the thickness of the wall increases, and thus to a greater accumulation of heat. In Figure 112, the scanning islands are represented by red squares and vectors inclined at 45°, while the sample sections are represented by black rectangles with a more pronounced thickness. Although the islands of the adopted scanning strategy have a size of 5x5 mm^2, only a portion of them is affectively scanned because the thicknesses of the realized samples have values less than or at most equal to the characteristic island size. Therefore, the portion of the island that falls within the core increases as the wall thickness increases. This temperature increase is most visible in the first 10 layers, also observing the temperature distribution in Figure 111a and becomes

less evident in the subsequent layers.

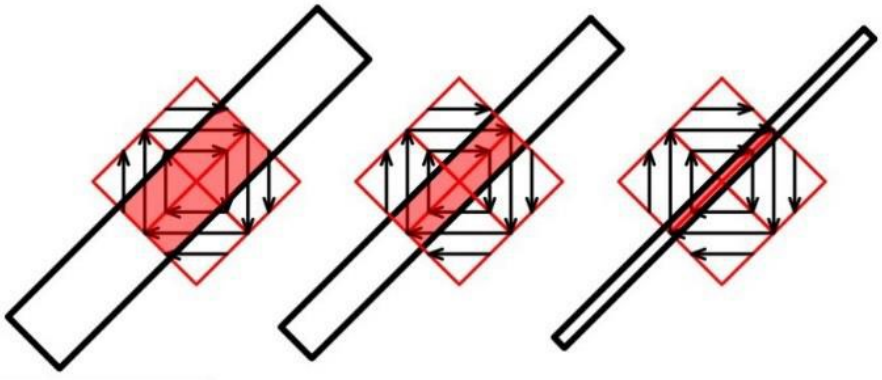

Figure 112. Schematic representation of the actual island portion scanned for the three thin walls under investigation.

3.3.4.3 Analysis of 3D thermograms of straight thin walls

In order to gain an overview of the temperature profile over the whole slice area as the construction height varies, three-dimensional thermograms were produced by superimposing two-dimensional heat maps. This makes it possible to better understand the vertical development of the manufactured samples and to identify, in 3D space, the presence of overheated zones. From Figure 113, referring to the colour bar, it can be seen that the contour of the individual thin walls has lower temperatures than the inner core area. The theoretical volume of the individual walls is delimited by black segments and no geometric distortions were found for the samples shown below. Due to the high pixel size of the thermal imaging camera, no correspondence between superheated areas and porosity could be found; the latter were analyzed with the micro-tomographic analysis instrumentation shown in a later section.

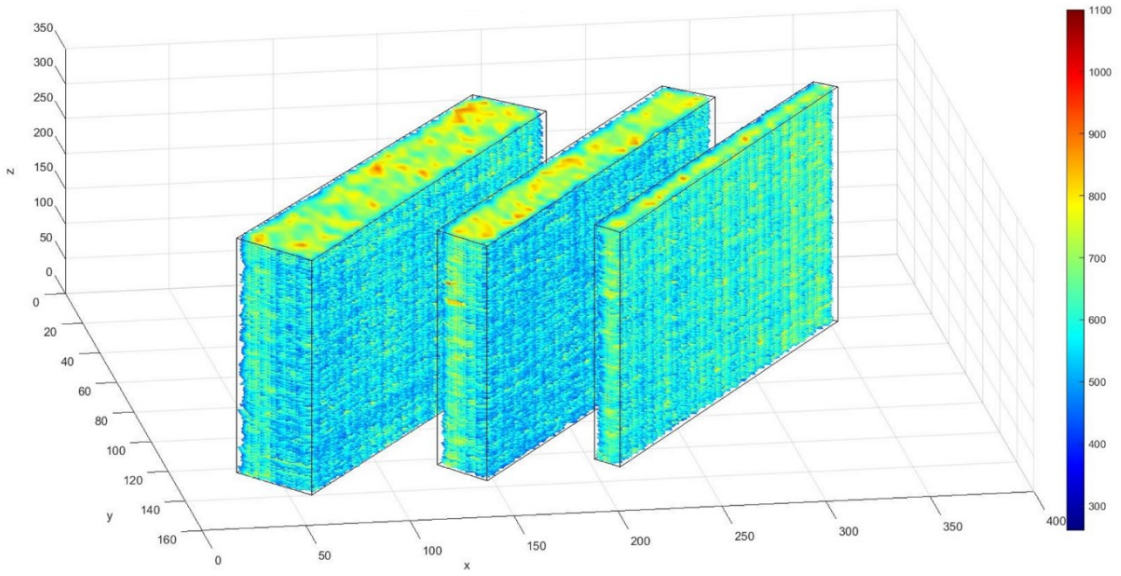

Figure 113. 3D thermograms of straight thin walls.

3.3.5 Thermal analysis of inclined thin walls

As with the straight thin walls, the surface temperature distributions were obtained for the inclined walls and both the contouring and core scanning phases were analyzed. In addition, given the non-perpendicular development of the building plane, the two major sides characterizing the three realized specimens were analyzed separately.

3.3.5.1 Thermal analysis of the contour scanning phase of inclined thin walls

Given the initial and final instants of the slice perimeter scan, it is possible to identify the maximum temperature distribution in the XY plane, as depicted in Figure 114.

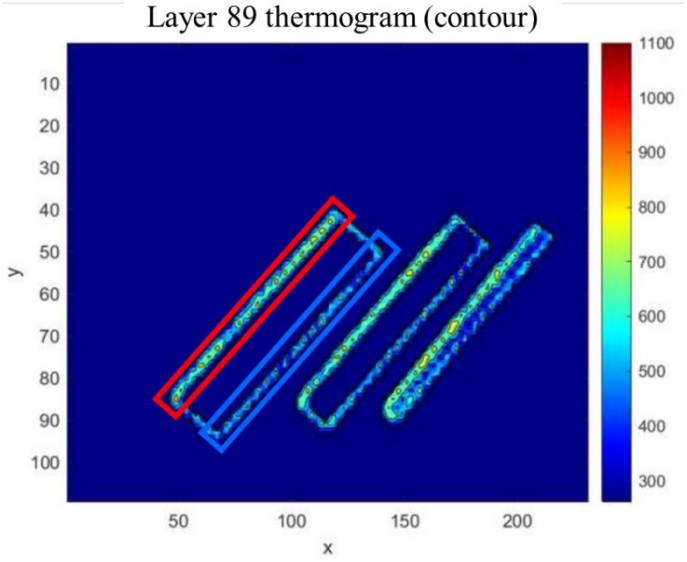

Figure 114. Thermogram of a generic inclined thin wall layer.

In contrast to straight thin walls, in inclined thin walls, one of the two largest sides is always warmer than the other. This observation is repeatable for all three samples of different thicknesses. This behaviour is due to the vertical development of the samples not being perpendicular to the building platform. In fact, the vertical inclination of the walls results in the presence of a protruding side (overhang), which is constantly built up on the material in the powdery state and not on the layers previously melted and then solidified. The material in its powdery state has a much lower thermal conductivity than the same material in its solid state. This justifies the accumulation of heat on the overhanging side compared to the non-overhanging side, respectively indicated in Figure 114 with the colours red and blue. Analyzing how the average maximum temperature varies during the contouring phase (Figure 74), an almost constant trend can be seen because the effect of the overhang side is balanced by the lower temperatures of the non-overhang side. In contrast to the straight walls, no significant differences can be seen between the different sample thicknesses. In fact, the two larger sides of the perimeter are spaced well apart so that there is no heat build-up or measurement error. This result is due to the increased cross-sectional width of the

inclined samples compared to the straight ones.

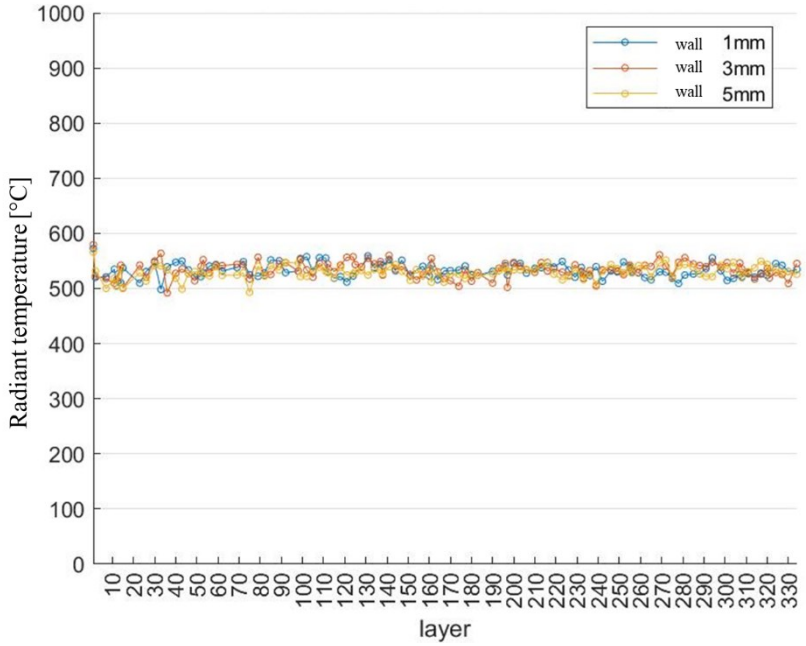

Figure 115. Average maximum temperature of the contouring phase for the three inclined thin walls.

Given the oblique growth of the samples, it is interesting to analyze the two largest sides that form the perimeter of the wall slice separately. In Additive Manufacturing processes, a part of a component that is not supported in the build phase by solidified material or a substrate on the underside is considered a cantilevered structure. In particular, it was possible to see differences from both a thermal and a geometric point of view. The two results are interrelated. In Figure 116a, Figure 116b and Figure 116c, it can be seen that for all three thin-wall thicknesses there are higher temperatures on the overhang section than on the non-overhang section. This behaviour is due, as already mentioned, to the inclined development of the wall, which always results in the presence of an overhang side that is not built on the previously scanned portion of the layer but on the powder. When the laser irradiates areas supported by solids, the rate of heat conduction is high. In contrast, when the laser irradiates areas supported by powder, the heat conduction velocity is much lower than in the area supported by solids. Therefore, the absorbed energy will be much higher when the laser irradiates areas supported by powder [130]. For the 5-mm and 3-mm thick specimens, there is a constant average temperature trend for both sides of the contour, but the same cannot be said for the 1-mm specimen. In fact, for this one there is a decreasing temperature trend for the overhang section (hot side) and an increasing trend for the non-overhang section (cold side). This anomalous behaviour is due to the presence of geometric distortions of increasing magnitude as the construction height increases. In particular, at the overhang side (hot side)

there is a vertical distortion that locally reduces the thickness of the powder bed (as the overhang is hindered by the distortion), and thus temperatures are also reduced (as there is remelting).

In addition to this distortion along the z-axis, there is a distortion in the XY-plane which causes the hot side to deviate from the inspection zone (mask), which is used to assess temperatures and is represented in Figure 117 by a red rectangle. Therefore, the presence of these two phenomena justifies the reduction in the temperature of the hot side.

For the 1 mm non-overhanging side of the wall (cold side), there is no significant vertical distortion but there is a bending in the XY plane (reference system of the wall (please see Figure 118)). This distortion causes part of this side to be built up not on the previous layer but on the powder, thus justifying the increase in temperature. Figure 119 shows a schematic representation of the distortion phenomenon in the XY plane. When the laser scanning path of layer n+1 (indicated by the black line) does not overlap with the previously constructed layer n (indicated in blue) but with the powder, a temperature increase occurs.

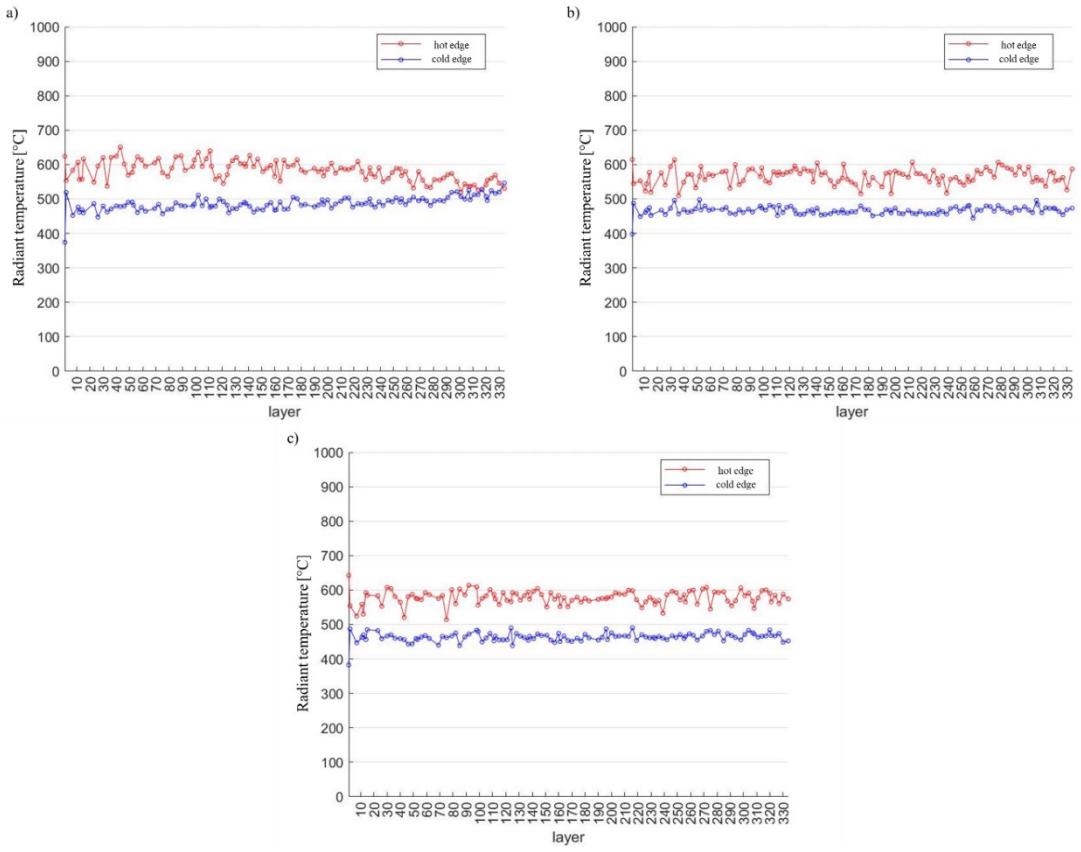

Figure 116. Analysis of the two largest sides of inclined walls with thickness: (a) 1 mm, (b) 3 mm, (c) 5 mm.

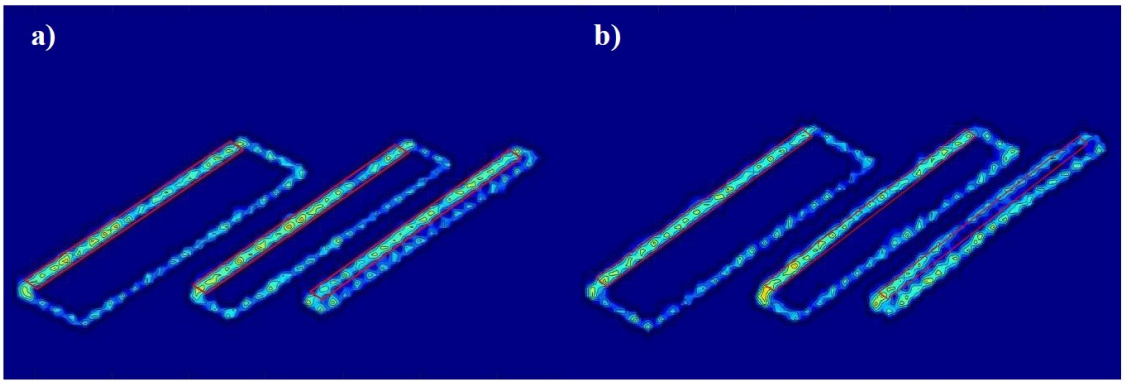

Figure 117. Geometrical configuration of the slice before (a) and after (b) the distortion of the 3- and 1-mm thick walls. Shown in red is the inspection area of the overhang side of each specimen.

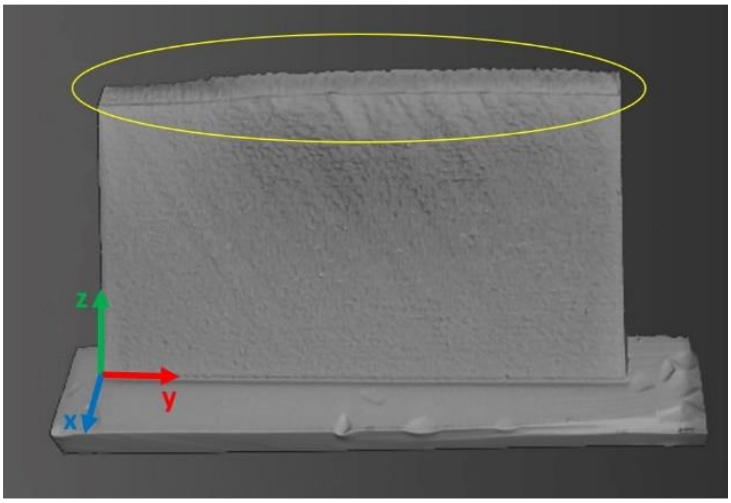

Figure 118. Tomographic scan of the inclined wall with a thickness of 1 mm. The reference system integral to the specimen is shown, and the presence of 3D distortions of the last layers is highlighted in yellow.

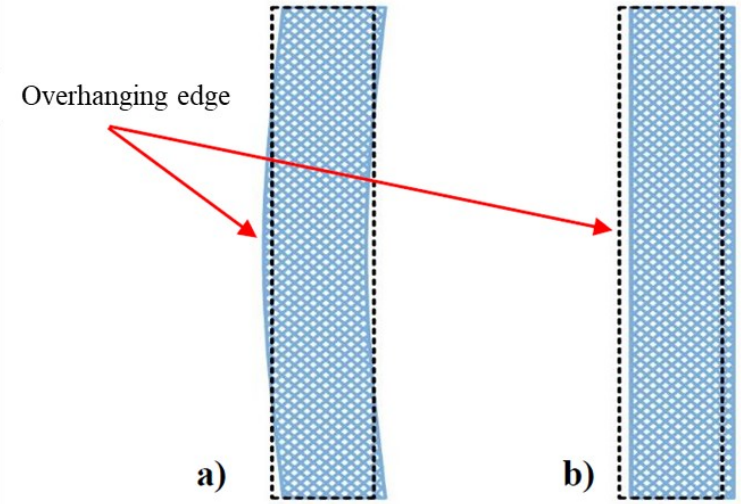

Figure 119. Schematic representation of the distortion phenomenon in the XY plane where the blue represents layer n; the black line represents the laser scanning path of layer n+1. (a) case with distortion; (b) case without distortion.

According to the article [131], thermal stress build-up causes stress and distortion in components during manufacture. Depending on the direction of the thermal stress, different damage modes can develop and lead to part failure. For example, an upwardly deformed component increases the risk of contact with the coating blade and a horizontally deformed component fails to provide a solid base for subsequent deposition.

Analyzing the individual thermograms of the last layers, a distortion of the overhang side is also present for the 3 mm sample, but to a much smaller extent than for the 1 mm sample (comparison of Figure 117a and Figure 117b). For this reason, there is no significant decrease in the temperature of the overhang side in Figure 116b.

3.3.5.2 Thermal analysis of the core scanning phase of inclined thin walls

Given the initial and final instants of the core scanning phase, it is possible to evaluate the surface temperature distribution between the different samples made and as the building height varies. Figure 120 shows the maximum temperature distribution reached in each pixel of a generic layer. As in the case of straight walls, the presence of overheated zones can be seen, which could conceal porosity in the underlying layers as discussed in the previous pages. Voids in the underlying material with non-sintered powder would result in heat retention and thus a localized increase in the IR signature on the surface. Overheated areas are indicated in the figure by red circles.

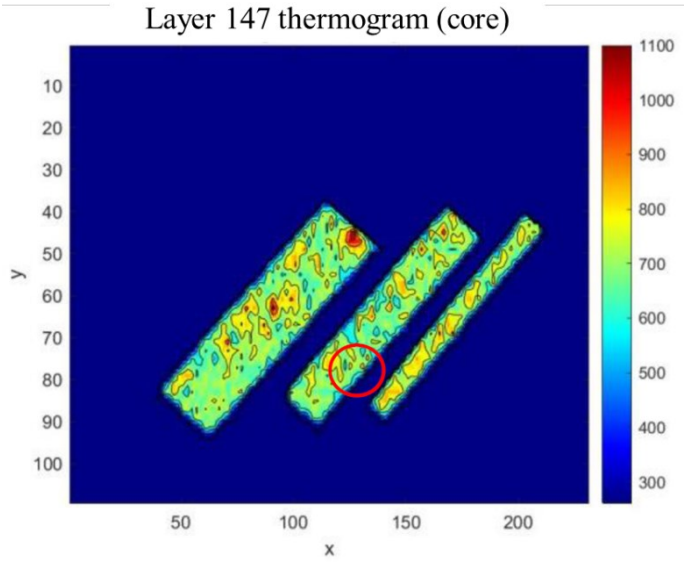

Figure 120. Thermogram of a generic inclined thin wall layer.

Analyzing the average maximum temperature reached in all the recorded layers of the three walls (Figure 121), initial heating due to the increase in the thickness of the powder bed of 150% can be seen, in analogy with the samples with orthogonal development to the base platform.

Also in this case, as with the straight walls, the first slice is characterized by lower temperatures because remelting of the exposure slice alone is carried out without the addition of powder. Subsequently, after the first 10 layers, there is an increasing temperature trend as the building height increases. This behaviour is due to the 'overheating' phenomenon that characterizes overhanging structures. As already mentioned, powdered material has a conductivity that is about an order of magnitude lower than bulk metal, which leads to

localized 'overheating' and a larger melt pool size. In addition, the powder bed cannot adequately support the liquid metal and, due to gravity, capillarity, turbulent fluid flow and other related physical phenomena, the resulting melt pool is more unstable and prone to defects. These problems typically create slag and failure on the downward face and negatively affect surface roughness and dimensional accuracy. To confirm this, Figure 122a and Figure 122b show a cross-section, obtained by nanotomography, of walls inclined at 45° with a thickness of 1 and 3 mm, respectively (the ideal geometry of the section under investigation is shown in red). Such problems are generally solved by the use of supports, i.e. load-bearing structures. The main purpose of supports is to provide heat conduction to the base plate, which acts as a heat sink or mechanically stabilizes the printed part or both.

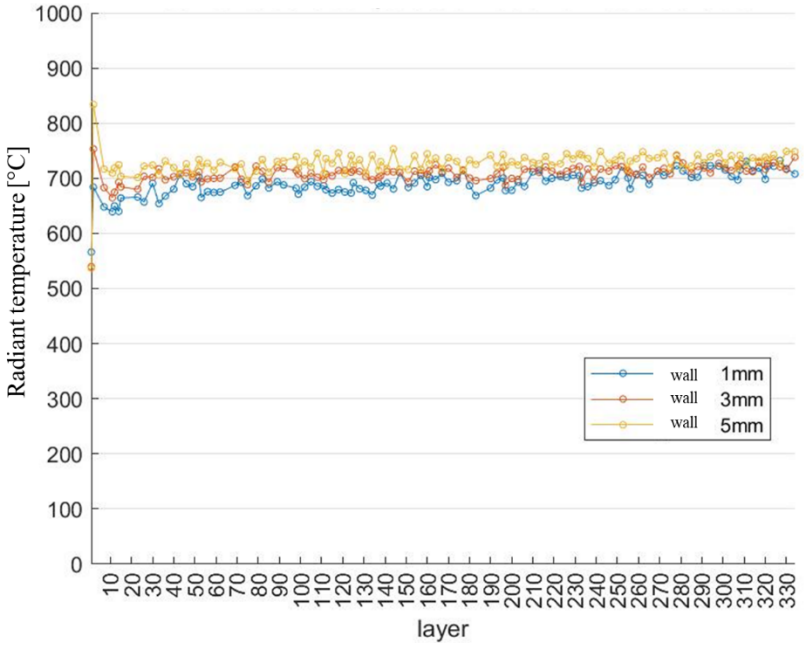

Figure 121. Average maximum temperature of the core phase for the three inclined thin walls.

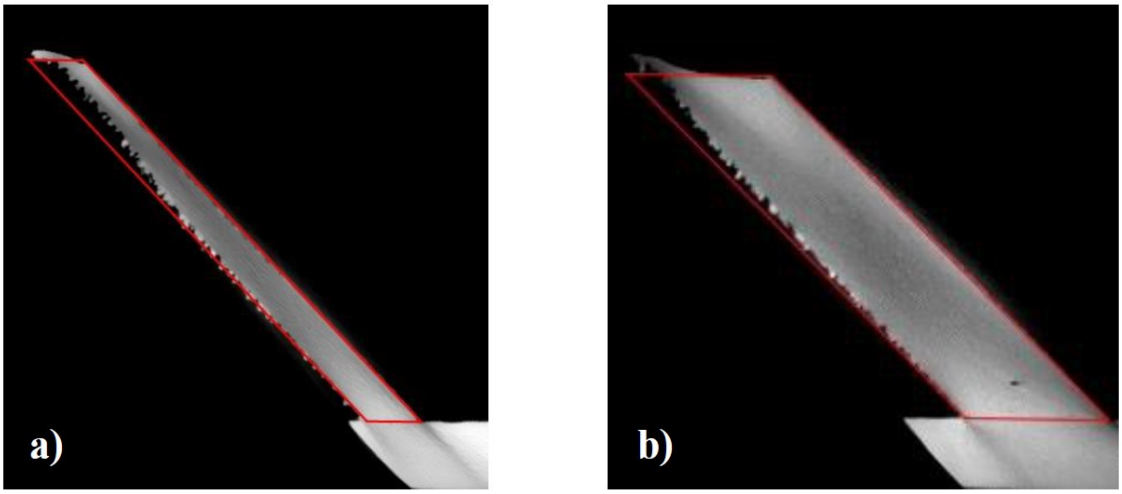

Figure 122. Macrographs obtained by nanotomography: (a) cross-section of the inclined wall 1 mm; (b) cross-section of the inclined wall 3 mm.

3.3.5.3 Analysis of 3D thermograms of inclined thin walls

In order to gain an overview of the surface temperature distribution as the construction height varies, three-dimensional thermograms were produced by superimposing two-dimensional heat maps. This enables a better understanding of the vertical development of the realized samples and the detection of overheated zones in 3D space. The theoretical geometry of the individual walls is delimited by black segments. In particular, it should be noted that the last layers of the 1 mm wall present a deviation from the ideal geometry due to the distortions previously discussed; on the other hand, the 3- and 5-mm thick samples follow the geometry derived from the CAD file quite closely (please see Figure 123).

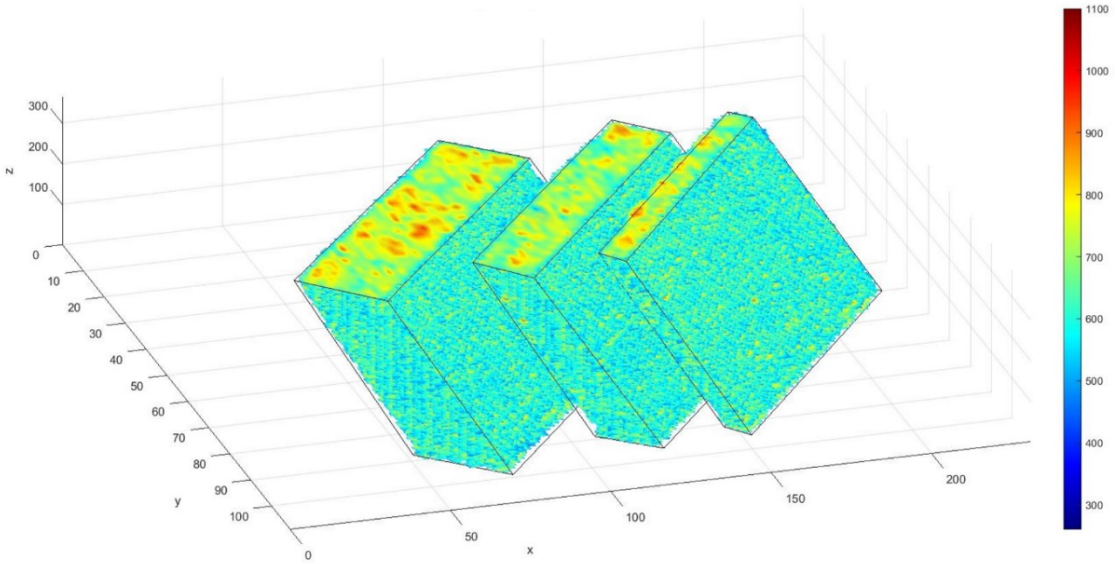

Figure 123. 3D thermograms of inclined thin walls.

3.3.6 Conclusions

This work focused on thermographic monitoring of the L-PBF process. This technique, which is currently undergoing great development in the high-tech and precision industry, is one of the fundamental processes in the field of additive manufacturing, and thanks to its versatility, it allows complex geometries to be obtained during the production phase and allows modifications to be made to a design with ease. To date, it is not yet possible to consider additive technologies as a substitute for conventional ones, but the sectors in which their use is a strong advantage are many, foremost among which are the aerospace and bio-medical sectors. From this study, it was seen how well this technique lends itself to the treatment of latest-generation materials such as single-crystal alloys or how, being an innovative technique, it is still characterized by numerous problems and uncertainties. And it is precisely the optimization of the process that is the focus of the experimentation

conducted here. To this end, a thermographic procedure was implemented for the experimental measurement of temperatures by means of real-time monitoring of the L-PBF process using an IR camera. An optimal set-up for the thermographic acquisition of the process was prepared, considering the various issues involved in controlling a process involving high temperatures and very fast running speeds. Two experimental planes were set up for the realization of 6 specimens at the variation of two geometric parameters: thickness and inclination of the walls. The thermographic data collected during the process were subsequently processed (post-process monitoring) thanks to the implementation of specific algorithms with Matlab software to identify thermal parameters that could be indicative of the efficiency of the process and the quality of the deposition. It was therefore possible to detect the maximum temperature trend, visualize 2D and 3D thermographic maps and analyze the temperature trend of characteristic zones. A key aspect to be emphasized is that all algorithms implemented in Matlab are standardized and can therefore be used for processing thermographic deposition data with different materials, various acquisition parameters and calibration ranges. The data analysis of the conducted experiment revealed a strong influence of the thickness of the samples on the maximum temperatures reached during both the contouring phase and the core scanning phase. Furthermore, an influence of the thickness of the powder bed on the temperatures reached during the process was found, with the same results as in the literature. In particular, an increase in the powder layer leads to an increase in temperatures due to its reduced thermal conductivity compared to the same material in its solid state. The analysis of characteristic areas, such as the overhang side that characterizes walls inclined at 45°, allowed the identification of anomalous situations that are reflected in the geometric defects of the samples. Geometric distortions were found on the inclined walls with thicknesses of 3 and 1 mm caused by the high thermal stress occurring in the overhang zone of the specimens. Finally, the construction of three-dimensional thermograms makes it possible to have an overview of the temperature distribution of the parts and to identify overheated zones that may be a symptom of the presence of defects in the lower layers. In conclusion, the analysis of the average wall temperatures as the construction height varies led to the identification of out-of-control conditions in the inclined walls, thus providing useful information for the laser machine to modify the scanning parameters of the next layer. The thermography information can also be used as a quality control tool to detect imperfections during construction. Thanks to the implementation of the algorithms and the results obtained, this work represents the starting point for future thermographic analyses that may be conducted on the L-PBF machine at the Politecnico di Bari laboratory. In the future, configurations with higher spatial and temporal resolution may

be considered in order to analyze the melt pool and cooling rates that develop during the process.

4. Applications of the developed monitoring systems

Finally, several case studies were examined, in which the different monitoring systems developed and described in the previous chapters were implemented. Several studies will be presented below.

First case study

4.1 Effect of L-DED coating and L-DED + Laser scanning on surface performance of L-PBF stainless steel parts

The following is the paper with the title "**Effect of DED coating and DED + Laser scanning on surface performance of L-PBF stainless steel parts**", published in *Surface & Coatings Technology* in 2022. See section 7 for the publication details.

4.1.1 Aim of the work

This experiment included applying a coating using the Laser-Directed Energy Deposition (L-DED) method on a substrate created using the Laser-Powder Bed Fusion (L-PBF) method. The intent was to circumvent a significant L-PBF process restriction, specifically the manufacture of components with subpar surface quality as a result of unsatisfactory surface roughness or flimsy metallurgical structures. According to a review of the literature, this study appears to be the first to apply, optimize, and monitor a coating to a component made using the L-PBF process utilizing the Laser-Directed Energy Deposition linked to the Laser Scanning (L-DED+LS) technique. To achieve the mechanical improvements of the coating on a sintered component, a preliminary experimental plan was carried out to identify the ideal combinations of process parameters used in the L-DED process. The substrate and the coating powders were both made of AISI 316L stainless steel. Improvements to the component's mechanical properties and surface features were also looked into. In order to monitor the L-DED process and perform LS parameter adjustment in order to overlap the thermal cycles associated with the two treatments, a thermal monitoring system was put into place utilizing a monochromatic IR pyrometer positioned off-axis to the laser beam. In order to monitor the melt pool's shape and confirm the stability of the linked L-DED-LS process, an optical monitoring system in the visible spectrum was put into place utilizing a coaxial CCD camera. Study and comparison of the microstructure and mechanical characteristics of coatings created using the coupled L-DED-LS on L-PBF substrates with those prepared by hot-rolling.

4.1.2 Experimental conditions and procedure

4.1.2.1 Experimental setup for depositions

The experiments for this paper were conducted using a Laser-Directed Energy Deposition (DED) apparatus, which is covered in detail in sections 2.2.1 and 2.2.2. A monochromatic IR pyrometer that was mounted off-axis to the laser beam was also used to track the melt pool's temperature during the procedure. However, an averaged emissivity for the melt pool region is needed for temperature measurements, and in this work, it was considered to be equal to 0.35 for AISI 316L stainless steel [132]. Figure 124 displays the schematic diagram of the entire experimental set-up used in this investigation.

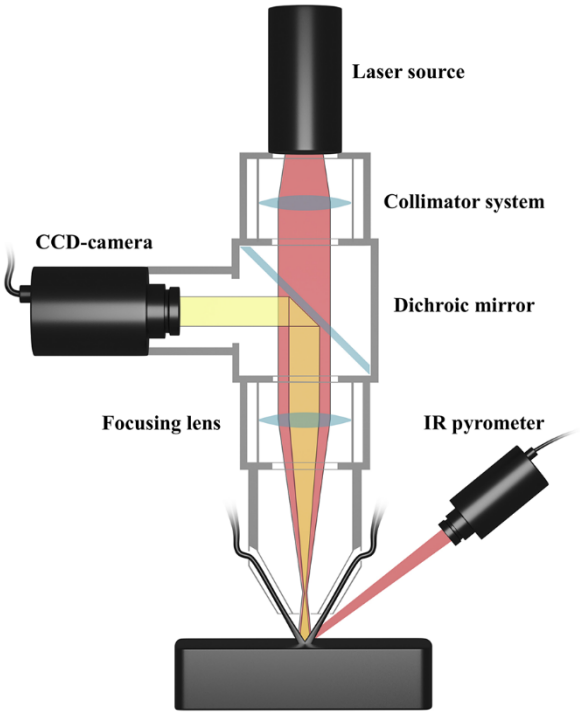

Figure 124. Diagrammatic representation of the Directed Energy Deposition apparatus with an optical and thermal setup for monitoring. CCD camera and a single-color infrared pyrometer.

4.1.2.2 Materials

In this work, it was examined how components made with L-PBF may be improved by employing a highly flexible technique like DED to produce a great coating with regard to its chemical and mechanical qualities. In order to compare the results, two AISI 316L stainless steel substrates with identical dimensions—50 mm in length, 50 mm in width, and 6 mm in thickness—were employed. One was produced utilizing the Laser-Powder Bed Fusion (L-PBF) technology, and the other was a hot-rolled bulk material. The manufacturer confirmed the hot-rolled substrate's chemical make-up, which is displayed in Table 18.

Table 18. The basic material's chemical makeup (weight %).

AISI 316L	Cr	Ni	C	Mn	Si	S	Mo	N	P	O	Cu	Fe

Nominal	16.0-18.0	11.0-13.0	0.03	2.0	0.75	0.010	2.0-3.0	0.10	0.025	0.10	0.50	Balance
Measured	16.7	10.1	0.015	1.0	0.48	0.004	2.04	0.029	0.035	-	-	Balance

Utilizing a selective laser melting device that is thoroughly detailed in section 3.2.2, the L-PBF substrates were produced. The substrates created in this manner are seen in Figure 125. In earlier research, the process parameters were adjusted, with the island scanning approach being employed in particular to lessen residual thermal stresses. According to the research under consideration, the best process parameters were used, producing L-PBF substrates with a relative density better than 99% as determined by the Archimedes technique. The following process parameters are being used: 100W laser power (P_s), 200mm/s scanning speed (v_s), 200µm laser spot diameter (d_s), 30µm layer thickness (l_t), and 140µm hatch distance (h_d). 140µm. No post-treatment has been applied to the substrates.

The chemical composition and microstructure of the metal powder used in the experiments were determined using the most recent GEMINI® technology, the Zeiss Sigma 300 VP Scanning Electron Microscope (SEM), followed by an Energy Dispersive X-ray (EDX) analysis carried out either in a heavily magnified area or at a single point of interest on the sample's surface (see Figure 126). The average composition of the powder was discovered utilizing the outcomes of the EDX microanalysis performed on seven powder samples (see Figure 126).

The chemical make-up of the AISI 316L stainless steel powders used to construct the L-PBF substrate, which were created by Cogne Acciai Speciali S.p.A. using gas atomization, is shown in Table 19. Figure 127 depicts the powder morphology; as can be observed, the particles had a round shape morphology and ranged in size from 15 to 53µm. The D-values, which are parameters that show the percentage of powder particles (10%, 50%, and 90%) that are below the maximum diameter indicated in the corresponding percentage, are also shown in Table 20 along with the distribution of the powder sizes (PSD), which was certified

Applications of the developed monitoring systems

by the manufacturer.

Figure 125. Substrates for laser-powder bed fusion.

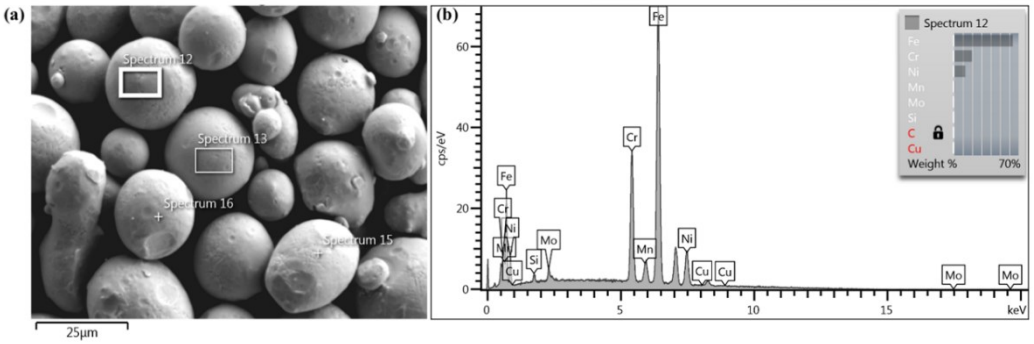

Figure 126. An illustration of an EDX microanalysis performed on a coating powder sample; SEM images of powder particles in (a); chemical species' spectrum distributions (b).

Table 19 The powder's chemical make-up (weight %).

AISI 316 L powder	Cr	Ni	C	Mn	Si	S	Mo	N	P	O	Cu	Fe
Nominal	16.0-18.0	11.0-13.0	0.03	2.0	0.75	0.010	2.0-3.0	0.10	0.025	0.10	0.50	Balance
Measured	17.8	11.4	0.012	1.40	0.45	0.003	2.60	-	0.015	-	-	Balance

Table 20. Particle size distribution (PSD).

PSD	Units	Diameter
Dv(10)	µm	20.803
Dv(50)	µm	35.404
Dv(90)	µm	58.027

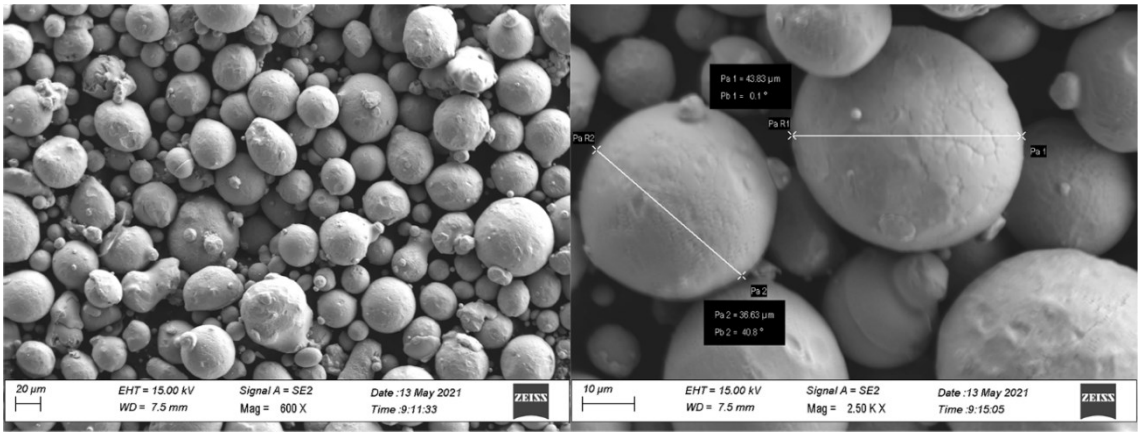

Figure 127. SEM images of the powdered AISI 316L used to make the L-PBF substrates. In the detail, the related dimensions are also mentioned.

The AISI 316L powder, with diameters in the range of 15-45µm (see Figure 128), was employed as a filler material for achieving the coating with the suggested DED treatment. Table 21 describes this powder's chemical makeup. It has a spherical form and was created by LPW South Europe using gas atomization. The manufacturer certified and the particle size distribution (PSD) for this powder was determined using laser diffraction, as shown in Table 22.

Table 21. The powder's chemical make-up (weight %).

AISI 316 L powder	**Cr**	**Ni**	**C**	**Mn**	**Si**	**S**	**Mo**	**N**	**P**	**O**	**Cu**	**Fe**
Nominal	16.0-18.0	11.0-13.0	0.03	2.0	0.75	0.010	2.0-3.0	0.10	0.025	0.10	0.50	Balance
Measured	17.6	12.6	0.02	0.93	0.58	0.004	2.32	0.09	0.009	0.03	0.02	Balance

Table 22. Particle size distribution (PSD) by Laser Diffraction.

PSD	**Units**	**Diameter**
-16 µm	volume %	3
-10 µm	volume %	0
Dv(10)	µm	19
Dv(50)	µm	30
Dv(90)	µm	46

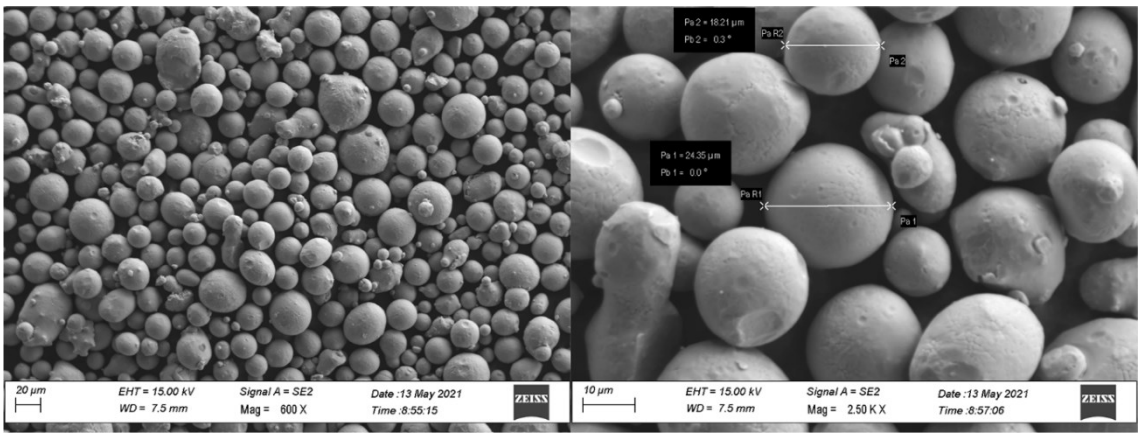

Figure 128. SEM images of the AISI 316L powder used to cover the substrate. In the detail, the related dimensions are also mentioned.

4.1.2.3 Experimental plan

In order to optimize various processing parameters, a series of single-track depositions were first performed on both the hot-rolled substrate and the L-PBF substrate (see Figure 129). To find the ideal process parameters for creating effective coatings, a Taguchi experimental plan was used, which reduced the number of experiments necessary for a full factorial design. An orthogonal L36 array was used to define the experimental design based on the five parameters to be researched and their various levels, which is shown in Table 23.

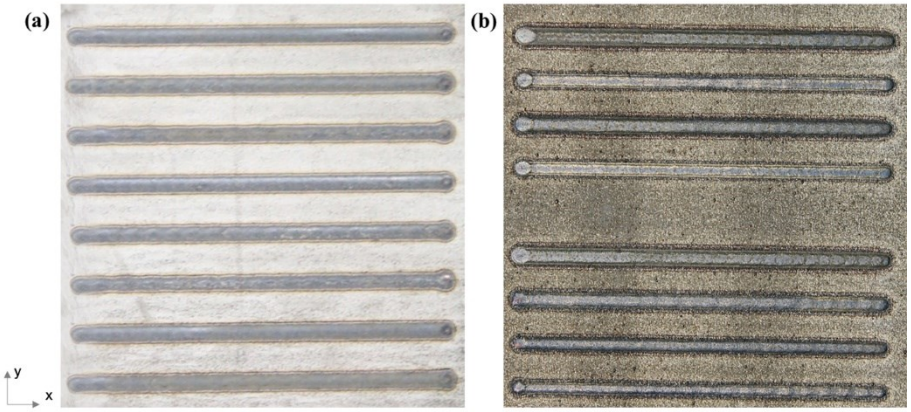

Figure 129. Two illustrations of single-track depositions: (a) on a hot-rolled substrate and (b) on an L-PBF substrate.

Table 23 Levels and parameters for the Taguchi experimental design.

Parameter	Units	Notation	Factor Levels		
			I	II	III
Laser power	W	P	400	600	-
Laser spot diameter	mm	d	1.5	2.0	2.5
Translation speed	mm/min	v	1000	1500	2000
Powder feed rate	g/min	Q	1.5	3.0	-
Carrier gas flow rate	l/min	G	10	15	-

On both L-PBF and hot-rolled substrates, rectangular coatings were created after choosing the proper process parameters. Two coating varieties, nevertheless, were created (see Figure 130):

a) Directed Energy Deposition only (DEDo): with a one-way deposition technique and 60s of dwell time in between every single track, a single layer of coating was formed;
b) Directed Energy Deposition + Laser Scanning (DED+LS): the same as with DEDo, a first coating layer was made, and after that, a laser scan was performed perpendicular to the underlying layer.

Specifically, three distinct DED+LS coatings were developed for each set of process parameters, where the laser power (P), translation speed (v), and laser spot width were changed while maintaining a constant global energy density (Ed =P/vd [133]) during laser scanning (d). As it was shown to be ideal during earlier research, the global energy density utilized during laser scanning was thought to be 70% of that used during DEDo coating [134]. Table 24 displays the process variables utilized to create the coatings.

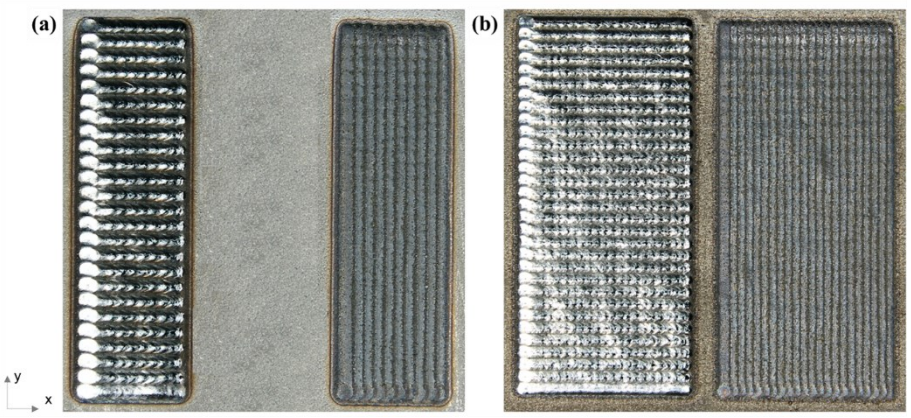

Figure 130. A macrophotography example using DEDo and DED+LS-1c coatings: (a) on a hot-rolled substrate; (b) on a substrate made of L-PBF.

Table 24. Process variables utilized for coatings DEDo and DED+LS.

Coating	P (W)	v (mm/min)	d (mm)	Q (g/min)	G (g/min)
DEDo - 1	600	1000	2.50	3.0	15.0
DEDo - 2	400	1000	2.00	3.0	15.0
DED+LS - 1a	600	1428	2.50	-	15.0
DED+LS - 1b	600	1000	3.60	-	15.0
DED+LS - 1c	420	1000	2.50	-	15.0
DED+LS - 2a	400	1428	2.00	-	15.0
DED+LS - 2b	400	1000	2.90	-	15.0

DED+LS - 2c	400	1250	2.30	-	15.0

A thorough surface analysis of the samples was done in order to look into how the suggested coatings would affect the final sample quality. On samples made before and after coating, the surface examination was done using the Zeiss Sigma 300 VP scanning electron microscope to look at the surface's appearance. With the help of the Taylor-Hobson Surtronic 25, roughness measurements were taken. The wavelengths in the area under inquiry were seen using a 4mm assessment length and a 0.8mm cut-off filter with mathematical averaging (Gaussian) to exclude or decrease unwanted data. With reference to Figure 130, the roughness index (R_a) was calculated by selecting two survey plans, one parallel to the x-axis ($R_{a,x}$) along the scanning direction and the other perpendicular to the x-axis ($R_{a,y}$). Additionally, metallographic samples were created in accordance with the ASTM Standard Test Technique for assessing the microstructure of the materials (E 407) using the conventional method T-29 in order to assess the quality of the coating microstructures. Using the Buehler IsoMet Low-Speed cutting machine, these samples were produced by cutting the specimens transversely to the direction of the laser head's progress. To make the cross-surface section highly reflective and free of blemishes and deformations, a polishing procedure was carried out using a series of #120-#2500 silicon carbide polishing papers and 6mm, 3mm, 1mm, and 0.04mm polishing cloths.

Additionally, the microstructure, shape, and flaws of the samples were described. Etching was done using the Glyceregia reagent (5mL HNO_3, 10mL HCl, 15mL glycerol). These samples were then investigated using an inverted light microscope (Nikon Eclipse MA200) and a scanning electron microscope (Zeiss Sigma 300 VP) for micrographic examination, along with microanalysis using Energy Dispersive X-rays (EDX) in the various zones of interest. In accordance with the ASTM Standard Test Method for Micro Indentation Hardness of Materials (E 384), microhardness was lastly assessed using an HMV-G by Shimadzu micro-Vickers hardness tester with a load of 0.3kgf for 10s.

During the creation of the coatings, a coaxial CCD camera and an off-axis monochromatic IR pyrometer (see Figure 124) were used to monitor the melt pool shape and temperature field, respectively. Section 2.2.1 of the manual has a detailed description of the CCD camera's specs. The pyrometer has a close-up lens with a 0.2–0.4 m focusing range and a 0.1–s detection interval for temperature readings. In order to monitor the morphology of the melt pool while the coatings (DEDo and DED-LS) were being created, videos through the CCD camera were acquired from which frames were extracted and elaborated. The specifications of the image analysis algorithm have been analyzed and described in detail in

a previous section 2.2.3. Due to earlier research, an emissivity of 0.35 was chosen for the monochromatic IR pyrometer, which was mounted off-axis with regard to the laser beam. This permitted measurements of the temperature achieved during the production of the coatings.

4.1.3 Experimental results and analysis

4.1.3.1 Optimization of different processing parameters

First, a number of single-track depositions on both the hot-rolled substrate and the L-PBF substrate were performed in order to optimize the various process parameters and produce a high-quality coating. To accomplish the best possible combination of the manufacturing process's factor levels, the Taguchi L36 plan was applied. According to Taguchi, by minimizing the amount of testing necessary in a full factorial design, this search for the ideal combination of levels typically results in greater quality and lower costs. The chosen process parameters and their corresponding levels are presented in Table 23 for optimization. Figure 131 displays the key geometric characteristics of a typical cross-section of a single deposited track:

1. coating width (w);
2. coating height (hs);
3. penetration depth (hi);
4. wetting angle (α).

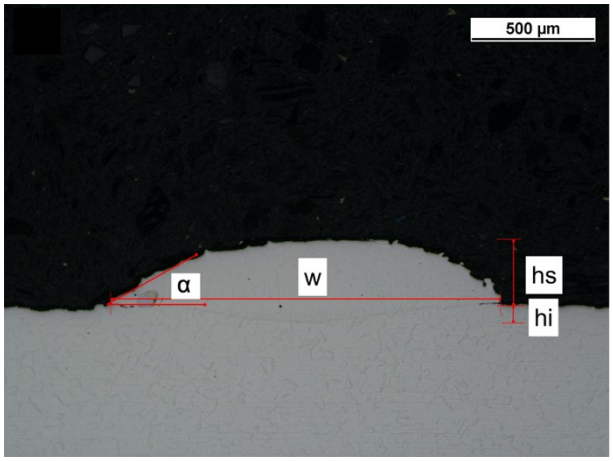

Figure 131. An illustration of the coating cross-macromorphology section showing its primary geometric elements: coating width (w); coating height (hs); penetration depth (hi) and wetting angle (α).

Furthermore, there are primarily three factors that define the operational zone to generate high-quality coated surfaces [133,135,136]: fine microstructure, superior mechanical properties, and homogenous chemical composition:

1. metal-substrate dilution (D = hi/hi+hs) of 10%–30% allows for low, but not zero, which would lead to coating separation from the substrate, melting, and bonding between the coating material and the substrate [136]; however, a dilution of 2%–10% is also acceptable if one wants to minimize mixing between coating material and substrate in order to preserve the chemical properties of the base material [137];
2. an acute wetting angle of fewer than 46 degrees would enable the creation of coatings with superior surface quality and minimal interlayer porosity [136];
3. the aspect ratio (H = w/hi) for the single track should be more than 5 for 30%–50% overlap, which would allow for the creation of coatings with minor waviness and the least amount of interlayer porosity [136].

Two sets of optimum process parameters were found for the following production of ideal coatings based on the three parameters mentioned above. Table 24 displays the coatings created using the appropriate process parameters. Table 25 displays the sets of optimum process parameters together with the corresponding: coating width (w), coating height (hs), penetration depth (hi), wetting angle (α), dilution (D), and aspect ratio (H). Additionally, using the mathematical model developed by Campanelli et al. [138] and the single tracks, geometric calculations were performed to determine the hatch distance (Sx) between neighboring tracks. Table 25 reports the Sx values.

$$S_x = \frac{1}{hs} \times \left(\frac{\left(\frac{w}{2}\right)^2 + hs^2}{2hs} \right)^2 \times \sin^{-1}\left(\frac{2\left(\frac{w}{2}\right)hs}{\left(\frac{w}{2}\right)^2 + hs^2} \right) - \left(\frac{w}{2}\right) \times \left(\frac{\left(\frac{w}{2}\right)^2 - hs^2}{2hs^2} \right) \quad (1)$$

Results are given in Table 25 for both single tracks that were deposited on L-PBF and Hot-Rolled (H-R) substrates. The single deposited tracks and the two coatings—produced using either directed energy deposition alone (DEDo) or directed energy deposition plus laser scanning (DED+LS)—are seen in Figures 129 and 130, respectively.

Table 25. Process parameters that have been optimized and associated geometric studies on the single track.

Sample	P (W)	v (mm/min)	d (mm)	Q (g/min)	G (g/min)	w (mm)	hs (mm)	hi (mm)	α (°)	D (%)	H	Sx
1(H-R)	600	1000	2.50	3.0	15.0	1.538	0.273	0.071	36	20.640	5.634	1.05
2(H-R)	400	1000	2.00	3.0	15.0	1.227	0.163	0.066	21	28.821	7.528	0.83
1(L-PBF)	600	1000	2.50	3.0	15.0	1.788	0.235	0.082	21	25.868	7.609	1.21
2(L-PBF)	400	1000	2.00	3.0	15.0	1.394	0.187	0.080	24	29.963	7.455	0.94

4.1.3.2 Surface appearance and surface roughness

Surface roughness has a significant impact on corrosion and the performance of the final component, as has already been mentioned in earlier research [139]. It is good knowledge that components created using additive manufacturing have rougher surfaces than those created using more conventional methods. Laser surface polishing is one method for reducing surface roughness [140]. Ra value drops as the energy density is reduced, notably when the translation speed is increased, as demonstrated in the study [141]. In this investigation, similar findings were attained. The Taylor-Hobson Surtronic 25 device was used to perform the roughness study, as was previously described. For each coating, five measurements were taken. Table 26 displays the results for roughness in terms of average measurement values and the relative standard deviation.

Table 26. Measured values for the mean and standard deviation of roughness.

Coating	$R_{a,x}$ (µm)	$R_{a,y}$ (µm)
L-PBF	10.20±0.74	9.80±0.82
DEDo - 1	9.00±0.12	5.60±0.71
DEDo - 2	8.30±0.65	5.60±0.78
DED+LS - 1a	2.00±0.35	4.00±0.61
DED+LS - 1b	2.30±0.42	4.30±0.54
DED+LS - 1c	2.10±0.48	4.00±0.68
DED+LS - 2a	2.40±0.22	4.40±0.32
DED+LS - 2b	2.40±0.28	4.20±0.24
DED+LS - 2c	2.30±0.36	4.60±0.41

As can be observed from the data in Table 26, the DEDo coating provides a noticeable improvement in roughness over the L-PBF substrate (10.20 µm and 9.80 µm, respectively), with minimal values of Ra,x and Ra,y reached at 8.30 µm and 5.60 µm, respectively. Additionally, the improvement in roughness that was attained after a laser scanning treatment can be seen; in this instance, the lowest roughness values were 2.1 µm and 4.0 µm, respectively. This improvement is seen in the SEM analysis (Figure 132). Ra values are greater in the L-PBF process than the DED process because more unmolten powder particles may be seen there (Figure 132a). In the review work by Everton et al. [142] it is revealed how unfused powder particles impact the melt pool size, resulting in surface discontinuities. This defect, typical of the L-PBF process, was further examined. Figure 132b demonstrates

that even after DEDo coating, the same unmolten particles are still present in excess, which has a detrimental effect on surface quality. As can be seen in Figure 132c, which represents the DED-LS - 1c coating, the surface melting of the unmolten particles still present downstream of the DEDo-1 coating has clearly improved the Ra values.

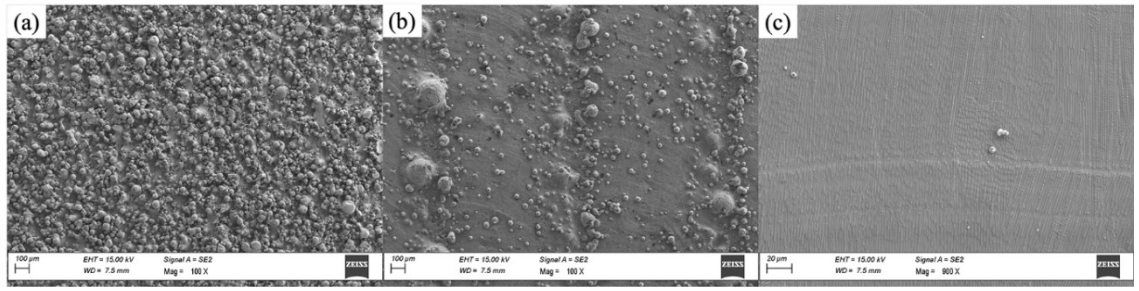

Figure 132. (a) L-PBF substrate; (b) DEDo coating; (c) DED-LS coating are shown in SEM images of the top surface.

4.1.3.3 The coatings' macro- and microstructure characteristics.

With the aid of a Nikon, Eclipse MA200 inverted light microscope, and a Zeiss Sigma 300 VP SEM, the coatings created were metallographically characterized. The hot-rolled substrate and the L-PBF substrate created with one of the two sets of optimal process parameters given in Table 25 are both used for two single-track depositions in Figure 133. Particularly, it can be seen that the coating width obtained during the single deposition on the L-PBF substrate is greater than on the hot-rolled substrate (1(H-R), see Figure 133b), which has caused the choice of a different Sx in the realization of the coating on the two different substrates.

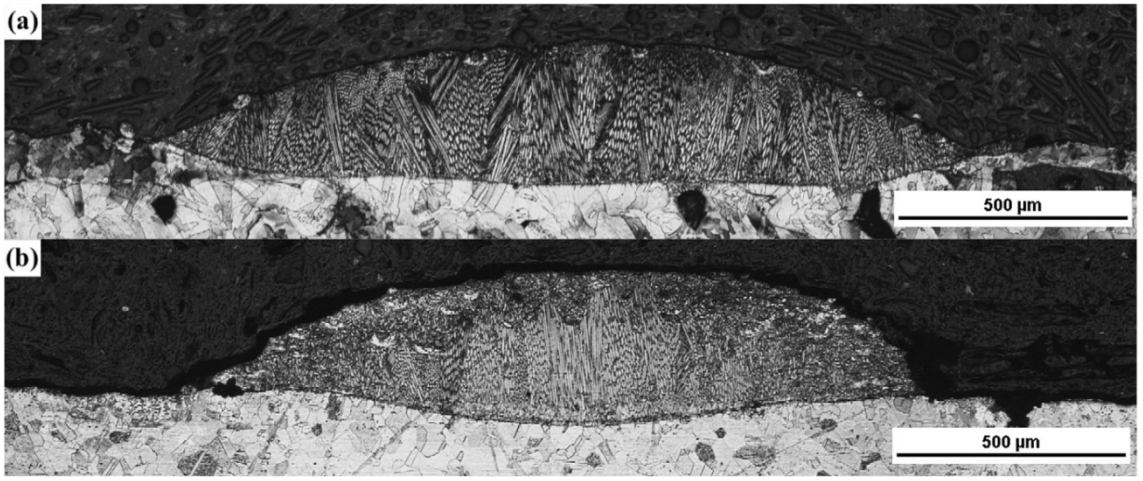

Figure 133. Macromorphology of a single track deposit as determined by set 1 of the optimal process parameters shown in Table 25. (a) A single track 1's cross-section on an L-PBF substrate, and (b) a single track 1's cross-section on a hot-rolled substrate

Figure 134 depicts the cross sections of the DED+LS - 1a coating on the hot-rolled and L-PBF substrates with respect to the DED scan direction. Figure 134a shows the hot-rolled substrate, DED, and LS zones, whereas Figure 134b shows the L-PBF substrate, DED, and LS zones. These three zones correlate to the three distinct procedures that were used.

According to studies by Errico et al. and Yan et al. on the microstructural analysis of stainless steel laser hybrid welding and laser powder welding, respectively [23,143], Figure 134a-b shows for both substrate types a fusion line at the interface between substrate and coating since the heat-affected zone (HAZ) was not detected because it was very thin. Localized heating and fast cooling produced by the DED technique result in a narrow HAZ [67]. According to the darker lines along the hot-rolling direction, Figure 134c depicts the usual equiaxed austenitic grain with ferrite at the grain edge, annealing twins, and etching bands [23,67]. While it is possible to identify a typical morphology of solidification structures in the L-PBF substrate (see Figure 134d), in which the boundaries of the depositions may be defined as melted/resolidified zones with curved edges (roughly parabolic) [144]. Additionally, the virtually total absence of flaws and lack of fusion demonstrate the overall excellent quality of the arrangement of the tracks in the substrate. The coating at the DED-LS contact zone is seen in Figure 134e–f. Due to the quick heat dissipation, some grains from the DED-LS interface zone have shown epitaxial growth [67].

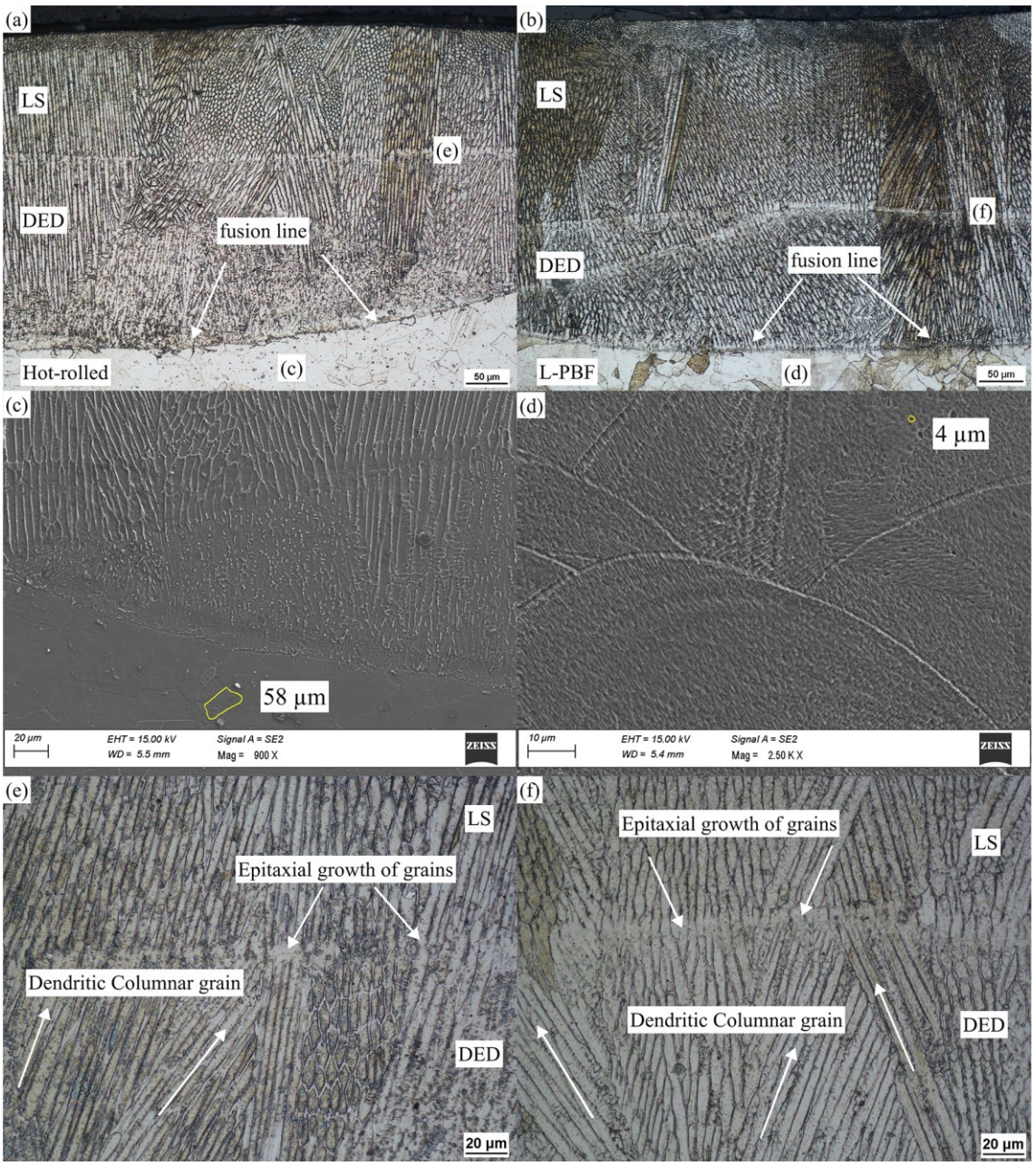

Figure 134. The images show the microstructural characterization of the DED+LS - 1a coating on the hot-rolled and L-PBF substrate types: (a) and (b): 200X magnification of the three coating zones: substrate (hot-rolled and L-PBF), DED and LS; (c): 900X magnification of the hot-rolled substrate and (d): 2.50KX magnification of the L-PBF substrate; (e) and (f): 500X magnification of the DED and LS interface zone.

Figure 135 depicts the cross-section of a single LS track as well as the semi-circular part of the track that was created during the DED procedure. According to research by Kim et al. [134], it is feasible to see a wider track width in the DED-LS interface zone (see Figure 135a) than in the DED-L-PBF substrate and DED-hot-rolled substrate interface zones. This impact is mostly caused by the distinct process circumstances that are present during LS since there is no powder supply, the laser beam is not attenuated by the presence of metal particles, and LS has a greater energy density at the surface than DED. As a result, the LS method transfers heat more favorably than the DED technique [134]. In a study by Errico et al. [23], it was

discovered that a wider track width was obtained in laser welding without powder than in laser welding with powder because the surface is partially shielded from the laser beam due to the presence of the powders. This finding was similar to the one made in the welding process. In fact, the DED method generates a melt pool that, depending on the selected overlapping parameter, only overlaps one side of the previously deposited track, and because the remaining section is in contact with air or an inert gas, the heat is mostly transmitted to that side [134]. In contrast, while the LS is in operation, this issue does not exist, and as a result, heat flows along both sides of the track, resulting in a broader track width. Both coatings have almost comparable microstructures in the DED and LS zones.

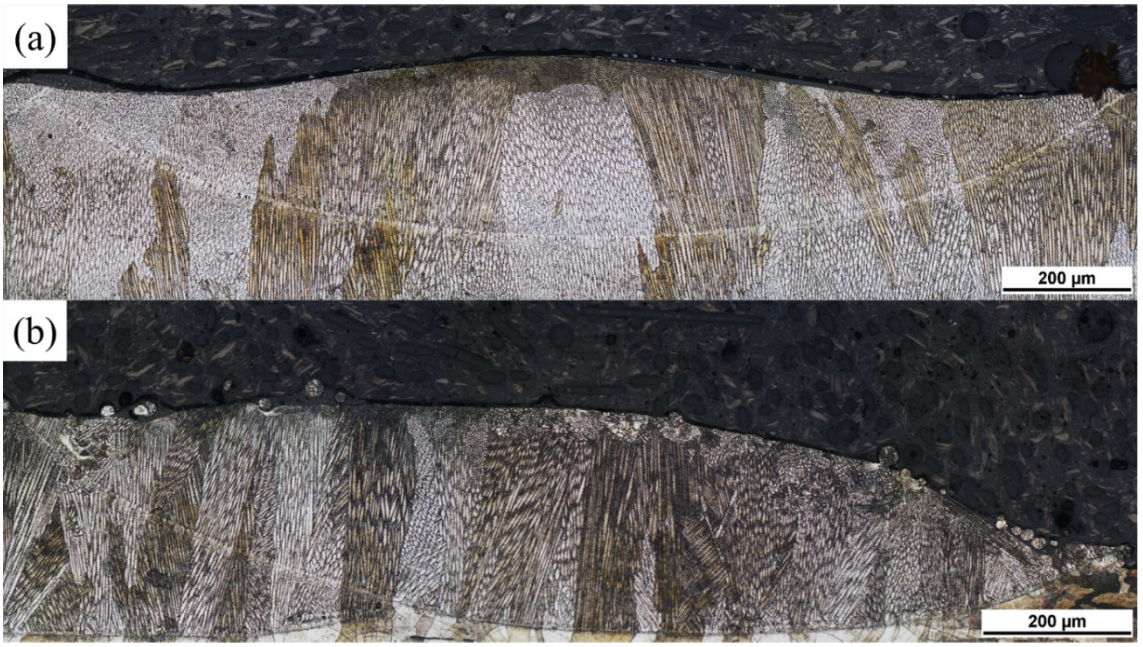

Figure 135. Macromorphology of coating sections on an L-PBF substrate: (a) cross-section of a single LS track coated with DED+LS - 1a; (b) cross-section of a single DED track coated with DEDo - 1.

A cross-section of the DED+LS - 1a coating on the L-PBF substrate was magnified in Figure 136a, and certain locations, in particular, were examined. Figure 136b depicts the area where the L-PBF substrate and DED come together. A white band line (planar crystal) that can be observed there indicates the successful application of metallurgy at the interface and is consistent with the findings of He et al [145]. The characteristic dendritic columnar shape seen in materials produced by quick melting and solidification cycles is seen in Figure 136c. The direction of heat transport determines how this structure develops. Figure 136d depicts a fine equiaxed grain produced by the quick solidification and remelting produced by laser scanning, which permits coatings with enhanced mechanical performance [134].

Additionally, a microanalysis was carried out using an energy dispersive X-ray (EDX) analysis and scanning electron microscopy (SEM) to examine the variations in the alloying elements present in the various zones of interest, including the LS, DED-LS interface,

DEDo, fusion line, and substrate. On both L-PBF and hot-rolled substrates, Figure 137 depicts the concentration of alloying elements in these regions for DED+LS-1a coating.

The L-PBF substrate and the coating zone (DED and LS) have relatively comparable compositions, as shown by the EDX results in Figure 137a; in fact, a uniform distribution of the different principal alloying elements tested can be seen. This outcome is a result of how chemically close the powders used to create the L-PBF substrate and the DEDo coating are. The sole difference is that the DEDo has 1% more nickel than the substrate because, as shown in Tables 19 and 21, the powder used to make the DED has more nickel than the powder used to make the L-PBF substrate. Additionally, variable outcomes in the case of the hot-rolled substrate (see Figure 137b) are caused by the various preparatory chemical compositions of the powders and base material, as detailed in Tables 18 and 21, as well as the various procedures used to create the substrate [67].

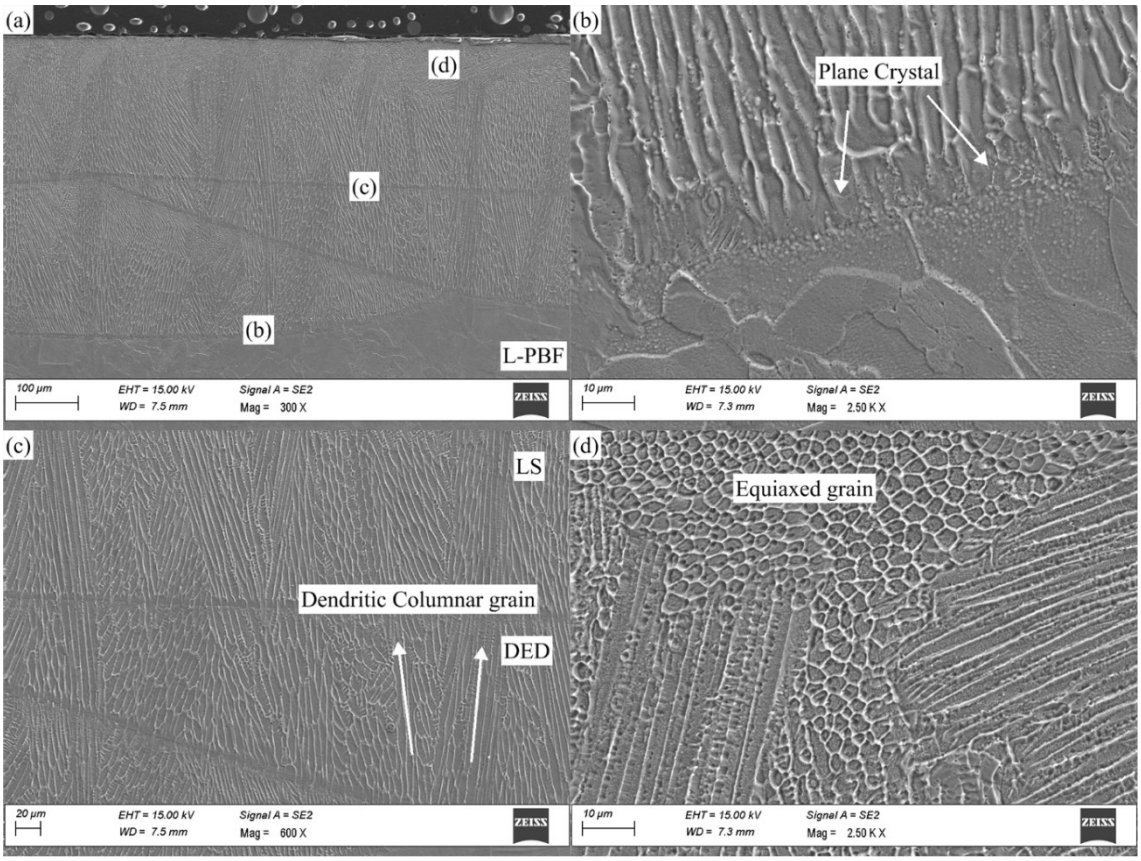

Figure 136. DED+LS - 1a coating's microstructure on an L-PBF substrate (a) 300X magnification of the L-PBF substrate, DED, and LS coating zones; (b) planar crystal at the DED/LS interface zone; (c) 600X magnification of the DED/LS interface zone; and (d) 2500X magnification of the top surface of the LS.

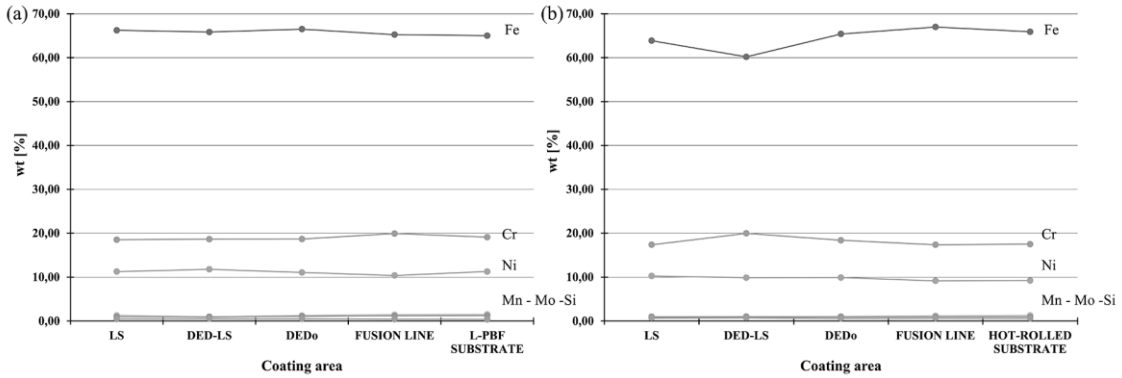

Figure 137. Findings from an EDX examination of the key alloying components in the various zones of the DED+LS - 1a coating. (a) on L-PBF substrates; (b) on hot-rolled substrates.

4.1.3.4 Microhardness

In a cross-section going from the substrate to the top surface, microhardness profiles were found. The DED coating and substrate contact was chosen as the zero-reference point. Moving the interface 0.25mm up and down yielded the remaining spots. The microhardness profiles of the DED+LS-1b coatings on both the hot-rolled (Figure 138a) and L-PBF (Figure 138b) substrates are shown in Figure 138. To ensure that the results were statistically significant, each test was repeated five times. Thus, average values from each measurement site were used to create each point in Figure 138. Due to the differing grain sizes produced by the two methods, the L-PBF substrate exhibits greater values than the hot-rolled one, respectively 235HV and 150HV. In fact, the hot-rolled substrate exhibits a higher grain size than that produced by the L-PBF technique, as demonstrated in Figure 134c. The literature is well aware of this conclusion, and several investigations support it [67]. The L-PBF process produces very fine grains because of the numerous heat treatments that each melted and re-solidified layer through. Because the L-PBF substrate has a finer grain than the hot-rolled substrate and has a larger density of dislocations in the austenite cells, it has a higher microhardness value [146]. Higher microhardness values are therefore a result of the creation of intricate networks of dislocations as a result of thermal stresses brought on by the quick solidification in the L-PBF process [147,148]. Figure 138, however, demonstrates the divergence in the two microhardness profiles' trends, particularly in the fusion line. In fact, in coatings applied to hot-rolled substrates, it is possible to see a hardness increase from 150HV to 205HV at the substrate-coating interface area because of the significant microstructural change in this region, where the grain size is finer than in the substrate [67,149]. Due to heat effects during the applied treatment, there is a progressive increase in hardness close to the substrate-coating interface zone. As shown by Kumar et al. [150], a progressive increase in microhardness is caused by the heat generated during DED and subsequent LS, as well as the repeated thermal cycles, which are transported to the substrate

adjacent to the interface. Regarding the microhardness profile of the coating applied to the L-PBF substrate, it was found that the microhardness decreased from 235HV to 209HV at the fusion line because the coating's grain size was greater than the substrate's in this instance. Due to the presence of a finer grain in this area created by remelting, both profiles show a rise in microhardness in the LS area of about 230HV for both coatings.

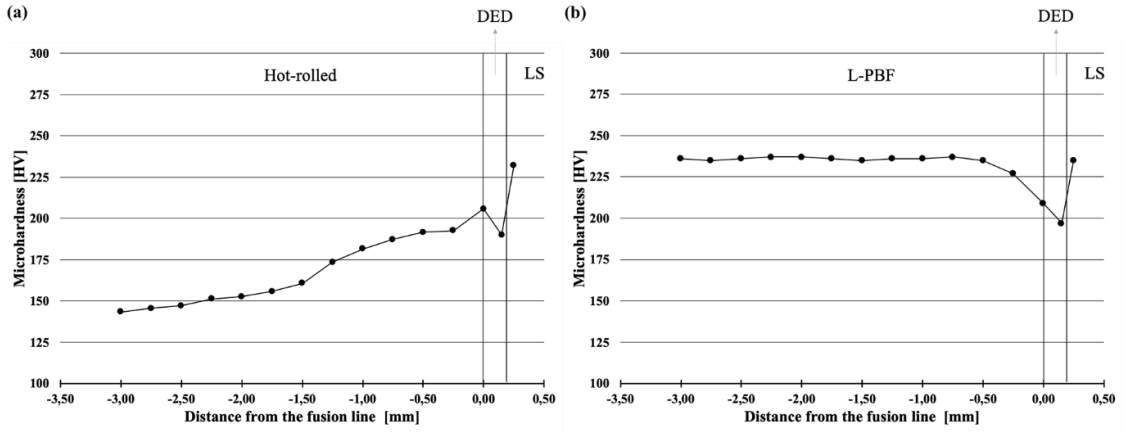

Figure 138. Graphs showing the microhardness of the coated component overall: (a) hot-rolled coating's microhardness; (b) L-PBF coating's microhardness.

4.1.3.5 Melt pool size and Temperature monitoring

The development of real-time monitoring techniques and process control were discovered to be important needs to overcome issues and enhance the surface quality of the coating improving its repeatability as a result of the review research carried out by L. Zhu et al. [135]. For this reason, during the creation of the coatings, a monitoring system consisting of a coaxial CCD camera and an off-axis monochromatic IR pyrometer (Figure 124) was used. This system improved the ability to monitor the melt pool shape and temperature field, respectively. Regarding the optical monitoring system, which uses a CCD camera, it has made it possible to investigate the shape of the melt pool produced during the DED coating and the LS treatment. Videos were specifically captured using the CCD camera, and then frames from those videos were retrieved and analyzed using an image analysis technique written in the MATLAB program. The area and coating breadth of the melt pool were discovered using the region-based active contour technique. This algorithm implements an iterative method with the definition of the level 0 contour (MASK), which iteratively evolves and adapts by using shrinking/expanding operations known as "contour evolution," driven by the minimization of an energy function; further specifications of the algorithm are described in detail in previous work [21].

On both hot-rolled and L-PBF substrates, Figure 139 depicts the effects of DEDo - 1 coating and LS - 1c treatment on the area and coating breadth of the melt pool. The average of the 10 frames that were taken and examined for each track is represented by each shown value.

According to Figure 139a, the melt pool area acquired by laser scanning on both substrates is 28% bigger than the area obtained by DEDo. The coating width is 10% wider during LS than it is during DEDo (see Figure 139b). This outcome supports the information in the previous caption (please see Figure 135). The stationarity of the melt pool, both in terms of area and width, can be seen throughout the entire coating process, though. This result was attained through the optimization of the process parameters described in the previous caption, which allowed us to identify a set of optimal parameters for the creation of coatings with the best possible surface quality. Additionally, Figure 139 shows that the size of the melt pool formed during the DEDo - 1 coating on the L-PBF substrate is around 10% greater than on the hot-rolled substrate while the coating width has increased by about 2%. These outcomes, which are depicted in Figures 133 and 140, are the result of the different substrates' different initial surface states. In particular, the L-PBF substrate's surface has a high degree of roughness, which causes multiple laser beam reflections and, as a result, higher absorption, which results in a larger and wider melt pool [151].

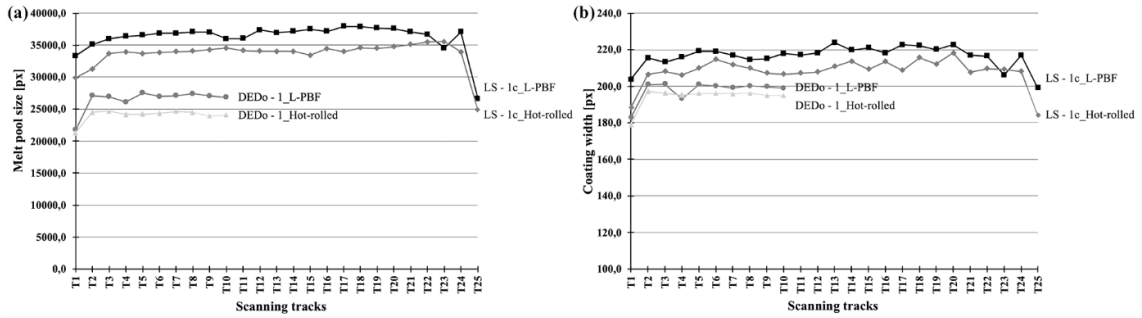

Figure 139. Measurements made when DEDo-1 coating and LS-1c treatment were being applied to hot-rolled and L-PBF substrates. (a) melt pool's dimensions and (b) its coating breadth.

Applications of the developed monitoring systems

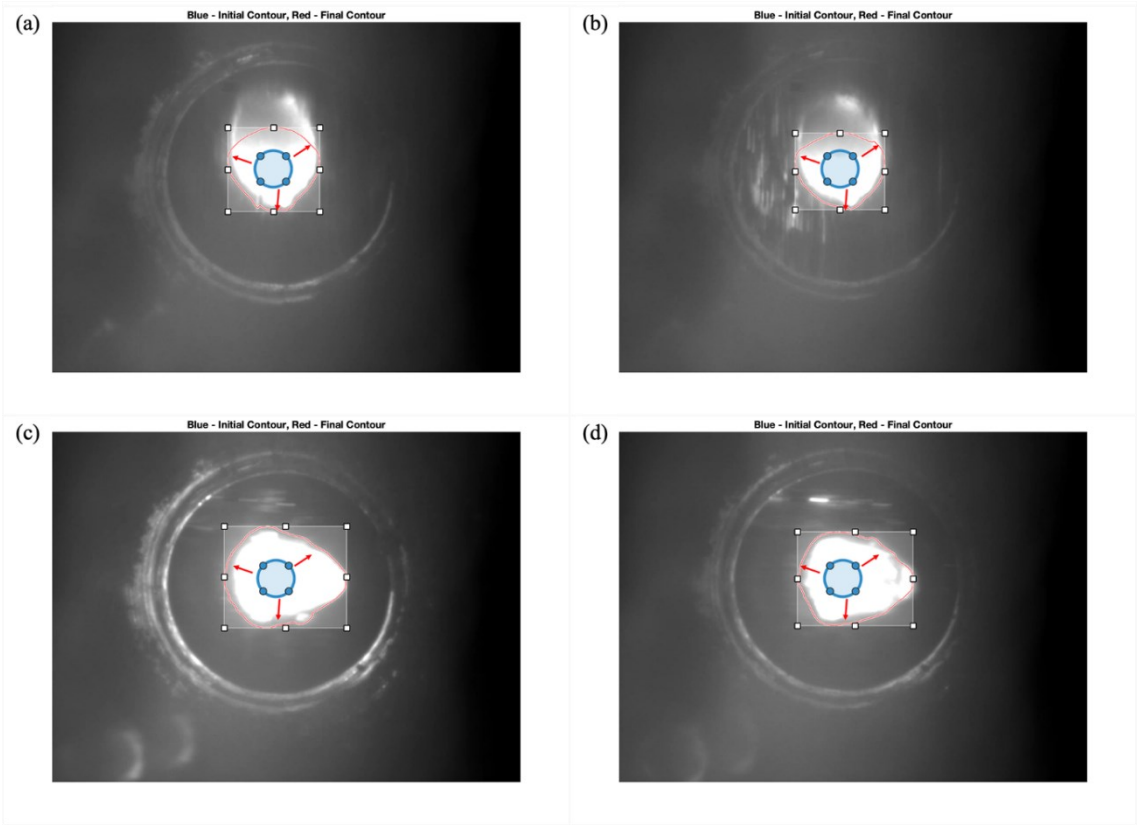

Figure 140. With the help of the region-based active contour algorithm, the area and coating width of the melt pool may be automatically determined from a video frame: (a) DEDo-1 coating on an L-PBF substrate, (b) DEDo-1 coating on a hot-rolled substrate, (c) LS-1c coating on an L-PBF substrate, and (d) LS-1c coating on a hot-rolled substrate.

Regarding the temperature monitoring system, it has been possible to monitor and regulate the melt pool's temperature throughout the procedures thanks to a monochromatic IR pyrometer. Table 27 displays the findings from temperature monitoring.

Table 27. The average temperature of DEDo and LS

Coating	AVG Temperature (°C)
DEDo - 1	1576.7±34.3
LS - 1c	1572.0±54.7
DEDo - 2	1460.2±31.4
LS - 2a	1467.9±34.9

The findings indicate that there were overlapping heat cycles throughout the realization of the two coatings since the average temperatures recorded during the DEDo coating and those recorded during LS are quite comparable to one another. This outcome is a consequence of the preliminary analysis completed, which enabled us to produce a very comparable and consistent thermal cycle during DEDo and LS by selecting the proper process parameters, such as Ed and the dwell time between two adjacent tracks. This outcome was wanted because it is possible to achieve a finer microstructure during the LS treatment in this way

due to rapid solidification [134], a lowering of the melt pool surface tension, a decrease in the balling phenomenon, and high surface roughness caused by an excessive thermal input. In addition, a high thermal input stirs the melt pool and raises the recoil pressure [139]. Consequently, temperature management and monitoring are crucial for enhancing the final coating's qualities.

4.1.4 Conclusions

In this paper, a coating was successfully applied to a component created by laser powder bed fusion that had poor surface quality due to unacceptable surface roughness and weak metallurgical structures by combining direct energy deposition with AISI 316L powder for the coating and a subsequent laser scanning treatment in the same setup:

1) for the implementation of the coating, two sets of ideal process parameters have been determined;
2) surface roughness is greatly reduced after DED coating and reduced even further following laser scanning treatment, attaining minimal Ra,x, and Ra,y values of 8.30 µm and 5.60 µm, 2.10 µm and 4.00 µm, respectively, from 10.20 µm and 9.80 µm of the L-PBF sample;
3) the microhardness, on the other hand, drops to 200 HV after the DED coating from an average value of 235 HV before rising once more to 230 HV following the laser scanning treatment;
4) the final outcome is closely tied to the microstructural characteristics the component attained following the treatments. In instance, compared to a columnar dendritic grain formed in the DED treatment zone, the grain size acquired following the laser scanning treatment is an equiaxial fine grain.
5) due to the melt pool's stability, which was determined by an optical and thermal monitoring system, the created coating was uniform..

Second case study

4.2 Effects of Laser Deposited Maraging Steel on L-PBF 316L component

The following is the paper with the title "**Effects of Laser Deposited Maraging Steel on L-PBF 316L component**", published in *Metals* in 2022. See section 7 for the publication details.

4.2.1 Aim of the work

The main aim of this work was to develop an innovative 18Ni (300) maraging steel DED coating on an L-PBF AISI 316L substrate, with a subsequent heat treatment, to obtain high

mechanical surface properties of the final component and reduce manufacturing costs of tools and molds. The cost-effectiveness of using additive technologies compared to traditional technologies for the production of components for high-tech industries, such as the aeronautics and automotive industries, has been widely demonstrated in the literature [152–154]. However, the combination of different technologies to produce the aforementioned components may represent a further breakthrough for the industry from an economic and sustainability perspective. L-PBF technology is used to create complex structures, such as lattices or components with conformal cooling channels. On the other hand, DED technology would be exploited to easily fabricate functional coatings by varying the composition of materials according to the required properties. Pending the development of this technology, the combination of L-PBF and DED technologies appears to be a viable solution to produce components that simultaneously have complex geometry and high mechanical properties. This possibility can be crucial for the production of tools and molds, allowing the use of a less mechanically performing and cheaper material for the core and of another more expensive material with superior characteristics for the surfaces that must work. This would reduce the production costs compared to those currently incurred in manufacturing a component entirely made of tool steel. In the work, the quality of the manufactured coatings was assessed in-process through the implementation of an optical monitoring system and real-time image processing. In addition, an in-depth metallurgical analysis (microstructural and chemical) of the interface between the DED coating and the L-PBF component was carried out. Finally, low-force Vickers hardness tests were performed on both the as-deposited and heat-treated coatings, in order to confirm the high mechanical performance of the final component surfaces. The results showed the feasibility of an innovative, economical, stable, and high-performance DED coating on an L-PBF component, useful for future applications on complex geometries. Furthermore, the results of this experimental study could also be applied to the development of repair procedures for worn components, as an efficient alternative to their replacement.

4.2.2 Materials and Methods

4.2.2.1 DED Coating and Monitoring Setup

The coatings were realized by means of a DED machine described in detail in section 2.2.2. In addition, the process was monitored through a CCD camera (IDS UI-6230RE-M-GL PoE Rev.3, Obersulm, Germany), installed in the deposition head, which is used both for positioning procedure and for in-process analysis of the shape of the melt pool. Figure 141 depicts the DED coating process scheme and the monitoring system employed.

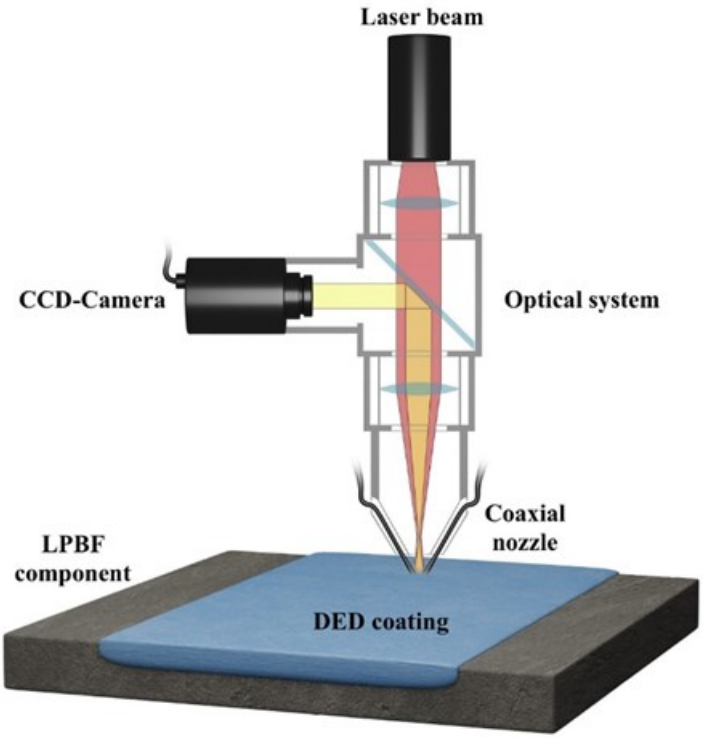

Figure 141. Schematic overview of the Directed Energy Deposition system and monitoring setup used for coating [155].

4.2.2.2 Materials and Heat Treatment

The material used for the coating was a commercial spherical powder of 18Ni (300) maraging steel, as can be seen in Figure 142a. AISI 316L stainless steel plates, fabricated by the L-PBF process, were used as substrates. Figure 142b shows the AISI 316L spherical powder used to manufacture the L-PBF substrates. The size and chemical distribution of the metal powders used for the coating and substrate are shown in Table 28 (data certified by the manufacturers). The 18Ni(300) gas atomized maraging steel powder was produced and certified by GE Additive Company, while the AISI 316L gas atomized stainless steel powder was produced and certified by Mimete Metal Powders. The substrates, shown in Figure 143, were fabricated by L-PBF with a set of process parameters optimized in previous works [69,72]. The resulting coatings were subjected to a subsequent two-step heat treatment based on the literature [156–158]: solution annealing (815°C for 1 h, air-cooled) followed by aging heat treatment (480 °C for 5 h) to improve the mechanical properties.

Table 28. Powder size and chemical composition (%wt) according to the test method: ASTM E2594-20 [155].

Powder material	Range of particle size (µm)	Cr	Ni	C	Mn	Si	Mo	Co	Ti	Fe
AISI 316L (substrate)	15-45	17.8	11.4	0.012	1.4	0.45	2.31	-	-	Bal.
18Ni (300) (coating)	15-53	-	18.7	0.02	-	-	3.73	10.4	1.15	Bal.

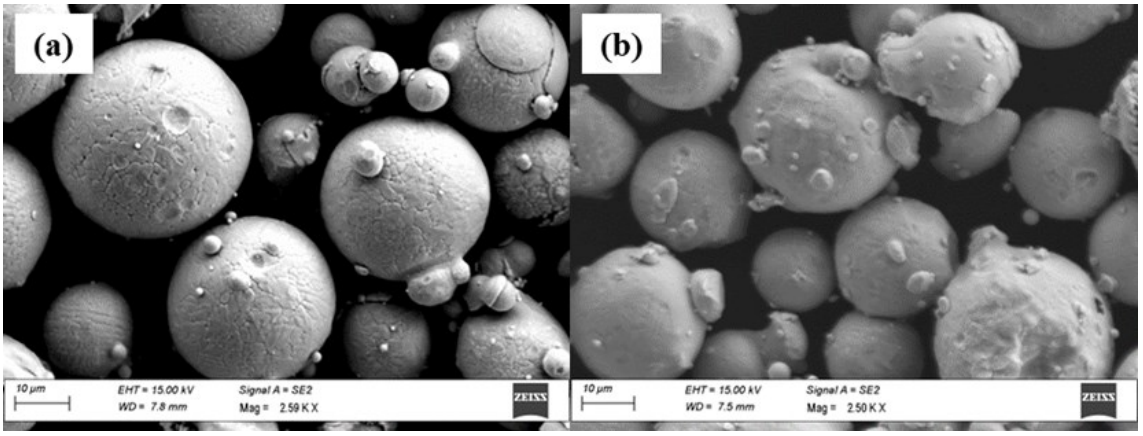

Figure 142. Metal powder morphology displayed by Scanning Electron Microscopy: (a) 18Ni (300)—coating; (b) AISI 316L—substrate [155].

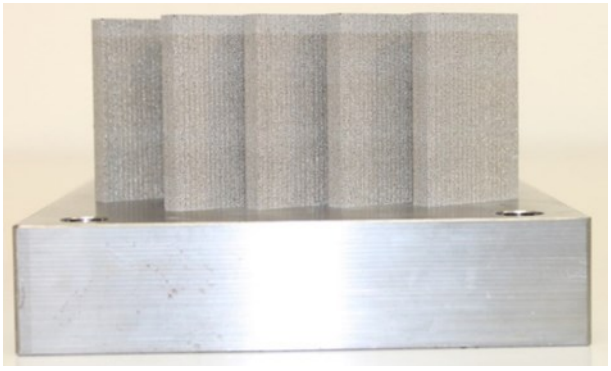

Figure 143. AISI 316L substrates manufactured by using L-PBF technology [155].

4.2.2.3 Experimental Details

The DED coatings were realized with a different number of layers (1, 3, 5, and 10 layers), as shown in Figure 144b. These were deposited on four L-PBF substrates adopting a one-way deposition strategy and 30s of dwelling time between every single track and between every layer (see Figure 144a). The specimen identification follows the nomenclature: N_C and N_T whit N=number of layers, C=as-coated, and T=treated. The process parameters for the deposition of coatings were: laser power = 400 W, spot diameter = 1.5 mm, scanning speed = 1000 mm/min, powder feed rate = 5.0 g/min, carrier gas flow rate = 10 l/min, hatch distance along y-direction = 0.906 mm and step height along z-direction = 0.096 mm. These process parameters were obtained after preliminary single-track tests performed on L-PBF substrates and subsequent geometrical characterization. The preliminary tests are based on a Taguchi orthogonal L36 experimental plan and are listed in Table 29. The methodology followed to identify the optimal process parameters, that resulted in a high-quality coating, was described in detail in the aforementioned work [69].

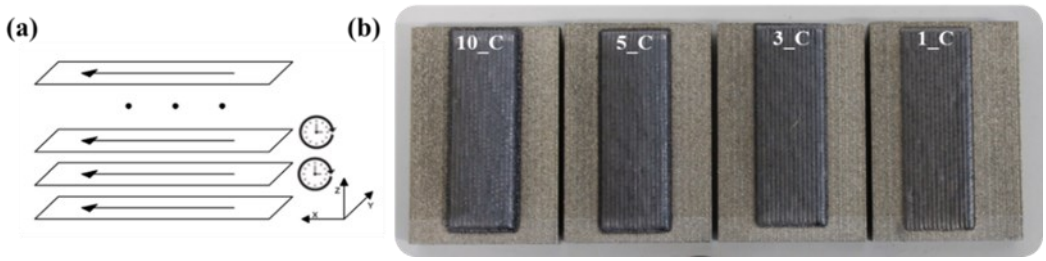

Figure 144. (a) Schematic representation of the deposition strategy; (b) DED coatings on L-PBF substrates [155].

Table 29. Taguchi orthogonal L36 preliminary single-track experimental plan [155].

Process parameter	Units	Factor Levels		
		1	2	3
Laser power	W	400	600	-
Spot diameter	mm	1.5	2.0	2.5
Scanning speed	mm/min	1000	1500	2000
Powder feed rate	g/min	2.5	5.0	-
Carrier gas flow rate	l/min	10	15	-

4.2.2.4 Analysis and Characterization Procedure

The quality of the manufactured coatings was assessed in-process through the implementation of an optical monitoring system and an image analysis methodology. In detail, the manufacturing process was monitored by means of a CCD camera located in the deposition head. Thanks to a dichroic mirror, this equipment allowed the observation and monitoring of the melt pool morphology, coaxially with respect to the laser beam (see Figure 141). The camera was set up with an acquisition frequency of 40 fps and a resolution of 1024 x 768 pixels (pixel size around 5 μm). For each video, the frames related to the manufacturing process were extracted and the melt pool evolution was examined by applying an image processing algorithm. Concerning the image analysis methodology, the workflow has been set of 3 steps: video capture, frame extraction, and image processing. The latter is performed in the MATLAB environment using an image segmentation algorithm called Region-Based Active Contour (R-BAC) described in detail in section 2.2.3. Furthermore, the coatings were carefully prepared through cutting, embedding, and polishing steps, followed by a chemical etching (Etchant: 6 mL acetic acid, 10 mL hydrochloric acid, 1-2 g picric acid, and 100 mL ethyl alcohol) to identify the optimal set of process parameters and to investigate their final quality in terms of geometrical characteristics, microstructural properties, and chemical composition. Microstructural analyses were conducted by means of the Nikon Eclipse MA200 inverted optical microscope and the Zeiss Sigma 300 VP scanning electron microscope, combined with EDX spectroscopy. Finally, low-force Vickers hardness tests were performed, on both the as-coated and heat-treated coatings, using the HMV-G by Shimadzu hardness tester, according to the ISO 6507-1 test method (0.3 kgf of load and 10 s of dwelling time).

4.2.3 Results and Discussion

4.2.3.1 Optical Monitoring of the DED Process

The Region-Based Active Contour is an iterative method capable to analyze the image brightness gradient in order to define regions with the same properties. The algorithm starts from an initial mask in the form of a closed curve, which iteratively changes its shape and size adapting to the image brightness, driven by the minimization of an energy function (see Figure 145a). This algorithm has already proved its effectiveness for the study of the melt pool during the laser deposition process, both to determine the evolution of its size and to identify potential production defects [21]. Figure 145b shows the result of the calculation of the melt pool area by means of the R-BAC algorithm on the 11000 frames extracted from the video recorded during the manufacture of specimen 1_C. The algorithm is capable to activate during the laser deposition process while returning null values during dwelling times between tracks when the laser is turned off.

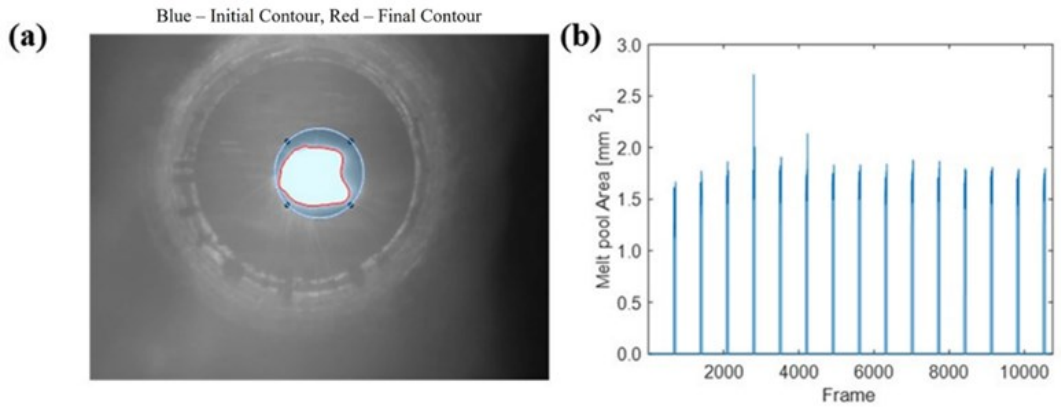

Figure 145. (a) Initial mask (blue) and final contour (red) of R-BAC algorithm; (b) melt pool area of specimen 1_C.

Figure 146a shows the variation of the melt pool area during the fabrication of the layer. It can be seen from the plot how the area has an average size of 1.42 mm^2 in the first track, which grows and stabilizes around the value of 1.65 mm^2 from the second track onward of the 15 traces that make up the layer. In addition, it is noted the reduced dimension of the box plot height indicated the low variability of the values and thus the good stability of the coating process. The red crosses represented the outliers of the analysis, often attributable to defects in the DED process caused by fluctuations in powder flow. The proximity of the outliers to the average values was another factor that characterized the stability of the deposition process.

Figure 146b, Figure 146c, and Figure 146d show the trend assumed by the melt pool during the construction of multilayer components 3_C, 5_C, and 10_C, respectively. As previously shown, the low divergence of the calculated value during the deposition of single traces (mainly due to the implementation of the dwelling times between each track) allowed the

reliable estimation of the average melt pool area for each layer. These summary values of the 15 tracks constituting each layer, showed a rather low range of variation with the sporadic presence of outliers. This was another corroboration of the stability of the deposition process even in the production of multilayer coatings.

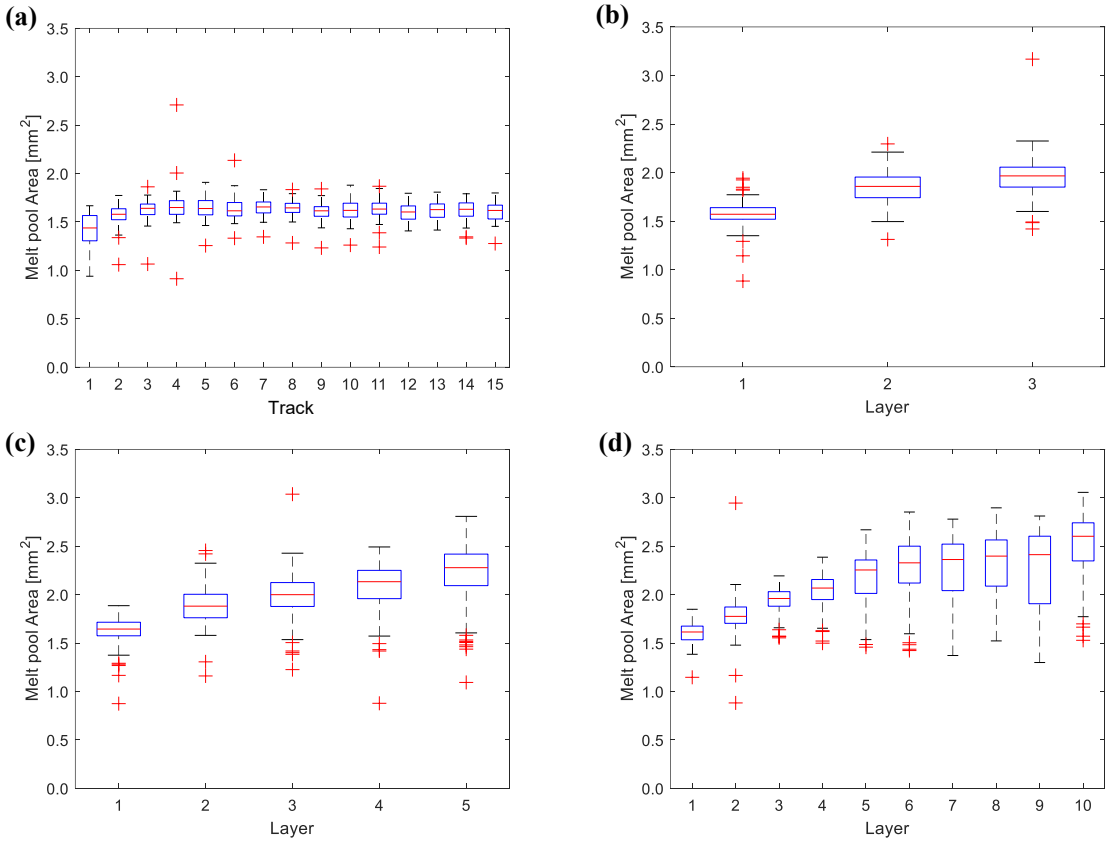

Figure 146. Trend of the melt pool area: (a) sample 1_C; (b) sample 3_C; (c) sample 5_C; (d) sample 10_C.

Analyzing the graphs, it was easy to discern the increasing trend of the melt pool area as the number of layers increased. This result can be attributed to a change in heat transfer conditions during the process [79]. Specifically, in the first layer, the deposition on a substrate at room temperature provided the greatest heat dissipation and the generation of a melt pool area smaller than the subsequent layers. Furthermore, the gradual increase of the melt pool area was caused by the difficulty of dissipating the heat produced during the laser deposition and its accumulation in the coating area. In this way, there was an increase in the average temperature of each layer with the consequent in-crease in the melt pool area, even though the same process parameters were used.

4.2.3.2 Microscopic Examination and Chemical Analysis

The SEM analysis showed that in as-coated specimens are present precipitates with moderate dimensions constituted by a Ti-rich phase (Figure 147a and Figure 147b) since the content of this element in the powder is 1.15% wt (Table 28). Differently, in the heat-treated specimens, this category of precipitates first dissolved in the metal matrix during the heating

stage and then reprecipitates during the cooling stage. This segregation mechanism is characterized by more finely dispersed precipitates, most of which are not observable under optical microscopy. Only a small fraction of slightly coarser spherical particles are visible, as can be seen in Figure 147c and Figure 147d. The precipitation of small-size Ti-rich particles leads to an improvement in the hardness value in the heat-treated specimens [159].

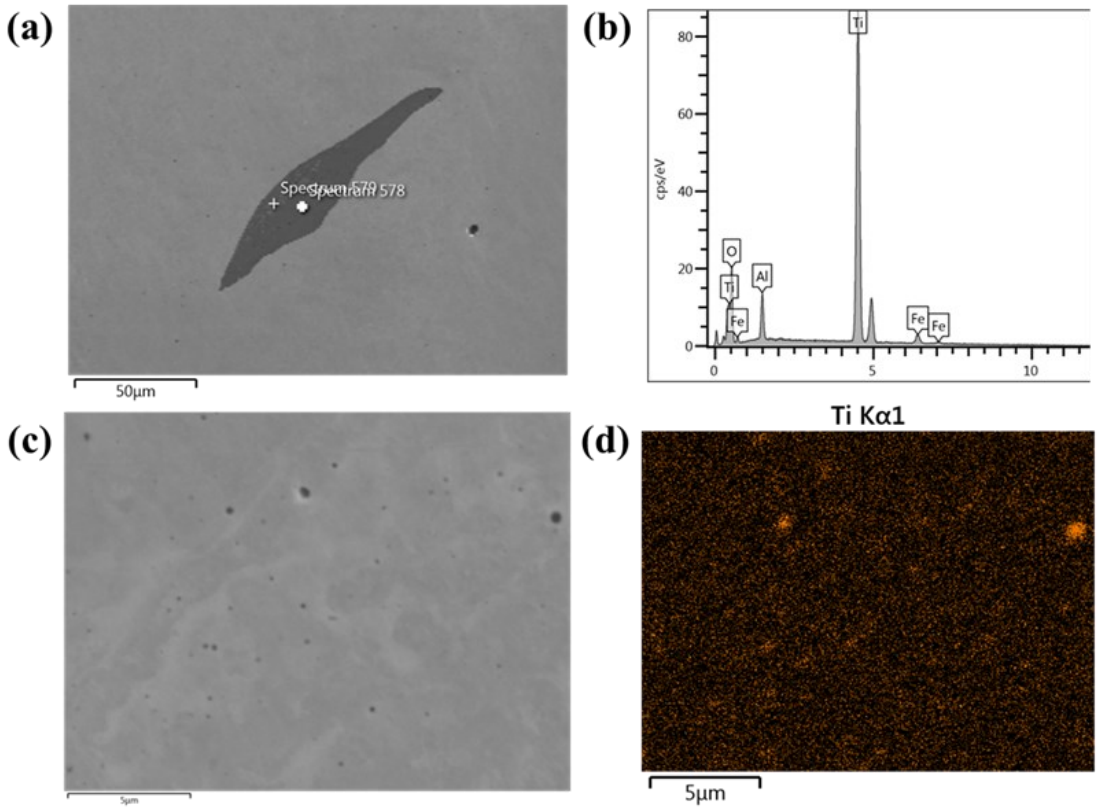

Figure 147. SEM analysis of precipitated particles in the as-coated specimen: (a) SEM image of precipitated particles and (b) spectral distribution of chemical species. Ti particles dispersion after heat treatment: (c) SEM image of Ti particles dispersion and (d) EDX scan map of Ti particles distribution [155].

Chemical analysis was conducted with the use of an EDX microprobe. It has been observed that the Chromium tended to transfer from the parent metal (substrate) to the first layer (Figure 148). The high Chromium concentration in the first layer can be explained by the Marangoni convection [160] during the deposition process. Therefore, the Marangoni convection effect and the diffusion of elements at the interface between the two materials facilitated the formation of a Cr-rich region in the first layer of the coating (see Figure 148b and Figure 148d). In addition, it can be seen from Figure 148c and Figure 148e that Co also exhibits a transient distribution between coating and substrate. The previous outcomes result in excellent adhesion achieved at the interface. These phenomena were present on both as-coated and heat-treated specimens, demonstrating that aging treatment does not influence Cr and Co distributions.

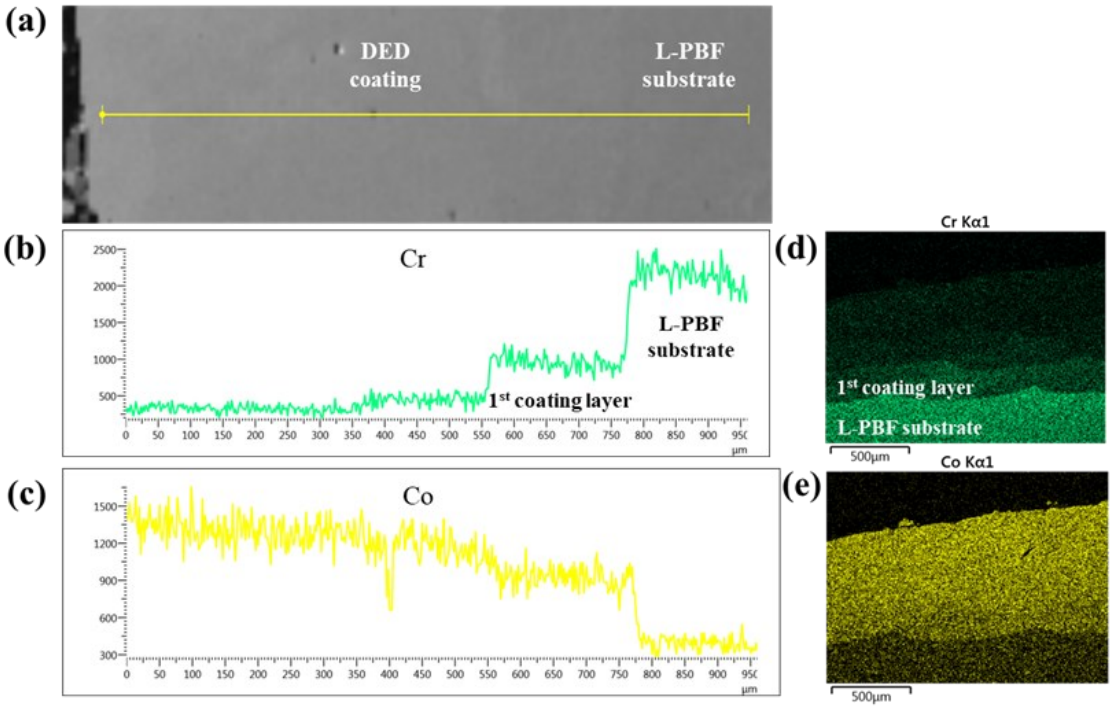

Figure 148. Chemical composition assessed by EDX microanalysis of Cr and Co concentration in 3_T specimen: (a) SEM image of coating and substrate zone, (b) EDX line scan of Cr distribution, (c) EDX line scan of Co distribution, (d) EDX scan map of Cr distribution and (e) EDX scan map of Co distribution [155].

Optical micrographs of the specimens before the chemical etches disclosed the presence of spherical discontinuities with diameters in the range of 10-30 µm (Figure 149), which can be considered acceptable in this type of manufacturing process [161].

Figure 149. Optical micrograph of 5_C specimen showing porosity [155].

Specimens were chemically etched in order to reveal the microstructure of the material. An interesting result concerns the difference between the microstructure in the first layer and in the successive layers of the heat-treated specimens. Micrographs show that Cr dispersion affected negatively the treatability of the material. The martensitic transformation that occurred by precipitation of intermetallic compounds was clearly visible in all the coating layers except in the first one (Figure 150). Only very few retained austenite areas were visible. It was also possible to observe that the metallurgical interface was regular and free

of significant defects (see Figure 150 and Figure 151). Discontinuities like lack of fusion and adhesion, cracks, delamination, or significant porosity were not observed, and intermetallic precipitates were also absent in all samples. Furthermore, Figure 151 shows the presence of a fusion line in the interface zone between substrate and coating instead of an extended heat-affected zone (HAZ). This is due to the localized heating and fast cooling distinctive of the Directed Energy Deposition process.

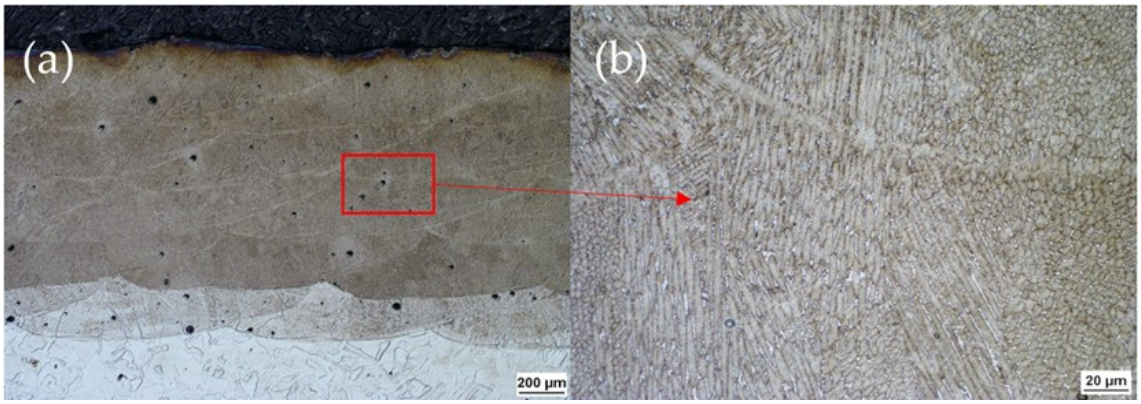

Figure 150. 5_T specimen showing (a) different microstructures in the coating, between the first and subsequent layers, and (b) complete martensitic microstructure in the upper layers [155].

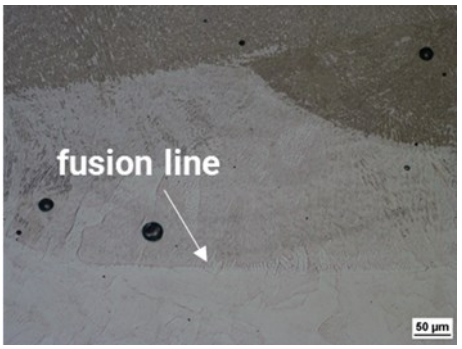

Figure 151. Optical micrograph of the interface zone in specimen 5_T at 200X magnification [155].

Figure 152 reports the microstructure of the 1_T specimen that shows only a partial transformation probably due to the inhibitor effect of Cr presence. In fact, it is well known that the Cr effect on iron-based materials is to lower martensite start (Ms) temperature promoting the austenite formation during the solidification step and hindering martensitic transformation in the aging treatment step. Moreover, the aggregation of a considerable amount of Cr in the first layer enhanced the austenite stability in this region due to the dissolution of Cr itself in it, forming Fe-Cr austenite.

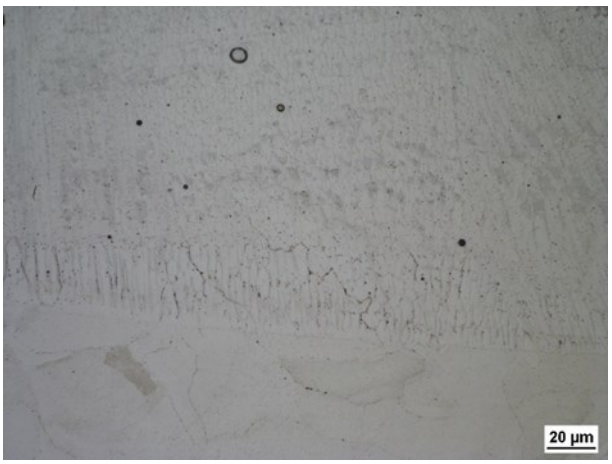

Figure 152. 1_T specimen microstructure showing the incomplete martensitic transformation [155].

The AISI 316L substrate resulted also affected by the heat treatment (Figure 153). In fact, while in the as-coated condition, the laser traces of the L-PBF process were clearly visible, these disappeared in the heat-treated substrate, because of the recrystallization that occurred during the heat treatment.

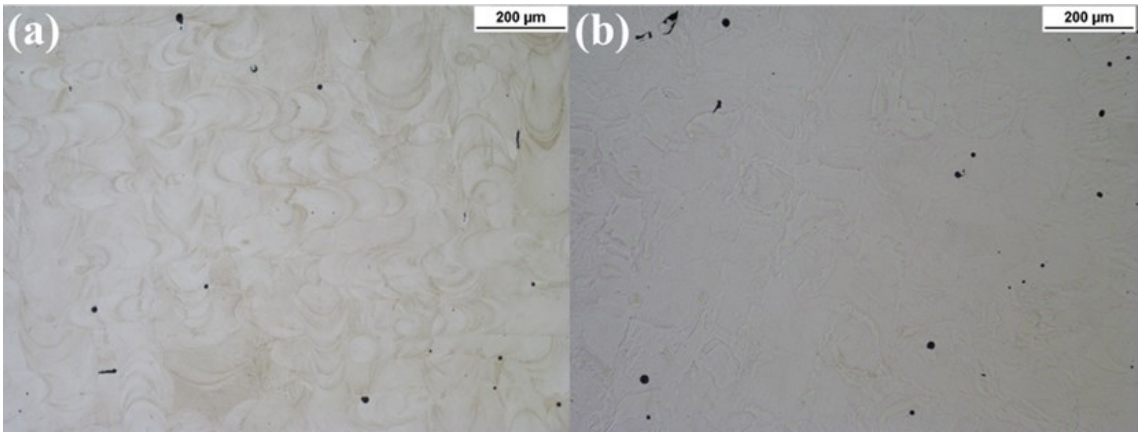

Figure 153. Substrate microstructure in (a) as-coated condition and (b) heat-treated condition [155].

4.2.3.3 Low-Force Vickers Hardness Test

Vickers hardness test was performed to determine the effects of aging heat treatment on the Maraging coating. All the samples were tested along the coating growth direction. Figure 154 shows that the hardness trend appears superimposable between the different samples. In fact, in all case studies, the as-coated sample hardness was in the 350÷390 HV range, which was consistent with a solution-annealed state of the 18Ni (300) maraging steel [162]. The samples subjected to aging treatment exhibited higher hardness values in all the deposited layers except for the first one. In fact, the hardness difference was ~200 HV, due to the martensitic microstructure of the treated coating. Furthermore, the hardness decreases to 200 HV at the substrate-coating interface and at the first layer, starting from an average value of 235 HV in the L-PBF component. For this reason, a single-layer coating should not be recommended (Figure 154a).

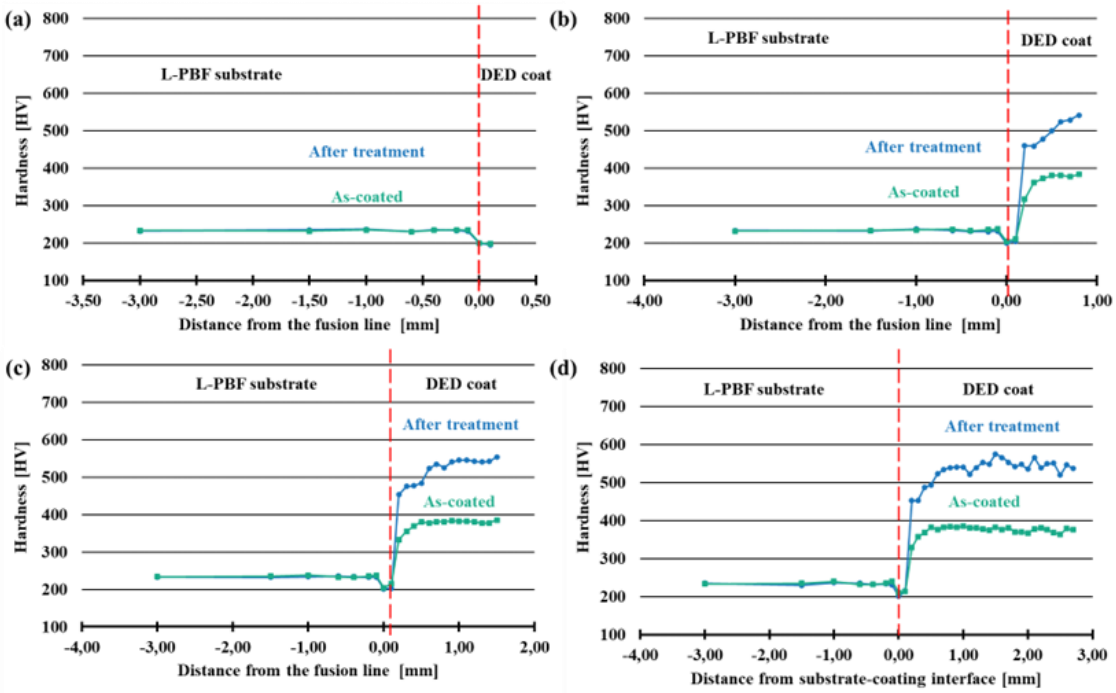

Figure 154. Hardness trends in as-coated and after-treatment samples: (a) 1-layer; (b) 3-layer; (c) 5-layer; (d) 10-layer.

As observed during the microscopic examination, the first layer of each coating had a different behavior also in mechanical properties. This aspect was attributable to the different chemical compositions generated by the mixture of substrate metal and maraging steel.

4.2.4 Conclusions

In this work, a Directed Energy Deposition (DED) coating, using 18 Ni(300) mar-aging steel powder and subsequent heat treatment, was successfully performed on AISI 316L components realized by Laser-Powder Bed Fusion (L-PBF). Below the main results are listed.

- The stability of the coating process was verified through the support of an optical monitoring methodology (CCD camera + real-time image processing), which allowed the observation of the melt pool in real-time.
- The hardness decreased to 200 HV at the substrate-coating interface and the 1st layer, starting from an average value of 235 HV in the L-PBF component. Coatings made with 3, 5 and 10 layers have a hardness equal to 375 HV (as-coated) and 580 HV (after treatment), according to the scientific literature.
- The hardness results are strongly related to the microstructural properties achieved by the as-coated and after-treatment coating. In particular, the microstructure obtained after solution annealing + age-hardening treatment is lath martensite. The aging involves the precipitation of nickel-rich intermetallic compounds in the lath martensitic structure, leading to a strengthening of the hardness by precipitation.

The results obtained from the work ascertained the feasibility of producing a component

with an AISI 316L core, obtained by the L-PBF process, and coated with the 18Ni (300) maraging tool steel by means of the DED technique. In fact, the coatings obtained, in the cases of 3-layer, 5-layer and 10-layer, were found to be highly performant as they had a metallurgical interface free of defects (discontinuities such as lack of fusion and adhesion, cracks, or delamination) and negligible porosity. Finally, this study aims to con-tribute to the reduction of tool and die manufacturing costs while still allowing for high surface mechanical properties of the final component, exploiting the strengths of the two AM technologies employed.

Third case study

4.3 In-process dimensional and geometrical characterization of laser-powder bed fusion lattice structures through high-resolution optical tomography

The following is the manuscript with the title **" In-process dimensional and geometrical characterization of laser-powder bed fusion lattice structures through high-resolution optical tomography"**, submitted to *Optics and Laser Technology*, and accepted for publication at the time of the thesis submission. See section 7 for the publication details.

4.3.1 Aim of the work

In this work, the High Resolution-Optical Tomography (HR-OT), first introduced in section 3.2.2, was implemented as an in-process monitoring system for lattice structures with a dual purpose: it is a layerwise monitoring method, thus it is able to detect in time the onset of geometric and dimensional inaccuracies, and, contemporary, it provides, at the end of the manufacturing process, a 3D reconstruction of the fabricated structure for dimensional and surface quality In comparison to the prior author's experience and other in-process monitoring systems and methods based on optical tomography proposed in earlier research articles [110,163], the resolution of the suggested system was further enhanced.

By utilizing thresholding-based techniques during the crucial image-processing phase, it resolves issues with the image pre-processing phase (correct background/foreground identification, filtering, noise elimination) and the segmentation phase, which can sometimes make it challenging to obtain accurate data from extremely complex geometries. The labour required to evaluate the post-process quality of lattice structures can be greatly reduced by applying this monitoring approach to the production of the structures. Additionally, in order to receive more trustworthy results from numerical simulation applications, having an accurate 3D model might be quite helpful. Given that lattice constructions are very susceptible to manufacturing flaws, numerical conclusions can, in fact, diverge significantly

from experimental data. The use of high-resolution optical tomography as an efficient in-process monitoring tool for quality inspection of complicated geometries and as a replacement for XCT for off-line dimensional and geometrical evaluation is represented by this work as a first step. It was mostly concentrated on the geometric distortions and dimensional errors of lattice structures, which have a substantial impact on lattice structures since they may significantly change the local and overall structural performance [166–168].

4.3.2 Materials and methods

4.3.2.1 Creation of the lattice structure sample and the experimental process

An Octet-Truss (OCT) elementary cell, which is symmetrical in all three directions, is the lightweight structural type that is the subject of this research. A parallelepiped volume with a square base section of 24 x 24 mm and a total height of 47 mm was filled with the unitary OCT cell, which had two skins with thicknesses of 5 and 2 mm, respectively. The unitary OCT cell was reproduced on a regular basis.

The cell and strut sizes were chosen in accordance with the printability constraints and process limitations that have been extensively discussed in the literature [169–172]: the particle size of the powder used, the ability of the laser beam to focus, and the impossibility of creating ad-hoc detachable supports without distorting the specimen. The CAD file and subsequent .stl file were created using the nTopology program, with the correct discretization settings used to produce an accurate model (Figure 155a and Figure 155b). In order to prepare for printing, the .stl file was then placed on the building platform and sliced using Materialize Magics software.

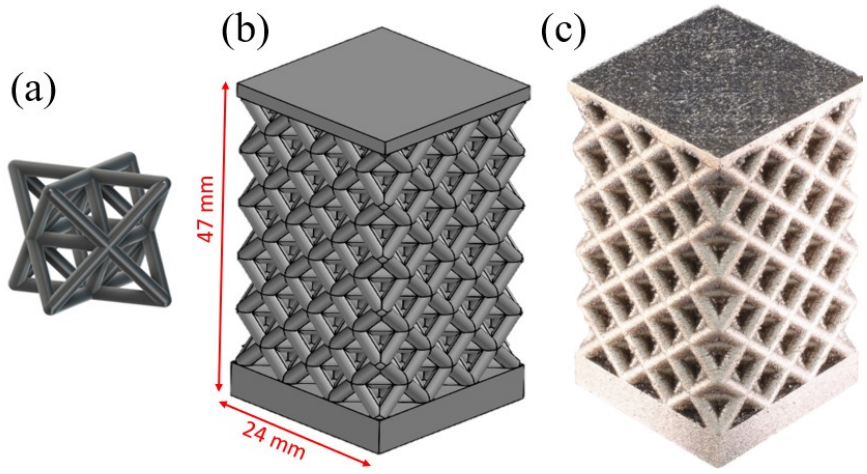

Figure 155. (a) A basic octet unit cell; (b) a CAD model made in the nTopology environment; and (c) a real-world octet specimen.

The building was created using L-PBF technology (Figure 155c). The Concept Laser M1 Cusing machine, which is covered in depth in section 3.2.2, was specifically utilized. The

specimen was produced using the best process settings discovered in earlier research [69]. More specifically, the laser power was adjusted to 100 W, the scanning speed to 180 mm/s, the layer thickness to 40 μm, and the hatch distance to 140 μm. In order to prevent barriers from being created during the recoating process, the structure was placed at a 45° angle to the recoater blade. To lessen the thermal stress created during printing, the contour infill scanning approach was applied, with scanning of arbitrary islands of 5x5 mm^2 [172].

4.3.2.2 HR-OT in-process layerwise monitoring equipment

The system that was used has a Canon Eos 760D off-axis camera with an EF 105 mm macro lens and a sensor size of APS-C (22.2 14.8 mm). The estimated optical resolution in this arrangement was 18 μm/pixel, which is further enhanced in comparison to the experiences of other authors and similar OT systems [110,163] while keeping a sizable field of view (108x72 mm^2). The camera aperture was kept to its smallest setting, and the exposure period was set to be equal to the amount of time required to complete the scan of each slice. Section 3.2.1 of this article contains a detailed description of the layerwise in-situ optical monitoring system, also known as "High-resolution optical tomography", and the technique used in this study. The camera was specifically automatically activated by a sensor attached to the coater system, allowing us to set the exposure period equal to the precise amount of time required for the completion of each layer, even if that time is variable, as it is for lattice constructions. The monitoring for various layers produced several photos that were reported after perspective correction (please see Figure 156).

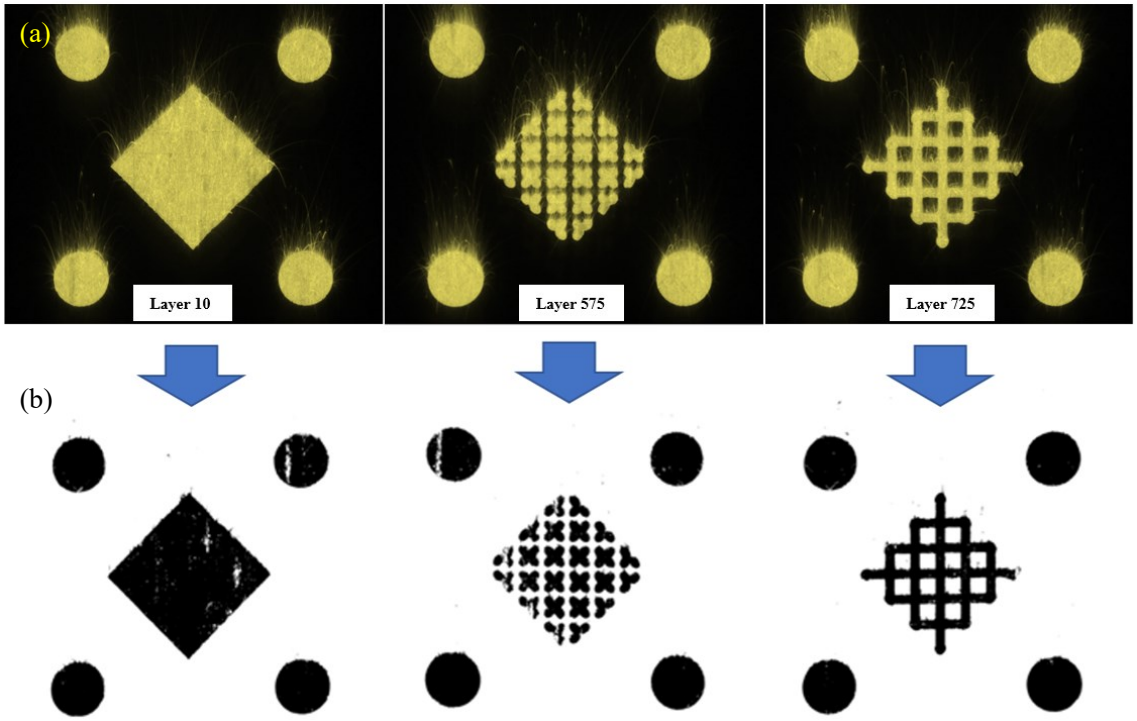

Figure 156. HR-OT images. Corrected (a) and after image processing (b).

The initial perspective adjustment was performed during the picture processing stage using the Matlab program for projective transformation using four control points (derived from four cylinders fabricated on the same building platform). Therefore, a number of easy procedures, including thresholding, contour extraction, and skeletonization, were applied to the obtained and corrected pictures (Figure 156a) (Figure 156b). For the in-process analyses described in the following sections, skeletonized images were used to obtain the XY coordinates of the sliced contour for each layer. At the conclusion of the process, these contours were stacked by adding the z-axis information of the layer height to form an XYZ point cloud representing the entire geometry. Finally, the aforementioned point cloud was used to create a highly detailed mesh. The data alignment was done in order to accurately superimpose the layer contour originating from the HR-OT and the relevant CAD section before executing the analysis mentioned in the following section. Subsequent layers were then affected by the transformation matrix that had been constructed using the first layers. The suggested system has two steps: the first is frame capture, and the second is picture processing. Since the camera is automatically activated by a sensor attached to the coater system, which begins the camera for picture capture once the recoating with a fresh powder layer is complete, the acquisition phase doesn't add time to the print. After that, it is possible to do the image processing steps of gray-scale conversion, binarization, contour extraction, and skeletonization. The time required for this phase varies depending on the performance of the computer processor, although it is typically less than the time required to finish

scanning each slice, allowing findings from one layer to be obtained before the completion of the next. The system may be used as a real-time approach for the aforementioned reasons, and it is appropriate for process control thereafter.

The measurement of reference geometries was done in order to evaluate the precision of the monitoring technique that was put into place, which included acquisition and image processing. Four 12-mm-diameter cylinders were built on the same construction platform and subjected to identical image processing steps for this purpose. So, the distances (diagonals) between two cylinders placed at different heights and opposing corners were taken into consideration. The monitored area is more accurately represented by diagonal measurements, which are also appropriate for measuring dimensional accuracy [126]. A combined 3D optical scanner based on structured light with a working surface of 100 x 70 mm2 and an optical resolution of 40 µm was compared to the average of five sections. As can be seen, variations were around 0.05 mm, which is equivalent to the normal process precision (Table 30).

Table 30. Results of measurements of length in one direction. Comparative analysis with the combined 3D optical scanning system.

Unidirectional Length	Average REF [mm]	Average HR-OT [mm]	Absolute Deviation [mm]
Diagonal 1	70.76	70.81	0.05
Diagonal 2	70.80	70.85	0.05
Average			**0.05**

4.3.2.3 Data Analysis Methodology

First, the slice contours derived from the obtained pictures (HR-OT data) and the matching CAD contours were compared as part of the in-process data analysis. To do this, the GOM Inspect program was employed, and for a few typical layers, coloured maps and histograms reporting the variances between homologous CAD/HR-OT points were provided. So, layer by layer, the average of the detected absolute deviations was gathered, and its trend was examined in relation to the sample height.

This 2D section analysis was able to identify the most crucial components and assess the dimensions and geometrical correctness of the as-built layer in comparison to the nominal. It is important to note that the method given here is the first to be able to rebuild a lattice structure's intrinsic features while it is still being created. The thickness and waviness of the strut, which have a significant impact on mechanical and energy absorption capabilities, are two such crucial factors that should be examined more closely, as determined by earlier research [166,168]. The central axis of the constructed strut is not collinear with the central

axis of the nominal strut since the strut waviness is defined as variations in the location of the strut axes. This factor is crucial because, according to [168], excessive strut waviness can cause eccentric loading, which can cause the struts to collapse under below-nominal loads and limit their ability to absorb energy. Another parameter utilized to analyze the strut shape is the strut thickness, which has a significant impact on the studied structure's mechanical characteristics [165,166].

This study examined the thickness and waviness of two typical, differently-orientated struts, designated A and B, as part of the local analysis (Figure 157). In particular, the A growth direction contrasts with the B growth direction in terms of the recoating movement direction. Layer by layer, the extracted contours were subjected to examination. The strut section is elliptical on the layer plane as a result of this inclination angle, and after the fitting procedure based on the least square framework, the minor axis length was employed to indicate the strut thickness. The centre coordinates (X, Y) of the elliptical strut section, taken from the contour of the collected picture, were used to build the strut waviness, which was defined as the distance between the nominal and actual axes. The created strut's central axis is a fictitious line that passes through the centres of the fitting ellipses. The strut waviness was calculated as the Euclidean distance between the fitted ellipses' centre and the nominal centre axis.

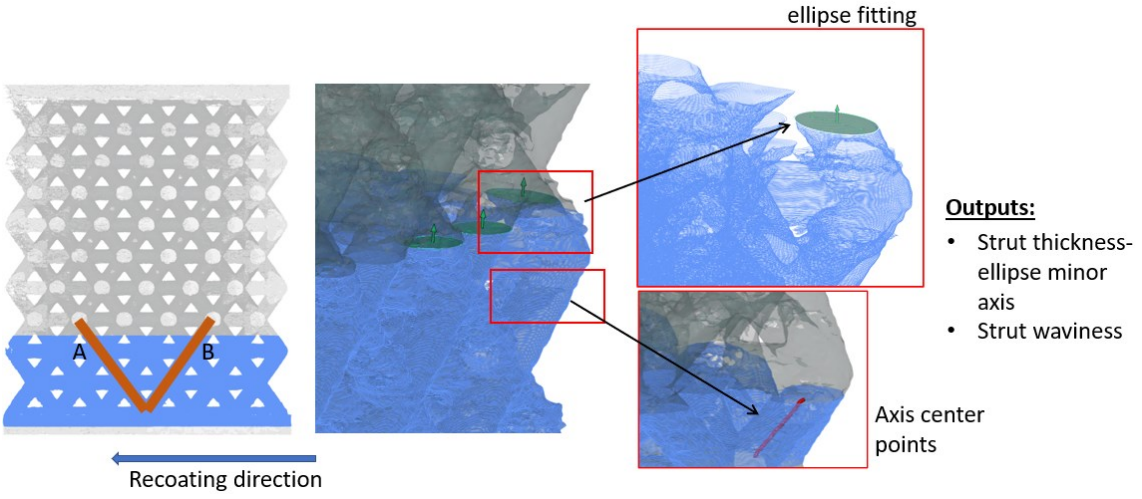

Figure 157. The analyzed struts A and B are indicated in the HR-OT 3D model. A typical fitted ellipse and axis centre points that were taken from a single strut were used to highlight the layers.

The applied method produced a high-resolution point cloud that was transformed into a precise 3D mesh at the conclusion of the manufacturing process by stacking the extracted layer contour points. The latter was utilized for a 3D comparison with the CAD model that took into account both exterior and interior aspects, allowing for more in-depth post-process structural evaluations or, perhaps, more accurate numerical simulation applications.

To obtain a high-resolution 3D model of the final built structure to support the discussion of

the results presented in the following section, an off-line measurement system was used. It was based on 3D digital close-range photogrammetry with a rotary table [173] and was distinguished by comparable accuracy to the structured light system [126] but with higher resolution. The Canon EF 50 mm f/1.8 II lens was utilized with two Digital SLR cameras Canon Eos 760D (24.2 Megapixels, Sensor Size APS-C 22.2 x 14.8 mm), at their closest focusing distance (350 mm). The Ground Sampling Distance (GSD), determined by the chosen optical setup, was 24.2 μm/pixel. In order to scale the model, coded targets were employed, and the acquisition method was created in accordance with the sample geometry. Being a 3D optical scanner, the output data corresponds to the structure's outside surface and will be utilized as a guide for later investigations.

4.3.3 Results and Discussion

First, the 2D deviation analysis between the HR-OT/CAD data is provided (Figure 158). As example cases, three layers at three different structural heights were taken into consideration, displaying a 2D comparison between CAD and HR-OT homologous locations that are now being done. These comprehensive tools for in-process monitoring of L-PBF structures, which provide quantitative dimensions and geometrical indications for each studied layer, include coloured maps and histograms of the recorded deviations.

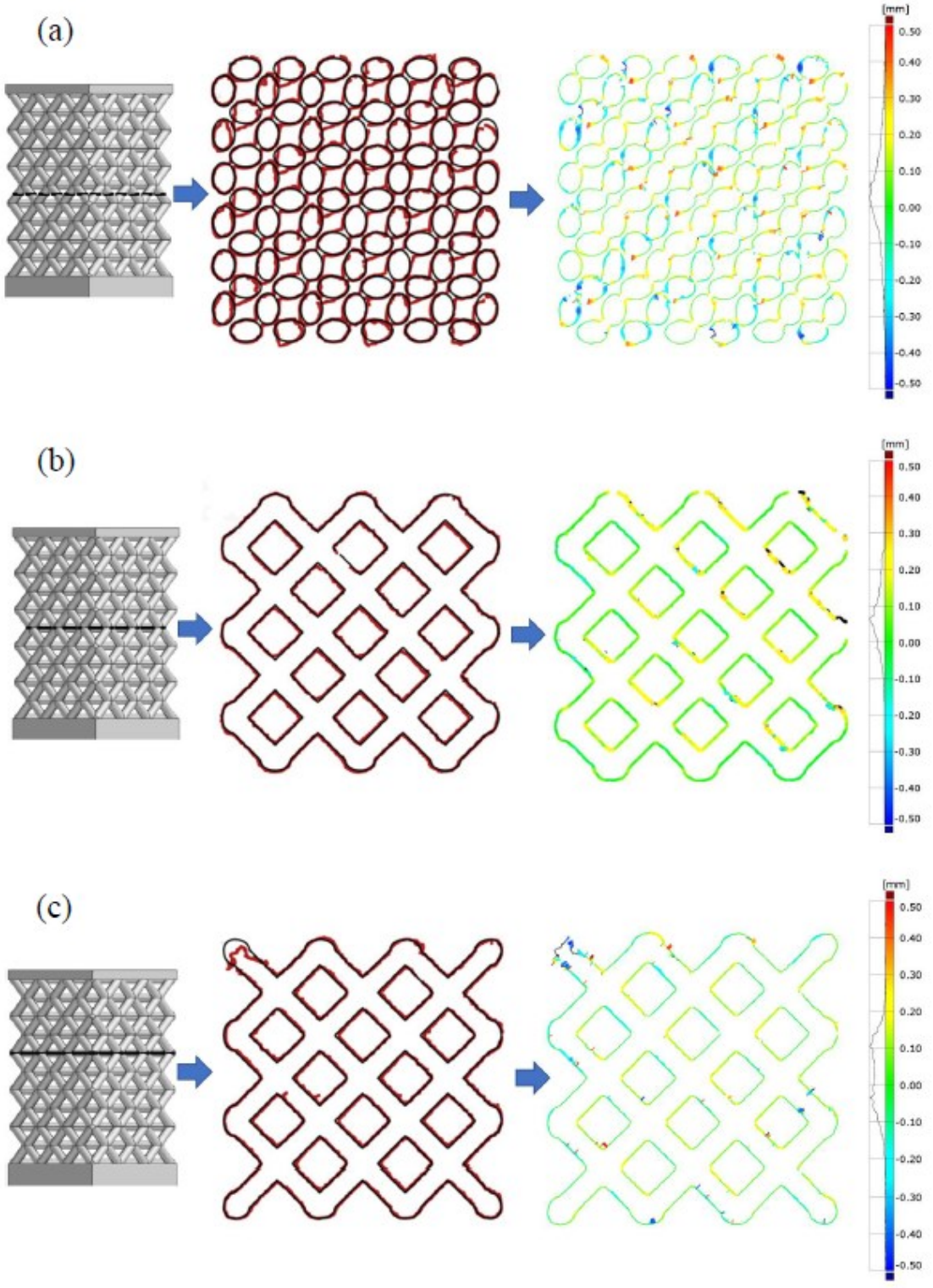

Figure 158. 2D deviations analysis at layers 575 (a), 625 (b), and 725 (c) with HR-OT (red) and CAD (black) contours overlay.

After being gathered layer by layer, the average of the absolute deviations between homologous CAD/HR-OT points as a consequence of the 2D analysis is shown in Figure 159 with regard to the sample height. The exterior nodes (Figure 158c) were the most crucial, with the majority of reported values being on the order of 0.1 mm and layers indicating the strut sections (Figure 158a). Due to the geometric distortions seen on the top skin section, deviations quickly grow up to 0.2 mm.

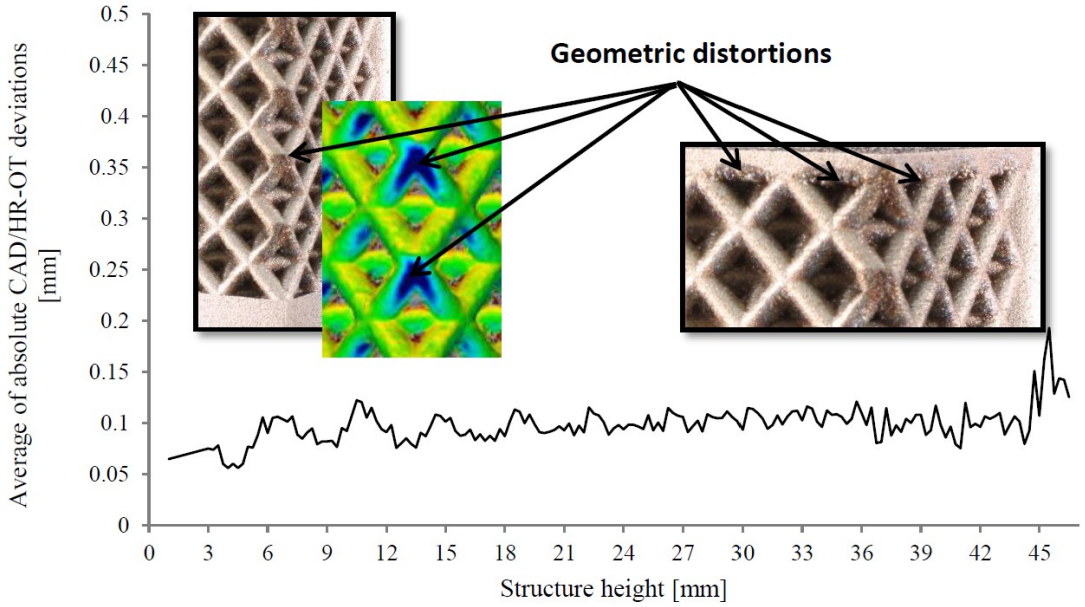

Figure 159. Analysis of the 2D deviations between the nominal data and the HR-OT in real- time. The 3D comparison of the photogrammetric and CAD models is shown on the coloured map.

The mesh created using HR-OT and the CAD model was compared in three dimensions at the conclusion of the L-PBF process in order to evaluate the overall quality of the structure. The coloured maps (Figure 160) show that deviations were mostly contained within 0.1 mm, and several critical locations on the exterior surfaces were found in agreement with the more external nodes and strut overhanging surfaces, validating the criticalities discovered by the 2D deviation analysis.

It should be emphasized that this 3D comparison was done offline, much like the XCT data analysis for geometric and dimensional characterization that was done after the procedure was finished. It's crucial to note that both methods—HR-OT and XCT—can produce a complete 3D reconstruction (internal and exterior) suited for offline studies of the entire 3D object. Although the first, the HR-OT, has a significant cost advantage and the capacity to capture data as it is being processed, layer by layer.

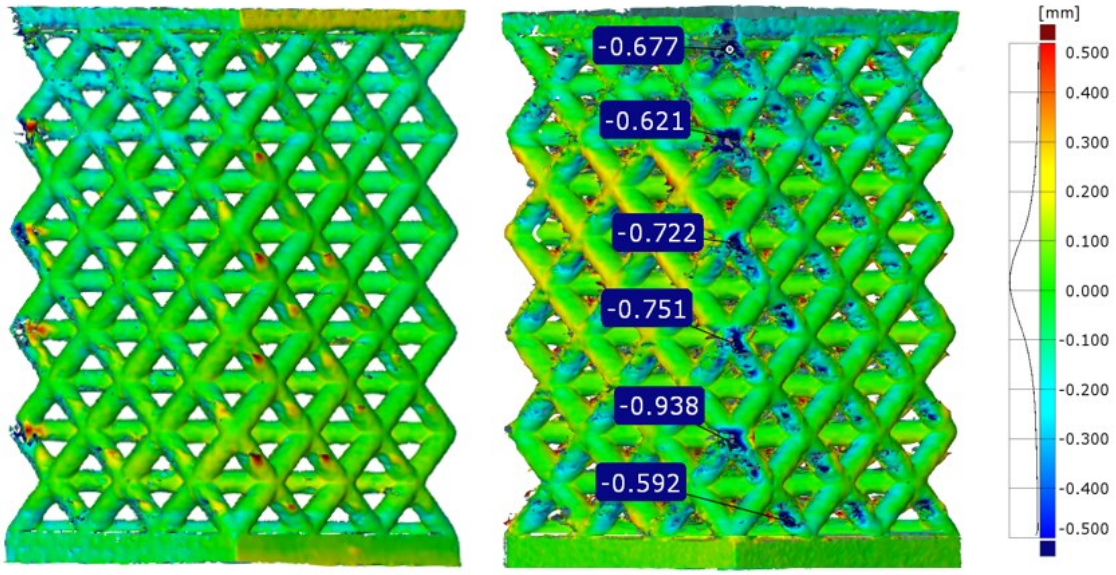

Figure 160. CAD-HR-OT mesh 3D comparison.

The local analysis is frequently necessary when studying complicated geometries, such as lattice systems, in order to assess the geometrical and dimensional correctness of the principal features, such as struts and nodes. The geometry of the strut was taken into account when doing the local analysis in this study. Results of the local study on the two A and B struts, which have distinct orientations, are provided (Figure 161 and Figure 162). The strut A (Figure 161a and Figure 161b) showed an average value of 1.98 mm with a standard deviation of 0.03 mm when the strut thickness was taken into consideration as the minor axis of the fitted ellipse. The minimum and maximum absolute percentage errors recorded were, respectively, 1.60% and 5.22%. The majority of the examined layers revealed a minor axis value for strut A that fell between 1.97 mm and 1.99 mm.

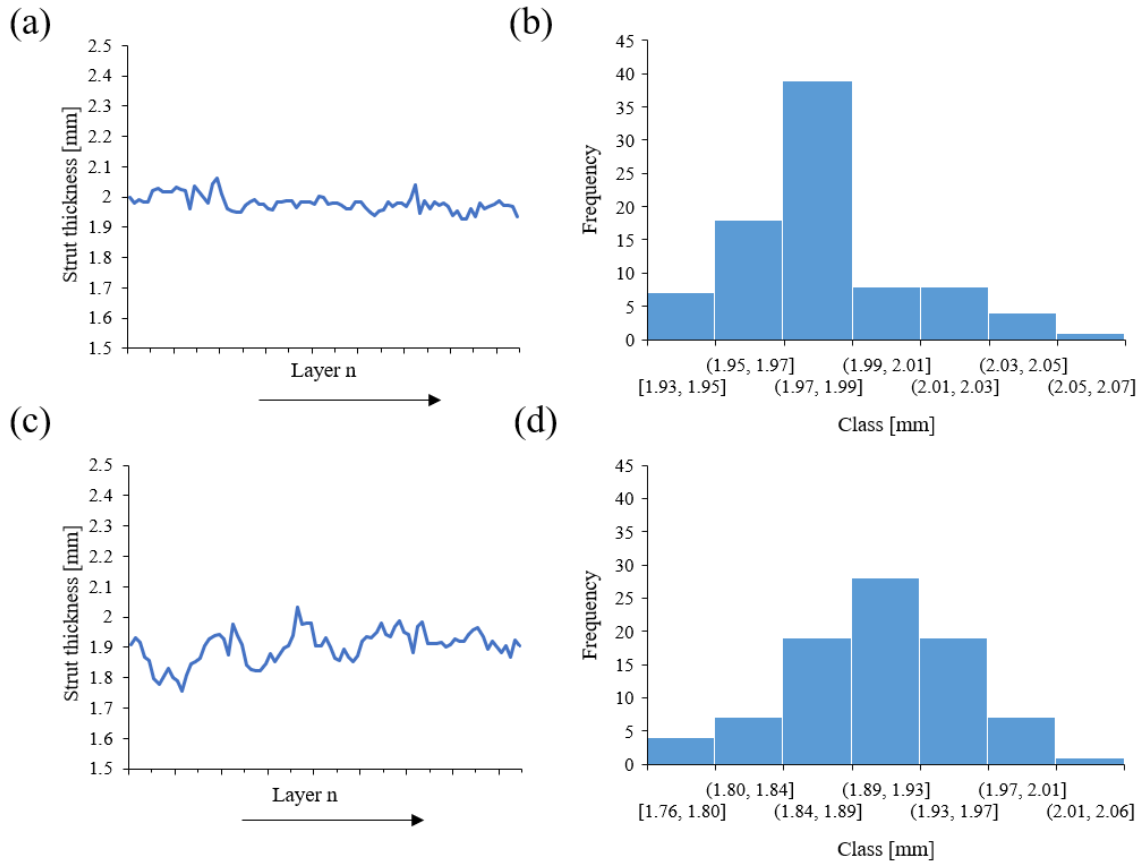

Figure 161. A and B's strut thickness variations were assessed in (a) (c). For struts A and B, respectively, the acquired values' histograms are shown in (b) and (d).

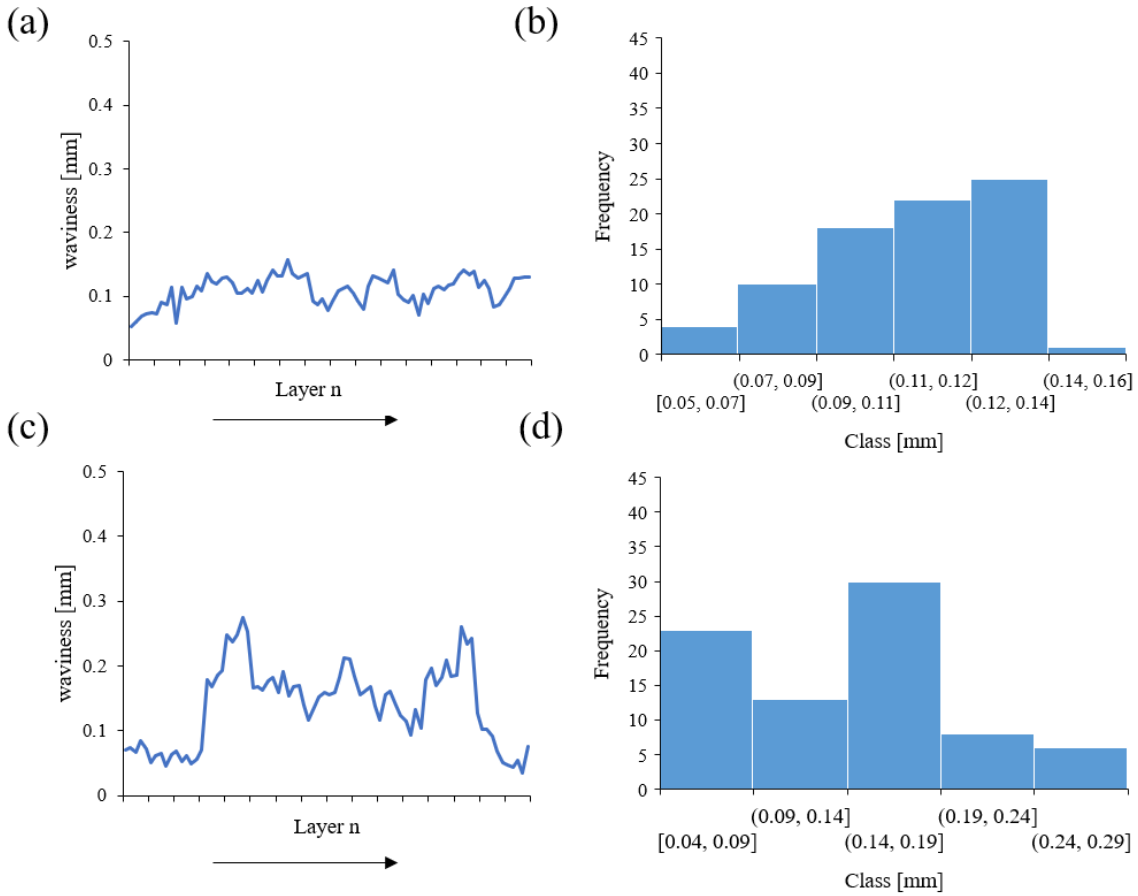

Figure 162. Evaluation of the strut waviness for strut A in (a) and strut B in (c). For struts A and B, respectively, histograms of the acquired values are presented in (b) and (d).

Figures 161c and 161d, which depict strut B, reveal a worse tendency. As can be seen, there were larger discrepancies between the nominal and real values, and the actual value was often much lower than the nominal value. Further information shows that the actual average value was 1.89 mm and the standard deviation was 0.06 mm. They were, in accordance with the minimal and greatest absolute percentage mistakes, 1.43% and 16.80%, respectively. Values in this instance were primarily included between 1.89 mm and 1.93 mm.

Results from the waviness study (Figure 162) revealed that strut A, (Figure 162a and Figure 162b), was characterized by an average value of 0.10 mm and a standard deviation of 0.03 mm. The strut B (Figures 162c and 162d) had an average value of 0.13 mm and a standard deviation of 0.07 mm. The primary distinction between the struts under consideration has to do with their development orientations. The A was moving in the same direction as the recoater, whilst the B was growing in the other way. This topic will be covered in more detail in the section after this one.

According to the literature [109,110], optical tomography is frequently employed to detect interior flaws, and in these setups, visible and near-infrared camera sensors are utilized. As was already said in the first section, this approach does actually capture a single picture for each layer that is made up of a collection of signals that are imaged into the associated pixel detector in accordance with the radiation strength produced by the laser-powder interaction. In this manner, the scanning method and hatching pattern may be understood and are consistent with the resolution capabilities [72,110]. If pictures are rendered in grayscale and then shown as a false-color image, changes in the laser-powder interaction are captured as a variation in the radiation that is emitted, followed by a variation in the gray-scale values that correspond to each pixel. As a result, irregularities in the normal melting process can be found and may be connected to the beginning of process problems. The amount of radiation emitted depends on the condition of the material being impacted by the laser; for example, more light is produced when the laser scans an area above unmelted powder than when it scans an area over fully melted and resolidified components. Due to the various cooling speeds of the unmelted powder and the melted and resolidified material, as well as the resulting differences in thermal conductivity, less light is released. A picture of the top skin's initial layer once the lattice structure has been completed, for instance, is reported (Figure 163a). The regions shown in red are those where the scanned layer was covered with unmelted powder. The red portions are distinguished by values close to 255, according to a profile plot of the grey values that shows them evaluated along a straight line, while the regions where the laser scans the powder with melted and resolidified layers underneath (corresponding to the lattice structure section) were distinguished by lower grey values.

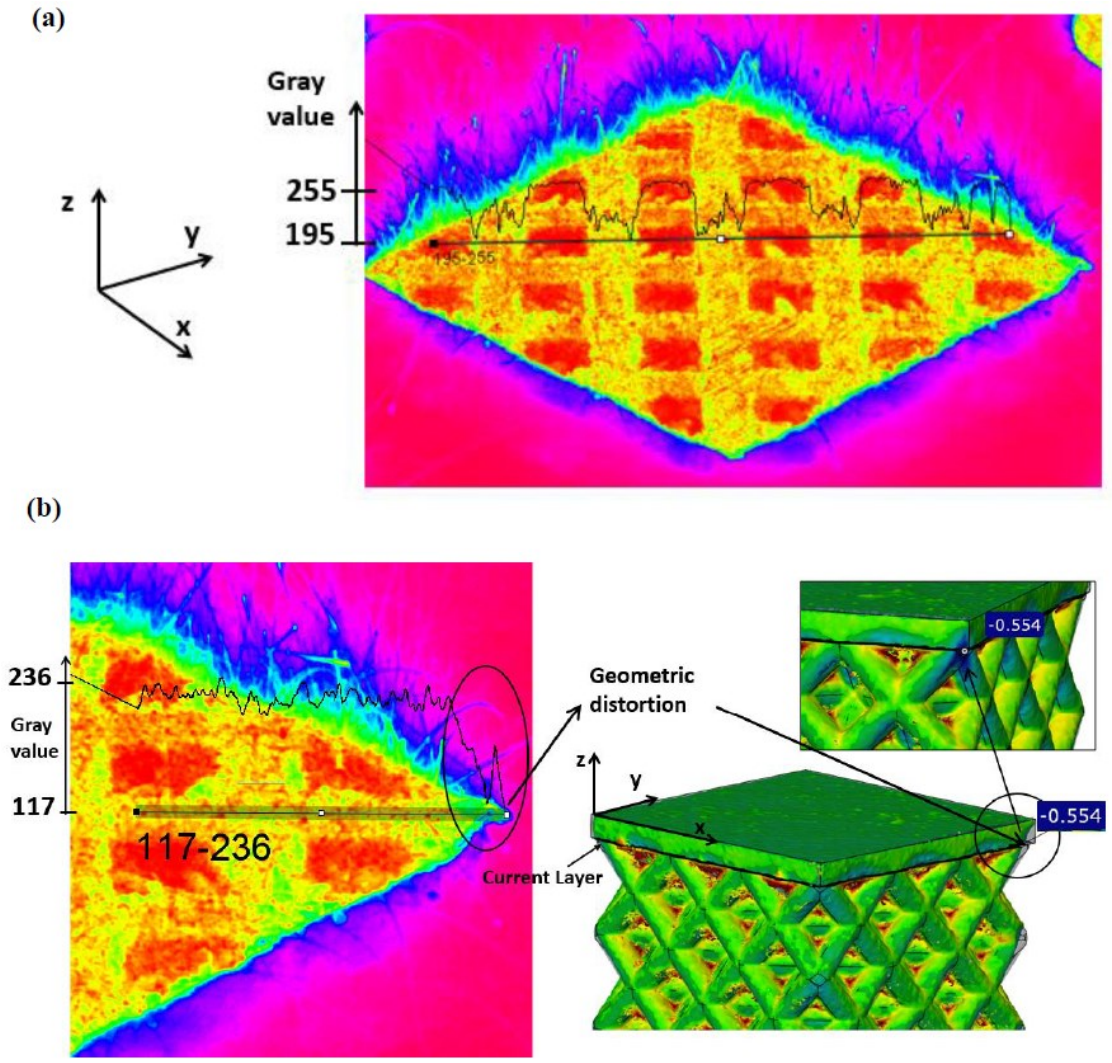

Figure 163. The first layer of the top skin follows the development of the overall lattice system. The false colour representation of the complete layer is displayed in (a). In (b), the emphasis is on a geometric distortion seen at the same layer. The image displays the coloured comparison map between the photogrammetric and the CAD models in three dimensions for reference.

The coloured map of the 3D comparison between the photogrammetric and the CAD model, Figure 163b, shows that areas with high geometric distortions, primarily in the form of superelevated areas and edges, correspond to pixels with lower intensity (lower grey values), as a result of remelting of previously melted areas (higher thermal conductivity with respect to unmelted powder and less heat accumulation). As a result of the tiny size of the strut sections and the intricacy of the lattice structure, these constructions are more susceptible to superelevated edge flaws (Figure 164). Furthermore, zone B in Figure 164 exhibits more distortion than zone A due to the fact that zone B was the first zone of the layer to be impacted by the recoater during its transition.

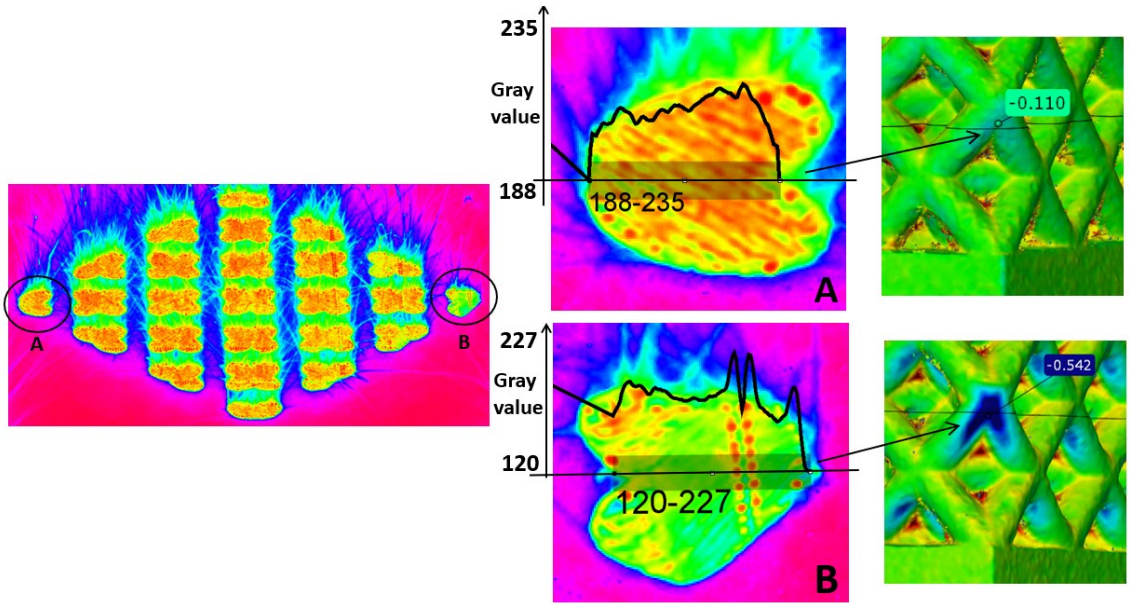

Figure 164. Layer showing the strut sections as they approach the nodes. The image provides a visual representation of the coloured comparison map between the CAD and 3D photogrammetric models.

The failure of the construction process may also be caused by superelevated regions and geometric deformities that were heavily concentrated on the margins of the recoating system that were expanding in the opposite direction (Figure 165).

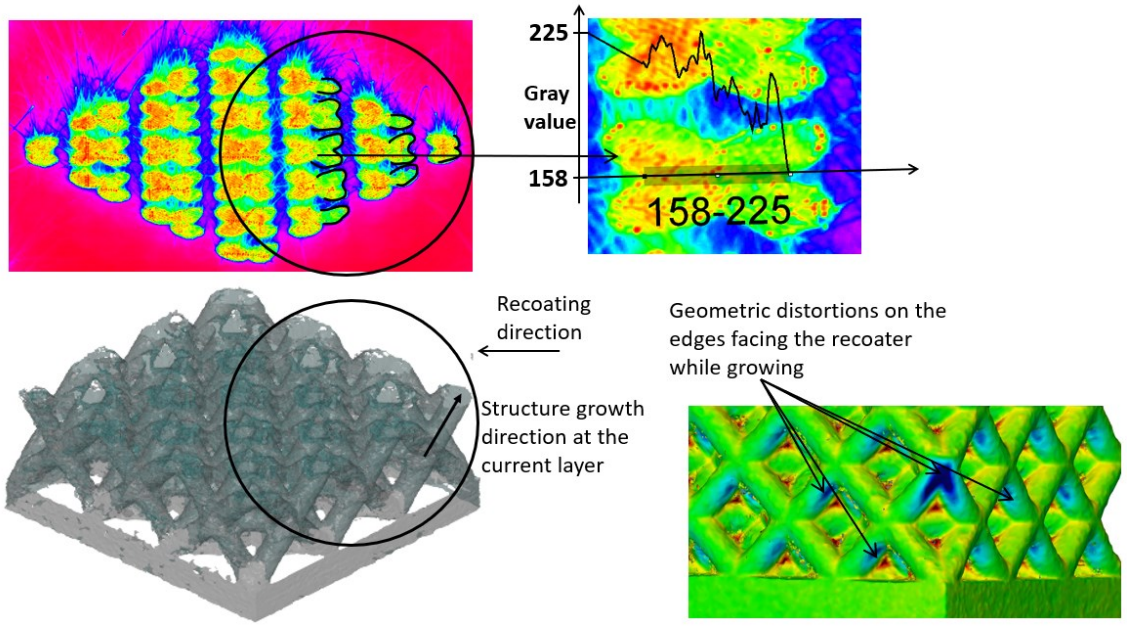

Figure 165. Strut portions that show which way their development is going in relation to the coater's direction. The coloured comparison map between the 3D photogrammetric and the CAD models is displayed in the image as a point of reference.

The studies that were done are illustrations of in-process quality inspections that are compatible with HR-OT data and may serve as the foundation for additional in-process statistical analytics and process control.

4.3.4 Conclusions

This study presents a novel and economically advantageous optical layerwise monitoring method based on HR-OT for the dimensions and geometrical characterization of lattice systems. Using 2D comparison tools and local analysis, the system may be used for online monitoring and can identify process errors layer by layer. Additionally, it offers a 3D reconstruction of the created structure at the conclusion of the production process for use in quality control and, maybe, numerical simulation applications. In-depth layerwise studies that took into account the comparison of 2D real and nominal data were carried out, and the results offered substantial hints regarding the geometrical and dimensional correctness. Additionally, a more focused investigation of the shape of the struts was made. The accuracy of the developed system was evaluated using standard geometries, and the average deviations from the reference data were in the range of 0.05 mm, which is equivalent to the precision of the L-PBF process. The findings of this study proved that high-resolution optical tomography is a viable in-process monitoring technique for complicated geometries and lattice structures made by L-PBF. It may be viewed as a highly cost-effective alternative to XCT for dimensional, geometrical, and surface quality evaluation because of its capacity to recreate interior characteristics.

Fourth case study

4.4 Intralayer Multi-material Structure Stainless-Steel/Nickel-superalloy fabricated via Laser-Powder Bed Fusion process

The following is the paper with the title "**Intralayer Multi-material Structure Stainless-Steel/Nickel-superalloy fabricated via Laser-Powder Bed Fusion process**", published in *Manufacturing Letters* in 2022. See section 7 for the publication details.

4.4.1 Aim of the work

The aim of this work was to study an innovative approach to demonstrate the producibility of an intralayer multi-material Stainless-Steel/Nickel-superalloy structure, produced via a blade-based L-PBF system. The cost-effective, flexible, and easy-to-use system developed can be implemented on already operating L-PBF machines. The microstructural and chemical properties at the interface of the multi-material component were studied extensively. This is the first work in which a layer-wise in-situ optical monitoring system was implemented during the fabrication of a multi-material component in order to ensure the high final quality of the manufactured components.

4.4.2 Materials and methods

4.4.2.1 Experimental setup and materials for the L-PBF process

Two bi-material rectangular parallelepipeds with dimensions 50x20x3 mm were fabricated

through an M1 Cusing (Concept Laser) machine. A partitioning system was developed and placed within the powder chamber, oriented in XZ plane (Figure 166a). This system allowed intralayer fabrication of the multi-material structure without contamination between two metal powders. The powders used were AISI 316L stainless-steel and a Nickel-superalloy, both gas-atomized, and having the chemical composition shown in Table 31. The particle size of the AISI 316L powder is in the range of 15-53 µm while the Nickel-superalloy is in the range of 15-45 µm, and both exhibit a spherical shape as shown in Figure 166b and Figure 166c. Table 31 also shows the set of process parameters used in this work, which had been optimized to obtain L-PBF parts of each powder above-mentioned with a density of about 99%.

Table 31.Chemical compositions and process parameter values.

Chemical composition of powder materials [wt.%]										
	C	Ni	Cr	Mn	Co	Mo	Al	Ti	W	Fe
Nickel-superalloy	0.16	Bal.	15.60	-	10.73	1.20	2.98	5.17	2.11	-
AISI 316L	0.02	10.10	16.70	1.00	-	2.04	-	-	-	Bal.

Process parameters						
Laser power [W]	Scan speed [mm/s]	Laser spot diameter [µm]	Hatch distance [µm]	Layer thickness [µm]	Scan strat-egy	Island size [mm^2]
100	200	200	140	30	Rand-om island	5x5

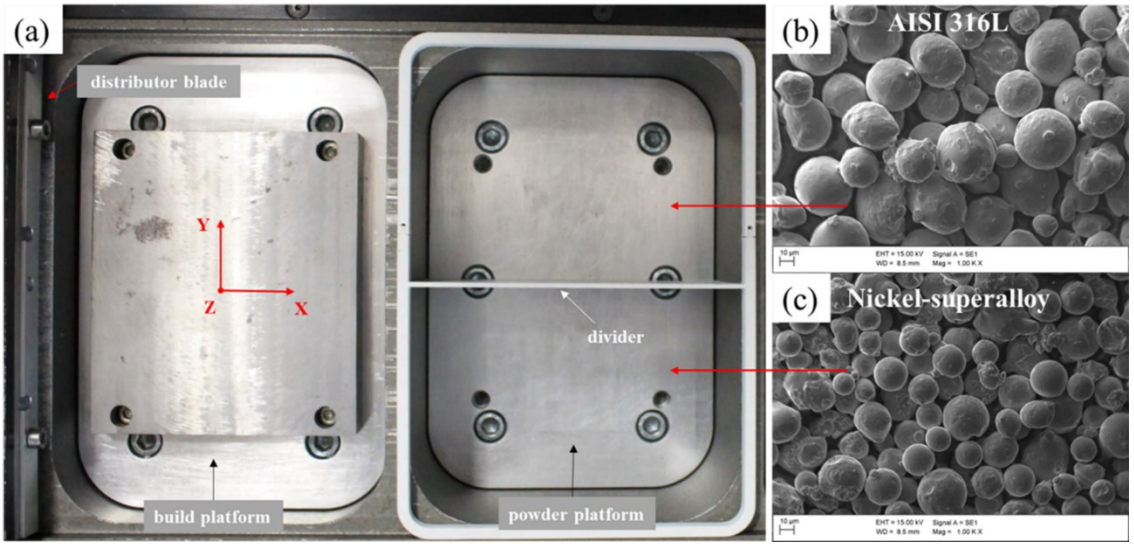

Figure 166. (a) Design of the partitioning system within the powder chamber that enabled the intralayer fabrication of the multi-material structure; (b) and (c) SEM images of AISI 316L and Nickel-superalloy powders.

4.4.2.2 In-situ optical monitoring system

To characterize in-situ and real-time the process during the fabrication of the multi-material

structure, a layerwise optical monitoring system called High Resolution-Optical Tomography (HR-OT) and an image processing methodology shown in detail in Figure 167, were implemented. Specifically, the monitoring system implemented consists of a high-resolution CMOS off-axis camera (Canon Eos 1100D), equipped with a lens and a set of neutral-density filters. The camera was set in bulb mode with an ISO equal to 100; furthermore, the exposure time was synchronized with the scanning time of each whole layer through a trigger. Further specifications on the implemented monitoring methodology and statistical process control are described in detail in previous section 3.2.1. As an output of the monitoring analysis, the deviation (D) of the interface real profile between the two materials from the ideal (linear) one was evaluated, as shown in Eq. 1.

$$D = \frac{1}{L}\sum_{i=1}^{L}|GV_i - \overline{GV}| \quad (1)$$

where L = width clipping window (px), GV_i = gray value after threshold segmentation, $(\overline{GV})$ = arithmetic mean of the GV_i values and i = i_{th} pixel in the clipping window.

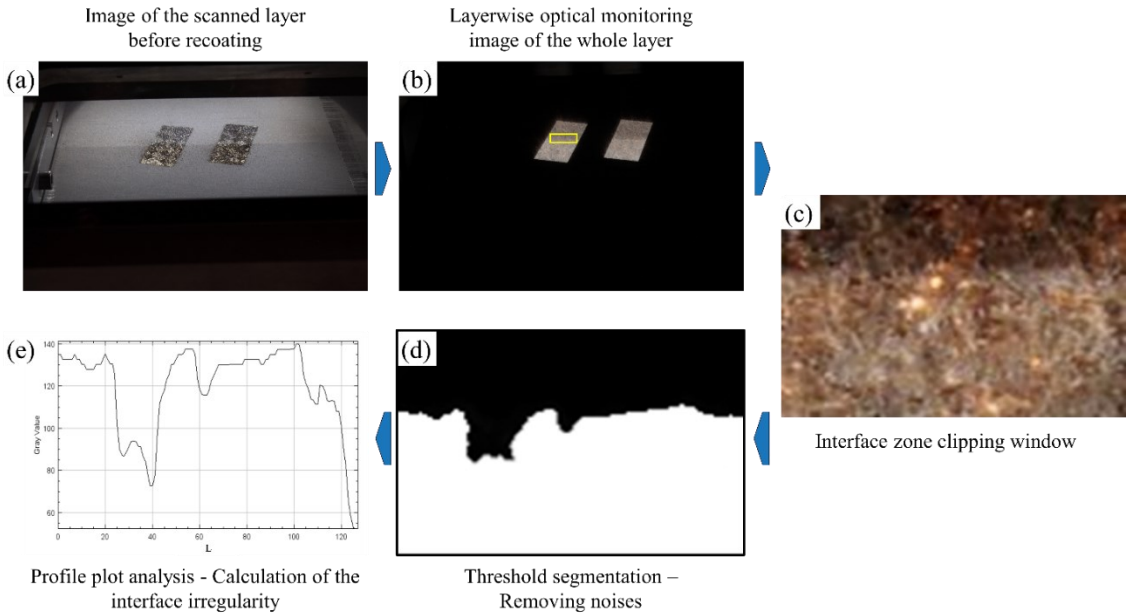

Figure 167. Workflow of the layer-by-layer image capture and processing steps. During the sintering of each layer, an image was captured showing the visible radiation emitted by the two materials (Fig. 2b). Subsequently, from each of these images, a rectangular window with a width of L (pixels) was selected to include the interface between the two materials (Fig. 2c). Using the image analysis tools, the window was converted into a binary image (Fig. 2d) from which the actual shape (a curve) of the interface between the two materials is derived (Fig. 2e). If one considers this binary image as being composed of a number of vertical stripes equal to L, for the i-th stripe the grey value (GVi) is given by the fraction of white (which is worth 255) compared to black (which is worth 0). In the ideal case, the interface would have the shape of a straight segment and the GVi values would all be equal: therefore, the index D would be 0.

4.4.2.3 Characterization of multi-material structure

To investigate the manufacturability of the fabricated multi-material structure, in-depth metallographic characterization of samples was carried out. The microstructural analysis was performed first with an inverted optical microscope, after having properly prepared the samples and having carried out a chemical etching suitable for both materials (10ml HNO_3 + 50ml HCl + 60ml glycerol). Subsequently, Energy Dispersive X-ray chemical microanalysis (EDX), through a scanning electron microscope, was performed especially to analyze the interface area. Finally, the Vickers microhardness profile was measured through a hardness tester, according to the ISO 6507-1 test standard (with 0.3 kgf applied load and 10 s dwell time).

4.4.3 Results and Discussion

Metallographic examination showed, as can be seen in Figure 168a and Figure 168d, that the Nickel-superalloy region presented γ' microstructure in a dendritic morphology [129,174]; however, the same region was affected by a non-negligible number of small cracks passing through laser tracks. The AISI 316L portion was characterized by a flawless structure with dendritic morphology and without porosity (Figure 168a and Figure 168b). The interface area between the two metals was crack- and porosity-free (Figure 168a). In Figure 168c swirls are visible, caused by the Marangoni effect between the two different materials. As stated in previous works, the circular flows induced by the Marangoni convection affected the molten pool size and, consequently, the migration of the elements from the two alloys, sorting in very strong bonding between them [175,176] This good result was also supported by SEM analysis (Figure 168e), which shows, at the interface, a gradual and regular variation of the concentration of some characteristic elements (i.e., Fe, Ni, Ti) of the two alloys. In addition, from the chemical analysis, the narrow width (≈600 microns) of the interface area between the two materials was identified; EDX maps also confirmed this result (Figure 168e). Figure 168f shows that within the interface zone (≈600 μm) the microhardness uniformly increases from the AISI316L (≈230HV) to the Nickel-superalloy (≈390HV). This result is a further confirmation of the sound metallurgical bonding between the two materials, as stated by Wang et al. [177]. It is also noteworthy that chemical, metallographic, and microhardness analyses excluded the presence of brittle intermetallic phases.

Finally, statistical control of the process, developed through the control chart shown in Figure 168g, demonstrates real-time layer-by-layer the absence of contamination between the two different materials since parameter D (defined in Eq. 1) remains under control throughout the whole print.

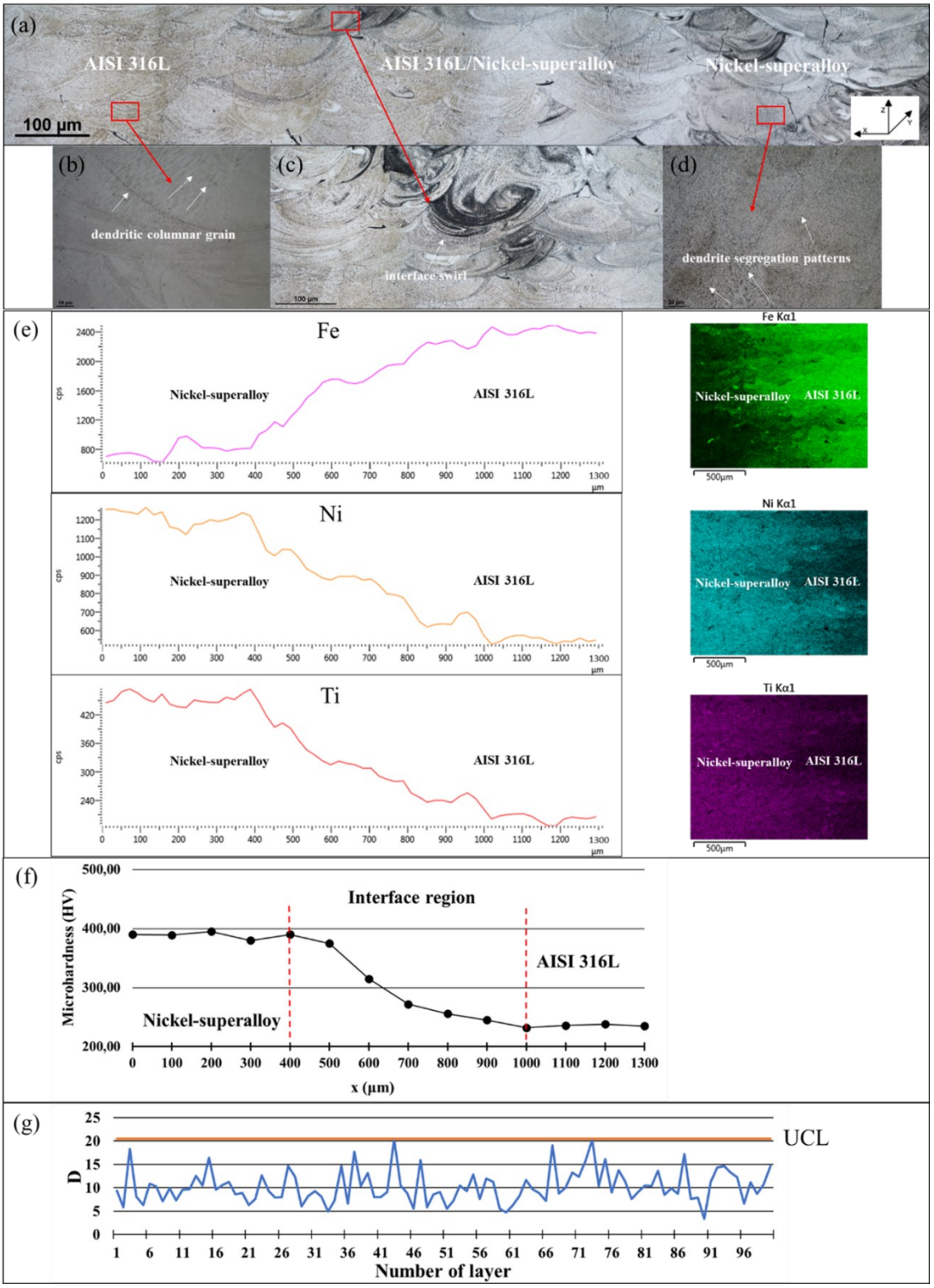

Figure 168. (a) Optical micrograph of the Stainless-Steel/Nickel-superalloy multi-material component cross-section at 500x magnification; (b) 1000x magnification of the AISI 316L area; (c) 500x magnification of the interface area; (d) 500x magnification of the Nickel-superalloy area; (e) results of the EDX analysis performed along the interface region: line scans and maps of the main alloying elements present in the two materials; (f) Vickers microhardness profile measured along the cross-section; (g) Shewhart Control Chart for Individual Measurements of the deviation parameter.

4.4.4 Conclusions

In this work, an innovative approach for the manufacturability of an intralayer multi-material

Stainless-Steel/Nickel-superalloy structure, produced via a blade-based L-PBF system, was studied. The main results are listed below.

- Excellent bonding between the two materials was detected; the interface appeared crack- and porosity-free and resulted in a very tiny (≈600 μm).
- Within the interface area, the presence of swirls induced by the Marangoni convection stated the sound metallurgical bonding between the two materials; this result was confirmed by the gradual and regular variation of both the concentration of the characteristic elements (Fe, Ni, Ti) of the two alloys and the microhardness.
- The deployment of the layer-wise in-situ optical monitoring system allowed real-time layer-by-layer monitoring of the deviation of the interface real profile between the two materials from the ideal (linear) one in the whole structure; this system allows to verify the lack of contamination between the different materials, ensuring the high quality of the produced component, without additional expensive and time-consuming inspections.

The present work demonstrates that the developed system enables the successful fabrication of intralayer multi-material structures. The results obtained demonstrate the significant potential of this new methodology, which could be extended in future works for the fabrication of functionally graded intralayer structures.

5. Conclusions

In this thesis work, new solutions were provided to overcome certain technological limitations that slow down the industrial development of the Metal Additive Manufacturing (MAM) technologies examined in this thesis, the Laser-Directed Energy Deposition (L-DED) and Laser-Powder Bed Fusion (L-PBF) processes.

The main contributions of the thesis are outlined below.

Initially, I carried out an in-depth study and analysis of the scientific literature relating to the L-DED and L-PBF processes, with particular reference to processes monitoring that would overcome the limitations of these two technologies. Specifically, as a preliminary step, I conducted some experimental studies of correlation and optimization of process parameters controllable in the L-DED process, investigating the effects of these input parameters on the output factors examined (final track geometry). For this experiment, I used tools such as analysis of variance (ANOVA) with a general liner model in order to obtain the statistical significance of the effects. Continuing this study and given the ambiguity in the literature on the effects of certain combined parameters on the geometry of the final trace, I subsequently conducted a robust experimental investigation that allowed me to study the combined effects of the parameters of laser defocusing distance and standoff distance on the geometrical characteristics of the single deposited clad. In particular, in order to provide an exhaustive explanation of the phenomena, an analytical model I have proposed on the track width (modified from Liu and Li's model) of a single deposition, which internally includes powder distribution and laser-material interaction.

Subsequently, I conducted preliminary studies on the in-situ and real-time monitoring systems of both examined processes. In particular, a new coaxial optical monitoring methodology was developed for the L-DED process, which exploits the combination of suitable coaxial optical sensors and the development of appropriate image processing algorithms to improve the accuracy and quality of depositions performed with complex deposition strategies and geometries. The implemented monitoring methodology proved to be fast and stable and can be successfully applied for closed-loop monitoring in real-time applications. It was used in several case studies, such as coating applications, presented in Chapter 4 of the thesis, which confirmed the validity of the developed methodology. With regard to the L-PBF process, on the other hand, I developed a cost-effective, flexible, and easy-to-use optical monitoring system called 'high-resolution optical tomography', which was implemented to detect geometric distortions occurring during the L-PBF process. As mentioned in Chapter 3, with this developed monitoring methodology it is possible to

investigate links still not deepened in the scientific literature, which is the study of geometric distortions through the monitoring of slice surface patterns. This monitoring methodology was subsequently implemented, with great success, in a very special case study, additive manufacturing of lattice structures; the result is a powerful in-situ and real-time monitoring for complex geometries and lattice structures produced by means of L-PBF. In fact, due to its ability to reconstruct internal features, with a non-complex and rapid image processing step, it could be considered a very cost-effective alternative to XCT for dimensional, geometric, and surface quality assessment. Furthermore, the output results of this implemented monitoring methodology could have a dual purpose: to support in-process the machine operator in deciding whether an instantaneous process stop is necessary, reducing waste and costs and increasing productivity, and offline, as a diagnostic support tool for subsequent qualification steps. As far as the thermal field is concerned, I implemented a preliminary thermal monitoring methodology, in collaboration with the ENEA (Agenzia Nazionale per le Nuove Tecnologie, l'Energia e lo Sviluppo Economico Sostenibile) Research Centre in Brindisi, on the L-PBF machine, in order to investigate defects such as local overheating, hence geometric distortions in the final part, and lack of melting, by monitoring the temperature profile over the whole slice area. Thermographic information can also be used as a quality control tool to detect imperfections during construction. The results obtained from this experiment have shown the feasibility of this, making this methodology the starting point for future thermographic analyses that can be conducted on the L-PBF machine at the Politecnico di Bari laboratory. Finally, the developed monitoring systems and methodologies were successfully applied to several case studies, which are presented in the final chapter of the thesis. The results have corroborated the validity of these technological solutions developed in this thesis work, which have made it possible to overcome some of the limitations of MAM processes such as the sub-optimal quality (in terms of dimensional accuracy and surface roughness) of the final parts, and the low repeatability, stability and robustness of the processes, which make them unsuitable for high-value applications requiring high-performance standards. In addition, the final results showed that it is possible to ensure a high quality of the manufactured part without additional costly and time-consuming inspections and to verify the stability of the process in-situ and in real-time. Finally, it can be said that this dissertation introduced new opportunities and technological solutions for in-situ and real-time detection and monitoring for zero-defect and first-time-right AM processes, with a focus on MAM processes.

6. Future perspectives

Despite the ongoing and rapid technological developments concerning in-situ and real-time monitoring and sensing methodologies, there are still many challenges and problems to be overcome for the production of new L-DED or L-PBF machines that would allow the production of defect-free artefacts the first time. Some ideas and suggestions for future research topics are mentioned below.

- To develop a process control system that allows, from the data collected in real-time, to operate in feedback on the manufacture by modifying and adjusting the controllable parameters. This results in less waste, less time to market, and consequently lower costs.
- One challenge is to perform a data fusion from the different optical and thermal monitoring systems, producing more accurate results.
- One challenge concerns the limitation of monitoring by layers. Indeed, the observation of the top layer prevents the collection of information on the physical phenomena occurring below the layer, which involve partial remelting for example, and the resulting effects on the volumetric, microstructural, and thermal stress properties of the material.
- An additional challenge concerns the lack of in-situ porosity detection methods. With the HR-OT process developed and presented in this thesis, this is being attempted.
- A further challenge concerns the handling of large amounts of data collected by in-situ monitoring methods. As the resolution of the implemented sensors increases, so does the size in terms of gigabytes of data and this drives the need for computationally efficient methodologies for processing in-situ and in-process data.

7. List of publications and contributions

Paper I:

On the feasibility of AISI 304 stainless steel laser welding with metal powder

Authors: V. Errico, S.L. Campanelli, A. Angelastro, M. Mazzarisi, G. Casalino

Journal: Journal of Manufacturing Processes

Status: published

DOI: 10.1016/j.jmapro.2020.04.065

Abstract
Laser welding is a manufacturing process that allows the joining of metallic parts even if accurate positioning and preparation of the welding edges are mandatory for successful welding. The use of a filler material in the form either of wire or powder can mitigate the drawback entangled with that preparation. In this work, bead-on-plates were performed on of AISI 304 stainless steel plate with AISI 316 L powder as filler material. Tests were carried out using different combinations of process parameters. The influence of process parameters like laser power, translation speed, powder feed rate, carrier gas flow rate and laser spot diameter on geometry, on microstructure and on porosity of the weld seams were investigated. The transition between conduction to keyhole regime was detected, both with and without powder addition during welding. It was found that the variation of laser spot diameter is fundamental in generating the different welding regimes. Moreover, porosity was detected only in the keyhole regime with a maximum value of 5.5%. Finally, "V-shaped" grooves were machined on AISI 304 substrate and filled by two overlapped tracks. The results of the study demonstrated the feasibility of the laser welding of AISI 304 stainless steel with AISI 316 L powder as filler material.

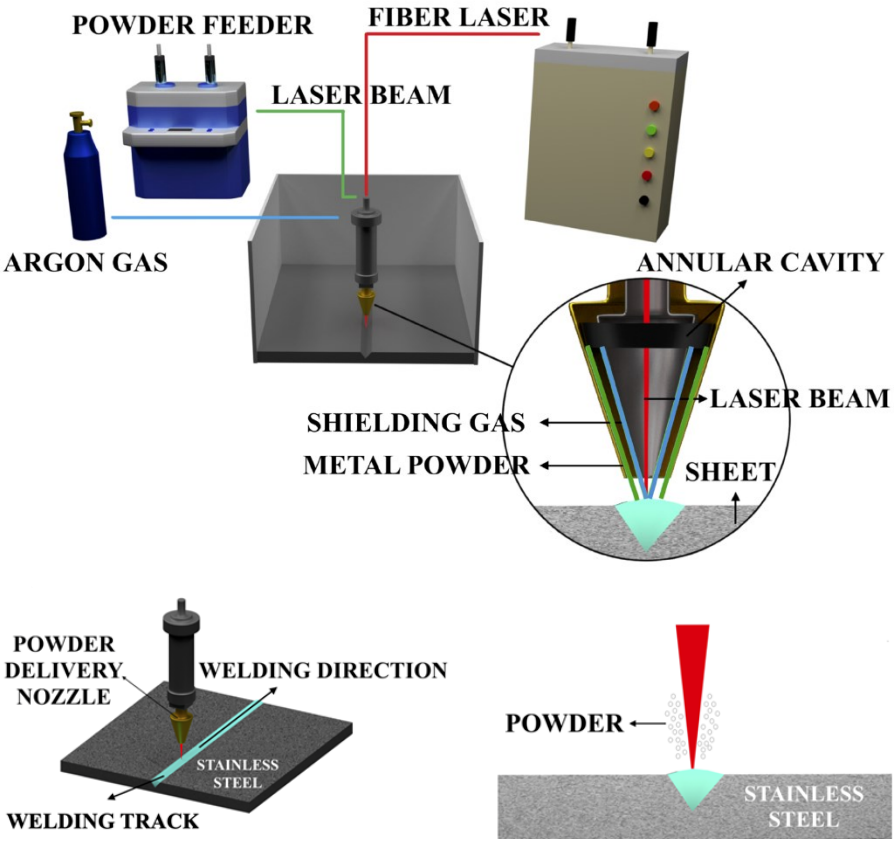

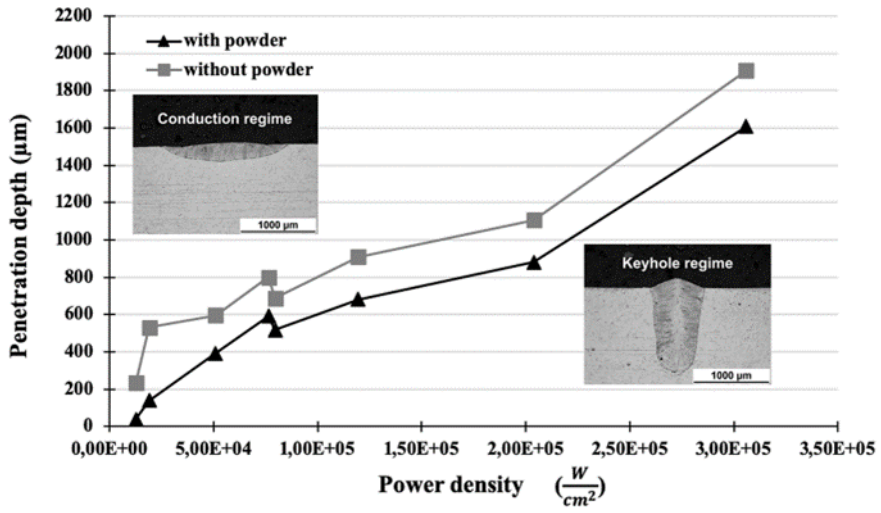

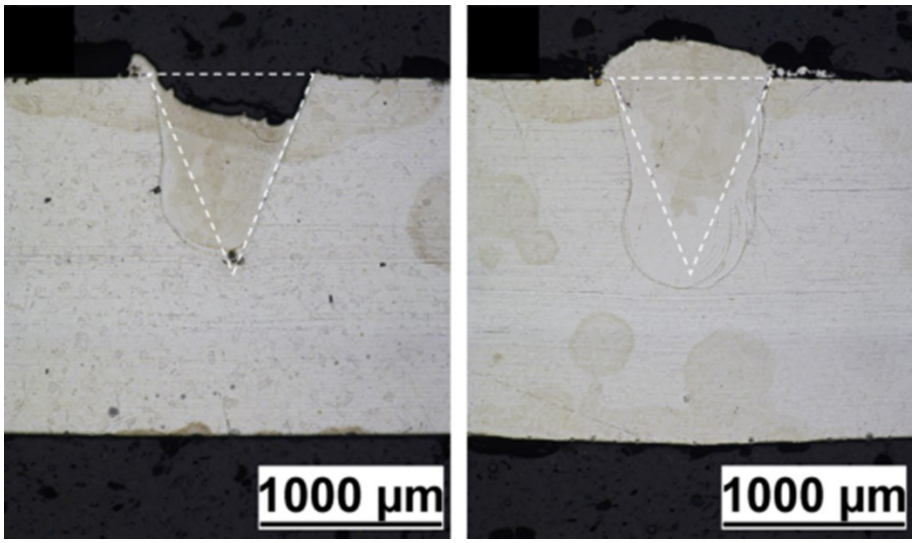

Keywords: laser welding; laser powder welding; stainless steel; weld defectiveness; statistical analysis

Author contributions:

V.E.: Conceptualization, Methodology, Software, Validation, Formal analysis, Investigation, Data Curation, Writing - Original Draft, Writing - Review & Editing, Visualization.
S.L.C.: Conceptualization, Validation, Resources, Writing - Review & Editing, Visualization, Supervision, Project administration, Funding acquisition.
A.A.: Conceptualization, Validation, Resources, Writing - Review & Editing, Visualization.
M.M.: Conceptualization, Methodology, Formal analysis, Investigation, Writing - Original Draft, Writing - Review & Editing.
G.C.: Conceptualization, Validation, Resources, Writing - Review & Editing, Visualization, Supervision, Project administration, Funding acquisition.

Paper II:

Coaxial Monitoring of AISI 316L Thin Walls Fabricated by Direct Metal Laser Deposition

Authors: V. Errico, S.L. Campanelli, A. Angelastro, M. Dassisti, M. Mazzarisi, C. Bonserio

Journal: Materials

Status: published

DOI: 10.3390/ma14030673

Abstract
Direct metal laser deposition (DMLD) is an additive manufacturing technique suitable for coating and repair, which has been gaining a growing interest in 3D manufacturing applications in recent years. However, its diffusion in the manufacturing industry is still limited due to technical challenges to be solved both the sub-optimal quality of the final parts and the low repeatability of the process make the DMLD inadequate for high-value applications requiring high-performance standards. Thus, real-time monitoring and process control are indispensable requirements for improving the DMLD process. The aim of this study was the optimization of deposition strategies for the fabrication of thin walls in AISI 316L stainless steel. For this purpose, a coaxial monitoring system and image processing algorithms were employed to study the melt pool geometry. The comparison tests carried out highlighted how the region-based active contour algorithm used for image processing is more efficient and stable than others covered in the literature. The results allowed the identification of the best deposition strategy. Therefore, it is shown how this monitoring methodology proved to be suitable for designing and implementing the right building strategy for DMLD manufactured 3D components. A fast and stable image processing method was achieved, which can be considered for future closed-loop monitoring in real-time applications.

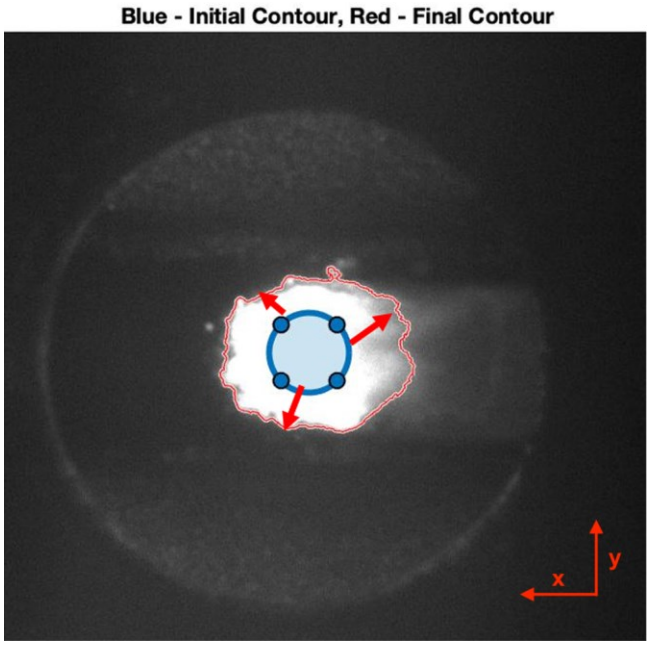

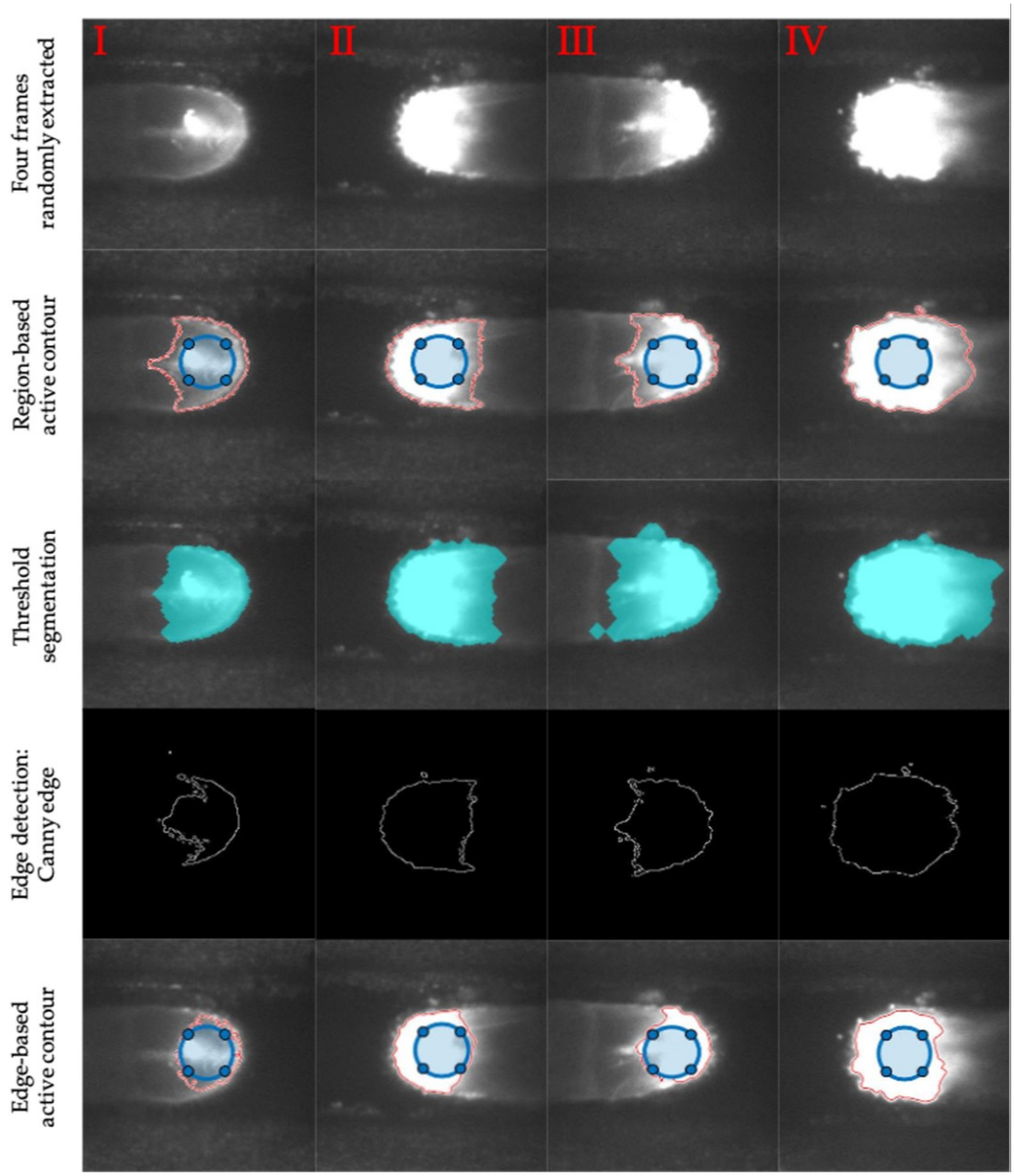

Keywords: direct metal laser deposition; melt pool; process monitoring; image processing

Author contributions (according to CRediT):

V.E.: Conceptualization, Methodology, Software, Validation, Formal analysis, Investigation, Resources, Data Curation, Writing - Original Draft.
S.L.C.: Conceptualization, Methodology, Validation, Investigation, Resources, Writing - Original Draft, Writing - Review & Editing, Visualization, Supervision, Project administration, Funding acquisition.
A.A.: Methodology, Validation, Investigation, Resources, Writing - Review & Editing, Visualization, Supervision, Project administration, Funding acquisition.
M.D.: Validation, Writing - Review & Editing, Visualization, Supervision, Project administration.
M.M.: Methodology, Software, Formal analysis, Investigation, Data Curation.
C.B.: Methodology, Software, Investigation.

Paper III:

Effect of DED coating and DED + Laser scanning on surface performance of L-PBF stainless steel parts

Authors: V. Errico, A. Fusco, S.L. Campanelli

Journal: Surface & Coatings Technology

Status: published

DOI: 10.1016/j.surfcoat.2021.127965

Abstract
The advantages of the Laser Powder Bed Fusion process have led to growing interest from an industrial and academic point of view. However, the diffusion of this process has been slowed by technical challenges that have yet to be resolved, including non-optimal surface quality and low repeatability. To fix these issues and recover surface quality, several treatments are available. Our study focuses on one of them: the Directed Energy Deposition (DED) treatment, which in addition can be exploited for the repair of damaged components. In fact, the proposed study has been conducted by using AISI 316 L alloy both for producing parts throughout the L-PBF process and for coating them. Furthermore, a final Laser Scanning (LS) treatment has been carried out with the aim of maximizing the DED coating performances, in terms of surface roughness, microhardness and microstructural properties. To detect the anomalies that can emerge during the previous surface treatments, an optical monitoring system was implemented in the visible range by using a coaxial CCD camera, to monitor the geometry and morphology of the melt pool related to the DED and to the subsequent LS treatment. The results revealed many improvements in terms of surface roughness for the DED coating and even more for the LS treatment. Moreover, the latter was fundamental to improve the microhardness and the microstructural characteristics of the final coating. The data gathered and analyzed by the implemented monitoring system will allow making the treatment more stable and performing for future applications on complex geometries.

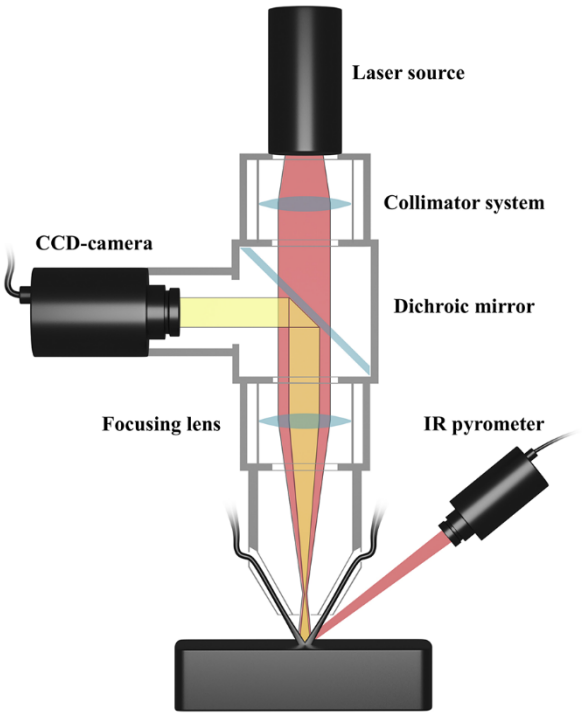

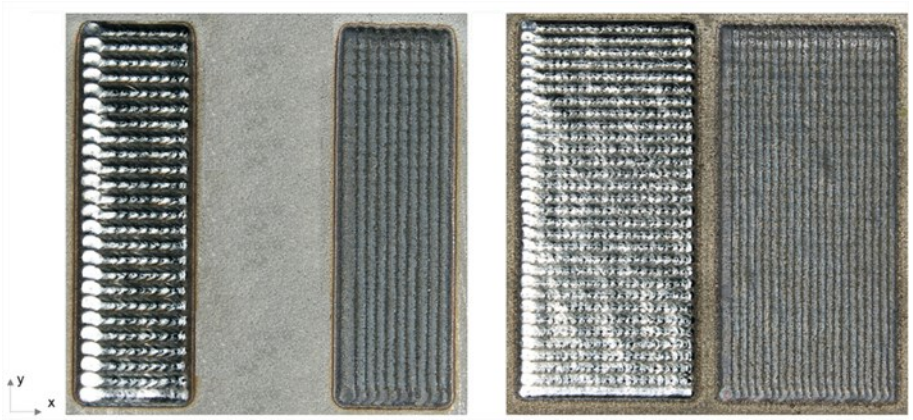

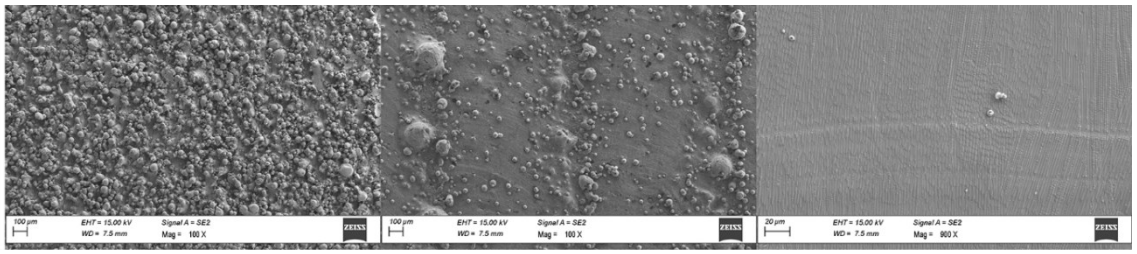

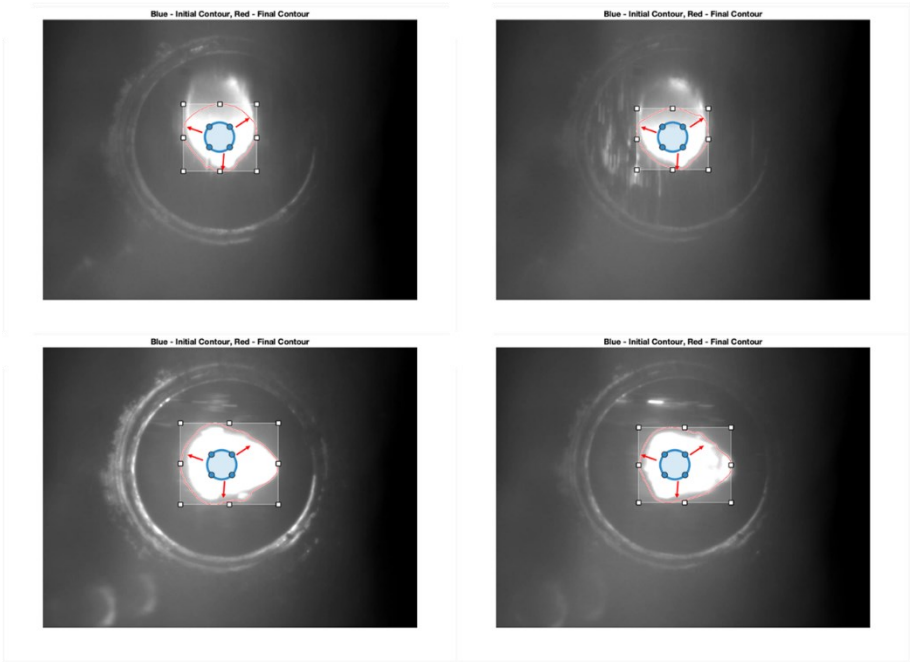

Keywords: laser treatments; laser powder bed fusion; AISI 316 L; directed energy deposition; laser scanning; process monitoring.

Author contributions (according to CRediT):

V.E.: Conceptualization, Methodology, Software, Validation, Formal analysis, Investigation, Data curation, Supervision, Visualization, Writing – original draft, Writing – review & editing.
A.F.: Conceptualization, Methodology, Software, Validation, Formal analysis, Investigation, Data curation, Writing – original draft.
S.L.C.: Conceptualization, Methodology, Validation, Data curation, Supervision, Visualization, Writing – original draft, Writing – review & editing, Project administration, Funding acquisition.

Paper IV:

Influence of standoff distance and laser defocusing distance on Direct Laser Metal Deposition of a Nickel-based superalloy

Authors: M. Mazzarisi, V. Errico, A. Angelastro, S.L. Campanelli

Journal: The International Journal of Advanced Manufacturing Technology

Status: published

DOI: 10.1007/s00170-022-08945-3

Abstract
The direct laser metal deposition (DLMD) is an additive manufacturing technology, based on laser cladding, which focuses mainly on 3D manufacturing applications. DLMD allows the production of thin-walled components by overlaying single-track depositions. Several issues can affect the deposition process and compromise the flatness of the surface on which subsequent tracks will be deposited. This work focused on deposition troubles simulated by means of a designed variation of the standoff distance and the laser defocusing distance. The effects of these two important process parameters on the deposition process were investigated. The experimental tests were performed by depositing a nickel-based superalloy powder on AISI 304 stainless steel plates through a coaxial nozzle. The work was carried out using an ytterbium fiber laser source and a deposition head equipped with an advanced and innovative motorized optics system. This allows the decoupled variation of the laser defocusing distance and consequently the laser spot size on the substrate surface with respect to the standoff distance. Results showed an influence of standoff distance and laser defocusing distance on the geometrical characteristics of the clad, such as clad width, clad height, penetration depth, and dilution. An experimental setup consisting of a light coaxial to the powder flow and a laterally positioned camera was designed to investigate the spatial powder distribution. Moreover, an analytical model for the powder distribution and clad width were proposed and validated. The analysis of variance (ANOVA) with a general linear model was also employed to describe the results.

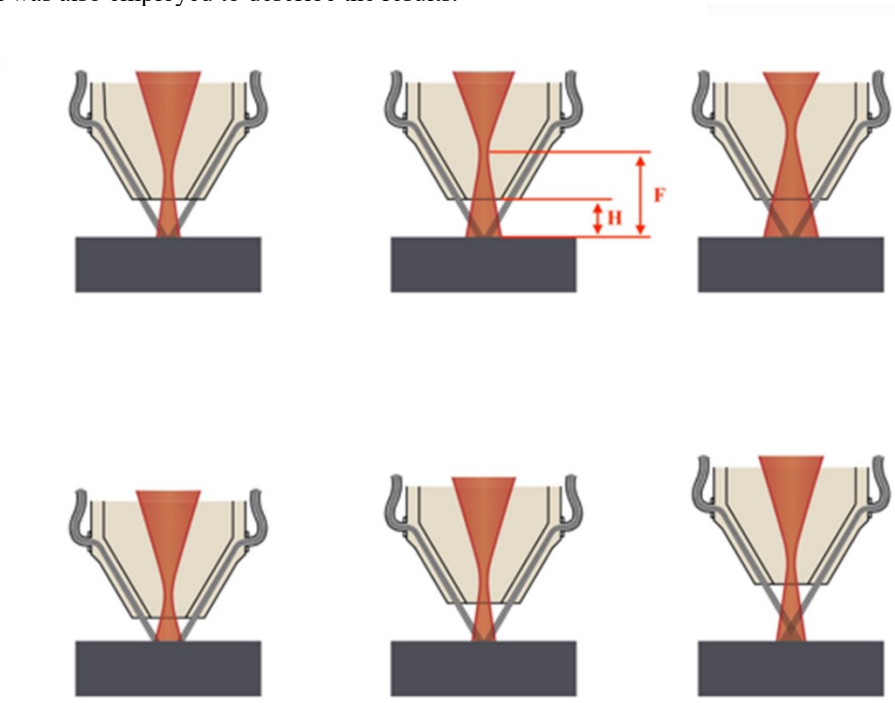

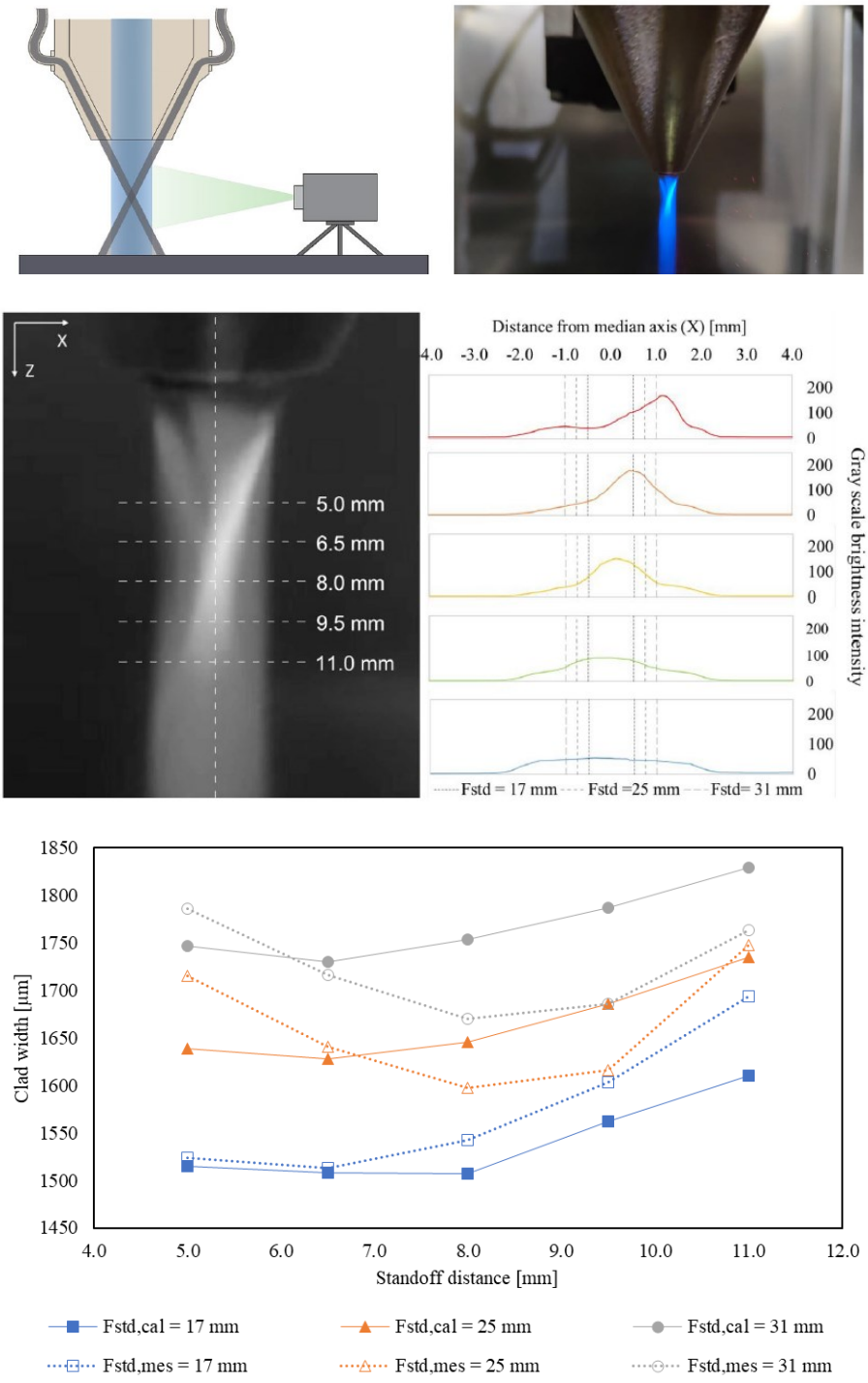

Keywords: direct laser metal deposition; standoff distance; laser defocusing distance; nickel-based superalloy; powder distribution

Author contributions:

M.M.: Conceptualization, Methodology, Software, Validation, Formal analysis, Investigation, Data Curation, Writing - Original Draft, Writing - Review & Editing, Visualization.
V.E.: Conceptualization, Methodology, Software, Validation, Formal analysis, Investigation, Data Curation, Writing - Original Draft, Writing - Review & Editing, Visualization.
A.A.: Conceptualization, Validation, Resources, Writing - Review & Editing, Visualization.
S.L.C.: Conceptualization, Validation, Resources, Writing - Review & Editing, Visualization, Supervision, Project administration, Funding acquisition.

Paper V:

High resolution-optical tomography for in-process layerwise monitoring of a laser-powder bed fusion technology

Authors: M.G. Guerra, V. Errico, A. Fusco, F. Lavecchia, S.L. Campanelli, L.M. Galantucci

Journal: Additive Manufacturing

Status: published

DOI: 10.1016/j.addma.2022.102850

Abstract
With the implementation of Laser Powder Bed Fusion technologies for industrial production, the need for in-process monitoring has emerged to ensure stable conditions and the process to succeed. Indeed, despite significant technological advances, the rejected parts are still too high if compared to the more conventional manufacturing techniques. Several defects are known to affect the process, more likely when complex geometries are fabricated. Among these, the production of inclined thin walls without support structures is still critical and, in most cases, geometric distortions are observed on the overhanging surfaces. In order to overcome the above mentioned problems and improve the quality of these critical structures, an high resolution monitoring system based on Optical Tomography (OT) was proposed, called High Resolution-Optical Tomography (HR-OT). It uses a very high-resolution sensor, operating in the visible spectrum of light, on a large area of the surface layers comprising the entire printing platform. This very recent technique, typically applied for the detection of volumetric defects, such as porosity or lack of fusion, was successfully applied, in this paper, for the detection of geometric distortions, allowing to avoid onerous pre-processing phases in the image processing workflow. Specific geometric indexes were selected as monitoring outputs and were used for the construction of appropriate control charts in order to carry out statistical process monitoring. Finally, an off-line 3D reconstruction, by means of digital close range photogrammetry, was used to verify the effectiveness of the proposed monitoring solution when applied for in-process detection of geometric distortions.

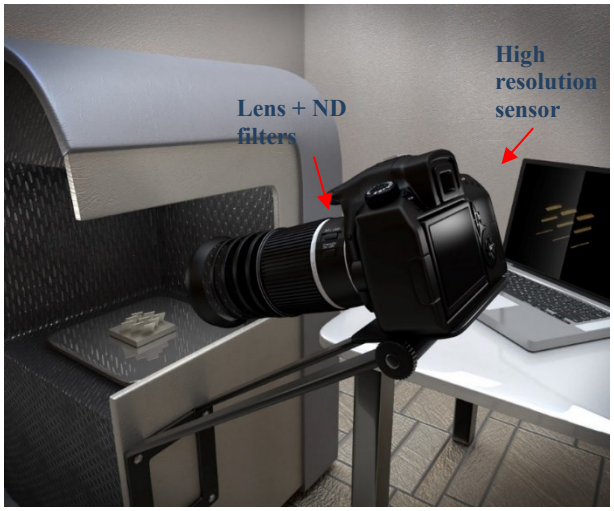

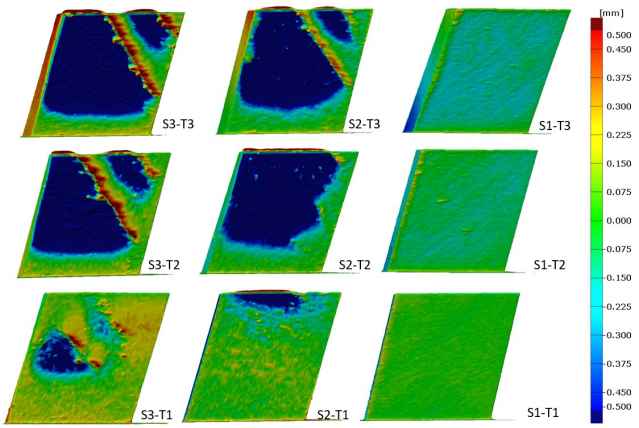

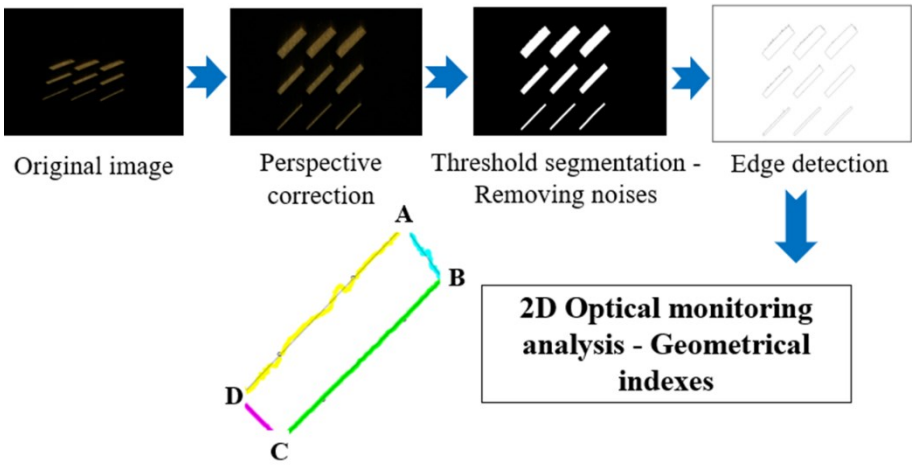

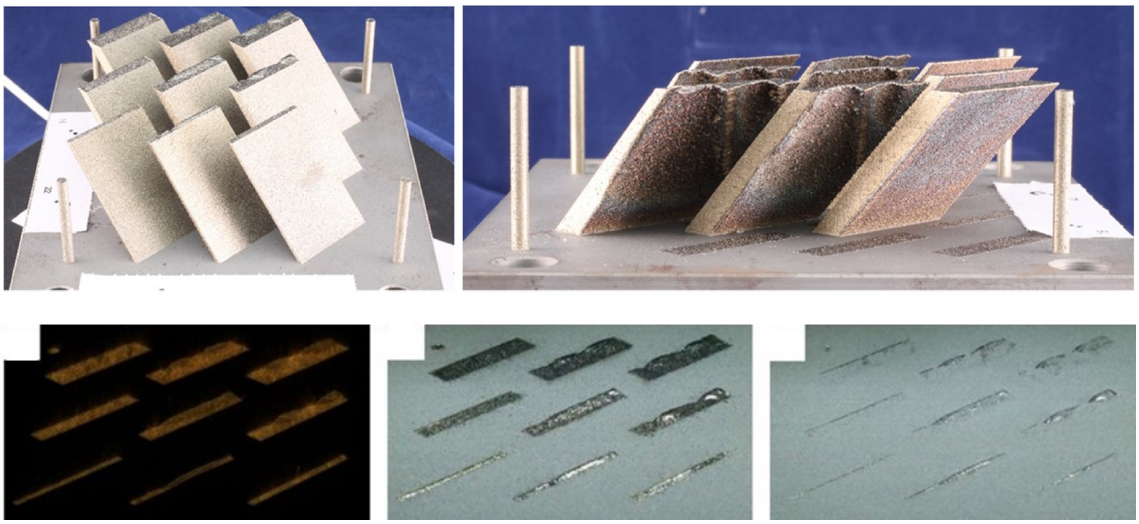

Keywords: Laser-powder bed fusion; AISI 316L; in-process monitoring; high resolution-optical tomography; photogrammetry

Author contributions (according to CRediT):

M.G.G.: Writing – review & editing, Writing – original draft, Supervision, Methodology, Formal analysis, Data curation, Conceptualization.
V.E.: Writing – review &, editing, Writing – original draft, Validation, Methodology, Investigation, Formal analysis, Data curation, Conceptualization.
A.F.: Software, Investigation, Formal analysis, Data curation.
F.L.: Writing – review & editing, Supervision, Methodology, Investigation, Conceptualization.
S.L.C.: Writing – review & editing, Supervision, Project administration, Methodology, Investigation, Conceptualization.
L.M.G.: Writing – review & editing, Supervision, Project administration, Methodology, Investigation, Conceptualization.

Paper VI:

Additive manufacturing and mechanical testing of functionally-graded steel strut-based lattice structures

Authors: F. Caiazzo, V. Alfieri, S.L. Campanelli, V. Errico

Journal: Journal of Manufacturing Processes

Status: published

DOI: 10.1016/j.jmapro.2022.09.031

Abstract
Functionally graded materials have been increasingly considered for many applications, spanning from aerospace to biomedicine, because directional mechanical or physical features are provided. Recent developments of additive manufacturing technologies allow to pursue new challenging metal structures, possibly designed on a case-by-case basis. Nevertheless, many studies in the literature have already pointed out the need for accurately defining the manufacturing limits of the technologies as well as the correlation between the geometries and the mechanical performance. In this frame, this paper is aimed at manufacturing and testing steel functionally graded strut-based lattice structures to map their mechanical properties as a function of the grading approach (uniform, size-graded and rod-graded) and the fractional density (15 %, 25 % and 35 %), even computing the calibration parameters to check the reliability of the usual Gibson-Ashby scaling laws. Results showed strut distortion and deviation from the designed geometry in samples with the lowest fractional density (15 %) and at thinner layers of the rod-graded geometries. Size-graded structures demonstrated higher mechanical properties, regardless of the fractional density.

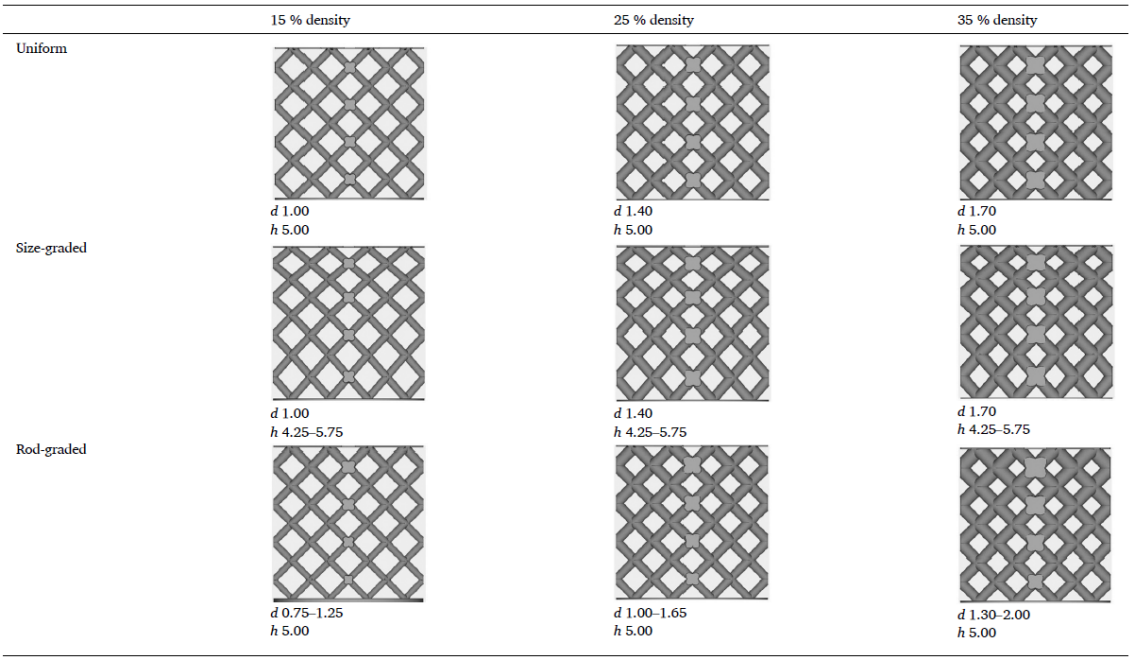

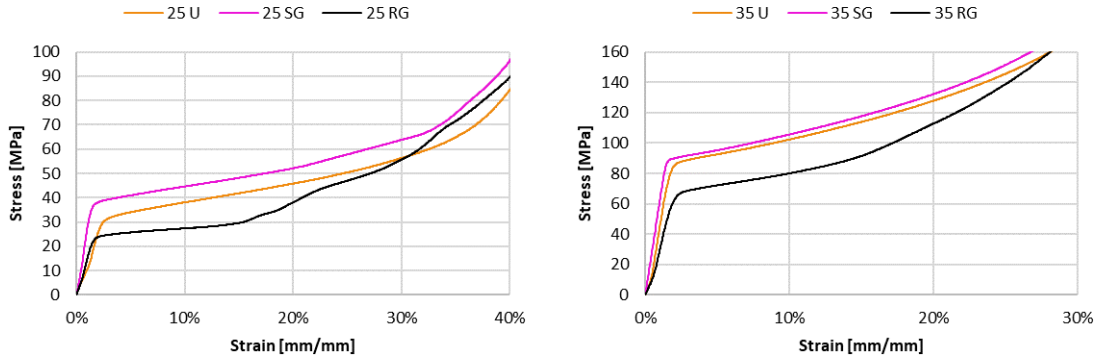

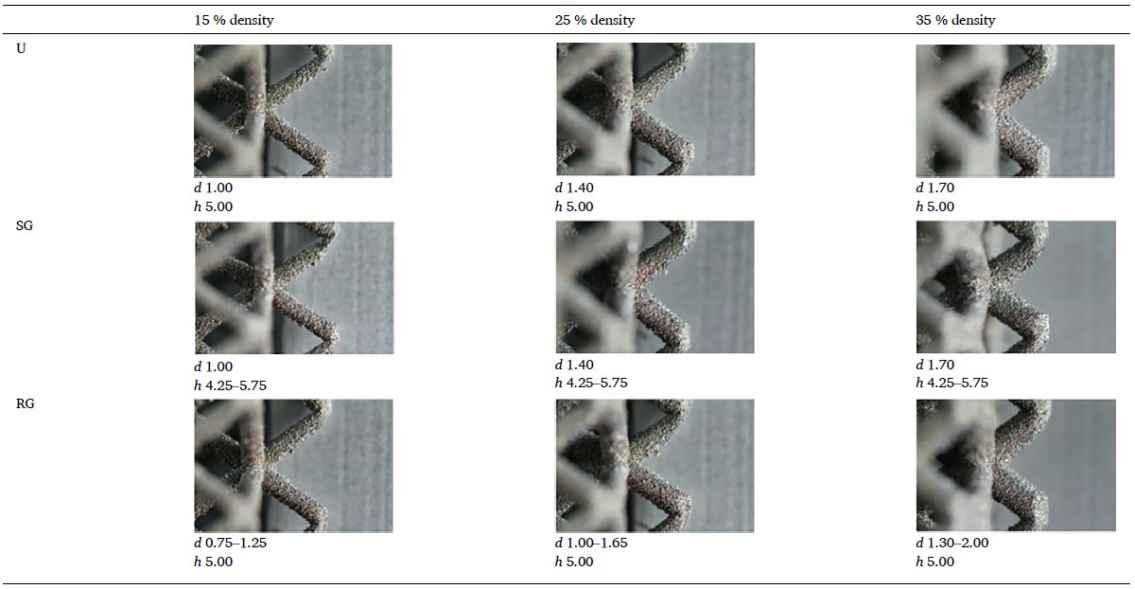

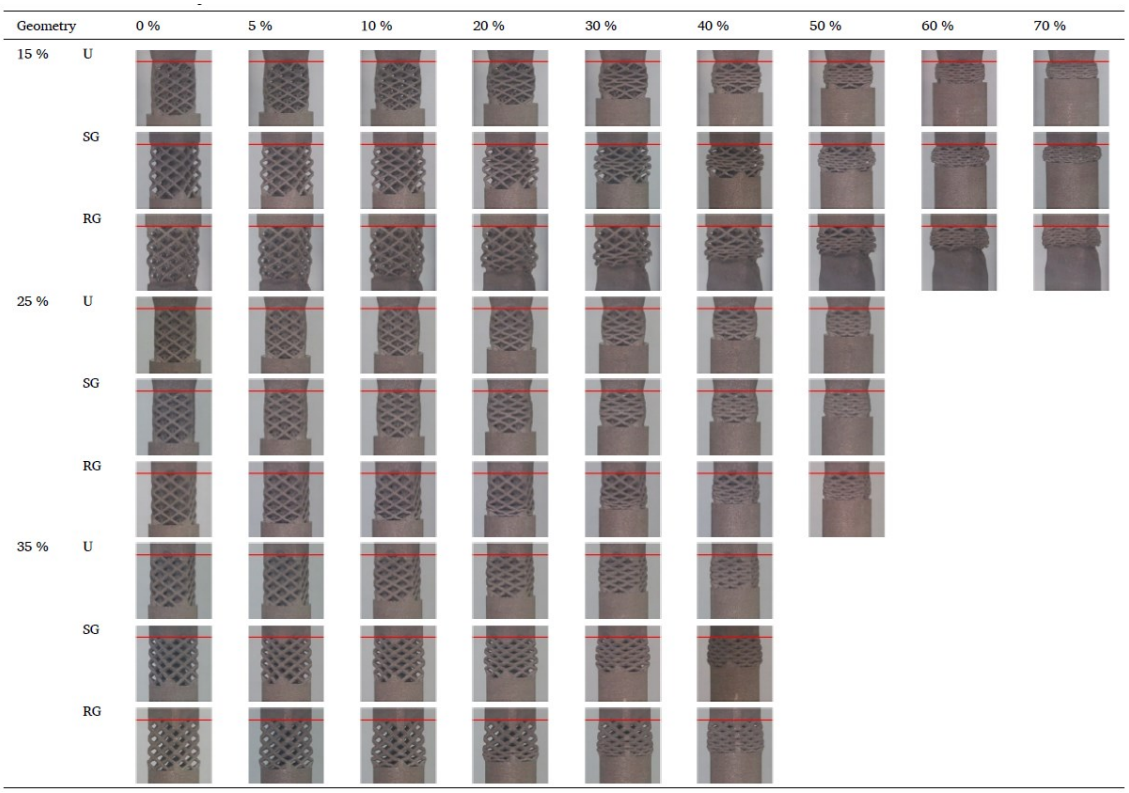

Keywords: Additive Manufacturing, functionally graded materials, lattice structures, Gibson-Ashby

Author contributions:

F.C.: Conceptualization, Validation, Supervision, Project administration, Methodology, Investigation, Funding acquisition.
V.A.: Conceptualization, Methodology, Software, Validation, Formal analysis, Investigation, Data Curation, Writing - Original Draft, Writing - Review & Editing, Visualization.
S.L.C.: Conceptualization, Methodology, Validation, Writing – review & editing, Supervision, Methodology, Investigation.
V.E.: Conceptualization, Methodology, Validation, Formal analysis, Investigation, Data Curation, Writing - Original Draft, Writing - Review & Editing, Visualization.

Paper VII:

Effects of Laser-Deposited Maraging Steel on L-PBF 316L Component

Authors: V. Errico, P. Posa, M. Mazzarisi, A. Angelastro, S.L. Campanelli

Journal: Metals

Status: published

DOI: 10.3390/met12101669

Abstract
The capabilities of additive manufacturing (AM) techniques have been extensively examined in the literature. However, scientific gaps persist on the feasibility of realizing a coated component manufactured by using various materials processed by combining different AM processes. From this perspective, this study focuses on the manufacturing of a directed energy deposition (DED) coating by using 18Ni (300) maraging steel powder on AISI 316L components realized by laser-powder bed fusion (L-PBF), in order to assess the production of components with high geometrical complexity combined with high mechanical surface properties in selected areas. The quality of the manufactured coatings was assessed in-process through the implementation of an optical monitoring system and real-time image processing. In addition, an in-depth metallurgical analysis (microstructural and chemical) of the interface between the DED coating and the L-PBF component was carried out. Finally, hardness tests were performed on both the as-deposited and heat-treated coatings to confirm the high mechanical performance of the final component surface. The results revealed the potential of producing cost-effective and geometrically complex parts, such as molds or tools with internal cooling channels, that implement mechanically high-performance surfaces.

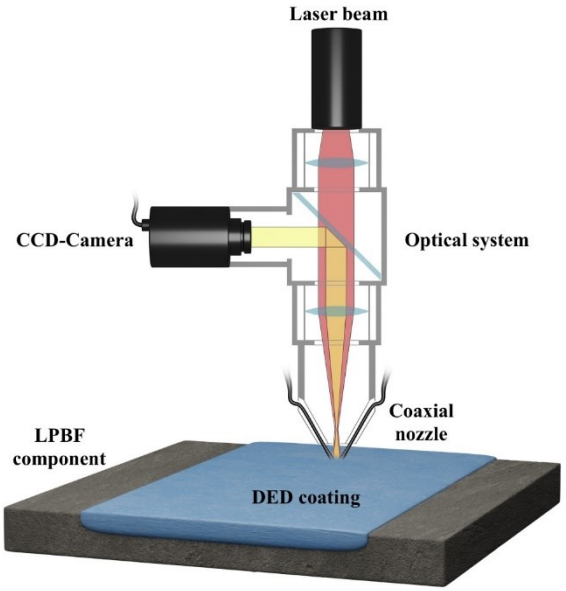

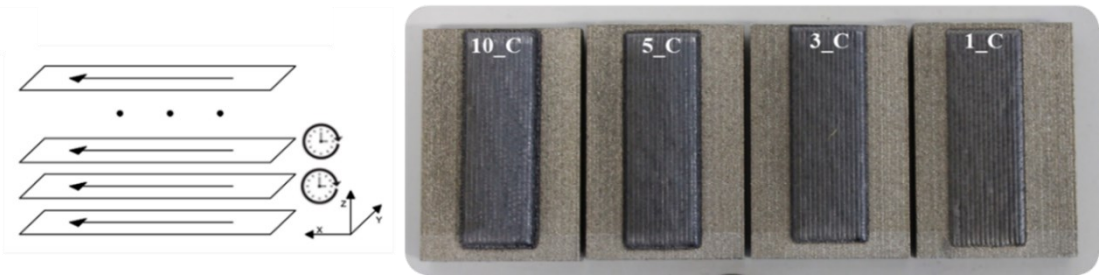

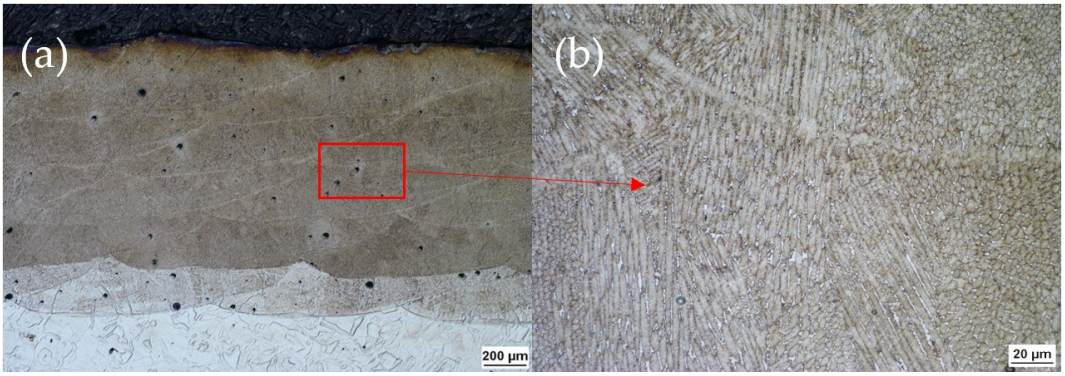

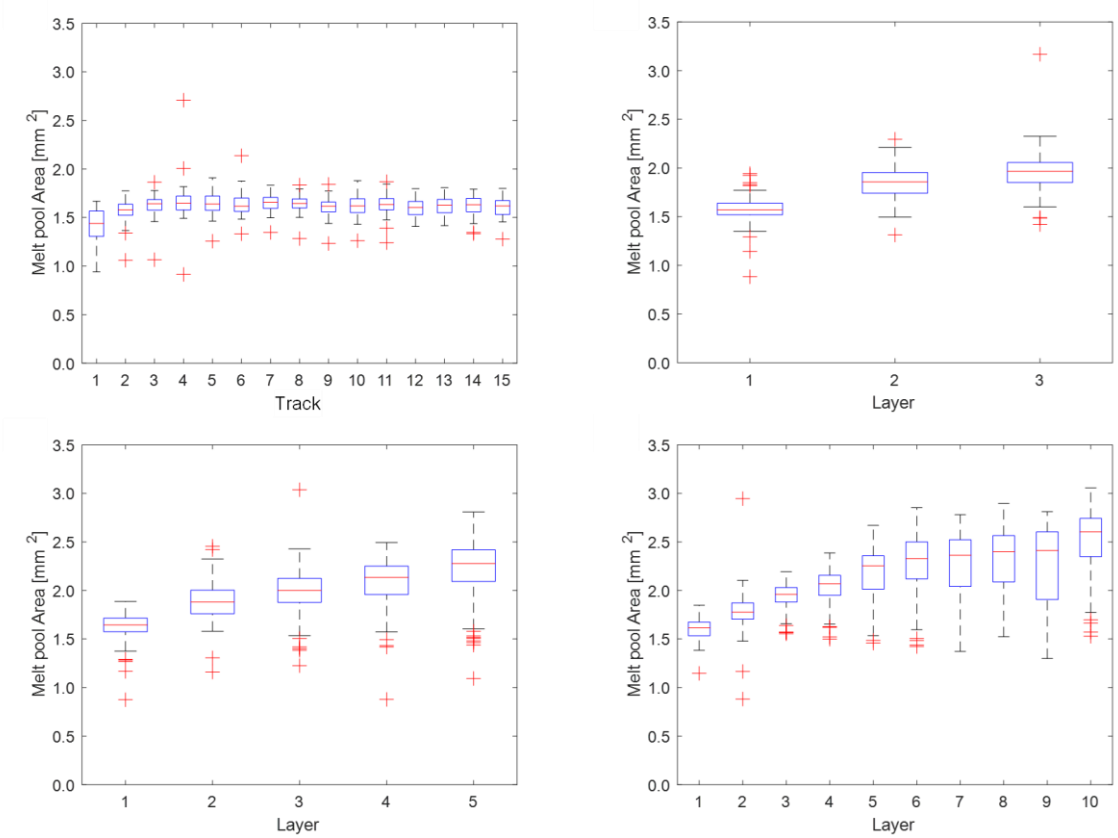

Keywords: laser-powder bed fusion; 18Ni (300) maraging steel; directed energy deposition; optical process monitoring; heat treatment; AISI 316L

Author contributions (according to CRediT):

V.E.: Conceptualization, Methodology, Software, Validation, Formal analysis, Investigation, Data Curation, Writing - Original Draft, Writing - Review & Editing, Visualization.
P.P.: Conceptualization, Methodology, Software, Formal analysis, Investigation, Data Curation, Writing - Original Draft, Visualization
M.M.: Software, Data Curation, Writing - Review & Editing
A.A.: Validation, Resources, Writing - Review & Editing, Supervision
S.L.C.: Validation, Resources, Writing - Review & Editing, Supervision, Project administration, Funding acquisition

Paper VIII:

Intralayer Multi-material Structure Stainless-Steel/Nickel-superalloy fabricated via Laser-Powder Bed Fusion process

Authors: V. Errico, P. Posa, A. Fusco, A. Angelastro, S.L. Campanelli

Journal: Manufacturing Letters

Status: published

DOI: 10.1016/j.mfglet.2022.11.004

Abstract
This work aims to contribute to the progress in the fabrication of multi-material structures using the Laser-Powder Bed Fusion technology. To manufacture an intralayer multi-material sample, an ad-hoc partitioning system was developed for the powder chamber. The manufacturability of a Stainless-Steel/Nickel-superalloy multi-material component, having a strong bond at the interface, which appeared cracks- and porosity free, was demonstrated. To characterize the sample in-situ and real-time, an optical monitoring system was implemented. The latter can allow for detection, in real-time and in a layer-by-layer manner, of any malfunctions during the process and contaminations between the two different materials.

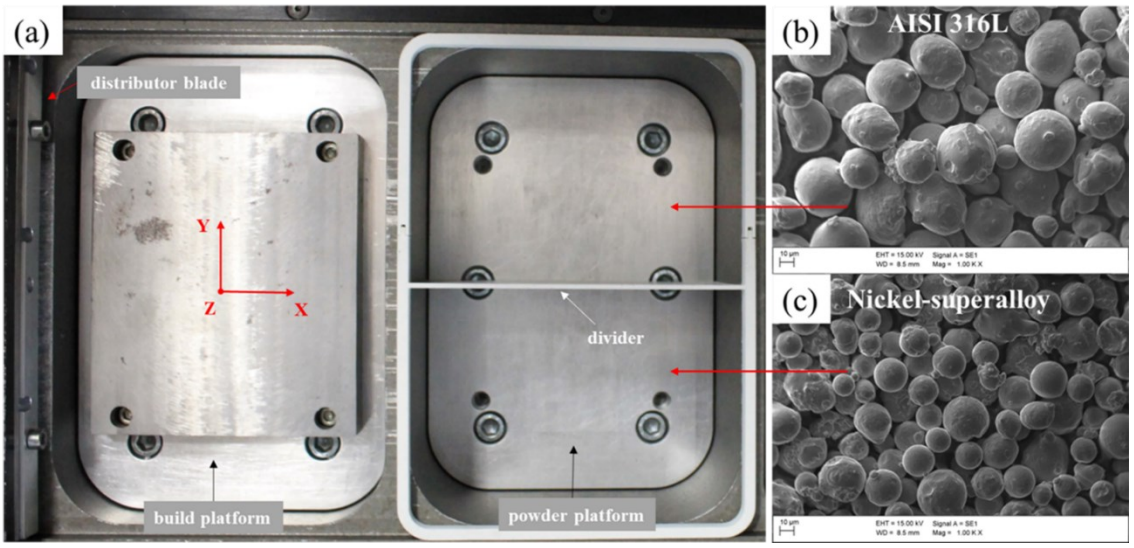

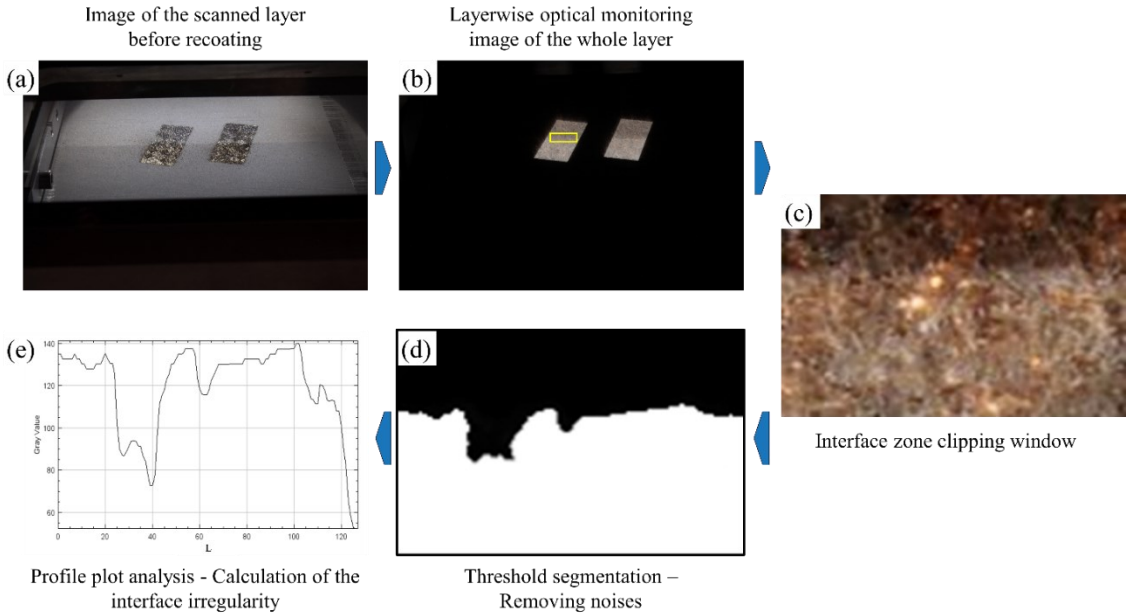

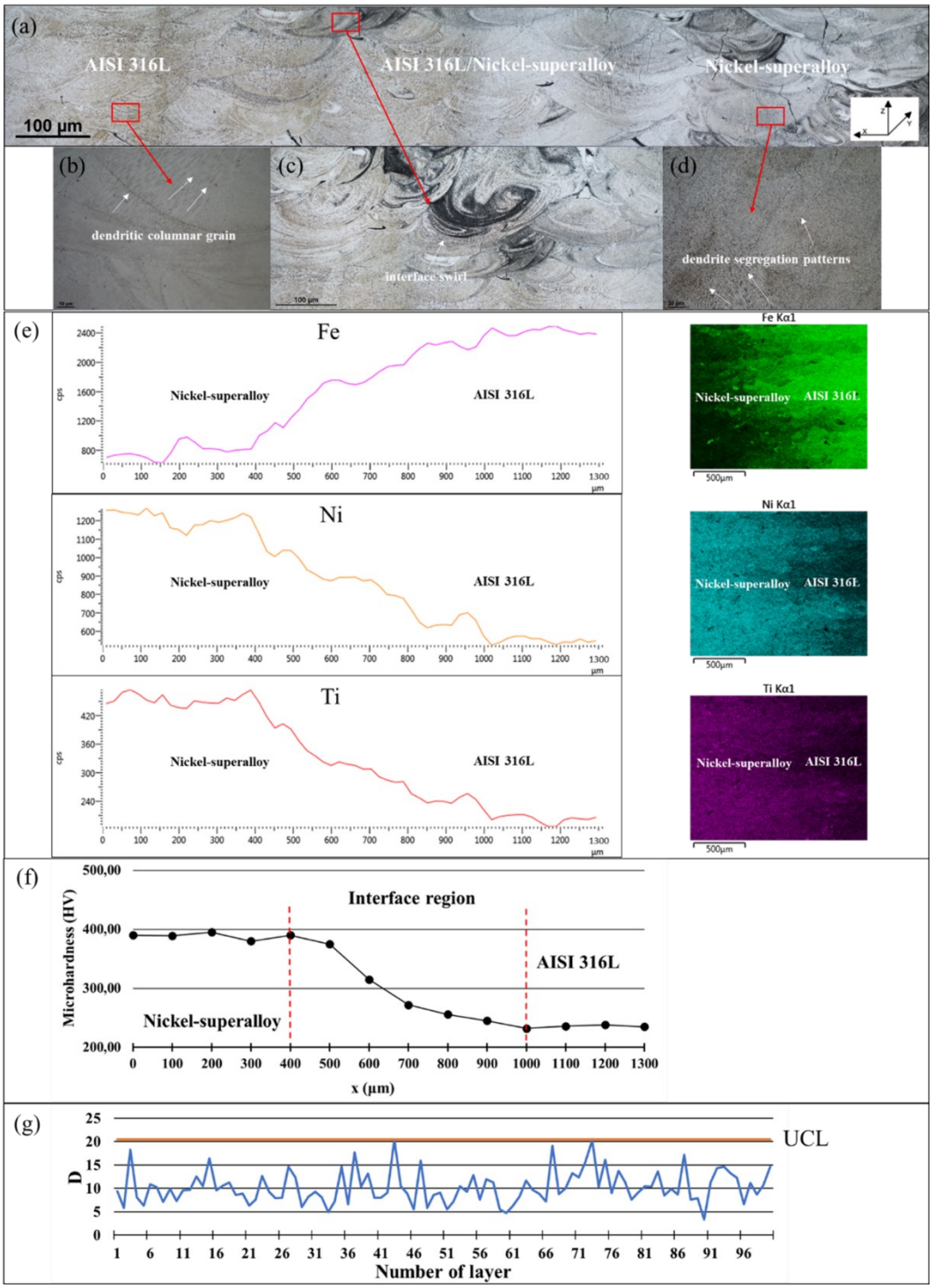

Keywords: Laser-Powder Bed Fusion; Nickel-superalloy; AISI 316L; Multi-material Structures; Optical Process Monitoring; Intralayer

Author contributions:

V.E.: Conceptualization, Methodology, Software, Validation, Formal analysis, Investigation, Data Curation, Writing - Original Draft, Writing - Review & Editing, Visualization.
P.P.: Conceptualization, Methodology, Software, Formal analysis, Investigation, Data Curation, Writing - Original Draft, Visualization
A.F.: Software, Data Curation, Visualization
A.A.: Validation, Resources, Writing - Review & Editing, Supervision
S.L.C.: Validation, Resources, Writing - Review & Editing, Supervision, Project administration, Funding acquisition

Paper IX:

In-process dimensional and geometrical characterization of laser-powder bed fusion lattice structures through high-resolution optical tomography

Authors: M.G. Guerra, M. Lafirenza, V. Errico, A. Angelastro

Journal: Optics and Laser Technology

Status: accepted for publication

DOI: -

Abstract
Additive Manufacturing (AM) technologies, i.e. Laser-Powder Bed Fusion (L-PBF), have made possible the fabrication of complex and lightweight components not feasible with conventional manufacturing processes, such as lattice structures. They have many advantages (high mechanical properties, thermal insulation and good energy absorption ability, etc.) which are limited by internal defects, poor surface quality and dimensional accuracy. In this context, X-ray-based Computed Tomography (XCT) is, currently, the only way for quality assessment of lattice structures, thanks to its capability to see also internal features, while optical scanning techniques can reconstruct only external surfaces. In this work, an innovative and cost-effective optical layerwise monitoring technique, for dimensional and geometrical characterization of lattice structures, is presented. It exploits the high-resolution optical tomography (HR-OT) and it has a double purpose: it is an in-process monitoring method able to detect timely and effectively the onset of geometric distortions layer by layer and contemporary, it provides, at the end of the manufacturing process, a 3D reconstruction of the fabricated structure suitable for dimensional and surface quality assessment, comprising external and internal features, and potentially, for numerical simulation applications. This article is among the first to show a monitoring methodology suitable for lattice structures realized by L-PBF technologies.

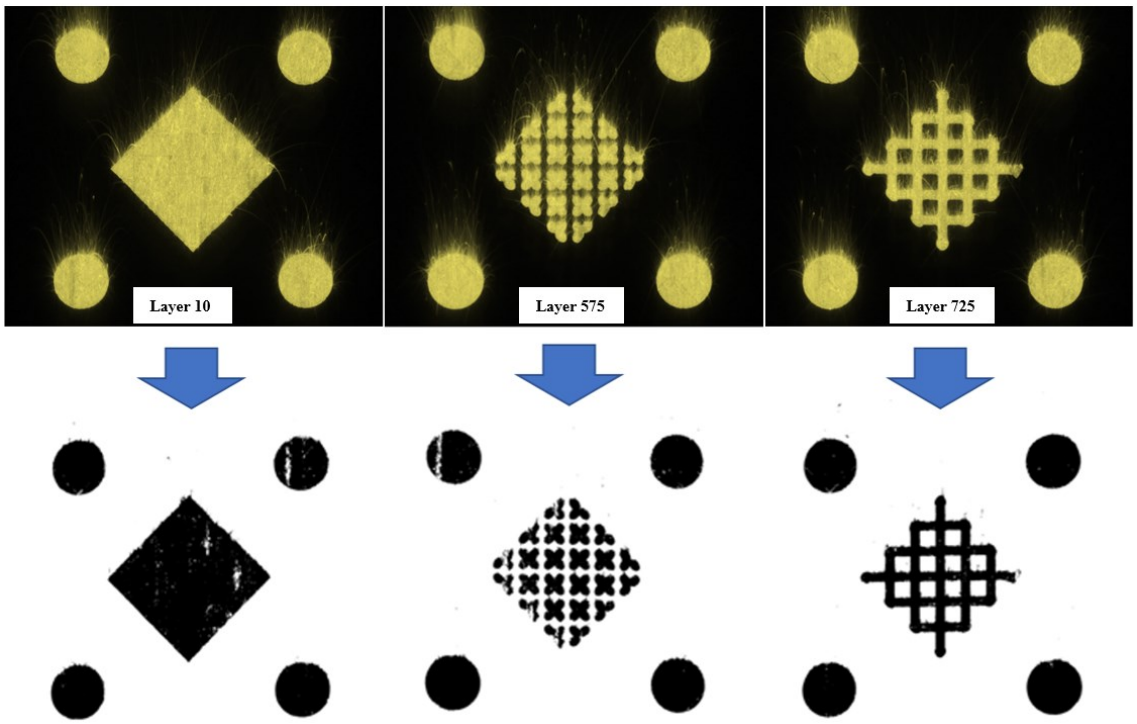

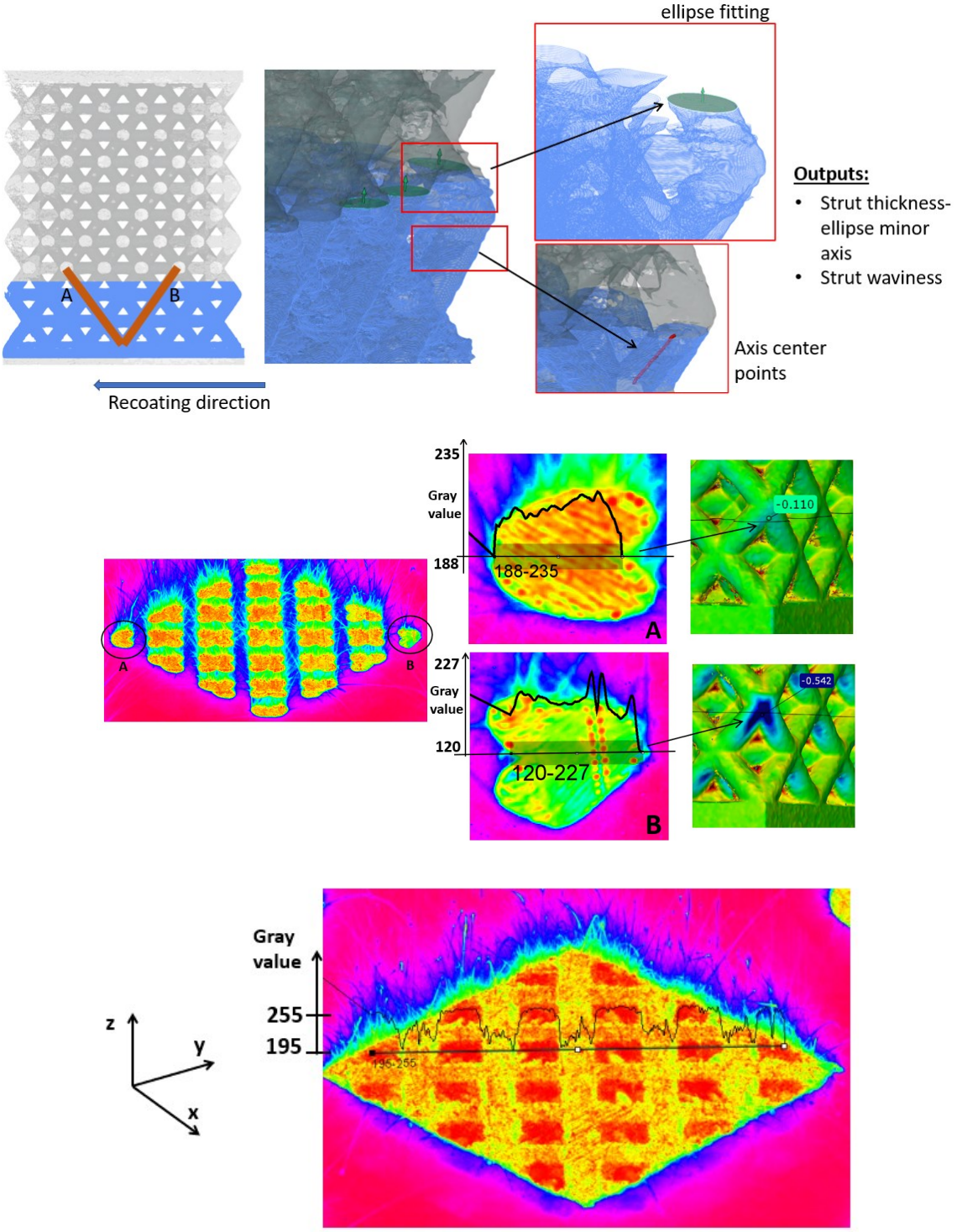

Keywords: Lattice structure; laser-powder bed fusion; AISI 316L; in-process monitoring; high-resolution optical tomography

Author contributions (according to CRediT):

M.G.G.: Writing – original draft, Writing – review & editing, Methodology, Data curation, Conceptualization, Supervision
M.L.: Writing – original draft, Software, Methodology, Data curation, Conceptualization
V.E.: Writing – original draft, Writing – review & editing, Software, Methodology, Data curation, Conceptualization
A.A.: Writing – review & editing, Methodology, Conceptualization, Supervision

Paper X:

Analysing the probability of detection of shallow spherical defects by means of Active Thermography

Authors: E. D'Accardi, D. Palumbo, V. Errico, A. Fusco, A. Angelastro, U. Galietti

Journal: Journal of Nondestructive Evaluation

Status: accepted for publication

DOI: -

Abstract
The capability of Active Thermography (AT) techniques in detecting shallow defects has been proved by many works in the last years, both on metals and composites. However, there are few works in which these techniques have been used adopting simulated defects more representative of the real ones. The aim of this work is to investigate the capability of Active Thermography of detecting shallow spherical defects in metal specimens produced with laser powder bed fusion (L-PBF) process and characterized by a thermal behaviour very far from the flat bottom hole and so near to the real one. In particular, the quantitative characterization of defects has been carried out to obtain the Probability of Detection (PoD) curves. In fact, it is very common in non-destructive controls to define the limits of defect detectability by referring to PoD curves based on the analysis of flat bottom holes with a more generous estimation and therefore not true to real defect conditions. For this purpose, a series of specimens, made by means of Laser-Powder Bed Fusion technology (L-PBF) in AISI 316L, were inspected using Pulsed Thermography (PT), adopting two flash lamps and a cooled infrared (IR) sensor. To improve the quality of the raw thermal data, different post-processing algorithms were adopted. The results provide indications about the advantages and limitations of Active Thermography (AT) for the non-destructive offline controls of the structural integrity of metallic components.

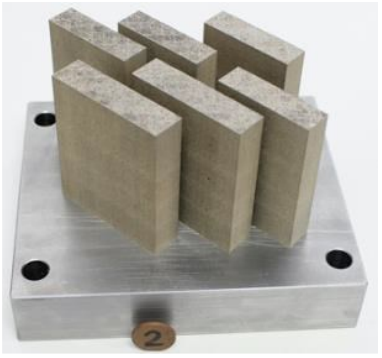

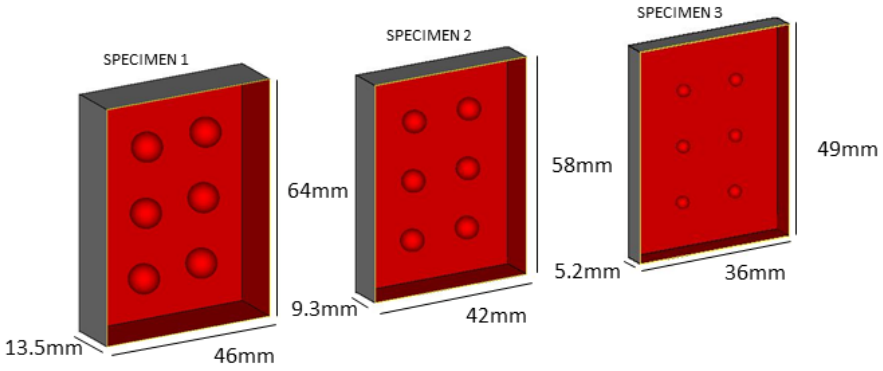

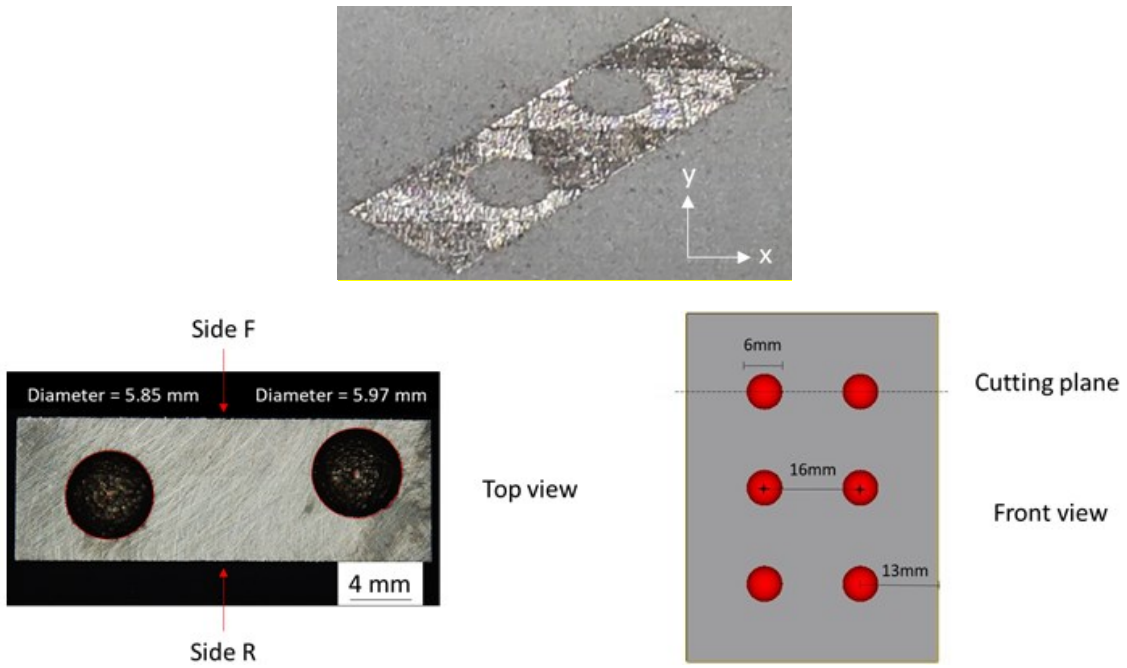

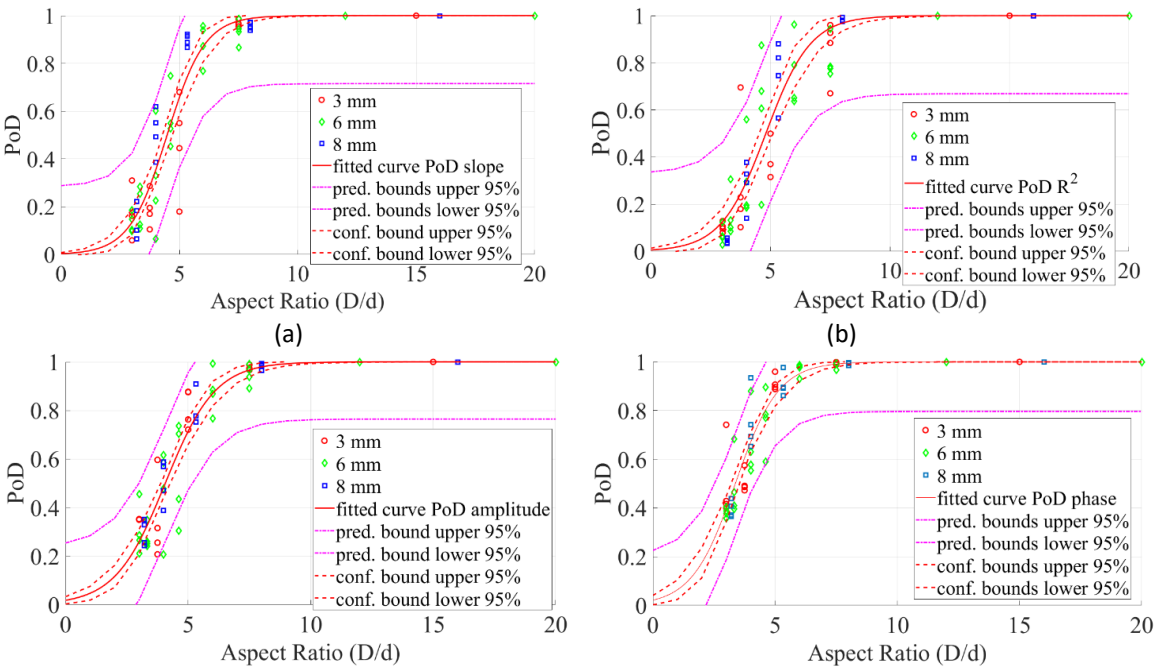

Keywords: Active Thermography (AT), non-destructive techniques, probability of detection (PoD), Laser-Powder Bed Fusion (L-PBF), Additive Manufacturing (AM)

Author contributions:

E. D.: Conceptualization, Methodology, Software, Validation, Formal analysis, Investigation, Data Curation, Writing - Original Draft, Writing - Review & Editing, Visualization
D.P.: Conceptualization, Methodology, Validation, Formal analysis, Data Curation, Writing - Review & Editing, Visualization, Supervision
V.E.: Conceptualization, Software, Validation, Data Curation, Writing - Original Draft, Writing - Review & Editing
A.F.: Conceptualization, Software, Writing - Original Draft
A.A.: Conceptualization, Validation, Writing - Review & Editing, Supervision, Funding acquisition
U.G.: Conceptualization, Validation, Writing - Review & Editing, Supervision, Project administration, Funding acquisition

Paper XI:

Laser-Powder Bed Fusion molds without post-processing for micro injection molding of mini/micro products

Authors: R. Surace, V. Errico, M. Valori, I. Fassi, S.L. Campanelli

Journal: The International Journal of Advanced Manufacturing Technology

Status: submitted, under review

DOI: -

Abstract
The use of Additive Manufacturing (AM) processes at the micro-scale helps to increase the development of microsystems, thus enabling shorter tooling development to be exploited for other micro-technologies, such as micro-injection molding (µ-IM). In recent years, these processes combination has shown their capability of providing greater flexibility to micro-technologies and facilitating a high production rate, in particular allowing µ-IM to be economically feasible for low-volume production. Therefore, in order to assess the feasibility of micro metal AM for µ-IM mold production, a set of mini and micro polymeric parts injected by using molds realized via the Laser-Powder Bed Fusion (L-PBF) process is discussed in this paper. The molds were manufactured in low-carbon steel, and have been characterized and tested experimentally, without any post-process treatment. Two selected geometries, corresponding to a mini dogbone for tensile tests and a micro flexural hinge, were designed and realized by the µ-IM process. These were replicated in order to assess the accuracy of the whole process. The obtained results of replication accuracy and mechanical tests confirm that the µ-IM process, performed with an L-PBF-made mold insert, is feasible and affordable for micro-production, although great accuracy, especially in mold design, fabrication and assembly is required.

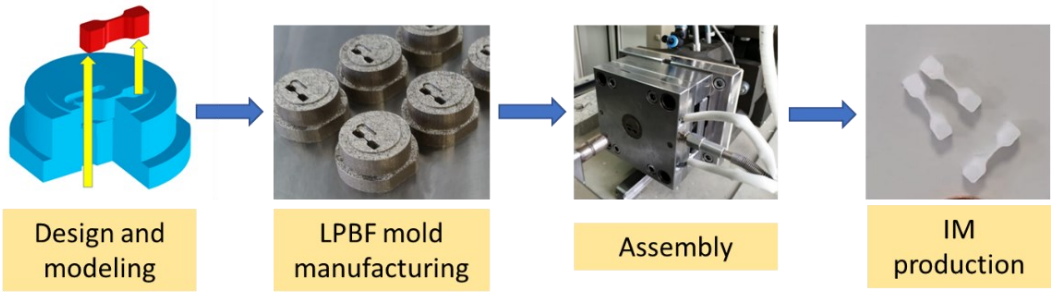

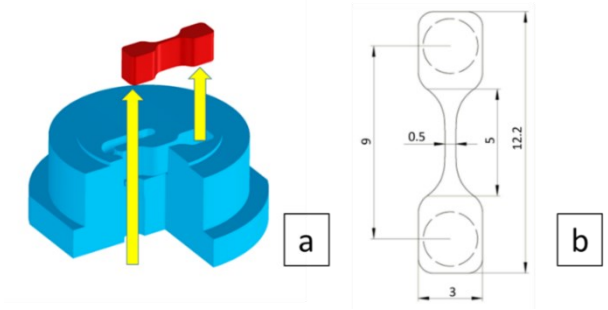

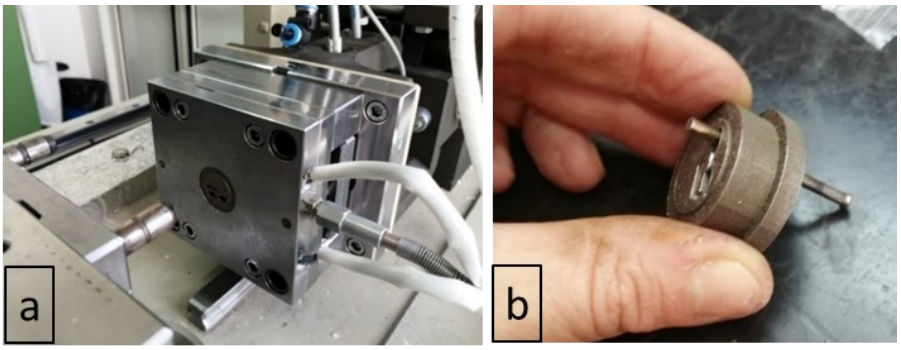

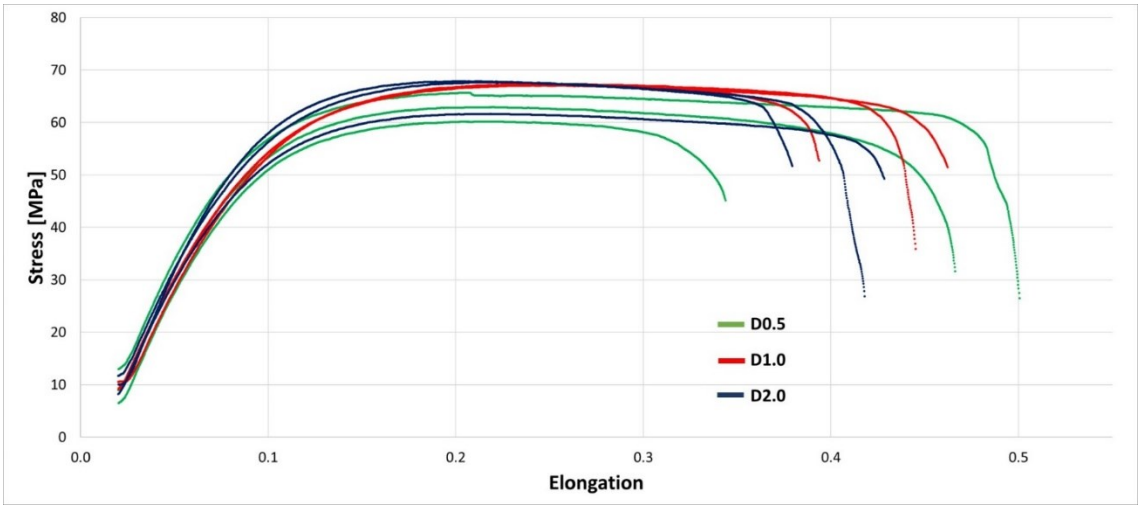

Keywords: Additive Manufacturing; Laser-Powder Bed Fusion; Micro-injection molding; steel molds; replication accuracy

Author contributions:

R. S.: Conceptualization, Methodology, Software, Validation, Formal analysis, Investigation, Data Curation, Writing - Original Draft, Writing - Review & Editing, Visualization
V.E.: Conceptualization, Methodology, Validation, Formal analysis, Investigation, Data Curation, Writing - Original Draft, Writing - Review & Editing, Visualization
M.V.: Conceptualization, Software, Formal analysis, Data Curation, Writing - Original Draft
I.F.: Conceptualization, Validation, Writing - Review & Editing, Supervision, Project administration, Funding acquisition
S.L.C.: Conceptualization, Validation, Writing - Review & Editing, Supervision, Project administration, Funding acquisition

8. References

[1] T.D. Ngo, A. Kashani, G. Imbalzano, K.T.Q. Nguyen, D. Hui, Additive manufacturing (3D printing): A review of materials, methods, applications and challenges, Compos. Part B Eng. 143 (2018) 172–196. https://doi.org/10.1016/j.compositesb.2018.02.012.

[2] J.-Y. Lee, J. An, C.K. Chua, Fundamentals and applications of 3D printing for novel materials, Appl. Mater. Today. 7 (2017) 120–133. https://doi.org/10.1016/j.apmt.2017.02.004.

[3] J. Ghorbani, J. Li, A.K. Srivastava, Application of optimized laser surface re-melting process on selective laser melted 316L stainless steel inclined parts, J. Manuf. Process. 56 (2020) 726–734. https://doi.org/10.1016/j.jmapro.2020.05.025.

[4] A.D. Ludovico, A. Angelastro, S.L. Campanelli, Experimental Analysis of the Direct Laser Metal Deposition Process, in: M.J. Er (Ed.), New Trends Technol. Devices, Comput. Commun. Ind. Syst., IntechOpen, Rijeka, 2010: p. Ch. 14. https://doi.org/10.5772/10431.

[5] S.A.M. Tofail, E.P. Koumoulos, A. Bandyopadhyay, S. Bose, L. O'Donoghue, C. Charitidis, Additive manufacturing: scientific and technological challenges, market uptake and opportunities, Mater. Today. 21 (2018) 22–37. https://doi.org/10.1016/j.mattod.2017.07.001.

[6] E. Langi, L.G. Zhao, P. Jamshidi, M.M. Attallah, V. V Silberschmidt, H. Willcock, F. Vogt, Microstructural and Mechanical Characterization of Thin-Walled Tube Manufactured with Selective Laser Melting for Stent Application, J. Mater. Eng. Perform. 30 (2021) 696–710. https://doi.org/10.1007/s11665-020-05366-9.

[7] F. Caiazzo, S.L. Campanelli, F. Cardaropoli, N. Contuzzi, V. Sergi, A.D. Ludovico, Manufacturing and characterization of similar to foam steel components processed through selective laser melting, Int. J. Adv. Manuf. Technol. 92 (2017) 2121–2130. https://doi.org/10.1007/s00170-017-0311-4.

[8] J. Sun, Y. Yang, D. Wang, Mechanical properties of regular hexahedral lattice structure formed by selective laser melting, Laser Phys. 23 (2013) 066101. https://doi.org/10.1088/1054-660X/23/6/066101.

[9] M. Hirsch, P. Dryburgh, S. Catchpole-Smith, R. Patel, L. Parry, S.D. Sharples, I.A. Ashcroft, A.T. Clare, Targeted rework strategies for powder bed additive manufacture, Addit. Manuf. 19 (2018) 127–133. https://doi.org/10.1016/j.addma.2017.11.011.

[10] L. Scime, J. Beuth, Anomaly detection and classification in a laser powder bed additive manufacturing process using a trained computer vision algorithm, Addit. Manuf. 19 (2018) 114–126. https://doi.org/10.1016/j.addma.2017.11.009.

[11] S.K. Everton, M. Hirsch, P. Stravroulakis, R.K. Leach, A.T. Clare, Review of in-situ process monitoring and in-situ metrology for metal additive manufacturing, Mater. Des. 95 (2016) 431–445. https://doi.org/10.1016/j.matdes.2016.01.099.

[12] G. Tapia, A. Elwany, A Review on Process Monitoring and Control in Metal-Based Additive Manufacturing, J. Manuf. Sci. Eng. 136 (2014). https://doi.org/10.1115/1.4028540.

[13] R. McCann, M.A. Obeidi, C. Hughes, É. McCarthy, D.S. Egan, R.K. Vijayaraghavan, A.M. Joshi, V. Acinas Garzon, D.P. Dowling, P.J. McNally, D. Brabazon, In-situ sensing, process monitoring and machine control in Laser Powder

Bed Fusion: A review, Addit. Manuf. 45 (2021) 102058. https://doi.org/10.1016/j.addma.2021.102058.

[14] B. Cheng, J. Lydon, K. Cooper, V. Cole, P. Northrop, K. Chou, Infrared thermal imaging for melt pool analysis in SLM: a feasibility investigation, Virtual Phys. Prototyp. 13 (2018) 8–13. https://doi.org/10.1080/17452759.2017.1392685.

[15] W. He, W. Shi, J. Li, H. Xie, In-situ monitoring and deformation characterization by optical techniques; part I: Laser-aided direct metal deposition for additive manufacturing, Opt. Lasers Eng. 122 (2019) 74–88. https://doi.org/10.1016/j.optlaseng.2019.05.020.

[16] Z. Tang, W. Liu, Y. Wang, K.M. Saleheen, Z. Liu, S. Peng, Z. Zhang, H. Zhang, A review on in situ monitoring technology for directed energy deposition of metals, Int. J. Adv. Manuf. Technol. 108 (2020) 3437–3463. https://doi.org/10.1007/s00170-020-05569-3.

[17] M. Molitch-Hou, Overview of additive manufacturing process, in: J. Zhang, Y.-G. Jung (Eds.), Addit. Manuf., Elsevier, 2018: pp. 1–38. https://doi.org/10.1016/B978-0-12-812155-9.00001-3.

[18] W.E. Frazier, Metal Additive Manufacturing: A Review, J. Mater. Eng. Perform. 23 (2014) 1917–1928. https://doi.org/10.1007/s11665-014-0958-z.

[19] M. Zenou, L. Grainger, Additive manufacturing of metallic materials, in: J. Zhang, Y.-G.B.T.-A.M. Jung (Eds.), Addit. Manuf., Elsevier, 2018: pp. 53–103. https://doi.org/10.1016/B978-0-12-812155-9.00003-7.

[20] Z. Sun, W. Guo, L. Li, Numerical modelling of heat transfer, mass transport and microstructure formation in a high deposition rate laser directed energy deposition process, Addit. Manuf. 33 (2020) 101175. https://doi.org/https://doi.org/10.1016/j.addma.2020.101175.

[21] V. Errico, S. Campanelli, A. Angelastro, M. Dassisti, M. Mazzarisi, C. Bonserio, Coaxial Monitoring of AISI 316L Thin Walls Fabricated by Direct Metal Laser Deposition, Materials (Basel). 14 (2021) 673. https://doi.org/10.3390/ma14030673.

[22] M. Mazzarisi, V. Errico, A. Angelastro, S.L. Campanelli, Influence of standoff distance and laser defocusing distance on direct laser metal deposition of a nickel-based superalloy, Int. J. Adv. Manuf. Technol. 120 (2022) 2407–2428. https://doi.org/10.1007/s00170-022-08945-3.

[23] V. Errico, S.L. Campanelli, A. Angelastro, M. Mazzarisi, G. Casalino, On the feasibility of AISI 304 stainless steel laser welding with metal powder, J. Manuf. Process. 56 (2020) 96–105. https://doi.org/10.1016/j.jmapro.2020.04.065.

[24] M. Izadi, A. Farzaneh, M. Mohammed, I. Gibson, B. Rolfe, A review of laser engineered net shaping (LENS) build and process parameters of metallic parts, Rapid Prototyp. J. 26 (2020) 1059–1078. https://doi.org/10.1108/RPJ-04-2018-0088.

[25] B.V. Krishna, S. Bose, A. Bandyopadhyay, Laser Processing of Net-Shape NiTi Shape Memory Alloy, Metall. Mater. Trans. A. 38 (2007) 1096–1103. https://doi.org/10.1007/s11661-007-9127-4.

[26] K.R. Balasubramanian, G. Buvanashekaran, K. Sankaranarayanasamy, Modeling of laser beam welding of stainless steel sheet butt joint using neural networks, CIRP J. Manuf. Sci. Technol. 3 (2010) 80–84. https://doi.org/10.1016/j.cirpj.2010.07.001.

[27] K. Manonmani, N. Murugan, G. Buvanasekaran, Effects of process parameters on the bead geometry of laser beam butt welded stainless steel sheets, Int. J. Adv. Manuf. Technol. 32 (2007) 1125–1133. https://doi.org/10.1007/s00170-006-0432-7.

[28] P. Pratt, S.D. Felicelli, L. Wang, C.R. Hubbard, Residual Stress Measurement of

Laser-Engineered Net Shaping AISI 410 Thin Plates Using Neutron Diffraction, Metall. Mater. Trans. A. 39 (2008) 3155–3163. https://doi.org/10.1007/s11661-008-9660-9.

[29] B. Vandenbroucke, J. Kruth, Selective laser melting of biocompatible metals for rapid manufacturing of medical parts, Rapid Prototyp. J. 13 (2007) 196–203. https://doi.org/10.1108/13552540710776142.

[30] J.B. Ferguson, B.F. Schultz, A.D. Moghadam, P.K. Rohatgi, Semi-empirical model of deposit size and porosity in 420 stainless steel and 4140 steel using laser engineered net shaping, J. Manuf. Process. 19 (2015) 163–170. https://doi.org/10.1016/j.jmapro.2015.06.026.

[31] P.A. Kobryn, E.H. Moore, S.L. Semiatin, The effect of laser power and traverse speed on microstructure, porosity, and build height in laser-deposited Ti-6Al-4V, Scr. Mater. 43 (2000) 299–305. https://doi.org/10.1016/S1359-6462(00)00408-5.

[32] W.A. Ayoola, W.J. Suder, S.W. Williams, Parameters controlling weld bead profile in conduction laser welding, J. Mater. Process. Technol. 249 (2017) 522–530. https://doi.org/https://doi.org/10.1016/j.jmatprotec.2017.06.026.

[33] E. Assuncao, S. Williams, D. Yapp, Interaction time and beam diameter effects on the conduction mode limit, Opt. Lasers Eng. 50 (2012) 823–828. https://doi.org/10.1016/j.optlaseng.2012.02.001.

[34] M. Ermurat, M. Ali Arslan, F. Erzincanli, I. Uzman, Process parameters investigation of a laser-generated single clad for minimum size using design of experiments, Rapid Prototyp. J. 19 (2013) 452–462. https://doi.org/10.1108/RPJ-06-2011-0062.

[35] G. Zhu, D. Li, A. Zhang, G. Pi, Y. Tang, The influence of standoff variations on the forming accuracy in laser direct metal deposition, Rapid Prototyp. J. 17 (2011) 98–106. https://doi.org/10.1108/13552541111113844.

[36] A.J. Pinkerton, L. Li, The significance of deposition point standoff variations in multiple-layer coaxial laser cladding (coaxial cladding standoff effects), Int. J. Mach. Tools Manuf. 44 (2004) 573–584. https://doi.org/https://doi.org/10.1016/j.ijmachtools.2004.01.001.

[37] G. Zhu, D. Li, A. Zhang, G. Pi, Y. Tang, The influence of laser and powder defocusing characteristics on the surface quality in laser direct metal deposition, Opt. Laser Technol. 44 (2012) 349–356. https://doi.org/10.1016/j.optlastec.2011.07.013.

[38] H. Tan, F. Zhang, R. Wen, J. Chen, W. Huang, Experiment study of powder flow feed behavior of laser solid forming, Opt. Lasers Eng. 50 (2012) 391–398. https://doi.org/https://doi.org/10.1016/j.optlaseng.2011.10.017.

[39] H. Tan, F. Zhang, X. Fu, J. Meng, G. Hu, W. Fan, W. Huang, Development of powder flow model of laser solid forming by analysis method, Int. J. Adv. Manuf. Technol. 82 (2016) 1421–1431. https://doi.org/10.1007/s00170-015-7481-8.

[40] H. Tan, W. Shang, F. Zhang, A.T. Clare, X. Lin, J. Chen, W. Huang, Process mechanisms based on powder flow spatial distribution in direct metal deposition, J. Mater. Process. Technol. 254 (2018) 361–372. https://doi.org/10.1016/j.jmatprotec.2017.11.026.

[41] J.I. Arrizubieta, A. Lamikiz, F. Klocke, S. Martínez, K. Arntz, E. Ukar, Evaluation of the relevance of melt pool dynamics in Laser Material Deposition process modeling, Int. J. Heat Mass Transf. 115 (2017) 80–91. https://doi.org/10.1016/j.ijheatmasstransfer.2017.07.011.

[42] D. Eisenbarth, P.M. Borges Esteves, F. Wirth, K. Wegener, Spatial powder flow measurement and efficiency prediction for laser direct metal deposition, Surf. Coatings Technol. 362 (2019) 397–408. https://doi.org/https://doi.org/10.1016/j.surfcoat.2019.02.009.

[43] H. Tan, C. Zhang, W. Fan, F. Zhang, X. Lin, J. Chen, W. Huang, Dynamic evolution of powder stream convergence with powder feeding durations in direct energy deposition, Int. J. Mach. Tools Manuf. 157 (2020) 103606. https://doi.org/https://doi.org/10.1016/j.ijmachtools.2020.103606.

[44] D. Abdoh, DIRECT MOVING LOAD ENVELOPE ANALYSIS EQUATIONS FOR BRIDGE GIRDERS, Int. J. Bridg. Eng. 7 (2019) 1–22. http://gateway.isiknowledge.com/gateway/Gateway.cgi?GWVersion=2&SrcAuth=LinksAMR&SrcApp=PARTNER_APP&DestLinkType=FullRecord&DestApp=WOS&KeyUT=000510169500001.

[45] E.J. O'Brien, R.E. Loov, A method for the derivation of load effect envelopes based on statistical considerations, Can. J. Civ. Eng. 20 (1993) 201–209. https://doi.org/10.1139/l93-025.

[46] M.J. Cassidy, M. Uzielli, Y. Tian, Probabilistic combined loading failure envelopes of a strip footing on spatially variable soil, Comput. Geotech. 49 (2013) 191–205. https://doi.org/https://doi.org/10.1016/j.compgeo.2012.10.008.

[47] J. Liu, L. Li, Effects of powder concentration distribution on fabrication of thin-wall parts in coaxial laser cladding, Opt. Laser Technol. 37 (2005) 287–292. https://doi.org/10.1016/j.optlastec.2004.04.009.

[48] M. Duocastella, C.B. Arnold, Bessel and annular beams for materials processing, Laser Photon. Rev. 6 (2012) 607–621. https://doi.org/10.1002/lpor.201100031.

[49] A. Hemmasian Ettefagh, S. Guo, J. Raush, Corrosion performance of additively manufactured stainless steel parts: A review, Addit. Manuf. 37 (2021) 101689. https://doi.org/10.1016/j.addma.2020.101689.

[50] K. Zhang, W. Liu, X. Shang, Research on the processing experiments of laser metal deposition shaping, Opt. Laser Technol. 39 (2007) 549–557. https://doi.org/10.1016/j.optlastec.2005.10.009.

[51] S. Ocylok, E. Alexeev, S. Mann, A. Weisheit, K. Wissenbach, I. Kelbassa, Correlations of Melt Pool Geometry and Process Parameters During Laser Metal Deposition by Coaxial Process Monitoring, Phys. Procedia. 56 (2014) 228–238. https://doi.org/10.1016/j.phpro.2014.08.167.

[52] A.J. Pinkerton, L. Li, The significance of deposition point standoff variations in multiple-layer coaxial laser cladding (coaxial cladding standoff effects), Int. J. Mach. Tools Manuf. 44 (2004) 573–584. https://doi.org/10.1016/j.ijmachtools.2004.01.001.

[53] M. Mazzarisi, S.L. Campanelli, A. Angelastro, F. Palano, M. Dassisti, In situ monitoring of direct laser metal deposition of a nickel-based superalloy using infrared thermography, Int. J. Adv. Manuf. Technol. 112 (2021) 157–173. https://doi.org/10.1007/s00170-020-06344-0.

[54] R. Parekh, R.K. Buddu, R.I. Patel, Multiphysics Simulation of Laser Cladding Process to Study the Effect of Process Parameters on Clad Geometry, Procedia Technol. 23 (2016) 529–536. https://doi.org/10.1016/j.protcy.2016.03.059.

[55] M. Mazzarisi, S.L. Campanelli, A. Angelastro, M. Dassisti, Phenomenological modelling of direct laser metal deposition for single tracks, Int. J. Adv. Manuf. Technol. 111 (2020) 1955–1970. https://doi.org/10.1007/s00170-020-06204-x.

[56] B. Dutta, Directed Energy Deposition (DED) Technology, in: F.G.B.T.-E. of M.M. and A. Caballero (Ed.), Encycl. Mater. Met. Alloy., Elsevier, Oxford, 2022: pp. 66–84. https://doi.org/10.1016/B978-0-12-819726-4.00035-1.

[57] K.S.B. Ribeiro, F.E. Mariani, R.T. Coelho, A Study of Different Deposition Strategies in Direct Energy Deposition (DED) Processes, Procedia Manuf. 48 (2020) 663–670. https://doi.org/10.1016/j.promfg.2020.05.158.

[58] J. Yu, X. Lin, L. Ma, J. Wang, X. Fu, J. Chen, W. Huang, Influence of laser deposition patterns on part distortion, interior quality and mechanical properties by laser solid forming (LSF), Mater. Sci. Eng. A. 528 (2011) 1094–1104. https://doi.org/10.1016/j.msea.2010.09.078.

[59] Z. Zhou, Q. Lei, Z. Yan, Z. Wang, Y. Shang, Y. Li, H. Qi, L. Jiang, Y. Liu, L. Huang, Effects of process parameters on microstructure and cracking susceptibility of a single crystal superalloy fabricated by directed energy deposition, Mater. Des. 198 (2021) 109296. https://doi.org/https://doi.org/10.1016/j.matdes.2020.109296.

[60] J. Yan, I. Battiato, G.M. Fadel, Planning the process parameters for the direct metal deposition of functionally graded parts based on mathematical models, J. Manuf. Process. 31 (2018) 56–71. https://doi.org/10.1016/j.jmapro.2017.11.001.

[61] C. Guévenoux, S. Hallais, A. Charles, E. Charkaluk, A. Constantinescu, Influence of interlayer dwell time on the microstructure of Inconel 718 Laser Cladded components, Opt. Laser Technol. 128 (2020) 106218. https://doi.org/10.1016/j.optlastec.2020.106218.

[62] M. Manjaiah, J.. Hascoët, M. Rauch, Effect of process parameters on track geometry, microstructural evolution on 316L stainless steel multi-layer clads, Mater. Sci. Eng. B. 259 (2020) 114583. https://doi.org/10.1016/j.mseb.2020.114583.

[63] F. Spranger, B. Graf, M. Schuch, K. Hilgenberg, M. Rethmeier, Build-up strategies for additive manufacturing of three dimensional Ti-6Al-4V-parts produced by laser metal deposition, J. Laser Appl. 30 (2018) 022001. https://doi.org/10.2351/1.4997852.

[64] X. Wang, F. Lv, L.-D. Shen, H.-X. Liang, D.-Q. Xie, Z.-J. Tian, Influence of Island Scanning Strategy on Microstructures and Mechanical Properties of Direct Laser-Deposited Ti–6Al–4V Structures, Acta Metall. Sin. (English Lett. 32 (2019) 1173–1180. https://doi.org/10.1007/s40195-018-0858-6.

[65] J. Wang, J. Zhang, G. Liu, L. Liang, G. Yang, A. Huang, S. Pang, Effects of scanning strategies on residual stress and deformation by high-power direct energy deposition: Island size and laser jump strategy between islands, J. Manuf. Process. 75 (2022) 23–40. https://doi.org/10.1016/j.jmapro.2021.12.054.

[66] S.R. Lewis, R. Lewis, D.I. Fletcher, Assessment of laser cladding as an option for repairing/enhancing rails, Wear. 330–331 (2015) 581–591. https://doi.org/10.1016/j.wear.2015.02.027.

[67] W.J. Oh, W.J. Lee, M.S. Kim, J.B. Jeon, D.S. Shim, Repairing additive-manufactured 316L stainless steel using direct energy deposition, Opt. Laser Technol. 117 (2019) 6–17. https://doi.org/10.1016/j.optlastec.2019.04.012.

[68] S. Wei, G. Wang, L. Wang, Y. Rong, Characteristics of microstructure and stresses and their effects on interfacial fracture behavior for laser-deposited maraging steel, Mater. Des. 137 (2018) 56–67. https://doi.org/10.1016/j.matdes.2017.10.020.

[69] V. Errico, A. Fusco, S.L. Campanelli, Effect of DED coating and DED + Laser scanning on surface performance of L-PBF stainless steel parts, Surf. Coatings Technol. 429 (2022) 127965. https://doi.org/10.1016/j.surfcoat.2021.127965.

[70] D.R. Feenstra, R. Banerjee, H.L. Fraser, A. Huang, A. Molotnikov, N. Birbilis, Critical review of the state of the art in multi-material fabrication via directed energy deposition, Curr. Opin. Solid State Mater. Sci. 25 (2021) 100924. https://doi.org/10.1016/j.cossms.2021.100924.

[71] N. Uçak, A. Çiçek, K. Aslantas, Machinability of 3D printed metallic materials fabricated by selective laser melting and electron beam melting: A review, J. Manuf. Process. 80 (2022) 414–457. https://doi.org/10.1016/j.jmapro.2022.06.023.

[72] M.G. Guerra, V. Errico, A. Fusco, F. Lavecchia, S.L. Campanelli, L.M. Galantucci, High resolution-optical tomography for in-process layerwise monitoring of a laser-powder bed fusion technology, Addit. Manuf. 55 (2022) 102850. https://doi.org/10.1016/j.addma.2022.102850.

[73] S. Sun, M. Brandt, M. Easton, Powder bed fusion processes, in: M.B.T.-L.A.M. Brandt (Ed.), Laser Addit. Manuf., Elsevier, 2017: pp. 55–77. https://doi.org/10.1016/B978-0-08-100433-3.00002-6.

[74] S. Shrestha, T. Starr, K. Chou, A Study of Keyhole Porosity in Selective Laser Melting: Single-Track Scanning With Micro-CT Analysis, J. Manuf. Sci. Eng. 141 (2019). https://doi.org/10.1115/1.4043622.

[75] A. Kirchheim, Y. Katrodiya, L. Zumofen, F. Ehrig, C. Wick, Dynamic conformal cooling improves injection molding, Int. J. Adv. Manuf. Technol. 114 (2021) 107–116. https://doi.org/10.1007/s00170-021-06794-0.

[76] F. Calignano, D. Manfredi, E.P. Ambrosio, S. Biamino, M. Lombardi, E. Atzeni, A. Salmi, P. Minetola, L. Iuliano, P. Fino, Overview on Additive Manufacturing Technologies, Proc. IEEE. 105 (2017) 593–612. https://doi.org/10.1109/JPROC.2016.2625098.

[77] C. Wei, L. Li, Recent progress and scientific challenges in multi-material additive manufacturing via laser-based powder bed fusion, Virtual Phys. Prototyp. 16 (2021) 347–371. https://doi.org/10.1080/17452759.2021.1928520.

[78] K. Lei, X. Qin, H. Liu, M. Ni, Analysis and modeling of melt pool morphology for high power diode laser cladding with a rectangle beam spot, Opt. Lasers Eng. 110 (2018) 89–99. https://doi.org/10.1016/j.optlaseng.2018.05.022.

[79] M. Akbari, R. Kovacevic, Closed loop control of melt pool width in robotized laser powder–directed energy deposition process, Int. J. Adv. Manuf. Technol. 104 (2019) 2887–2898. https://doi.org/10.1007/s00170-019-04195-y.

[80] S. Ocylok, E. Alexeev, S. Mann, A. Weisheit, K. Wissenbach, I. Kelbassa, Correlations of Melt Pool Geometry and Process Parameters During Laser Metal Deposition by Coaxial Process Monitoring, Phys. Procedia. 56 (2014) 228–238. https://doi.org/10.1016/j.phpro.2014.08.167.

[81] R. Sampson, R. Lancaster, M. Sutcliffe, D. Carswell, C. Hauser, J. Barras, An improved methodology of melt pool monitoring of direct energy deposition processes, Opt. Laser Technol. 127 (2020) 106194. https://doi.org/10.1016/j.optlastec.2020.106194.

[82] A. Vandone, S. Baraldo, A. Valente, F. Mazzucato, Vision-based melt pool monitoring system setup for additive manufacturing, Procedia CIRP. 81 (2019) 747–752. https://doi.org/10.1016/j.procir.2019.03.188.

[83] Y. Ding, J. Warton, R. Kovacevic, Development of sensing and control system for robotized laser-based direct metal addition system, Addit. Manuf. 10 (2016) 24–35. https://doi.org/10.1016/j.addma.2016.01.002.

[84] C. Kledwig, H. Perfahl, M. Reisacher, F. Brückner, J. Bliedtner, C. Leyens,

Analysis of Melt Pool Characteristics and Process Parameters Using a Coaxial Monitoring System during Directed Energy Deposition in Additive Manufacturing, Materials (Basel). 12 (2019) 308. https://doi.org/10.3390/ma12020308.

[85] I. Garmendia, J. Pujana, A. Lamikiz, M. Madarieta, J. Leunda, Structured light-based height control for laser metal deposition, J. Manuf. Process. 42 (2019) 20–27. https://doi.org/10.1016/j.jmapro.2019.04.018.

[86] H.-W. Hsu, Y.-L. Lo, M.-H. Lee, Vision-based inspection system for cladding height measurement in Direct Energy Deposition (DED), Addit. Manuf. 27 (2019) 372–378. https://doi.org/10.1016/j.addma.2019.03.017.

[87] R.D. Murphy, E.C. Forrest, A Review of In-situ Temperature Measurements for Additive Manufacturing Technologies, 2016 NCSL Int. Work. Symp. (2016).

[88] A. Emamian, M.H. Farshidianfar, A. Khajepour, Thermal monitoring of microstructure and carbide morphology in direct metal deposition of Fe-Ti-C metal matrix composites, J. Alloys Compd. 710 (2017) 20–28. https://doi.org/10.1016/j.jallcom.2017.03.207.

[89] I. Smurov, M. Doubenskaia, S. Grigoriev, A. Nazarov, Optical Monitoring in Laser Cladding of Ti6Al4V, J. Therm. Spray Technol. 21 (2012) 1357–1362. https://doi.org/10.1007/s11666-012-9808-4.

[90] D. De Baere, W. Devesse, B. De Pauw, L. Smeesters, H. Thienpont, P. Guillaume, Spectroscopic monitoring and melt pool temperature estimation during the laser metal deposition process, J. Laser Appl. 28 (2016) 022303. https://doi.org/10.2351/1.4943995.

[91] L. Song, V. Bagavath-Singh, B. Dutta, J. Mazumder, Control of melt pool temperature and deposition height during direct metal deposition process, Int. J. Adv. Manuf. Technol. 58 (2012) 247–256. https://doi.org/10.1007/s00170-011-3395-2.

[92] S. Liu, P. Farahmand, R. Kovacevic, Optical monitoring of high power direct diode laser cladding, Opt. Laser Technol. 64 (2014) 363–376. https://doi.org/10.1016/j.optlastec.2014.06.002.

[93] F. Caltanissetta, M. Grasso, S. Petrò, B.M. Colosimo, Characterization of in-situ measurements based on layerwise imaging in laser powder bed fusion, Addit. Manuf. 24 (2018) 183–199. https://doi.org/10.1016/j.addma.2018.09.017.

[94] J. Liu, Z. Fan, S.I. Olsen, K.H. Christensen, J.K. Kristensen, Boosting Active Contours for Weld Pool Visual Tracking in Automatic Arc Welding, IEEE Trans. Autom. Sci. Eng. 14 (2017) 1096–1108. https://doi.org/10.1109/TASE.2015.2498929.

[95] T.F. Chan, L.A. Vese, Active contours without edges, IEEE Trans. Image Process. 10 (2001) 266–277. https://doi.org/10.1109/83.902291.

[96] M. Doubenskaia, M. Pavlov, S. Grigoriev, I. Smurov, Definition of brightness temperature and restoration of true temperature in laser cladding using infrared camera, Surf. Coatings Technol. 220 (2013) 244–247. https://doi.org/10.1016/j.surfcoat.2012.10.044.

[97] Q. Yang, Z. Yuan, X. Zhi, Z. Yan, H. Tian, X. Chen, Real-time width control of molten pool in laser engineered net shaping based on dual-color image, Opt. Laser Technol. 123 (2020) 105925. https://doi.org/10.1016/j.optlastec.2019.105925.

[98] P. Yadav, O. Rigo, C. Arvieu, E. Le Guen, E. Lacoste, In Situ Monitoring Systems of The SLM Process: On the Need to Develop Machine Learning Models for Data Processing, Crystals. 10 (2020) 524. https://doi.org/10.3390/cryst10060524.

[99] M. Grasso, B.M. Colosimo, Process defects and in situ monitoring methods in metal powder bed fusion: a review, Meas. Sci. Technol. 28 (2017) 044005. https://doi.org/10.1088/1361-6501/aa5c4f.

[100] M. Mani, B. Lane, A. Donmez, S. Feng, S. Moylan, R. Fesperman, Measurement Science Needs for Real-time Control of Additive Manufacturing Powder Bed Fusion Processes, NIST Interagency/Internal Report (NISTIR), National Institute of Standards and Technology, Gaithersburg, MD, Gaithersburg, MD, 2015. https://doi.org/10.6028/NIST.IR.8036.

[101] B.M. Colosimo, M. Grasso, In-situ monitoring in L-PBF: opportunities and challenges, Procedia CIRP. 94 (2020) 388–391. https://doi.org/10.1016/j.procir.2020.09.151.

[102] S. Coeck, M. Bisht, J. Plas, F. Verbist, Prediction of lack of fusion porosity in selective laser melting based on melt pool monitoring data, Addit. Manuf. 25 (2019) 347–356. https://doi.org/10.1016/j.addma.2018.11.015.

[103] S. Berumen, F. Bechmann, S. Lindner, J.-P. Kruth, T. Craeghs, Quality control of laser- and powder bed-based Additive Manufacturing (AM) technologies, Phys. Procedia. 5 (2010) 617–622. https://doi.org/10.1016/j.phpro.2010.08.089.

[104] D. Yang, H. Li, S. Liu, C. Song, Y. Yang, S. Shen, J. Lu, Z. Liu, Y. Zhu, In situ capture of spatter signature of SLM process using maximum entropy double threshold image processing method based on genetic algorithm, Opt. Laser Technol. 131 (2020) 106371. https://doi.org/10.1016/j.optlastec.2020.106371.

[105] P.J. DePond, G. Guss, S. Ly, N.P. Calta, D. Deane, S. Khairallah, M.J. Matthews, In situ measurements of layer roughness during laser powder bed fusion additive manufacturing using low coherence scanning interferometry, Mater. Des. 154 (2018) 347–359. https://doi.org/10.1016/j.matdes.2018.05.050.

[106] B. Zhang, J. Ziegert, F. Farahi, A. Davies, In situ surface topography of laser powder bed fusion using fringe projection, Addit. Manuf. 12 (2016) 100–107. https://doi.org/10.1016/j.addma.2016.08.001.

[107] J. zur Jacobsmühlen, J. Achterhold, S. Kleszczynski, G. Witt, D. Merhof, In situ measurement of part geometries in layer images from laser beam melting processes, Prog. Addit. Manuf. 4 (2019) 155–165. https://doi.org/10.1007/s40964-018-0068-9.

[108] L. Pagani, M. Grasso, P.J. Scott, B.M. Colosimo, Automated layerwise detection of geometrical distortions in laser powder bed fusion, Addit. Manuf. 36 (2020) 101435. https://doi.org/10.1016/j.addma.2020.101435.

[109] J. Bamberg, G. Zenzinger, A. Ladewig, In-Process Control of Selective Laser Melting by Quantitative Optical Tomography, in: 19th World Conf. Non-Destructive Test. 2016, 2016.

[110] G. Mohr, S.J. Altenburg, A. Ulbricht, P. Heinrich, D. Baum, C. Maierhofer, K. Hilgenberg, In-Situ Defect Detection in Laser Powder Bed Fusion by Using Thermography and Optical Tomography—Comparison to Computed Tomography, Metals (Basel). 10 (2020) 103. https://doi.org/10.3390/met10010103.

[111] M.G. Guerra, L. De Chiffre, F. Lavecchia, L.M. Galantucci, Use of Miniature Step Gauges to Assess the Performance of 3D Optical Scanners and to Evaluate the Accuracy of a Novel Additive Manufacture Process, Sensors. 20 (2020) 738. https://doi.org/10.3390/s20030738.

[112] E. Cuesta, S. Giganto, B.J. Alvarez, J. Barreiro, S. Martínez-Pellitero, V. Meana, Laser line scanner aptitude for the measurement of Selective Laser Melting parts, Opt. Lasers Eng. 138 (2021) 106406.

https://doi.org/10.1016/j.optlaseng.2020.106406.

[113] F. Imani, A. Gaikwad, M. Montazeri, P. Rao, H. Yang, E. Reutzel, Process Mapping and In-Process Monitoring of Porosity in Laser Powder Bed Fusion Using Layerwise Optical Imaging, J. Manuf. Sci. Eng. 140 (2018). https://doi.org/10.1115/1.4040615.

[114] F. Imani, A. Gaikwad, M. Montazeri, P. Rao, H. Yang, E. Reutzel, Layerwise In-Process Quality Monitoring in Laser Powder Bed Fusion, in: Vol. 1 Addit. Manuf. Bio Sustain. Manuf., American Society of Mechanical Engineers, 2018. https://doi.org/10.1115/MSEC2018-6477.

[115] B. Lane, S. Moylan, E.P. Whitenton, L. Ma, Thermographic measurements of the commercial laser powder bed fusion process at NIST, Rapid Prototyp. J. 22 (2016) 778–787. https://doi.org/10.1108/RPJ-11-2015-0161.

[116] H. Krauss, T. Zeugner, M.F. Zaeh, Layerwise Monitoring of the Selective Laser Melting Process by Thermography, Phys. Procedia. 56 (2014) 64–71. https://doi.org/10.1016/j.phpro.2014.08.097.

[117] H. Krauss, C. Eschey, M.F. Zaeh, Thermography for monitoring the selective laser melting process, 23rd Annu. Int. Solid Free. Fabr. Symp. - An Addit. Manuf. Conf. SFF 2012. (2012) 999–1014.

[118] J.C. Heigel, B.M. Lane, Measurement of the Melt Pool Length During Single Scan Tracks in a Commercial Laser Powder Bed Fusion Process, J. Manuf. Sci. Eng. 140 (2018). https://doi.org/10.1115/1.4037571.

[119] C.S. Lough, X. Wang, C.C. Smith, O. Adeniji, R.G. Landers, D.A. Bristow, E.C. Kinzel, Use of SWIR imaging to monitor layer-to-layer part quality during SLM of 304L stainless steel, Solid Free. Fabr. 2018 Proc. 29th Annu. Int. Solid Free. Fabr. Symp. - An Addit. Manuf. Conf. SFF 2018. (2020) 2228–2241.

[120] M. McMillan, M. Leary, C. Emmelmann, M. Brandt, SLM lattice thermal fields acquired by wide-field thermal camera, Procedia CIRP. 74 (2018) 122–126. https://doi.org/10.1016/j.procir.2018.08.059.

[121] E. Yasa, J. Deckers, T. Craeghs, M. Badrossamay, J.-P. Kruth, Investigation on occurrence of elevated edges in Selective Laser Melting, in: Twent. Annu. Int. Solid Free. Fabr. Symp., -, 2009.

[122] S. Kleszczynski, J. zur Jacobsmühlen, J.T. Sehrt, G. Witt, Error Detection in Laser Beam Melting Systems by High Resolution Imaging BT - Solid freeform fabrication proceedings, in: D.L. Bourell (Ed.), Solid Free. Fabr. Proc. / Bourell, David L. (Eds.). - 23rd Annu. Int. Solid Free. Fabr. Symp., Univ. of Texas at Austin, Austin, Tex., 2012: pp. 975–987.

[123] T.R. Gentile, A. Frenkel, A.L. Migdall, Z.M. Zhang, Neutral density filter measurements at the National Institute of Standards and Technology, in: C. Burgess, D.G.B.T.-A.S.L. Jones (Eds.), Spectrophotometry, Lumin. Colour; Sci. Compliance, Elsevier, 1995: pp. 129–136. https://doi.org/10.1016/S0926-4345(06)80011-8.

[124] T. Yang, T. Liu, W. Liao, H. Wei, C. Zhang, X. Chen, K. Zhang, Effect of processing parameters on overhanging surface roughness during laser powder bed fusion of AlSi10Mg, J. Manuf. Process. 61 (2021) 440–453. https://doi.org/10.1016/j.jmapro.2020.11.030.

[125] K. He, Q. Zhang, Y. Hong, Profile monitoring based quality control method for fused deposition modeling process, J. Intell. Manuf. 30 (2019) 947–958. https://doi.org/10.1007/s10845-018-1424-9.

[126] M.G. Guerra, F. Lavecchia, G. Maggipinto, L.M. Galantucci, G.A. Longo,

Measuring techniques suitable for verification and repairing of industrial components: A comparison among optical systems, CIRP J. Manuf. Sci. Technol. 27 (2019) 114–123. https://doi.org/10.1016/j.cirpj.2019.09.003.

[127] F. Bayle, M. Doubenskaia, Selective laser melting process monitoring with high speed infrared camera and pyrometer, in: V.P. Veiko (Ed.), Proc SPIE, 2008: pp. 698505-698505–8. https://doi.org/10.1117/12.786940.

[128] G. Mohr, S. Nowakowski, S.J. Altenburg, C. Maierhofer, K. Hilgenberg, Experimental Determination of the Emissivity of Powder Layers and Bulk Material in Laser Powder Bed Fusion Using Infrared Thermography and Thermocouples, Metals (Basel). 10 (2020) 1546. https://doi.org/10.3390/met10111546.

[129] J.-U. Park, S.-Y. Jun, B.H. Lee, J.H. Jang, B.-S. Lee, H.-J. Lee, J.-H. Lee, H.-U. Hong, Alloy design of Ni-based superalloy with high γ′ volume fraction suitable for additive manufacturing and its deformation behavior, Addit. Manuf. 52 (2022) 102680. https://doi.org/10.1016/j.addma.2022.102680.

[130] F. Calignano, Design optimization of supports for overhanging structures in aluminum and titanium alloys by selective laser melting, Mater. Des. 64 (2014) 203–213. https://doi.org/10.1016/j.matdes.2014.07.043.

[131] Z. Wu, S.P. Narra, A. Rollett, Exploring the fabrication limits of thin-wall structures in a laser powder bed fusion process, Int. J. Adv. Manuf. Technol. 110 (2020) 191–207. https://doi.org/10.1007/s00170-020-05827-4.

[132] G. Zhu, D. Li, A. Zhang, G. Pi, Y. Tang, The influence of laser and powder defocusing characteristics on the surface quality in laser direct metal deposition, Opt. Laser Technol. 44 (2012) 349–356. https://doi.org/10.1016/j.optlastec.2011.07.013.

[133] A. Dass, A. Moridi, State of the Art in Directed Energy Deposition: From Additive Manufacturing to Materials Design, Coatings. 9 (2019) 418. https://doi.org/10.3390/coatings9070418.

[134] T.H. Kim, G.Y. Baek, J.B. Jeon, K.Y. Lee, D. Shim, W. Lee, Effect of laser rescanning on microstructure and mechanical properties of direct energy deposited AISI 316L stainless steel, Surf. Coatings Technol. 405 (2021) 126540. https://doi.org/10.1016/j.surfcoat.2020.126540.

[135] L. Zhu, P. Xue, Q. Lan, G. Meng, Y. Ren, Z. Yang, P. Xu, Z. Liu, Recent research and development status of laser cladding: A review, Opt. Laser Technol. 138 (2021) 106915. https://doi.org/10.1016/j.optlastec.2021.106915.

[136] W.M. Steen, V.M. Weerasinghe, P. Monson, Some Aspects Of The Formation Of Laser Clad Tracks, in: Proc.SPIE, 1986: pp. 226–234. https://doi.org/10.1117/12.938104.

[137] J.T. Hofman, D.F. de Lange, B. Pathiraj, J. Meijer, FEM modeling and experimental verification for dilution control in laser cladding, J. Mater. Process. Technol. 211 (2011) 187–196. https://doi.org/10.1016/j.jmatprotec.2010.09.007.

[138] S.L. Campanelli, A. Angelastro, C.G. Signorile, G. Casalino, Investigation on direct laser powder deposition of 18 Ni (300) marage steel using mathematical model and experimental characterisation, Int. J. Adv. Manuf. Technol. 89 (2017) 885–895. https://doi.org/10.1007/s00170-016-9135-x.

[139] A. Hemmasian Ettefagh, S. Guo, J. Raush, Corrosion performance of additively manufactured stainless steel parts: A review, Addit. Manuf. 37 (2021) 101689. https://doi.org/10.1016/j.addma.2020.101689.

[140] J.A. Ramos, D.L. Bourell, Modeling of surface roughness enhancement of indirect-

SLS metal parts by laser surface polishing, in: TMS Fall Meet., 2002: pp. 191–202. https://doi.org/http://dx.doi.org/10.26153/tsw/3233.

[141] J.A. Ramos, D.L. Bourell, J.J. Beaman, Surface Over-Melt During Laser Polishing of Indirect-SLS Metal Parts, MRS Proc. 758 (2002) LL1.9. https://doi.org/10.1557/PROC-758-LL1.9.

[142] S.K. Everton, M. Hirsch, P. Stravroulakis, R.K. Leach, A.T. Clare, Review of in-situ process monitoring and in-situ metrology for metal additive manufacturing, Mater. Des. 95 (2016) 431–445. https://doi.org/10.1016/j.matdes.2016.01.099.

[143] J. Yan, M. Gao, X. Zeng, Study on microstructure and mechanical properties of 304 stainless steel joints by TIG, laser and laser-TIG hybrid welding, Opt. Lasers Eng. 48 (2010) 512–517. https://doi.org/10.1016/j.optlaseng.2009.08.009.

[144] E. Yasa, J. Deckers, J. Kruth, The investigation of the influence of laser re-melting on density, surface quality and microstructure of selective laser melting parts, Rapid Prototyp. J. 17 (2011) 312–327. https://doi.org/10.1108/13552541111156450.

[145] B. He, L. Zhang, Q. Zhu, J. Wang, X. Yun, J. Luo, Z. Chen, Effect of solution treated 316L layer fabricated by laser cladding on wear and corrosive wear resistance, Opt. Laser Technol. 121 (2020) 105788. https://doi.org/10.1016/j.optlastec.2019.105788.

[146] S. Yusuf, Y. Chen, R. Boardman, S. Yang, N. Gao, Investigation on Porosity and Microhardness of 316L Stainless Steel Fabricated by Selective Laser Melting, Metals (Basel). 7 (2017) 64. https://doi.org/10.3390/met7020064.

[147] K. Saeidi, X. Gao, Y. Zhong, Z.J. Shen, Hardened austenite steel with columnar sub-grain structure formed by laser melting, Mater. Sci. Eng. A. 625 (2015) 221–229. https://doi.org/10.1016/j.msea.2014.12.018.

[148] S. Gorsse, C. Hutchinson, M. Gouné, R. Banerjee, Additive manufacturing of metals: a brief review of the characteristic microstructures and properties of steels, Ti-6Al-4V and high-entropy alloys, Sci. Technol. Adv. Mater. 18 (2017) 584–610. https://doi.org/10.1080/14686996.2017.1361305.

[149] M.J. Zhan, G.F. Sun, Z.D. Wang, X.T. Shen, Y. Yan, Z.H. Ni, Numerical and experimental investigation on laser metal deposition as repair technology for 316L stainless steel, Opt. Laser Technol. 118 (2019) 84–92. https://doi.org/10.1016/j.optlastec.2019.05.011.

[150] B. Ravi Kumar, S. Sharma, B. Mahato, Formation of ultrafine grained microstructure in the austenitic stainless steel and its impact on tensile properties, Mater. Sci. Eng. A. 528 (2011) 2209–2216. https://doi.org/10.1016/j.msea.2010.11.034.

[151] L.K. Ang, Y.Y. Lau, R.M. Gilgenbach, H.L. Spindler, Analysis of laser absorption on a rough metal surface, Appl. Phys. Lett. 70 (1997) 696–698. https://doi.org/10.1063/1.118242.

[152] B. Blakey-Milner, P. Gradl, G. Snedden, M. Brooks, J. Pitot, E. Lopez, M. Leary, F. Berto, A. du Plessis, Metal additive manufacturing in aerospace: A review, Mater. Des. 209 (2021) 110008. https://doi.org/10.1016/j.matdes.2021.110008.

[153] M. Jiménez, L. Romero, I.A. Domínguez, M. del M. Espinosa, M. Domínguez, Additive Manufacturing Technologies: An Overview about 3D Printing Methods and Future Prospects, Complexity. 2019 (2019) 1–30. https://doi.org/10.1155/2019/9656938.

[154] S.G. Sarvankar, S.N. Yewale, Additive Manufacturing in Automobile Industry, Int. J. Res. Aeronaut. Mech. Eng. 7 (2019) 1–10.

https://www.mendeley.com/catalogue/8da7c324-eb1a-32f2-87d5-43f66643cff7/?utm_source=desktop&utm_medium=1.19.8&utm_campaign=open_catalog&userDocumentId=%7B6fca5734-d72e-43c2-9125-8e3f7f5b155d%7D.

[155] V. Errico, P. Posa, M. Mazzarisi, A. Angelastro, S.L. Campanelli, Effects of Laser-Deposited Maraging Steel on L-PBF 316L Component, Metals (Basel). 12 (2022) 1669. https://doi.org/10.3390/met12101669.

[156] J. Samei, H. Asgari, C. Pelligra, M. Sanjari, S. Salavati, A. Shahriari, M. Amirmaleki, M. Jahanbakht, A. Hadadzadeh, B.S. Amirkhiz, M. Mohammadi, A hybrid additively manufactured martensitic-maraging stainless steel with superior strength and corrosion resistance for plastic injection molding dies, Addit. Manuf. 45 (2021) 102068. https://doi.org/10.1016/j.addma.2021.102068.

[157] A.G. Demir, J. Kim, F. Caltanissetta, A.J. Hart, C.C. Tasan, B. Previtali, B.M. Colosimo, Enabling multi-material gradient structure in laser powder bed fusion, J. Mater. Process. Technol. 301 (2022) 117439. https://doi.org/10.1016/j.jmatprotec.2021.117439.

[158] S.L. Campanelli, N. Contuzzi, P. Posa, A. Angelastro, Study of the aging treatment on selective laser melted maraging 300 steel, Mater. Res. Express. 6 (2019) 066580. https://doi.org/10.1088/2053-1591/ab0c6e.

[159] M. Niu, G. Zhou, W. Wang, M.B. Shahzad, Y. Shan, K. Yang, Precipitate evolution and strengthening behavior during aging process in a 2.5 GPa grade maraging steel, Acta Mater. 179 (2019) 296–307. https://doi.org/10.1016/j.actamat.2019.08.042.

[160] Y. Jiang, Y. Cheng, X. Zhang, J. Yang, X. Yang, Z. Cheng, Simulation and experimental investigations on the effect of Marangoni convection on thermal field during laser cladding process, Optik (Stuttg). 203 (2020) 164044. https://doi.org/10.1016/j.ijleo.2019.164044.

[161] P. Bidare, A. Jiménez, H. Hassanin, K. Essa, Porosity, cracks, and mechanical properties of additively manufactured tooling alloys: a review, Adv. Manuf. 10 (2022) 175–204. https://doi.org/10.1007/s40436-021-00365-y.

[162] T. Simson, J. Koch, J. Rosenthal, M. Kepka, M. Zetek, I. Zetková, G. Wolf, P. Tomčík, J. Kulhánek, Mechanical Properties of 18Ni-300 maraging steel manufactured by LPBF, Procedia Struct. Integr. 17 (2019) 843–849. https://doi.org/10.1016/j.prostr.2019.08.112.

[163] G. Zenzinger, J. Bamberg, A. Ladewig, T. Hess, B. Henkel, W. Satzger, Process monitoring of additive manufacturing by using optical tomography, in: AIP Conf. Proc., American Institute of Physics, 2015: pp. 164–170. https://doi.org/10.1063/1.4914606.

[164] T. Maconachie, M. Leary, B. Lozanovski, X. Zhang, M. Qian, O. Faruque, M. Brandt, SLM lattice structures: Properties, performance, applications and challenges, Mater. Des. 183 (2019) 108137. https://doi.org/10.1016/j.matdes.2019.108137.

[165] I. Echeta, X. Feng, B. Dutton, R. Leach, S. Piano, Review of defects in lattice structures manufactured by powder bed fusion, Int. J. Adv. Manuf. Technol. 106 (2020) 2649–2668. https://doi.org/10.1007/s00170-019-04753-4.

[166] D. Li, R. Qin, B. Chen, J. Zhou, Analysis of mechanical properties of lattice structures with stochastic geometric defects in additive manufacturing, Mater. Sci. Eng. A. 822 (2021) 141666. https://doi.org/10.1016/j.msea.2021.141666.

[167] B. Lozanovski, D. Downing, R. Tino, P. Tran, D. Shidid, C. Emmelmann, M. Qian, P. Choong, M. Brandt, M. Leary, Image-Based Geometrical Characterization of

Nodes in Additively Manufactured Lattice Structures, 3D Print. Addit. Manuf. 8 (2021) 51–68. https://doi.org/10.1089/3dp.2020.0091.

[168] E.W. Jost, D.G. Moore, C. Saldana, Evolution of global and local deformation in additively manufactured octet truss lattice structures, Addit. Manuf. Lett. 1 (2021) 100010. https://doi.org/10.1016/j.addlet.2021.100010.

[169] F. Caiazzo, V. Alfieri, B.D. Bujazha, Additive manufacturing of biomorphic scaffolds for bone tissue engineering, Int. J. Adv. Manuf. Technol. 113 (2021) 2909–2923. https://doi.org/10.1007/s00170-021-06773-5.

[170] N. Contuzzi, S.L. Campanelli, F. Caiazzo, V. Alfieri, Design and Fabrication of Random Metal Foam Structures for Laser Powder Bed Fusion, Materials (Basel). 12 (2019) 1301. https://doi.org/10.3390/ma12081301.

[171] M. Mazur, M. Leary, M. McMillan, S. Sun, D. Shidid, M. Brandt, Mechanical properties of Ti6Al4V and AlSi12Mg lattice structures manufactured by Selective Laser Melting (SLM), in: M.B.T.-L.A.M. Brandt (Ed.), Laser Addit. Manuf., Elsevier, 2017: pp. 119–161. https://doi.org/10.1016/B978-0-08-100433-3.00005-1.

[172] F. Scalzo, G. Totis, E. Vaglio, M. Sortino, Experimental study on the high-damping properties of metallic lattice structures obtained from SLM, Precis. Eng. 71 (2021) 63–77. https://doi.org/10.1016/j.precisioneng.2021.02.010.

[173] M.G. Guerra, L.M. Galantucci, F. Lavecchia, L. De Chiffre, Reconstruction of small components using photogrammetry: a quantitative analysis of the depth of field influence using a miniature step gauge, Metrol. Meas. Syst. 28 (2021) 323–342–323–342. https://doi.org/10.24425/mms.2021.136610.

[174] R. Acharya, R. Bansal, J.J. Gambone, M.A. Kaplan, G.E. Fuchs, N.G. Rudawski, S. Das, Additive Manufacturing and Characterization of René 80 Superalloy Processed Through Scanning Laser Epitaxy for Turbine Engine Hot-Section Component Repair, Adv. Eng. Mater. 17 (2015) 942–950. https://doi.org/10.1002/adem.201400589.

[175] C. Tan, X. Zhang, D. Dong, B. Attard, D. Wang, M. Kuang, W. Ma, K. Zhou, In-situ synthesised interlayer enhances bonding strength in additively manufactured multi-material hybrid tooling, Int. J. Mach. Tools Manuf. 155 (2020) 103592. https://doi.org/10.1016/j.ijmachtools.2020.103592.

[176] C. Wei, L. Liu, H. Cao, X. Zhong, X. Xu, Y. Gu, D. Cheng, Y. Huang, Z. Li, W. Guo, Z. Liu, L. Li, Cu10Sn to Ti6Al4V bonding mechanisms in laser-based powder bed fusion multiple material additive manufacturing with different build strategies, Addit. Manuf. 51 (2022) 102588. https://doi.org/10.1016/j.addma.2021.102588.

[177] R. Wang, D. Gu, K. Lin, C. Chen, Q. Ge, D. Li, Multi-material additive manufacturing of a bio-inspired layered ceramic/metal structure: Formation mechanisms and mechanical properties, Int. J. Mach. Tools Manuf. 175 (2022) 103872. https://doi.org/10.1016/j.ijmachtools.2022.103872.